RESPONSE OF SUCTION CAISSONS IN SOFT CLAY UNDER VERTICAL AND HORIZONTAL LOADING FOR TIDAL ENERGY CONVERTER APPLICATIONS

BY

JEFF FRANKLIN WALLACE

DISSERTATION

Submitted in partial fulfillment of the requirements
for the degree of Doctor of Philosophy in Civil Engineering
in the Graduate College of the
University of Illinois at Urbana-Champaign, 2018

Urbana, Illinois

Doctoral Committee:

Assistant Professor Cassandra J. Rutherford, Chair and Director of Research
Professor Marcelo H. Garcia
Associate Professor Scott M. Olson
Assistant Professor Leonardo Particio Chamorro Chavez

ABSTRACT

In recent years, the push to reduce oil dependence has driven the research and use of renewable energy sources both on and offshore. Of the available offshore renewable energy resources, the tidal current serves as a promising and consistent source of energy due to its dependence on the rotation of the earth and the orbit of both the earth and the moon. Harnessing this energy requires the use of tidal energy converters (TECs), a technology that is still primarily in the development and prototyping phases. As such, design standards for TECs have not yet been developed. In order to develop such standards and deploy an economical, efficient, and reliable final product, all components of the TEC including the foundations must be thoroughly understood.

TEC loading conditions will primarily be cyclic with the static loads resulting from the dead weight of the structure. The cyclic loads will have various components with periods up to approximately 24 hours and be strongly correlated to the tidal current's flow characteristics. The TEC's function and the tidal current's flow characteristics provide a unique set of loading conditions when compared to traditional offshore energy structures for oil and gas. First, the vertical dead weight of the structure will be relatively low. Second, the TEC will be designed to interact with the horizontal flow of water. Third, the primarily environmental load will reverse direction approximately every 12 to 24 hours with the ebb and flood of the tide. Suction caissons provide a foundation element that are theoretically well equipped to resist these unique set of loading conditions while further contributing to the 'green' nature of the TEC.

This study investigated the response of intermediate aspect ratio suction caissons in clay under loads applicable to TEC loading through the use of loads tests on three types of scaled physical models. The 1-g model scale load tests in kaolin and 90-g centrifuge scale load tests in kaolin allowed for the investigation of a wide range of loading conditions both monotonic and cyclic in the vertical and horizontal direction. These vertically and horizontally directed loads functioned as simplified loading conditions on suction caissons configured as multipods and monopods. The 1-g model scale load tests in laponite allowed for visualization of the failure mechanism of clay during vertical loading of suction caissons. These visualizations allowed for a comparison of the mobilized failure mechanism to the failure mechanism assumed in the design of suction caissons.

To my family and my friends who have become like family

ACKNOWLEDGEMENTS

I would like to express my sincerest gratitude to my advisor Professor Cassandra J. Rutherford for her unwavering support throughout my Ph.D. degree. The completion of this dissertation and the research and coursework leading up to it would not have been possible without her guidance and mentorship. I could not have asked for a better advisor throughout my dissertation studies.

In addition to my advisor, I would like to thank the remainder of my dissertation committee: Professors Marcelo H. Garcia, Scott M. Olson, and Leonardo Particio Chamorro Chavez. Their support, questions, and commentary regarding my dissertation topic allowed me to approach my research from various perspectives as seen through their various research specialty areas. In addition to my committee members, I would like to also thank all faculty that have supported me throughout my undergraduate education at UCLA and graduate educations at CPSLO and UIUC. Particularly, Prof. Gholamreza Mesri, James H. Long, and Gregg Fiegel.

I thank my fellow classmates and labmates at UIUC for their stimulating discussions, early mornings and late nights while working on projects, and great times over the last six years. Also, I would like to thank my friends at UIUC and beyond for allowing me to keep a healthy work-life balance. A special thank you to Hannah A.C. Lohman for her love and support. A shout out to members of the "geotechnical trinity", "boy's house / girl's house", Christ Community CU, and Inter Varsity Graduate Christian Fellowship for their support as well.

A very special thank you must be extended to my mother and father. For without their unwavering love and support throughout my life, I would not have made it to this point in my academic career. They serve as critical role models and motivation in all aspects of my life.

Lastly, I would like to thank God for all he has done throughout my life and this degree.

All the best,

Jeff Franklin Wallace

TABLE OF CONTENTS

CHAPTER 1. INTRODUCTION

1.1 General

Suction caissons are foundations that can be best described as overturned steel buckets as shown in Figure 1.1 and Figure 1.2. First used in the offshore energy industry to replace piles for the Europipe 16/11-E Jacket (Tjelta 1994), suction caisson foundations are installed by a combination of self weight embedment followed by suction generated by pumping water out of the inside cavity. This installation method does not require the use of equipment such as large, heavy-duty cranes or hammers needed to install large gravity base foundations or piles respectively. However, this method does require specialized equipment such as remote operated vehicles and may require larger transport vessels due to the larger diameter of suction caissons compared to piles. Even with these considerations, the reduction of installation time combined with not needing to mobilize the aforementioned equipment offers a potential for cost savings making suction caissons an attractive foundation for offshore use (Byrne 2000). Additionally, the suction caisson contributes towards the "green" aspect of alternative energy structures as they can be removed at the end of their design life by reversing the installation process and they mitigate the environmental impact of hammer driven installation via noise reduction.

1.2 Motivation

The drive to reduce oil dependence has driven the exploration and use of renewable or "green" energy sources available offshore. Tidal currents are one such renewable energy source. They are highly promising due to their dependence on the consistent global processes of the earth's and the moon's respective rotations and due to their proximity to the coastline where population centers exist. In recent years, extracting energy from the moving water of tidal currents through the use of Tidal Energy Converters (TECs) has received global interest with over 110 developers identified around the world (EPRI 2005, EMEC 2016). In the United States alone, over 207 sites across 13 states shown in Figure 1.3 through Figure 1.5 have been identified with high potential for producing tidal energy with a total theoretical available power of 51 GW (GTRC 2011). Multiple prototypes and scaled turbines have undergone deployment and testing in the U.S. (Johnson and Pride 2010, Verdant Power 2010). Of the six main types of TECs in development, over 55% utilize a design known as the horizontal axis turbine (EMEC

2016) where the rotor is oriented parallel to the seabed as shown in Figure 1.6. When the blade orientation is perpendicular to the rotor on a horizontal axis turbine, the TEC resembles the common configuration of the large offshore wind turbines in use today. This horizontal rotor configuration will be the assumed configuration of this study and resembles prototypes that have been deployed in East River, New York (Verdant Power 2010), Kvalsund, Norway (Andritz Hydro Hammerfest 2012), and Strangford Lough, Ireland (Marine Current Turbine 2013).

Due to the TEC being primarily in the prototyping and development phase, it is critical to thoroughly understand all components (e.g.) blades, rotor, generator, tower, foundation to deploy an economical and reliable final product. Thorough understanding of the foundation system's ability to maintain the orientation of the TEC in the water current profile requires an investigation of the foundation's load response under TEC loading. Similar to most offshore structures, TEC loading will be cyclic. However, the TEC exhibits the following unique loading aspects in comparison to traditional offshore oil and gas structures:

1. Similar to a wind turbine, the vertical dead weight of the TEC is typically low resulting in horizontal loading being a significant component of the overall loading conditions (Byrne and Houlsby 2003).
2. The TEC is designed to directly interact with the horizontal flow of water, an interaction that is typically minimized in most offshore structures (Houlsby et al. 2005, O'Doherty et al. 2009), resulting in direct correlation between current velocity and the lateral loads and resulting moments on the structure and therefore the foundation or foundations (Sæterstad 2011).
3. The ebb and flow of the tide results in a direction reversal of the current and thus the direction of the lateral loads on the structure up to approximately 4 times a day depending on the tidal classification at the site.

These three aspects require that careful attention be paid to the load response of the foundation due to fluctuations in the current velocity.

The suction caisson, described above, is an ideal foundation system for a TEC. It provides lateral and overturning resistance more efficiently than shallow foundation alternatives while not requiring hammer mobilization and minimizing noise pollution in comparison to deep foundation alternatives. The ability to remove the foundation after the design life of the structure further reinforces the "green" nature of the TEC system. Suction caisson foundations can be

placed in two configurations: the monopod (1 foundation) and the multipod (typically 3 to 4 foundations) as shown in Figure 1.1 and Figure 1.2 respectively. The former primarily resists the current loads on the structure by means of the foundation's moment and lateral resistance while the latter primarily resists the current loads by means of the foundation's compression and uplift resistance from opposing foundation legs (Byrne and Cassidy 2002). Regardless of the configuration, the suction caisson foundation must transfer the loads applied to or from the structure to the soil to prevent failure by either bearing capacity and serviceability constraints. Failure poses a threat to both human life and financial investment of a project making it critical that all components of the system perform reliably while at the same time being economical. Understanding how suction caissons behave under both standard and extreme TEC loading conditions allows for increased reliability in the foundation design resulting in greater cost efficiency of the TEC. The foundation element of the closely related offshore wind turbine can account for up to 35% of the installed cost (Byrne and Houlsby 2003). By increasing the efficiency and reliability of the foundation design, TEC technology can become a more economically feasible "green" energy resource.

While suction caissons have been utilized as foundation elements and anchoring elements, the majority of usage has been in the latter function. Additionally, suction caissons as a foundation element for offshore renewable energy sources has yet to find widespread use as of 2018. While significant research has been conducted for suction caisson foundations in relation to offshore wind turbine design, the behavior of suction caisson foundations in soft clay for TEC applications has yet to be conducted and design guidelines have yet to be developed.

1.3 Objectives and scope of research

The objectives of this research are as follows: 1) determine response of top-loaded suction caissons in the monopod and multipod configurations with aspect ratios or skirt length to diameter ratios of 1 and 2 in soft clay (kaolin) subjected to vertical and horizontal cyclic loads relevant to TEC applications; 2) visualize the failure mechanism of clay when subjected to monotonic vertical loading from a suction caisson with aspect ratios of 1 and 2 using laponite, a transparent soft clay surrogate; and 3) develop recommendations in regards to TEC foundation design. These objectives will be fulfilled by completion of the following tasks:

- **Task 1:** Study of background and existing literature

- **Task 2:** Determine relevant kaolin and laponite parameters
- **Task 3:** Design, setup, and conduct model scale tests in kaolin and laponite
- **Task 4:** Analyze load test data
- **Task 5:** Develop design recommendations

1.4 Figures

Figure 1.1: Monopod suction caisson foundation for a meteorological mast (Bakmar 2009)

Figure 1.2: Tripod suction caissons for a mooring application (Zhang et al. 2013)

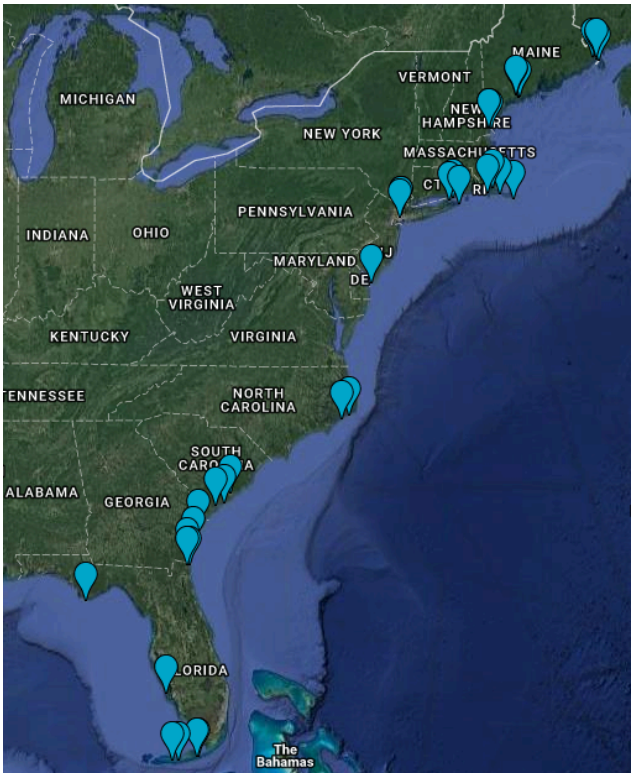

Figure 1.3: Tidal current hotspots located in the eastern half of the contiguous United States as identified by GTRC (2011)

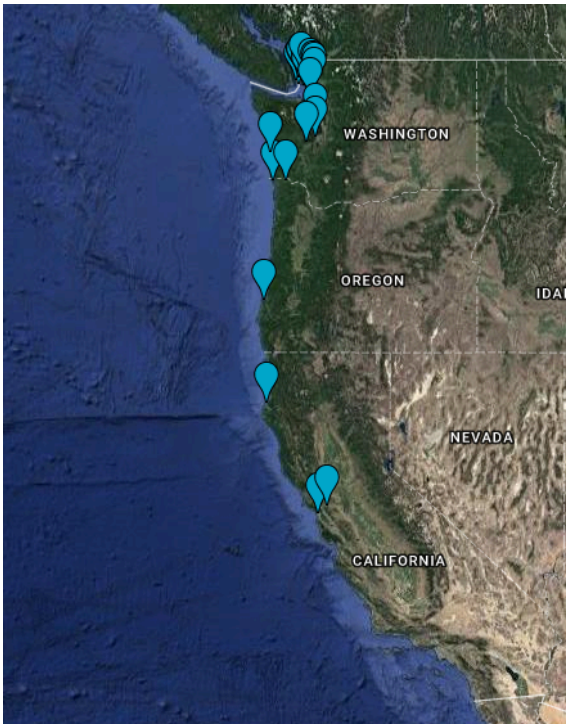

Figure 1.4: Tidal current hotspots located in the western half of the contiguous United States as identified by GTRC (2011)

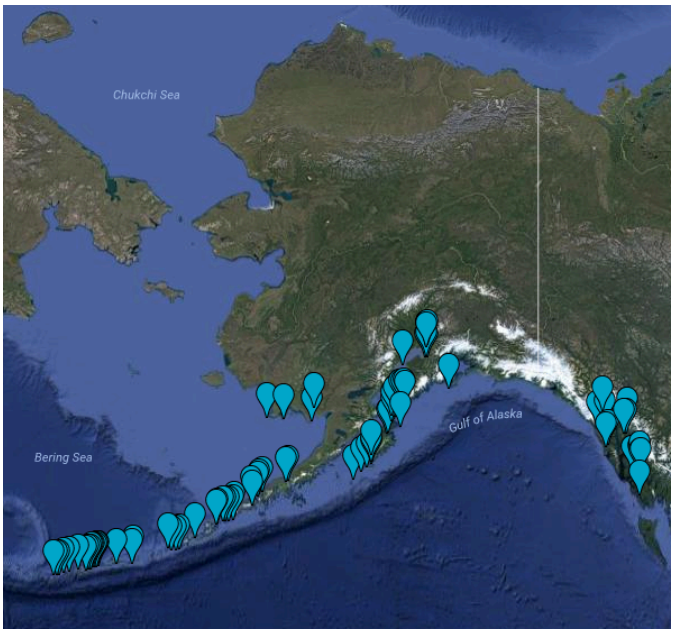

Figure 1.5: Tidal current hotspots located in Alaska as identified by GTRC (2011)

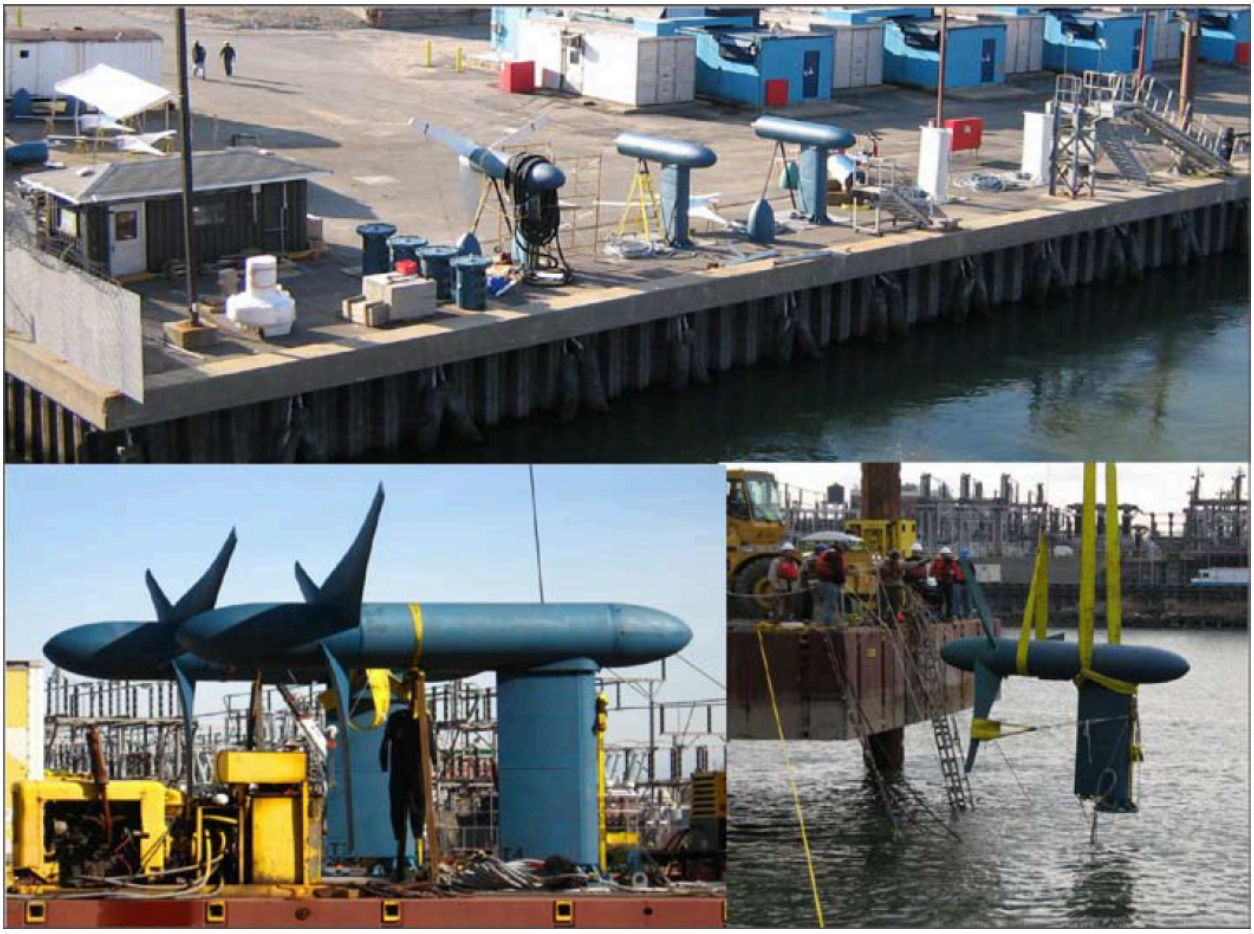

Figure 1.6: Horizontal axis tidal current turbine prototype assembly and deployment in the East River, New York (Verdant Power 2010)

1.5 References

Andritz Hydro Hammerfest. (2012). "ANDRITZ HYDRO Hammerfest – Renewable energy from tidal currents." Andritz Hydro Hammerfest, Hammerfest, Norway.

Bakmar, C.L. (2009). "The Monopod Bucket Foundation – Recent Experience and Challenges Ahead." Hamburg Offshore Wind 2009, 12 May 2009.

Byrne, B.W. (2000). "Investigations of suction caissons in dense sand." DPhil thesis. Univ. of Oxford, Oxford, England.

Byrne, B.W. & Cassidy, M.J. (2002). "Investigating the response of offshore foundations in soft clay soils." *Proceedings of OMAE'02 21st International conference of Offshore Mechanics and Arctic Engineering.* Oslo, Norway.

Byrne, B.W. & Houlsby, G.T. (2003). "Foundations for offshore wind turbines." *Phil. Trans. R. Soc. Lond.* A 361:2909-2930.

Electric Power Research Institute, Inc. (2005). *Ocean Tidal and Wave Energy – Renewable Energy Technical Assessment Guide – TAG-RE: 2005.* Electric Power Research Institute, Inc.

European Marine Energy Centre. (2016). "European Marine Energy Centre – Tidal Developers." European Marine Energy Centre (EMEC) Ltd., Stromness, Orkney, United Kingdom. Accessed January 2016.

Georgia Tech Research Corporation. (2011). "Assessment of energy Production Potential from Tidal Streams in the United States – Final Project Report." Georgia Tech Research Corporation, Atlanta, GA, USA.

Houlsby, G.T., Kelly, R.B., Huxtable, J., & Byrne, B.W. (2005). "Field trials of suction caissons in clay for offshore wind turbine foundations." *Geotechnique*. 55(4):287-296.

Johnson, J.B. & Pride, D.J. (2010). "River, Tidal, and Ocean Current Hydrokinetic Energy Technologies: Status and Future Opportunities in Alaska." Report prepared for Alaska Energy Authority by the Alaska Center for Energy and Power.

Marine Current Turbines. (2013). "SeaGen-S 2MW." Marine Current Turbines Ltd., Camberley, Surrey, United Kingdom.

O'Doherty, T., Egarr, D.A., Mason-Jones, A., & O'Doherty, D.M. (2009). "An assessment of axial loading on a five turbine array." *Proc. ICE, Energy*. 162(EN2):57–65.

Sæterstad, M.L. (2011). "Dimensioning Loads for a Tidal Turbine." M.S. Thesis, Norwegian University of Science and Technology.

Tjelta, T.I. (1994). "Geotechnical aspects of bucket foundations replacing piles for the Europipe 16/11E jacket." Offshore Technology Conference, Houston, Texas, USA.

Verdant Power. (2010). "Pilot License Application Roosevelt Island Tidal Energy Project: FERC No. 12611." Verdant Power, LLC, New York, NY, USA.

Zhang, P., Ding, H. & Le, C. (2013). "Installation and Removal Records of Field Trials for Two Mooring Dolphin Platforms with Three Suction Caissons." *Journal of Waterway, Port, Coastal, and Ocean Engineering*. 139(6):502-517.

CHAPTER 2. BACKGROUND AND CURRENT STATE OF KNOWLEDGE

2.1 Offshore foundation options for the TEC

Multiple options are available to fix offshore structures to the seabed, selections of which are shown in Figure 2.1. These options are categorized as foundations or anchors based on whether the water depth is less than or greater than 60 m respectively. Foundations are fixed directly to the structure while anchors are fixed to the structure via cables. The vast majority of tidal current hotspots reported in GTRC (2011) have a mean water depth less than 60 m indicating that foundations rather than anchors will be the primary option used to fix TECs to the seabed.

Foundations are generally categorized based on their aspect ratio which is defined as the ratio of the depth of embedment (D) to the width (B) of the foundation. These categories are shallow foundations ($D/B < 1$), deep foundations ($D/B > 4$), and intermediate or "stout" foundations ($1 \leq D/B \leq 4$). Shallow foundations transfer loads to the uppermost layers of the soil strata through the base area of the foundation. Examples of offshore shallow foundations include spudcans, gravity base footings, mudmats, and smaller aspect ratio suction caissons (a.k.a. suction installed skirted foundations). In general, shallow foundations are not well suited to resist significant lateral and overturning loads or are inefficient in doing so. Deep foundations are utilized in cases where the soil located near the surface is insufficient to provide the required bearing capacity, results in unacceptable settlement, or if significant horizontal resistance is required. The resistance of deep foundations is mobilized through a combination of two sources, the side resistance and the tip resistance. Deep foundations can provide additional resistance in comparison to a shallow foundation in the same location since the foundation can transfer the structural load to a larger area of soil and to deeper layers in the soil strata where soils generally have increased shear strength in comparison to those near the surface. Examples of offshore deep foundations include driven or drilled open-ended pipe piles and suction caissons. Currently open-ended pipe piles represent the largest knowledge base in terms of design and performance largely due to experience from their use in onshore applications. Suction caissons are a newer technology and have seen a rise in popularity since their first use in the early 1990s. "Intermediate" or "stout" foundations in the area of offshore geotechnics refer to shortened versions of deep foundations that mobilize resistance from both side resistance and tip resistance.

A wide range of foundations, both shallow and deep, have been identified as potential foundation types for TECs (Starling and Scott 2009, EMEC 2016). Shallow foundations, however, are limited to small-scale turbine devices as larger turbines will likely result in an unreasonably large and inefficient shallow foundation (Fraenkel 2010). This is particularly true in the very soft to soft clay deposits such as those identified at the Cobscook Bay tidal current turbine site (Maynard et al. 2013) which was identified as a tidal current "hotspot" by the GTRC (2011). The suction caisson has the following advantages in comparison to other deep foundation alternatives making it an ideal foundation for a TEC: quieter installation through the use of suction for locations with noise restrictions and for areas with environmental noise related concerns, able to be installed in deeper water where hammer use can be either very costly or not feasible, and can be easily removed after the design life of the TEC. This study will focus on the use of a suction caissons with an aspect ratio of 1 and 2 (shorter spectrum of intermediate aspect ratios) as the majority of past model testing has focused on suction caissons with aspect ratios considered shallow or deep and not those in between.

The environmental and operational loads of the TEC will be resisted primarily by differing mechanisms based on the configuration of the suction caisson foundations (Byrne and Cassidy 2002). With a tripod or tetrapod configuration, the loads will primarily be transmitted to the foundations as compression and uplift on opposing elements as shown in Figure 2.2a. With a monopod foundation, the loads will primarily be resisted directly by the rotational and lateral resistance of a single foundation element as shown in Figure 2.2b. While the multipod system can typically more efficiently resist TEC loads by mobilizing the resistance from the vertical loading mechanism, they also have the potential for increased fabrication costs due to the superstructure required to connect the suction caissons. This study will investigate the behavior of both the monopod and multipod system by generalizing the loading components to horizontal loading and vertical loading respectively.

2.2 TEC Foundation Loading

The tidal current has the largest influence on the loading of suction caisson foundations for a TEC. First and foremost, the TEC is designed to interact with the horizontal flow of water (in this case the tidal current). This is an interaction that results in a horizontal load component that is a relatively large percentage of the vertical load component and is an interaction that a vast majority of offshore oil and gas structures attempt to minimize (Houlsby et al. 2005,

O'Doherty et al. 2009). The rotating turbine blades and shafts, fluctuations in tidal current speed and direction, wave loading, turbulence, and vibrations all result in the combined loading of the foundation being cyclic with load components of varying frequency. All of these loading components can trace their dependence to the horizontal flow of water. The static loading of the foundation will result from the self-weight of the TEC and its support structure. The foundation must be designed to withstand these static and cyclic loads within required serviceability constraints. Figure 2.3 shows the nomenclature of potential loads on a single suction caisson foundation.

Since all but the dead weight are in some way related to the horizontal flow of water, it is important to understand the phenomena that is driving this flow. Tides are the periodic vertical movement of sea or ocean water resulting from the gravitational forces of the Sun and Moon. While the tide is the vertical rise and fall of water, the tidal current is the horizontal movement of water associated with the fluctuating tide. The tidal current floods when the tide rises and ebbs when the tide falls. Where the bathymetry or geography constrains the flow, the tidal current will have two peak velocities in approximately opposite directions with two periods of slack where the velocity is near zero.

Tides and tidal currents can fall into three classifications depending on the combination of their magnitude and frequency: semidiurnal, diurnal, or mixed. The semidiurnal tide has two high and low tides each day with a relatively small difference in high tides and low tides, the diurnal tide has a single high and low tide each day, and the mixed tide has a relatively large difference between either the high tide height, low tide height, or both and has the potential to occasionally transition between two high and low tides each day to one each day. These classifications will determine the period (approximately 12 hours for semidiurnal, approximately 24 hours for diurnal) and amplitude (approximately equal for semidiurnal and diurnal) of the loading resulting from the tidal current component of the current velocity. The classification will also provide an indicator of when the slack periods will occur during which the flow will not be a high enough magnitude to operate the TEC. Typical current velocities greater than 1 to 2 m/s are the typical required to operate TECs (Johnson and Pride 2010). A maximum current speed at which the TEC can be operational also exists and will be determined by the design of the TEC. During both conditions, the TEC will be designed to not rotate resulting in significantly smaller loads on the foundations. While the operational tidal current velocities may be slower than that

of wind, the density of seawater is greater than that of air allowing for TECs to gain over four times as much energy per square meter in comparison to a wind turbine (Couch and Bryden 2004). This also allows for a smaller turbine area to harness the equivalent amount of energy as a wind turbine.

The generalized tidal current velocity with no wave effects is not uniform with depth. At the upper boundary between the water and the air, the maximum velocity occurs and this velocity decreases to zero at the lower boundary between the water and the seabed due to an assumed no slip condition where the water has no slip relative to the seabed boundary. This vertical velocity profile can be represented by the following power law:

$$\boldsymbol{v_{H_2O}(z) = v_{H_2O,ref}(\frac{z}{z_{ref}})^p} \qquad \textbf{Equation 2.1}$$

where:

v_{H_2O} = tidal current velocity at height z measured from the seabed

$v_{H_2O,ref}$ = known reference flow velocity at z_{ref}

p = power coefficient normally considered to be between 0.10 to 0.14 (Dyer 1970)

The maximum velocity component of the profile will fluctuate in magnitude and direction based on the tidal state under a relatively constant period for semidiurnal and diurnal tides. An example of this distribution is shown in Figure 2.4.

Waves will additionally cause fluctuations in the velocity profile. A wave causes water particles to move in circular orbits where the highest and lowest points of the orbit are referred to as the wave crest and trough respectively. At the wave crest the movement of the particles is in the direction of wave propagation resulting in an increase in the velocity profile in the propagation direction as shown in Figure 2.4b. At the wave trough the movement of the particles is in the opposite direction of wave propagation resulting in an increase in velocity opposite of the propagation direction as shown in Figure 2.4a. This will affect the velocity profile of the tidal current creating periodic changes in the loading equivalent to the average wave period at a tidal site. Based on available National Oceanic and Atmospheric Administration (NOAA 2015) data, the mean wave period across the tidal current hotspots identified by the GTRC (2011) is approximately 5 seconds.

The current velocity will drive the rotation of the turbine resulting in both a thrust load and various moments. The thrust force results in a lateral load calculated as follows:

$$F_T = \frac{1}{2}\rho A v_{H_2O,i}^2 C_T \qquad \textbf{Equation 2.2}$$

where:

ρ = density of seawater

A = cross-sectional area of the swept by the turbine blades during single rotation

$v_{H_2O,i}$ = tidal current velocity prior to influence by the turbine

C_T = thrust coefficient which represents the loss of the water's momentum

In addition to the overturning moment due to the moment arm of the thrust load, the rotating turbine blades generate a yaw and shaft moment that must be resisted by the suction caisson. The current velocity will also interact with the non-rotating portions of the TEC as it flows past resulting in additional lateral loading and corresponding moment. Since these are all related to the current velocity, these loads will also be cyclic with simplified periods equal to the tidal period and the wave period.

The rotor rotation and number of blades have an additional effect on the loading pattern on the TEC foundations. Due to slight weight imbalances in the rotating components of the TEC, load fluctuations will occur at a period equal to the period of rotation of the TEC (known as "1P loads" in wind turbine design). The number of blades will have an effect on the blade shadowing which will cause additional load fluctuations at the period of rotation divided by the number of blades if a single pole support is used (known as "3P loads" in three-bladed wind turbine design). Blade shadowing is the result of the decrease in current velocity directly in front of the support due to the water having to flow around the structure. The blades rotating past the support structure will also vary the effect of turbulence on the structure at the same period. Current prototype horizontal axis TEC's have maximum rotation rates between 10 - 40 rpm resulting in minimum 1P load periods of 1.5 to 6 seconds and minimum 3P load periods of 0.5 to 2 seconds (Cornelius and Smith 2009, Verdant Power 2010, Andritz Hydro Hammerfest 2012, Marine Current Turbines 2013).

In summary, the cyclic loading imparted on the foundation by the tidal current will have periods ranging from 0.5 seconds to 24 hours due to the above conditions. The behavior of cyclic loads at periods of 5 seconds (fluctuations due to wave effects on current profile and turbine rotation), 15 minutes (storm wave loading), and 10.8 hours (approx. semidiurnal tidal current direction reversal) were analyzed in this study. These selected periods are shown in Figure 2.5

overlain on the possible ocean wave spectrum reported by Munk (1950). While the selection of these three individual periods covered a range of cyclic loading periods, it did not cover every possible cyclic loading period resulting from TECs nor did it cover multi-period loading combinations. The three selected periods, however, did allow for a cost efficient investigation of the general response to each source of cyclic loading described previously in this section. In regards to multi-period load combinations, the testing of individual frequencies will be more conservative for two reasons. First, repetitive high amplitude cycles can provide higher loads and larger accumulated displacements than combined loading cycles with rare to occasional large amplitude cycles. Second, short period cycles overlain over long period cycles will result in pore pressure generation. This pore pressure generation overcomes the potential for drainage of the interior suction caisson during long period cycles, a critical condition during uplift of suction caissons.

2.3 Suction caissons in clay

The behavior of suction caissons in clay have been examined using scaled model tests in a number of studies at 1-g (Steesen-Bach 1992, Rao et al. 1997, El-Gharbawy and Olson 1998, Whittle et al. 1998, House et al. 1999, Luke et al. 2003, Micic et al. 2003, Olson et al. 2003, Rauch et al. 2003, Coffman et al. 2004, Chen and Randolph 2006, Kelly et al. 2006a, Villalobos et al. 2010, Cotter et al. 2011, Wang et al. 2011, Guo et al. 2012, Li and Wang 2013, Zhang et al. 2013a, Chen et al. 2015, among others) and in the centrifuge (Clukey et al. 1995, Randolph et al. 1998, Watson et al. 2000, Allersma et al. 1999, House and Randolph 2001, Byrne and Cassidy 2002, Cao et al. 2002, Chen and Randolph 2004, Acosta-Martinez and Gourvenec 2008, Westgate et al. 2009, Brennan et al. 2011, Colliat et al. 2011, Mana et al. 2012, among others). A smaller number of field studies in clay have also been reported (Andersen et al. 1993, Dendani 2003, Houlsby et al. 2005, Colliat and Colliard 2011, Zhang et al. 2013b, among others). The early studies on suction caissons in clay focused on their use as anchors with large aspect ratios. Suction caissons with small aspect ratios (typically less than 1) have recently garnered considerable interest for their use as foundation elements for supporting offshore wind turbines and related meteorological towers, but they have yet to receive wide spread use in these applications. While a selection of the above studies has investigated the behavior of intermediate aspect ratio suction caissons in clay, they have not investigated their behavior as it applies to cyclic TEC loading components.

2.3.1 Capacity determination of suction caissons in soft clay

2.3.1.1 Penetration analysis

The penetration analysis of a suction caisson foundation pertains to the installation phase. Both Houlsby and Byrne (2005) and API RP 2SK (2008) provide design calculation recommendations. The three critical geotechnical aspects of this analysis are the self-weight embedment depth, suction required for complete installation, and the allowable suction.

The penetration resistance of a suction caisson during installation can be estimated using the alpha method. The resistance is derived from the side friction along the inside and outside wall of the suction caisson and the end bearing along the thickness of the wall at the tip. Equations shown below are used to calculate the penetration resistance:

$$\boldsymbol{Q_{side} = (\alpha s_u) A_{side}} \qquad \textbf{Equation 2.3}$$

$$\boldsymbol{Q_{tip} = (N_c s_u + \gamma' z) A_{tip,wall}} \qquad \textbf{Equation 2.4}$$

$$\boldsymbol{Q_{total} = Q_{side} + Q_{tip}} \qquad \textbf{Equation 2.5}$$

where:

Q_{side} = resistance along the inside and outside wall

α = adhesion factor

s_u = relevant undrained shear strength for the given area of strength mobilization

A_{side} = sum of the inside and outside wall area embedded into the soil

Q_{tip} = resistance at the tip

N_c = bearing capacity factor

γ' = buoyant unit weight of the soil

$A_{tip,wall}$ = area of the suction caisson tip

Q_{total} = total penetration resistance.

The adhesion factor is typically taken as the inverse of the clay sensitivity. This assumption indicates that the clay will be remolded due to the large displacement of the foundation during the installation process and that the residual strength of the soil as measured by the laboratory vane will be mobilized in full without any reduction due to the interaction with the foundation material. However, a previous study by Dendani (2003) has indicated that the inverse of sensitivity overestimates the installation resistance based on field measurements of suction

caissons off the coast of Africa. The bearing capacity factor for the tip resistance is assumed to be the same as that of a deeply embedded strip footing or 7.5. The depth at which the penetration resistance equals the buoyant weight of the foundation and structure will determine the self-weight depth of embedment. At this point, the suction required to complete penetration must be calculated. An illustration of the suction penetration process is shown in Figure 2.6.

The suction required to complete penetration is determined using the following equation:

$$\boldsymbol{s_{req} = \frac{Q_{total} - W'}{A_i}} \qquad \textbf{Equation 2.6}$$

where:

s_{req} = required suction to complete installation

Q_{total} = penetration resistance at the full embedment depth

W' = buoyant weight of the foundation and structure

A_i = inside cross sectional area of the foundation

Once the required suction is calculated, the critical suction must be determined. This is the suction at which a reverse bearing capacity failure will occur, characterized by soil being drawn into the caisson. The critical suction is calculated as follows:

$$\boldsymbol{s_{critical} = N_c s_u + \frac{A_{in} \alpha s_u}{A_i}} \qquad \textbf{Equation 2.7}$$

where:

$s_{critical}$ = critical suction

A_{in} = surface area of the inside wall

This critical suction can then be used to determine the allowable suction based on the design factor of safety.

2.3.1.2 Axial capacity analysis

The alpha method can again be used to determine the axial capacity of the suction caisson based on recommendations by API RP 2GEO (2011). Since the top cap of the suction caisson is assumed to be sealed after installation resulting in the soil plug moving in unison with the foundation, the resistance is derived from the side friction along the outside wall and tip resistance along the entire diameter of the tip. The axial capacity can be calculated as follows:

$$\boldsymbol{V' = \alpha s_u A_{wall,outside} + N_c s_u A_{tip} - W'} \qquad \textbf{Equation 2.8}$$

where:

α = adhesion factor different from penetration analysis

$A_{wall,outside}$ = area of the outside wall of the suction caisson

A_{tip} = entire area of the tip including the soil mass within the suction caisson

The adhesion factor recommended by API RP 2GEO (2011) during axial capacity analysis is not the same as that used in the installation procedure described in Section 2.3.1.1. This axial capacity adhesion factor does not account for the remolding of the soil during installation and results in a differing factor based on a differing design equation. The recommended adhesion factor depends on the ratio of the undrained shear strength and the effective stress at a given depth as follows:

$$\boldsymbol{\alpha = 0.5\left(\frac{s_u}{\sigma'_{vo}}\right)^{-0.5} \quad for \frac{s_u}{\sigma'_{vo}} \leq 1.0} \qquad \textbf{Equation 2.9}$$

$$\boldsymbol{\alpha = 0.5\left(\frac{s_u}{\sigma'_{vo}}\right)^{-0.25} \quad for \frac{s_u}{\sigma'_{vo}} > 1.0} \qquad \textbf{Equation 2.10}$$

where:

σ'_{vo} = in-situ effective vertical stress

The maximum limiting value of alpha theoretically is 1, however, studies by Andersen and Jostad (1999) suggest that a lower than calculated value of alpha be used due to a reduction in stresses on the outside wall during the suction installation process. API recommends that the end bearing factor of 9 be used based on recommendations by Skempton (1951) for deeply embedded circular foundations. This bearing factor assumes that the tip of the suction caisson is at a depth of 4 times the diameter and that a plastic equilibrium theory based mechanism (example in Figure 2.7) is fully mobilized during failure. As the ratio of the embedded depth to the diameter of the foundation decreases, the bearing factor decreases to a value of 6.2 at a ratio of zero (Skempton 1951). Studies by Luke et al. (2005) have indicated that back-calculated values of α and N_c are subject to the assumptions used during the analysis. With this in mind however, back-calculated values of 0.25 to 0.8 and 6 to 16 have been determined for α and N_c, respectively (El-Sherbiny 2005, Luke et al. 2005). While these adhesion factors were reasonable, the range of bearing capacity factors verified that the Skempton (1951) methods were not applicable to suction caisson foundations in soft clay.

2.3.1.3 Lateral capacity analysis

Finite element analysis, limit equilibrium analysis, and plastic limit analysis are all recommended by API RP 2SK (2008) to determine the lateral capacity of a suction caisson. API RP 2GEO (2011) also recommends a p-y analyses for suction caissons loaded primarily in the lateral direction, however this method is applicable to long, flexible piles in clay and must be modified for short, large diameter suction caissons.

Of the three API RP 2SK (2008) recommended analysis methods, finite element methods are the most numerically rigorous. Finite element analyses have been conducted on laterally loaded suction caissons in clay by Sukumaran et al. (1999), Templeton (2002), Maniar (2004), Sharma (2004), Edgers et al. (2009), Andresen et al. (2011), Gourvenec and Barnett (2011), Jostad et al. (2014), Kourkoulis et al. (2014), Murali et al. (2015), among others. Most of these studies focused on the suction caisson utilized as an anchor and loaded at a connection point or padeye located below the clay surface as opposed to a top-loaded suction caisson used as a foundation. If utilized correctly with an appropriate soil model, finite element analyses provide the monotonic ultimate capacity without the need to assume a specific failure surface. Determining the cyclic capacity of the foundation involves some difficulty since soil models that incorporate cyclic strength degradation, such as UDCAM (NGI 2012), are not readily available within commercially available finite element programs.

Limit equilibrium methods and plastic limit methods provide a more economical alternative to determining suction caisson capacity. It is important to note however that finite element analyses are typically utilized to develop and/or verify various limit equilibrium methods (Fugro 2009, Kennedy et al. 2013) or plastic limit methods (Aubeny et al. 2001, 2003a, 2003b) for suction caissons in clays. These methods assume a failure surface or mechanism that may not necessarily be applicable to all suction caisson geometries and loading conditions or assume that only a limited amount of mechanism variations exist. While the more recent limit equilibrium methods have been developed for shallow and intermediate aspect ratio suction caissons that are top loaded, Randolph and House (2002) and Aubeny et al. (2003a) have reported that the simplified plastic limit models that assume a conical soil wedge at the surface and flow-around at depth provide good agreements at aspect ratios greater than six and over predict capacities of shorter suction caissons. The plastic limit model failure mechanism assumed by Murff and Hamilton (1993) and further simplified by Aubeny et al. (2001) is shown in Figure

2.8 while examples of assumed limit equilibrium failure mechanisms determined or verified with numerical studies are shown in Figure 2.9.

Matlock (1970) developed static and cyclic loading p-y curves for piles in clays based on field and lab tests. The ultimate resistance of the soil per unit length can be calculated as follows:

$$\boldsymbol{p_u = N_p s_u D} \qquad \textbf{Equation 2.11}$$

where:

N_p = lateral bearing capacity factor

s_u = undrained strength of the soil

D = pile diameter

N_p is assumed to be 9 at any point below the critical depth where the failure mechanism is considered to be a flow mechanism around the pile. The critical depth can be calculated as follows:

$$\boldsymbol{z_{crit} = \frac{6D}{\frac{\gamma' D}{s_u} + 0.5}} \qquad \textbf{Equation 2.12}$$

where:

z_{crit} = critical depth below which flow around failure occurs

γ' = buoyant unit weight

Near the clay surface, the failure mechanism is assumed to be wedge-shaped due to low overburden pressures. This reduces the N_p to the following values:

$$\boldsymbol{N_p = 3 + \frac{\gamma' z}{s_u} + \frac{0.5z}{D}} \qquad \textbf{Equation 2.13}$$

where:

z = depth below clay surface

Half of the ultimate resistance of the soil is mobilized after the following pile deflection:

$$\boldsymbol{y_{50} = 2.5\epsilon_{50} D} \qquad \textbf{Equation 2.14}$$

where:

y_{50} = pile deflection to mobilize half of the ultimate resistance

ϵ_{50} = axial strain at which half the ultimate strength is mobilized in a UU triaxial test

This value of y_{50} is then used to calculate the ratio of the mobilized resistance to the ultimate resistance based on the pile deflection. This generates the p-y curves as follows for static loading:

$$\frac{p}{p_u} = 0.5\left(\frac{y}{y_{50}}\right)^{\frac{1}{3}} \leq 1.0$$ **Equation 2.15**

For cyclic loading, the ultimate soil resistance is decreased to $0.72p_u$ and the soil resistance mobilized at deflections greater than $3y_{50}$ are also decreased at depths less than z_{crit}. An example of a static and cyclic p-y curve for soft clays as given by Matlock (1970) is shown in Figure 2.10.

The above p-y formulations by Matlock (1970) are based on field tests of 12.75 inch diameter piles. Stevens and Audibert (1979) reported that these p-y curves significantly overestimated the lateral deflections in load tests on piles with diameters up to 59 inches in soft to medium clay, the maximum bending moment was underestimated, and the ultimate resistance at deeper depths was underestimated. This prompted the following modification to the y_{50}, for large diameter piles:

$$y_{50} = 8.9\epsilon_{50}D^{0.5}$$ **Equation 2.16**

The modifications to N_p as suggested by Stevens and Audibert (1979) are shown in Figure 2.11. Since these modifications were presented, multiple studies have reported larger N_p values ranging from 9.14 to 13.4 for the deep flow around failure mechanism and that the deep flow around mechanism begins to occur at much shallower depths (Randolph and Houlsby 1984, Murff and Hamilton 1993, Jeanjean 2009, among others). These factors suggest that the capacity and lateral deflections are underestimated and overestimated respectively if API RP 2GEO (2011) recommendations are used.

2.3.2 Laboratory bench scale models

The following studies on laboratory bench scale 1-g model studies have been conducted on top loaded suction caissons with aspect ratios similar to the focus of this investigation considered to be 0.75 to 3. The studies have been grouped into three categories: installation, vertical loading, and horizontal/combined loading.

2.3.2.1 Installation

Previous studies have investigated the installation of suction caissons in kaolin at aspect ratios of 0.95, 1, 1.7, and 1.96 by various methods including combined self-weight embedment and suction and by jacking only (Cotter 2009, Cotter et al. 2011, House et al. 1999, Villalobos et al. 2010). These studies found good agreement with the theoretical required suction and the

actual value applied during testing. In the case of Cotter (2009), it was found that the required suction with depth fell between the theoretical suction calculated using the peak undrained shear strength and that calculated using the residual undrained shear strength. Villalobos et al. (2010) found no substantial difference between jacked and suction installation as shown in Figure 2.12. House (2002), Rauch et al. (2003), and Chen and Randolph (2004) have also reported no substantial difference between jacked and suction installation for higher aspect ratio suction caissons in kaolin. Zhang et al. (2013a) conducted installation studies on suction caissons with aspect ratios of 1.5 configured as a tripod in clay taken from the Bohai bay in China and reported that varying suction pressures across the three suction caissons can be used to adjust the tilt during installation.

2.3.2.2 Vertical loading

The uplift capacity of suction caissons with aspect ratios ranging from 1 to 2 have been investigated by Steesen-Bach (1992), Rao et al. (1997), Whittle et al. (1998), and Chen (2013) in various clays including Nivaa clay, kaolin, and a marine clay obtained off the east coast of India. These studies indicated that a failure mechanism with plug retention occurred during undrained uplift while a failure mechanism with no plug retention occurred if suction was not allowed to develop within the suction caisson cavity. The uplift capacity was reported to be greater during undrained conditions than for drained conditions due to the retention of the plug resulting in tip capacity to be developed along the full diameter of the suction caisson rather than the thickness of the suction caisson wall.

Villalobos et al. (2010) investigated the monotonic compressive and uplift capacity and vertical cyclic capacity in heavily overconsolidated kaolin for suction caisson models with an aspect ratio of 1. Reported results concluded that the ultimate tensile and compressive capacity were equivalent when converted to a bearing capacity factor indicating that the failure mechanism was similar. This similarity also indicated that the failure mechanism was not a general shear mechanism as the development of a general shear mechanism in uplift is not physically feasible based on the typical tensile response of clay. The tensile capacity was softened if preceded by compressive failure. The cyclic loading resulted in differing settlements based on the average cyclic load. For short-term loading, it was reported that the suction within the caisson affects the results of subsequent cyclic loading.

2.3.2.3 Horizontal and combined loading

Chen (2013) investigated the response of suction caissons to horizontal loading on suction caissons with an aspect ratio of 1 in normally consolidated (NC) and overconsolidated (OC) kaolin. The installation process in the normally consolidated clay was purely by self-weight and in the overconsolidated clay was by a combination of self-weight and surcharge weight placement. For both clays, the cyclic load was applied above the top cap using displacement control over 1000 cycles. The cyclic amplitudes were +/- 0.5, +/- 1.0, and +/- 2.5 degrees with periods of 3, 5, and 10 seconds in addition to a static mean load component. For the NC kaolin, the vertical and lateral displacement for the smallest amplitudes were not significant, but they increased up to 0.17D and 0.24D at the largest cyclic amplitude. For the OC kaolin, the vertical and lateral displacements were reported to be insignificant across all displacements as they did not exceed 0.03D. For both NC and OC kaolin, a circular zone of disturbed soil developed on the surface extending about 0.8D and 0.6D away from the foundation respectively. For the OC case, fissuring, cracking, and gap formation was observed around the foundation. With regards to the lateral capacity mobilized with the cycling, degradation was prevalent when significant values of lateral and vertical displacement were observed. Examples are shown in Figure 2.13. At the smaller rotations or those with relatively small vertical and horizontal displacements, no capacity degradation was observed.

2.3.3 Centrifuge models

The following centrifuge model studies have been conducted on top loaded suction caissons with aspect ratios similar to the focus of this investigation considered to be values of 0.75 to 3. The studies have been grouped into three categories: installation, vertical loading, and horizontal/combined loading.

2.3.3.1 Installation

Cao et al. (2002) conducted a single penetration test on a suction caisson with an aspect ratio of 2.4 in kaolin and found that a soil plug was not formed inside the model caisson during the self-weight installation.

2.3.3.2 Vertical loading

Clukey et al. (1995) investigated the pure cyclic uplift capacity on a suction caisson with an aspect ratio of 2.3 in kaolin as a part of a larger study involving combined loading. The study reported that the monotonic uplift capacity post cycling did not exhibit capacity degradation due to cycling when compared to that of the monotonic test not preceded by cyclic loading indicating that the performance of the foundation will not progressively degrade with successive storms. Additionally, for frequencies between 1 and 5 Hz there was no indication of a loss of excess pore pressure generation within the caisson.

Allersma et al. (2000) investigated the cyclic uplift response of a suction caisson with an aspect ratio of 1.2 in kaolin. It was reported the suction caisson was able to resist cyclic loads with no progressive failure even when cycling higher than the ultimate static capacity at low speed due to suction that developed within the caisson. This study also investigated the monotonic rate dependent effects on loading. It was observed that the uplift failure mechanism of suction caissons in clay is rate dependent. At high speeds (undrained), a general shear failure involving a clay plug is present. At low speeds (drained), the pile moves up without any plug movement. These results are similar to the 1-g tests described above.

Byrne and Cassidy (2002) conducted undrained vertical unload-reload tests on a suction caisson with an aspect ratio of 1 in kaolin. The suction caisson was first loaded in uplift to determine the capacity, then loaded in compression, and subsequently loaded again in uplift. The subsequent uplift loads provided a softer response with a decreased uplift capacity in comparison to the initial uplift loading similar to the 1-g tests described above.

Colliat et al. (2011) investigated the uplift capacity of a suction caisson with an aspect ratio of 3 in deep water Nigeria clay. The tests investigated the rapid and slow uplift capacity for ring stiffened and unstiffened suction caissons and the effect of set up time (10 days to 1 year) on the capacity. It was found that the stiffeners increase the penetration resistance by 30% to 45% and the pull out capacity by 10% to 35%. The capacities of the slow uplift tests were 30% to 40% lower than the corresponding rapid uplift tests, a similar trend to 1-g lab tests. The uplift capacity was found to increase by up to 40% for one year of set time for the stiffened suction caissons.

2.3.3.3 Horizontal and combined loading

Clukey et al. (1995) investigated the cyclic uplift resistance at various angles up to 8^{o} from the vertical for a suction caisson with an aspect ratio of 2.3 in kaolin. In addition to the results from the purely uplift testing described above, it was reported that the load inclination variations up to 8^{o} did not significantly affect the number of cycles required to reach similar foundation responses.

2.3.4 Field scale tests

The majority of available data on full-scale suctions caissons with aspect ratios similar to the focus of this investigation considered to be values of 0.75 to 3 are limited to installation and removal studies (Colliat and Colliard 2011, Zhang et al. 2013b). Both report the existence of set-up phenomena post-installation, similar to results of centrifuge testing described above. Colliat and Colliard (2011) reported an increased removal capacity with time for suction caissons with aspect ratios ranging from 2.4 to 4.5 over periods of 1 day to 3.5 years in Gulf of Guinea clays. Zhang et al. (2013b) reported an increased removal capacity of a tripod suction caisson system with aspect ratios of 1.5 over a period of 7 years in Bohai organic silt, silty clay, and clay. Colliat and Colliard (2011) reported good agreement of the set-up strength with aging tests carried out on the same clay.

2.3.5 Kelly et al. (2006) on comparison of field and laboratory scale models

Kelly et al. (2006) compared the results of field (D = 3 m) and 1-g laboratory tests (D = 0.2 m) on suction caisson foundations in clay. While these suction caisson models were of an aspect ratio of 0.5 and shorter than those proposed in this study, the implication of the results are important to this study. The field tests were conducted at Bothkennar in silty clay and installed by suction. The horizontal loads applied to the field test were cyclic with increasing amplitude at a moment arm of 4.23 m above the lid. The 1-g scaled model tests were conducted in kaolin and installed by jacking. The loads applied in this test were conducted by applying fixed rotations determined from the field trial values. Non-dimensional comparisons between the two tests are shown in Figure 2.14 through Figure 2.16. Based on these results, it was found that the non-dimensionalization procedures provide more similar results at lower rotations than at larger rotations. While the results are not an exact match, the non-dimensionalization brings absolute magnitudes of capacity and stiffness that were orders of magnitude apart to within 30% of one

another. Considering this context, the quality of agreement between the two scales of testing are highly satisfactory.

2.4 Transparent soils for modeling clay

2.4.1 General

The opaque nature of natural soils makes visualization of internal deformations nearly impossible in the laboratory setting without installing foreign objects such as lead shot or piano wire. However, if these objects have different properties from the soil they can alter the soil behavior while only giving localized indicators of deformation. Transparent soil surrogates overcome this limitation by using materials such as amorphous silica powder, silica gel, aquabeads, fused quartz, and laponite to make a transparent soil surrogate that has similar properties to natural soils to allow for visualization of deformations along an entire plane (Sadek et al. 2003, Liu and Iskander 2004, Liu and Iskander 2010, Lo et al. 2010, Chen et al. 2014, Wallace and Rutherford 2015, Chini et al. 2015, Iskander et al. 2015, among others). Deformations can be visualized using various methods including digital image correlation (DIC) (Sadek et al. 2003, Pan et al. 2009) and extended coarse-to-fine refinement framework optical flow estimation (Xu et al. 2012, Zheng and Hryciw 2014, Wallace et al. 2018). All of these methods are non-contact, full field optical techniques utilizing various mathematical processes to determine displacement within a two dimensional image. DIC programs developed for soil mechanics such as GeoPIV (White et al. 2003), OPEN PIV (Taylor et al. 2010), and GeoPIV-RG (Stanier et al. 2015) are available in open source format. During soil loading, images are taken of a plane of the transparent soil illuminated by laser light. When illuminated by laser light, the transparent soil generates a speckle pattern as shown in Figure 2.17 that generates the contrast allowing for digital analysis.

2.4.2 Transparent soil families to model clay

In Iskander et al. (2015), the available transparent soils were separated into five separate families: amorphous silica, silica gel, hydrogel (Aquabeads), fused quartz, and laponite. Of these families, three were shown to model natural clay behavior: amorphous silica (Mannheimer 1990, Mannheimer and Oswald 1993, Iskander et al. 1994), hydrogel (Lo et al. 2010, Fernandez Serrano et al. 2011), and laponite (Wallace and Rutherford 2015). Hydrogels primarily model the

flow of fluid through clay while amorphous silica and laponite have been shown to model deformation and strength properties of clay. Laponite was a family of transparent soils investigated by the author for offshore geotechnical physical modeling (Wallace and Rutherford 2015, Chini et al. 2015). The transparency of laponite is demonstrated in Figure 2.18. It was developed with the intention of overcoming known limitations of amorphous silica, the original transparent clay soil surrogate. Amorphous silica requires the use of pore fluids such as mineral oil and calcium bromide brine that pose limitations in regards to their stability, toxicity, flammability, degradation of latex, transparency degradation with evaporation, and difficulty in handling (Zhao et al. 2010). The solvent initially used to manufacture amorphous silica has also proven difficult to source in the United States (Iskander et al. 2015). These limitations led to the use of distilled, de-aired water as the pore fluid of laponite (Wallace and Rutherford 2015). Since then, a sodium pyrophosphate decahydrate and water pore fluid has been utilized to mix laponite at higher concentrations, thereby increasing strength (Beemer et al. 2016). Additional information in regards to the specific laponite used in this project and its properties are discussed in Section 3.3.

2.5 Figures

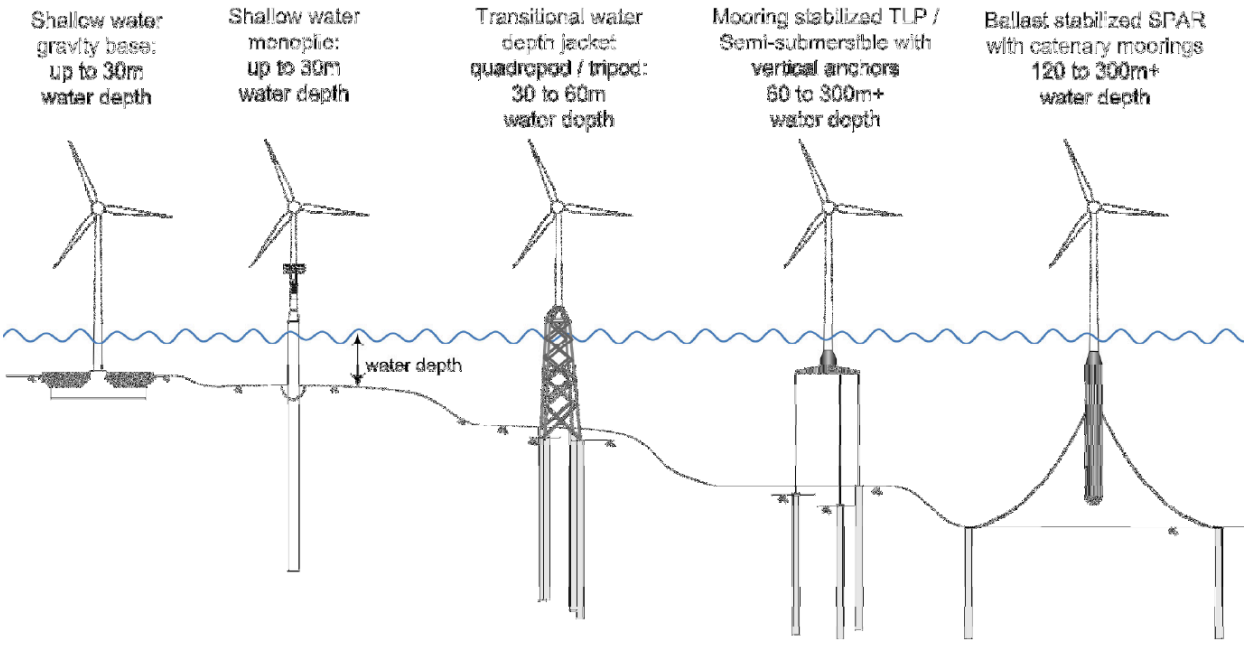

Figure 2.1: Various foundation or anchoring options with increasing water depth for renewable energy applications (Schneider and Senders 2010)

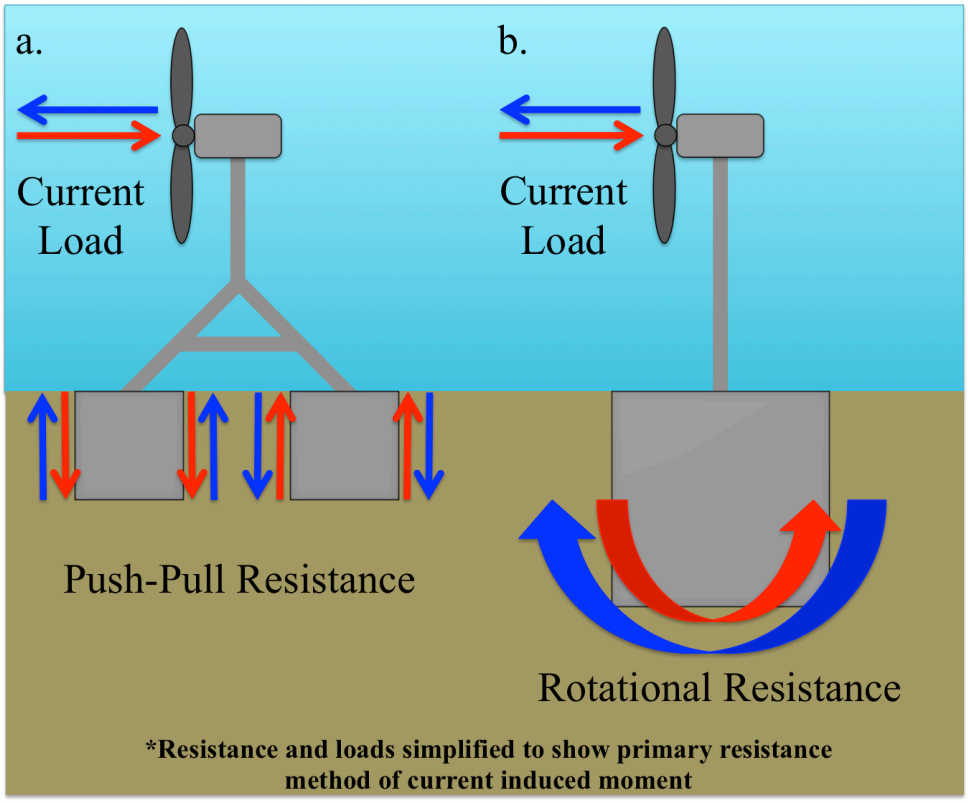

Figure 2.2: The simplified primary resistance mechanisms in regards to the current induced moment for the a. tripod/tetrapod configuration and b. monopod configuration

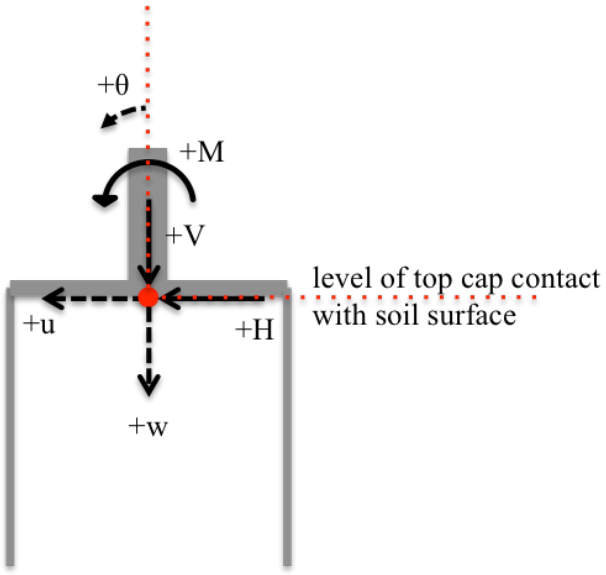

Figure 2.3: Loading and displacement nomenclature for a single suction caisson foundation

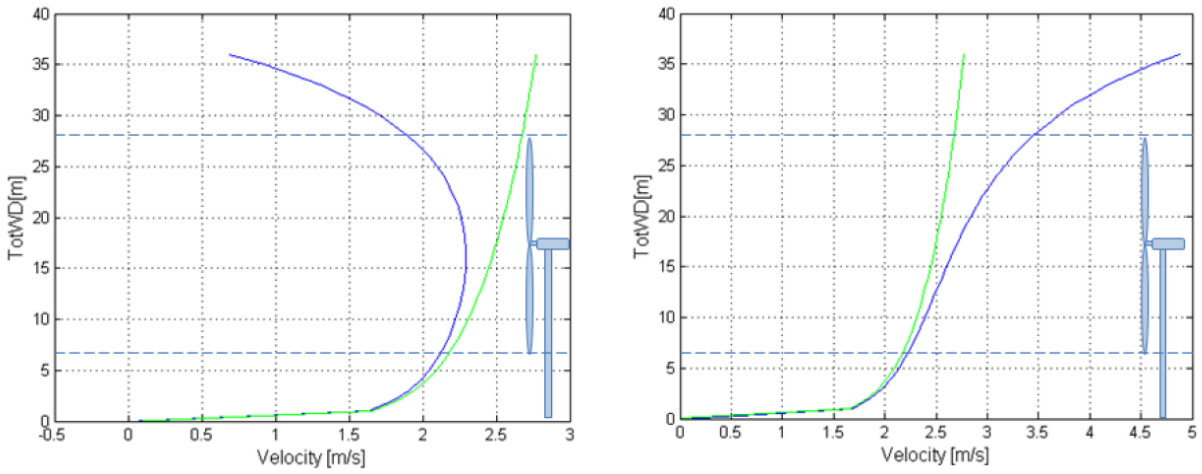

Figure 2.4: Example of velocity profiles with the no-slip current velocity with no wave effects shown in green and the no slip current velocity at the a. wave through and b. the wave crest (Sæterstad 2011)

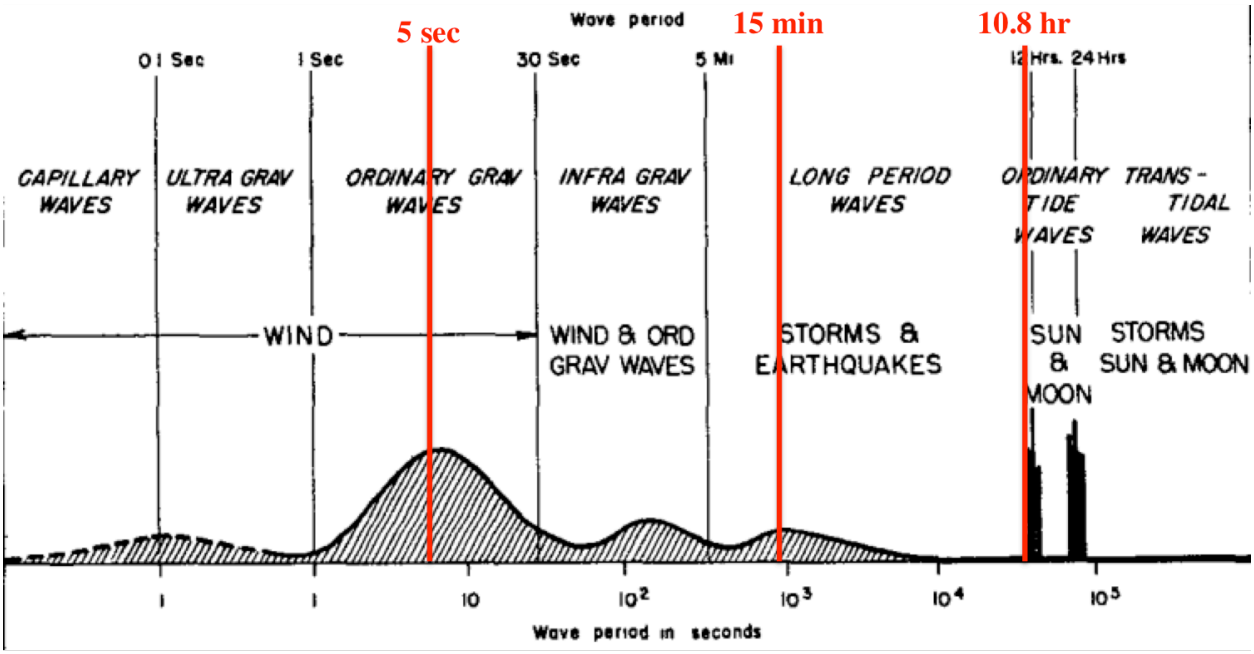

Figure 2.5: The periods of cyclic loading that will be investigated in this study (adapted from Munk 1950)

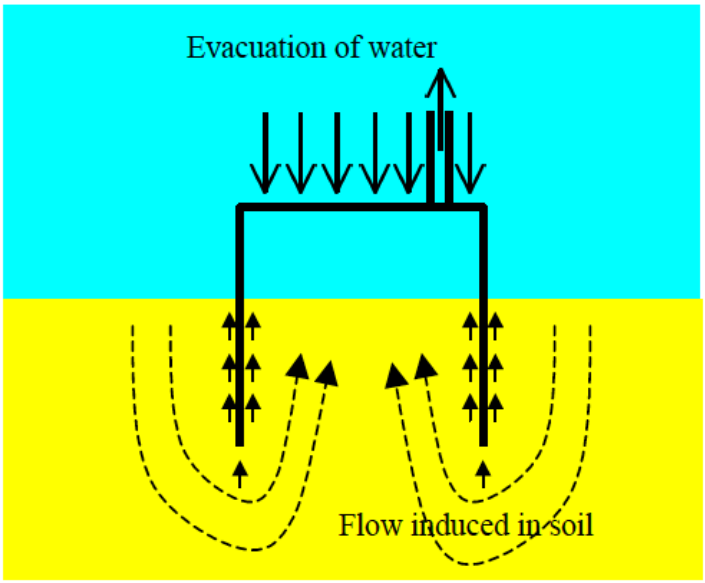

Figure 2.6: Illustration of the suction installation process (Byrne 2000)

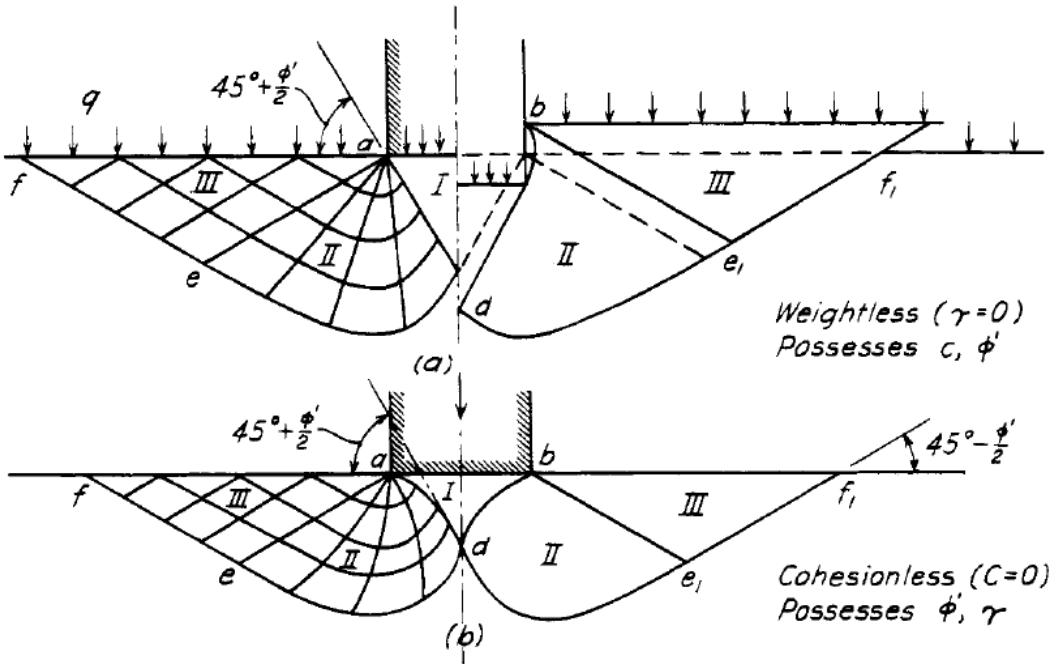

Figure 2.7: Example of a general shear mechanism for shallow foundations (Terzaghi et al. 1996)

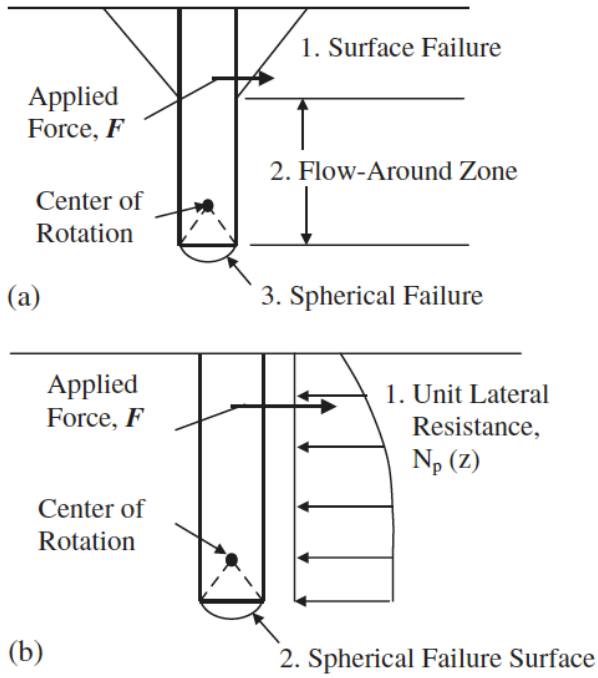

Figure 2.8: The plastic limit model a. assumed by Murff and Hamilton (1993) and b. simplified analysis of Aubeny et al. (2001) as shown in Aubeny et al. (2003)

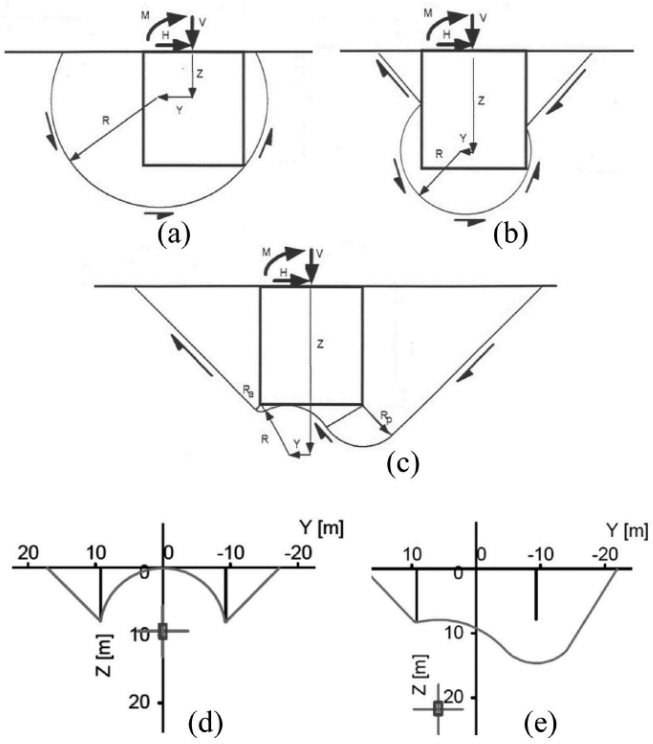

Figure 2.9: Failure modes utilized in the limit equilibrium program CANCAP2 verified with PLAXIS3D FEA results where a., b., and c. are typical of aspect ratios greater than 1 in clay while d. and e. are typical for aspect ratios of 0.5 (Palix et al. 2011)

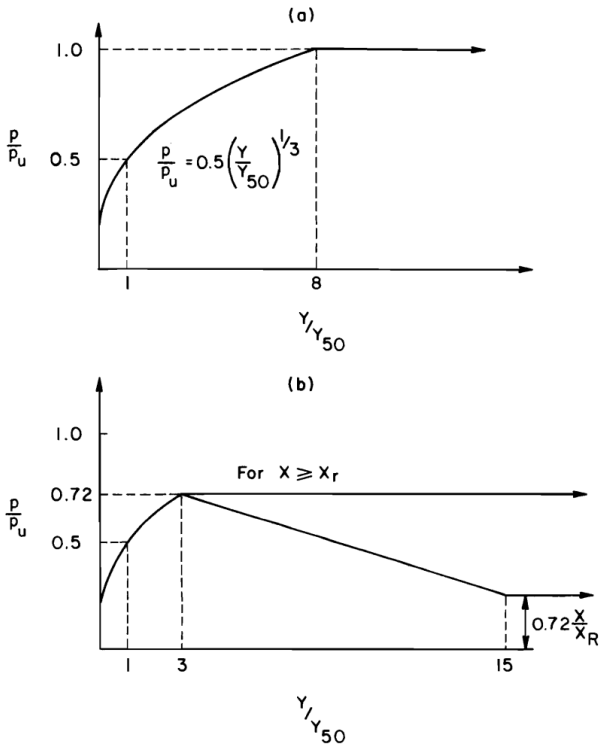

Figure 2.10: Example p-y curves for laterally loaded piles in soft clay for a. static loading and b. cyclic loading (Matlock 1970)

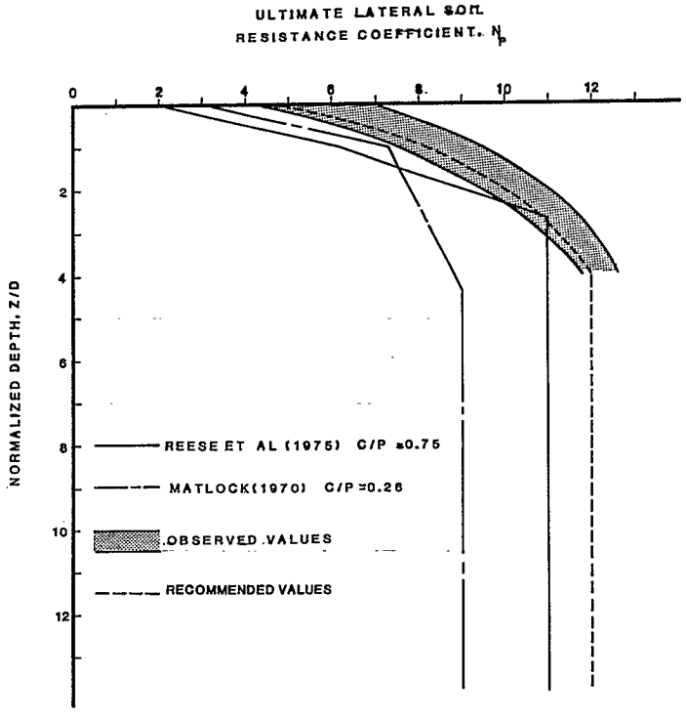

Figure 2.11: Modified N_p parameter of the p=y method as suggested by Stevens and Audibert (1979)

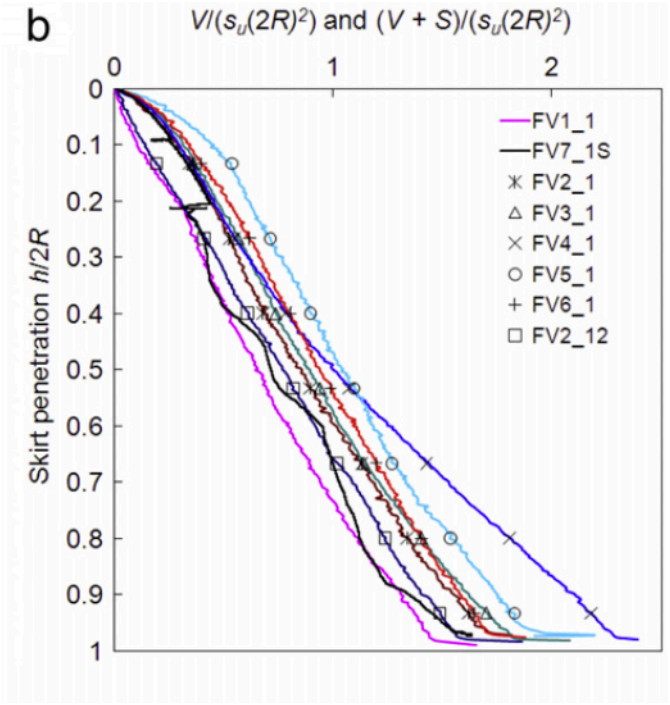

Figure 2.12: Normalized penetration resistance of suction caissons installed by combined self weight embedment and suction (denoted by an D) and those installed by jacking only (Villalobos et al. 2010)

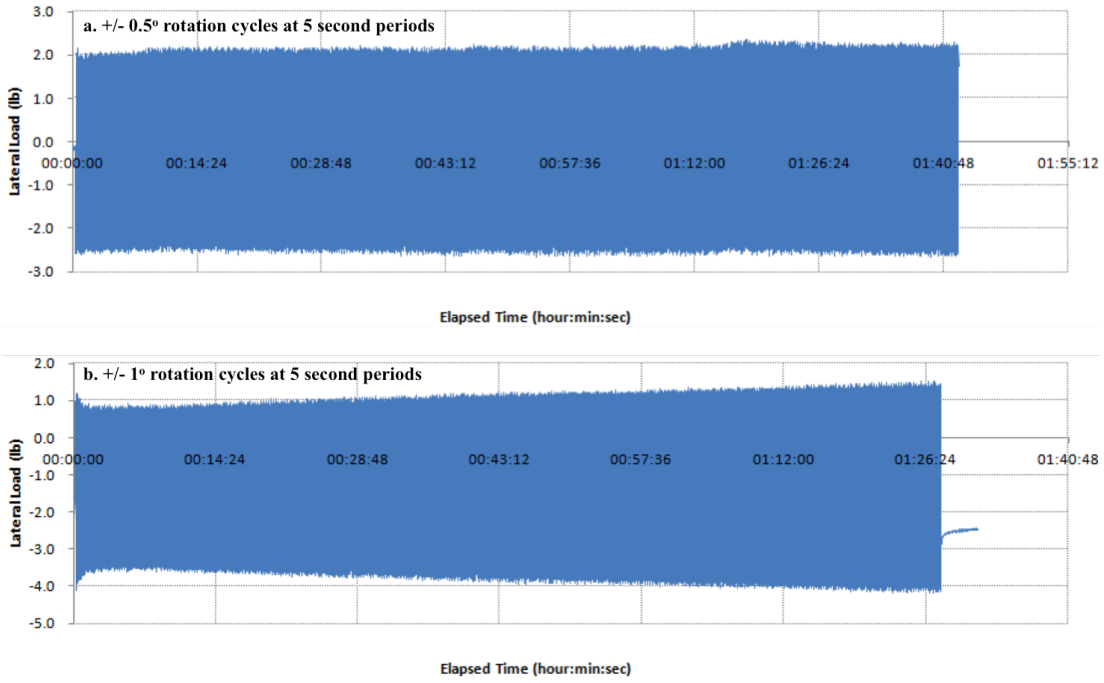

Figure 2.13: Lateral load with time for rotation controlled cycling on a suction caisson in kaolin with AR=1 showing capacity changes with increasing amplitude (Chen 2013)

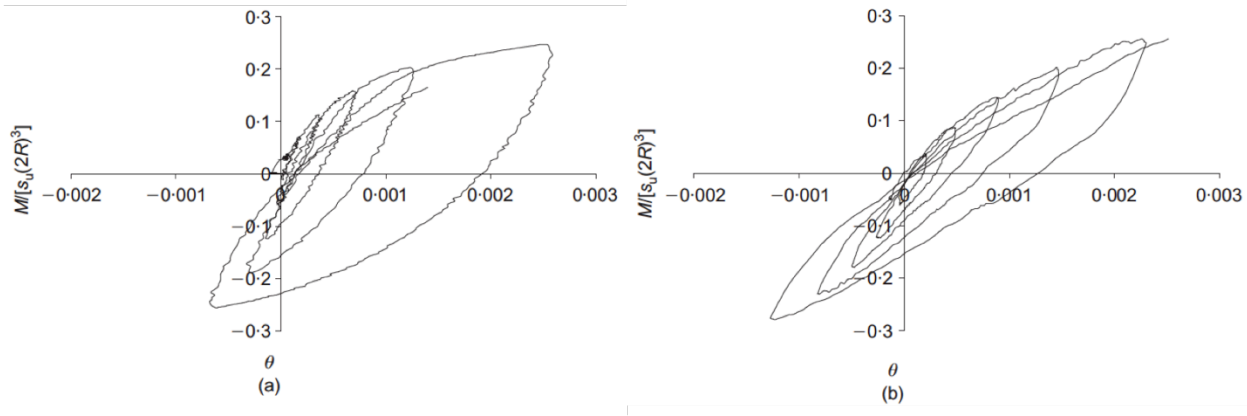

Figure 2.14: Non-dimensional moment versus rotation graphs comparing two AR=0.5 suction caisson models at a. 1-g model scale at 0.2 m diameter and b. field scale at 3 m diameter in clay at small rotations (Kelly et al. 2006)

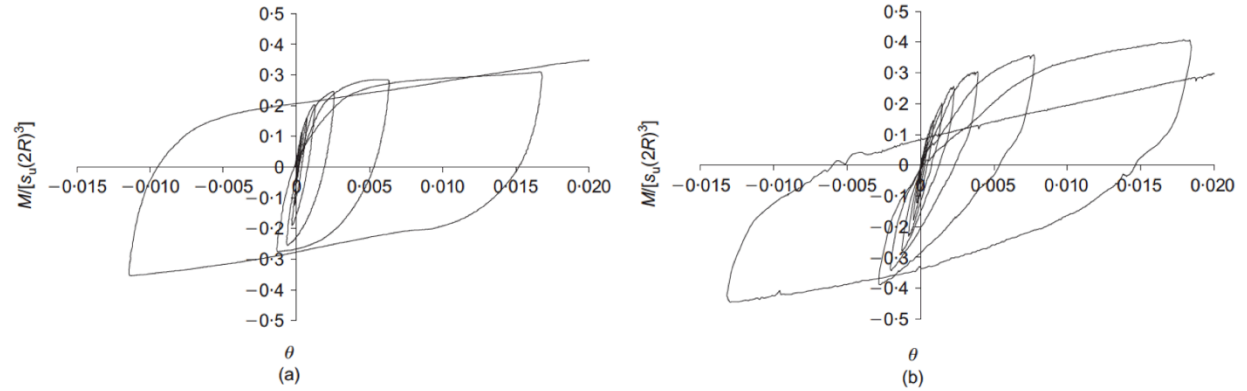

Figure 2.15: Non-dimensional moment versus rotation graphs comparing two AR=0.5 suction caisson models at a. 1-g model scale at 0.2 m diameter and b. field scale at 3 m diameter in clay at larger rotations (Kelly et al. 2006)

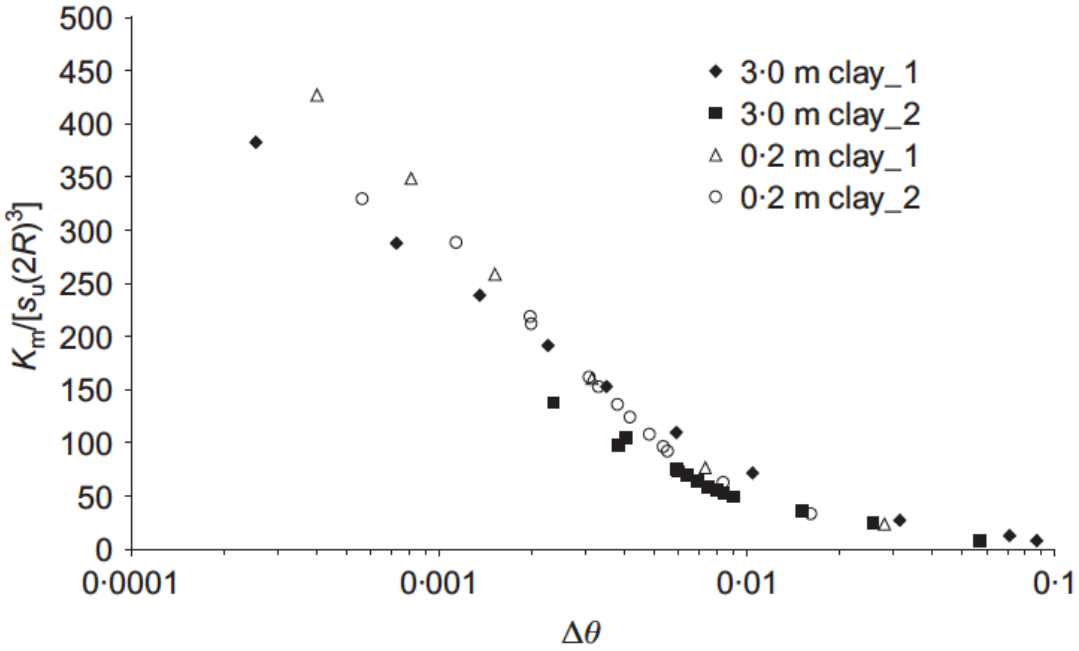

Figure 2.16: Non-dimensional stiffness values in regards to moment testing for two AR=0.5 suction caisson models at the lab scale with a 0.2 m diameter and the field scale with 3 m diameter (Kelly et al. 2006)

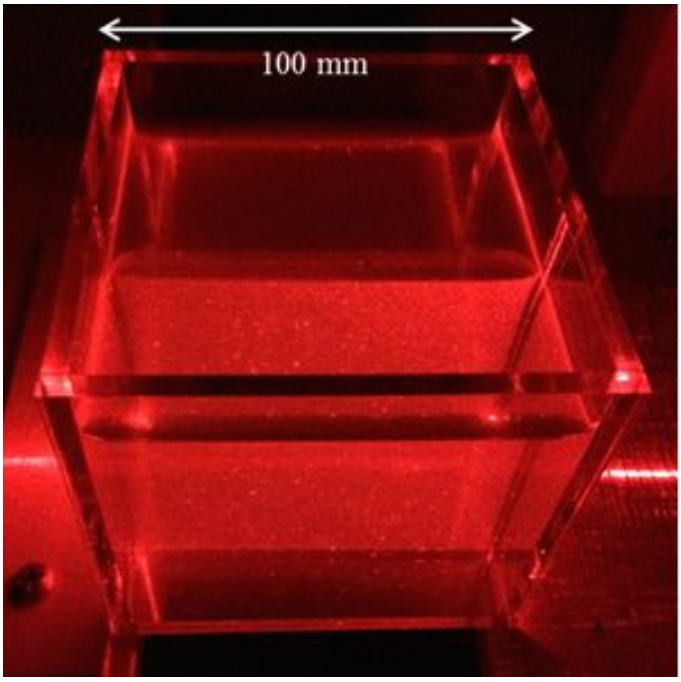

Figure 2.17: The speckle pattern generated in laponite when illuminated by laser light

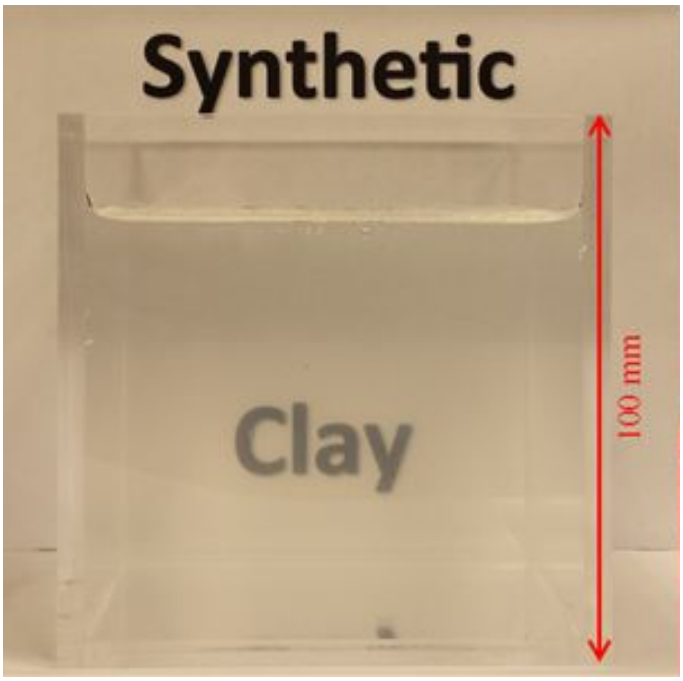

Figure 2.18: Sample of laponite where "Synthetic" is viewed without hindrance and "Clay" is viewed through 100 mm of laponite

2.6 References

Acosta-Martinez, H.E. & Gourvenec, S.M. (2008). "Response of skirted foundations for buoyant facilities subjected to cyclic uplift loading." *Proceedings of the Eighteenth (2008) International Offshore and Polar Engineering Conference.* Vancouver, BC, Canada.

Allersma, H.G.B., Kierstein, A.A., Brinkgreve, R.B.J. & Simon, T. (1999). "Centrifuge and Numerical Modelling of Horizontally Loaded Suction Piles." *Proceedings of the Ninth (1999) International Offshore and Polar Engineering Conference*. Brest, France.

Allersma, H.G.B., Kierstein, A.A. & Maes, D. (2000). "Centrifuge Modelling on Suction Piles Under Cyclic and Long Term Vertical Loading." *Proceedings of the Tenth (2000) International Offshore and Polar Engineering Conference*. Seattle, WA, USA.

Andresen, L., Jostad, H.P. & Andersen, K.H. (2011). "Finite Element Analyses Applied in Design of Foundations and Anchors for Offshore Structures." *International Journal of Geomechanics*. 11(6):417-430.

API RP 2GEO. (2011). "Geotechnical and Foundation Design Considerations." ANSI/API Recommended Practice 2GEO, First Edition, American Petroleum Institute.

API RP 2SK. (2008). “Design and Analysis of Stationkeeping Systems for Floating Structures.” API Recommended Practice 2SK, Third Edition, American Petroleum Institute.

Andersen, K.H., Dyvik, R., Schroder, K, Hansteen, O.E. & Bysveen, S. (1993). “Field Tests of Anchors in Clay II: Predictions and Interpretation.” *J. Geotech. Engrg.* 119(10):1532-1549.

Andersen, K.H. & Jostad, H.P. (1999). “Foundation Design of Skirted Foundations and Anchors in Clay.” Offshore Technology Conference. Houston, TX, USA.

Andritz Hydro Hammerfest. (2012). “ANDRITZ HYDRO Hammerfest – Renewable energy from tidal currents.” Andritz Hydro Hammerfest, Hammerfest, Norway.

Aubeny, C.P., Han, S.W. & Murff, J.D. (2003a). “Inclined load capacity of suction caissons.” *Int. J. Numer. Anal. Meth. Geomech.* 27:1256-1254.

Aubeny, C.P., Han. S.W. & Murff, J.D. (2003b). “Suction Caisson Capacity in Anisotropic Purely Cohesive Soil.” *International Journal of Geomechanics*. 3(2):225-235.

Aubeny, C.P., Moon, S.K. & Murff, J.D. (2001). “Lateral undrained resistance of suction caisson anchors.” *International Journal of Offshore and Polar Engineering.* 11(2):95-103.

Beemer, R.D., Shaughnessy, E., Ewert, K.R., Boardman, N., Biscontin, G., Aubeny, C.P. & Grajales, F.J. (2016). “The Use of Sodium Pyrophosphate to Improve a Translucent Clay Simulate.” Geo-Chicago 2016. Chicago, IL, USA.

Brennan, A.J., Madabhushi, S.P.G. & Cooper, P. (2011). “Seismically-induced displacements of a suction caisson in soft clay.” Frontiers in Offshore Geotechnics II. Perth, Australia.

Byrne, B.W. (2000). “Investigations of suction caissons in dense sand.” DPhil thesis. Univ. of Oxford, Oxford, England.

Byrne, B.W. & Cassidy, M.J. (2002). “Investigating the response of offshore foundations in soft clay soils.” *Proceedings of OMAE’02 21st International conference of Offshore Mechanics and Arctic Engineering.* Oslo, Norway.

Cao, J., Phillips, R., Popescu, R., Al-Khafaji, Z. & Audibert, J.M.E. (2002). “Penetration Resistance of Suction Caissons in Clay.” *Proceedings of the Twelfth (2002) International Offshore and Polar Engineering Conference.* Kitakyushu, Japan.

Chen, C.H. (2013). “Performance of Suction Caissons with a Small Aspect Ratio.” Ph.D. thesis, The University of Texas at Austin.

Chen, C.H., Gilbert, R.B., Gerkus, H., Saleh, A.A. & Finn, L. (2015). "Laterally loaded suction caissons with aspect ratio of one." Frontiers in Offshore Geotechnics III. Oslo, Norway.

Chen, Z., Omidvar, M., Iskander, M. & Bless, S. (2014). "Modelling of Projectile Penetration Into Transparent Sand." *Int. J. Phys. Model. Geotech.* 14(3):68-79.

Chen, W. & Randolph, M. (2004). "Radial Stress Changes around Caissons Installed in Clay by Jacking and by Suction." *Proceedings of the Fourteenth (2004) International Offshore and Polar Engineering Conference.* Toulon, France.

Chen, W. & Randolph, M.F. (2006). "Measuring Radial Total Stresses on Model Suction Caissons in Clay." *Geotechnical Testing Journal*. 30(2):1-9.

Chini, C.M., Wallace, J.F., Rutherford, C.J. & Peschel, J.M. (2015). "Shearing Failure Visualization Using Digital Image Correlation and Particle Image Velocimetry in Soft Clay Using a Transparent Soil." *Geotech. Test. J.* 38(5):1-17.

Clukey, E.C., Morrison, M.J., Garnier, J. & Corte, J.F. (1995). "The Response of Suction Caissons in Normally Consolidated Clays to Cyclic TLP Loading Conditions." Offshore Technology Conference. Houston, TX, USA.

Coffman, R.A., El-Sherbiny, R.M., Rauch, A.F. & Olson, R.E. (2004). "Measured Horizontal Capacity of Suction Caissons." Offshore Technology Conference. Houston, TX, USA.

Colliat, J.L. & Colliard, D. (2011). "Set-up of suction piles in deepwater Gulf of Guinea clays." Frontiers in Offshore Geotechnics II. Perth, Australia.

Colliat, J.L., Dendani, H., Jostad, H.P., Andersen, K.H., Thorel, L., Garnier, J. & Rault, G. (2011). "Centrifuge testing of suction piles in deepwater Nigeria clay – Effect of stiffeners and set-up time." Frontiers in Offshore Geotechnics II. Perth, Australia.

Cornelius, T. & Smith, M. (2009). "Presentation to Offshore Engineering Society – Tidal Stream Energy." Atlantis Resources Ltd., Singapore.

Cotter, O. (2009). "The installation of suction caisson foundations for offshore renewable energy structures." D. Phil. Thesis, University of Oxford.

Cotter, O.J., Byrne, B.W. & Houlsby G.T. (2011). "Installation of suction caissons for offshore renewable energy structures." Frontiers in Offshore Geotechnics II. Perth, Australia.

Couch, S.J. & Bryden, I. (2004). "The impact of energy extraction on tidal flow development." *Proceedings of the 3rd IMarEST International Conference on Marine Renewable Energy.*

Dendani, H. (2003). “Suction Anchors: Some critical aspects for their design and installation in clayey soils.” Offshore Technology Conference. Houston, TX, USA.

Dyer, K.R. (1970). “Current Velocity Profiles in a Tidal Channel.” *Geophys. J. R. astr. Doc.* 1970(22):153-161.

Edgers, L., Andresen, L. & Jostad, H.P. (2009). “Capacity analysis of suction anchors in clay by 3D finite element analysis.” *1st Int. Symp. on Computational Geomechanics (ComGeo I).* Juan-les-Pins, France.

El-Gharbawy, S. & Olson, R. (1998). “The Pullout Capacity of Suction Caisson Foundations for Tension Leg Platforms.” *Proceedings of the Eighth (1998) International Offshore and Polar Engineering Conference*. Montreal, Canada.

European Marine Energy Centre. (2016). “European Marine Energy Centre – Tidal Developers.” European Marine Energy Centre (EMEC) Ltd., Stromness, Orkney, United Kingdom. Accessed January 2016.

Fernandez Serrano, R., Iskander, M. & Tabe, K. (2011). “3D Contaminant Flow Imaging in Transparent Granular Porous Media.” *Geotech. Lett.,* 1(3):71-78.

Fraenkel, P. (2010). “Practical turbine design considerations: a review of technical alternatives and key design decisions leading to the development of the SeaGen 1.2 MW tidal turbine.” *Proceedings – Fluid Machinery Group – Ocean Power Fluid Machinery Seminar.* Institution of Mechanical Engineers. London, England.

Fugro (2009). “CANCAP2 user’s manual.” CANCAP2 00.17.

Georgia Tech Research Corporation. (2011). “Assessment of energy Production Potential from Tidal Streams in the United States – Final Project Report.” Georgia Tech Research Corporation, Atlanta, GA, USA.

Gourvenec, S. & Barnett, S. (2011). “Undrained failure envelope for skirted foundations under general loading.” *Geotechnique*. 61(3):263-270.

Guo, Z., Wang, L., Yuan, F. & Li, L. (2012). “Model tests on installation techniques of suction caissons in a soft clay seabed.” *Applied Ocean Research*. 34(2012):116-125.

Houlsby, G.T. & Byrne, B.W. (2005). “Design procedures for installation of suction caissons in clay and other materials.” *Geotechnical Engineering*. 158(GE2):75-82.

Houlsby, G.T., Kelly, R.B., Huxtable, J., & Byrne, B.W. (2005). “Field trials of suction caissons in clay for offshore wind turbine foundations.” *Geotechnique*. 55(4):287-296.

House, A. (2002). “Suction caisson foundations for buoyant offshore facilities.” Ph.D. thesis, University of Western Australia.

House, A.R. & Randolph, M.F. (2001). “Installation and Pull-Out Capacity of Stiffened Suction Caissons in Cohesive Sediments.” *Proceedings of the Eleventh (2001) International Offshore and Polar Engineering Conference.* Stavanger, Norway.

House, A.R., Randolph, M.F. & Borbas, M.E. (1999). “Limiting Aspect Ratio for Suction Caisson Installation in Clay.” *Proceedings of the Ninth (1999) International Offshore and Polar Engineering Conference.* Brest, France.

Iskander, M., Bathurst, R.J. & Omidvar, M. (2015). “Past, Present, and Future of Transparent Soils.” *Geotechnical Testing Journal*. 38(5):557-573.

Iskander, M., Lai, J., Oswald, C. & Mannheimer, R. (1994). “Development of a Transparent Material to Model the Geotechnical Properties of Soil.” *Geotech. Test. J.* 17(4):425-433.

Jeanjean, P. (2009). “Re-Assessment of P-Y Curves for Soft Clays from Centrifuge Testing and Finite Element Modeling.” Offshore Technology Conference. Houston, TX, USA.

Johnson, J.B. & Pride, D.J. (2010). “River, Tidal, and Ocean Current Hydrokinetic Energy Technologies: Status and Future Opportunities in Alaska.” Report prepared for Alaska Energy Authority by the Alaska Center for Energy and Power.

Jostad, H.P., Grimstad, G., Andersen, K.H., Saue, M., Shin, Y. & You, D. (2014). “A FE Procedure for Foundation Design of Offshore Structures – Applied to Study Potential OWT Monopile Foundation in the Korean Western Sea.” *Geotechnical Engineering Journal of the SEAGS & AGSSEA*. 45(4):63-72.

Kelly, R.B., Houslby, G.T. & Byrne, B.W. (2006). “A comparison of field and laboratory tests of caisson foundations in sand and clay.” *Geotechnique*. 56(9):617-626.

Kennedy, J., Oliphant, J., Maconochie, A., Stuyts, B. & Cathie, D. (2013). *Proceedings of the ASME 2013 32nd International Conference on Ocean, Offshore and Arctic Engineering*. Nantes, France.

Kourkoulis, R.S., Lekkakis, P.C., Gelagota, F.M. & Kaynia, A.M. (2014). “Suction caisson foundations for offshore wind turbines subjected to wave and earthquake loading: effect of soil-foundation interface. *Geotechnique*. 64(3):171-185.

Li, S. & Wang, J. (2013). "Analysis of Suction Anchors Bearing Capacity in Soft Clay." *Proceedings of the Twenty-third (2013) International Offshore and Polar Engineering.* Anchorage, Alaska, USA.

Liu, J.Y. & Iskander, M. (2004). "Adaptive Cross Correlation for Imaging Displacements in Soils." *J. Comput. Civ. Eng.* 18(1):46-57.

Liu, J. & Iskander, M.G. (2010). "Modelling Capacity of Transparent Soil." *Can. Geotech. J.* 47(4):451-460.

Lo, H.C., Tabe, K., Iskander, M. & Yoon, S.H. (2010). "A Transparent Water-Based Polymer for Simulating Multiphase Flow." *Geotech. Test. J.* 33(1):1-13.

Luke, A.M., Rauch A.F., Olson R.E. & Mecham, E.C. (2003). "Behavior of suction caissons measure in laboratory pullout tests." *Proceedings of OMAE03 22nd International Conference of Offshore Mechanics and Arctic Engineering*. Cancun, Mexico.

Mana, D.S.K., Gourvenec, S., Randolph, M.F. & Hossain, M.S. (2012). "Effect of gapping on the uplift resistance of a shallow skirted foundation." *Offshore Site Investigation and Geotechnics: Integrated Technologies – Present and Future.* London, UK.

Maniar, D.R. (2004). "A Computational Procedure for Simulation of Suction Caisson Behavior Under Axial and Inclined Loads." Ph.D. Dissertation, The University of Texas at Austin.

Mannheimer, R. (1990). "Slurries You Can See Through." *Technology Today*. Southwest Research Institute, San Antonio, TX.

Mannheimer, R.J. & Oswald, C.J. (1993). "Development of Transparent Porous Media with Permeability of Soil and Reservoir Materials." *Ground Water*. 31(5):781-788.

Marine Current Turbines. (2013). SeaGen-S 2MW. Marine Current Turbines Ltd., Camberley, Surrey, United Kingdom.

Matlock, H. (1970). "Correlations for Design of Laterally loaded Piles in Soft Clay." Offshore Technology Conference. Houston, TX, USA.

Maynard, M.L., Schneider, J.A., McEntee, J., & Newberg, E. (2013). "Suction caissons for cross-flow tidal power system." *Geotechnical Engineering*, 166(GE2): 99-110.

Micic, S., Lo, K.Y. & Shang, J.Q. (2003). "A New Technology for Increasing the Load-Carrying Capacities of Offshore Foundations in Soft Clays." Offshore Technology Conference. Houston, USA.

Munk, W.H. (1950). "Origin and generation of waves." *Proc. 1st International Conference on Coastal Engineering*. Long Beach, CA, USA.

Murali, M., Grajales F., Beemer, R.D., Biscontin, G. & Aubeny, C. (2015). "Centrifuge and numerical modeling of monopoles for offshore wind towers installed in clay." *Proceedings of the ASME 2015 34th International Conference on Ocean, Offshore and Arctic Engineering.* St. John's, Newfoundland, Canada.

Murff, J.D. & Hamilton, J.M. (1993). "P-ultimate for Undrained Analysis of Laterally Loaded Piles." *J. Geotechnical Engineering.* 119(1):95-107.

National Oceanic and Atmospheric Administration (2015). "National Oceanic and Atmospheric Administration's National Data Buoy Center." National Oceanic and Atmospheric Administration, Washington D.C., USA. Accessed June 2015.

Norwegian Geotechnical Engineering (2012). "Study on Offshore Wind Turbine Foundations – User manual for equivalent cyclic ADP model for undrained behavior – 'UDCAM'." Norwegian Geotechnical Institute, Oslo, Norway.

O'Doherty, T., Egarr, D.A., Mason-Jones, A., & O'Doherty, D.M. (2009). "An assessment of axial loading on a five turbine array." *Proc. ICE, Energy*. 162(EN2):57–65.

Olson, R.E., Rauch, A.F., Luke, A.M., Maniar, D.R., Tassoulas, J.L. & Mecham, E.C. (2003). "Soil Reconsolidation Following the Installation of Suction Caissons." Offshore Technology Conference. Houston, TX, USA.

Palix, E., Willems, T., & Kay, S. (2011). "Caisson capacity in clay: VHM resistance envelope – Part 1: 3D FEM numerical study." Frontiers in Offshore Geotechnics II. Perth, Australia.

Pan, B., Qian, K., Xie, H. & Asundi, A. (2009). "Two Dimensional Digital Image Correlation for in Plane Displacement and Strain Measurement: A Review." *Meas. Sci. Technol.* 20.

Randolph, M.F. & Houlsby, G.T. (1984). "The Limiting Pressure on a Circular Pile Loaded Laterally in Cohesive Soil." *Geotechnique*. 34(4):613-623.

Randolph, M.F. & House, A.R. (2002). "Analysis of Suction Caisson Capacity in Clay." *Offshore Technology Conference*. Houston, TX, USA.

Randolph, M.F., O'Neill, M.P., Stewart, D.P. & Erbrich, C. (1998). "Performance of Suction Anchors in Fine-Grained Calcareous Soils." Offshore Technology Conference. Houston, TX, USA.

Rao, S.N., Ravi, R. & Ganapathy, C. (1997). "Pullout Behavior of Model Suction Anchors in Soft Marine Clays." *Proceedings of the Seventh (1997) International Offshore and Polar Engineering Conference*. Honolulu, HI, USA.

Rauch, A.F., Olson, R.E., Luke, A.M. & Mecham, E.C. (2003). "Measured Response during Laboratory Installation of Suction Caissons." *Proceedings of The Thirteenth (2003) International Offshore and Polar Engineering Conference*. Honolulu, HI, USA.

Sæterstad, M.L. (2011). "Dimensioning Loads for a Tidal Turbine." M.S. Thesis, Norwegian University of Science and Technology.

Sadek, S., Iskander, M. & Liu, J. (2003). "Accuracy of Digital Image Correlation for Measuring Deformations in Transparent Media." *ASCE J. Comput. Civ. Eng.* 17(2):88–96.

Schneider, J. & Senders, M. (2010). "Foundation design – a comparison of oil and gas platforms with offshore wind turbines." *Marine Technology Society Journal*. 44(1):32-51.

Sharma, P.P. (2004). "Ultimate capacity of suction caisson in normally and lightly overconsolidated clays." M.S. thesis, Texas A&M University.

Skempton, A.W. (1951). "The bearing capacity of clays." *Proceedings, Building Research Congress*. London, UK.

Stanier, S.A., Blaber, J., Take, W.A. & White, D.J. (2015). "Improved image-based deformation measurement for geotechnical applications." *Canadian geotechnical Journal*.

Starling, M. & Scott, A. (2009). "Foundations and Mooring for Tidal Stream Systems." Produced on behalf of The Carbon Trust. *BMT Cordah*, Report No. L.CAR.002W.

Steensen-Bach, J.O. (1992). "Recent Model Tests With Suction Piles in Clay and Sand." Offshore Technology Conference. Houston, TX, USA.

Stevens, J.B. & Audibert, J.M.E. (1979). "Re-examination of P-y Curve Formulations." Offshore Technology Conference. Houston, TX, USA.

Sukumaran, B. McCarron, W.O., Jeanjean, P. & Abouseeda, H. (1999). "Efficient Finite element techniques for limit analysis of suction caissons under lateral loads." *Computers and Geotechnics.* 24(2):89-107.

Taylor, Z.J., Gurka, R., Kopp, G.A. & Liberzon, A. (2010). "Long-Duration Time-Resolved PIV to Study Unsteady Aerodynamics." *IEEE Trans. Instrum. Meas.* 59(12):3262-3269.

Templeton, J.S. (2002). "The Role of Finite Elements in Suction Foundation Design Analysis." Offshore Technology Conference. Houston, Texas, USA.

Terzaghi, K., Peck, R.B., & Mesri, G. (1996) *Soil Mechanics in Engineering Practice*. 3rd Edition. John Wiley & Sons, Inc. New York City, New York, USA.

Verdant Power. (2010). "Pilot License Application Roosevelt Island Tidal Energy Project: FERC No. 12611." Verdant Power, LLC, New York, NY, USA.

Villalobos, F.A., Byrne, B.W. & Houlsby, G.T. (2010). "Model testing of suction caissons in clay subjected to vertical loading." *Applied Ocean Research*. 32(2010):414-424.

Wallace, J.F. & Rutherford, C.J. (2015). "Geotechnical Properties of Laponite RD." *Geotech. Test. J.* 38(5):1-14.

Wallace, J.F., Rutherford, C.J., and Zheng, J., 2018, "Visualizing Failure Surfaces in Soft Clay Due to Suction Caisson Loading," The 2018 International Foundations Congress & Equipment Exposition (IFCEE 2018), 5-10 March 2018, Orlando, Florida. (In Review)

Wang, J., Yang, Y. & Liu, J. (2011). "Model Tests and Analysis Method on Cyclic Bearing Capacity of Suction Caissons with the Taut Mooring System in Soft Clays." *Proceedings of the Twenty-first (2011) International Offshore and Polar Engineering Conference*. Maui, HI, USA.

Watson, P.G., Randolph, M.F. & Bransby, M.F. (2000). "Combined Lateral and Vertical Loading of Caisson Foundations." Offshore Technology Conference. Houston, TX, USA.

Westgate, Z.J., Tapper, L., Lehane, B.M. & Gaudin C. (2009). "Modelling the installation of stiffened caissons in overconsolidated clay." *Proceedings of the ASME 2009 28th International Conference on Ocean, Offshore and Arctic Engineering*. Honolulu, HI, USA.

White, D.J., Take, W.A. & Bolton, M.D. (2003). "Soil Deformation Measurement Using Particle Image velocimetry (PIV) and Photogrammetry." *Geotechnique.* 53(7):619-631.

Whittle, A.J., Germaine, J.T. & Cauble, D.F. (1998). "Behavior of miniature suction caissons in clay." *Offshore Site Investigation and Foundation Behaviour.*

Xu, L., Jia, J., & Matsushita, Y. (2012). "Motion Detail Preserving Optical Flow Estimation." *IEEE Transactions on Pattern Analysis and Machine Intelligence*. 34(9):1744-1757.

Zhang, P., Ding, H. & Le, C. (2013a). "Model tests on tilt adjustment techniques for a mooring dolphin platform with three suction caisson foundations in clay." *Ocean Engineering*. 73(2013):96-105.

Zhang, P., Ding, H. & Le, C. (2013b). “Installation and Removal Records of Field Trials for Two Mooring Dolphin Platforms with Three Suction Caissons.” *Journal of Waterway, Port, Coastal, and Ocean Engineering*. 139(6):502-517.

Zhao, H., Ge, L. & Luna, R. (2010). “Low Viscosity Pore Fluid to Manufacture Transparent Soil.” *Geotech. Test. J.* 33(6):1-6.

Zheng, J. & Hryciw, R.D. (2014). “Optical Flow Analysis of Internal Erosion and Piping in Soil Images Captured by the VisCPT.” *Tunneling and Underground Construction GSP 242*. 55-64.

CHAPTER 3. SOIL TEST BEDS

3.1 Kaolin 1-g model test beds

3.1.1 General and geotechnical properties

The clay utilized in the fifteen kaolin 1-g model test beds was manufactured by Edgar Minerals, Inc., and known commercially as Edgar Plastic Kaolin or EPK Kaolin. The as shipped reported composition by weight of the kaolin was 96 to 99.9% kaolinite and 0.1 to 4% crystalline silica. General and geotechnical properties of the kaolin are given in Table 3.1 while geotechnical properties specific to the kaolin 1-g model test beds are given in Table 3.2. The properties were obtained from various sources including geotechnical laboratory tests conducted by the author, reports form the manufacturer, and/or literature. In the case of the geotechnical laboratory tests conducted by the author, the tests involving consolidation were all consolidated from the same initial slurry that was used to consolidate the model test beds (described in Section 3.1.2) in order to obtain the geotechnical properties applicable to the specific consolidation method. Figure 3.1 through Figure 3.5 show the data obtained from these geotechnical laboratory tests including Atterberg limits, hydrometer, and incremental load consolidation.

3.1.2 Slurry preparation

The slurry from which the test beds were consolidated was prepared by mixing the as-shipped, dry, powdered kaolin with a saltwater pore fluid. A sodium chloride (NaCl) saltwater pore fluid was utilized to better model properties of offshore clay that would typically be deposited and undergo consolidation in a saltwater environment. The NaCl was first dissolved in distilled water at a concentration of 35 g/L using a bottom-up mortar mixer. The as-shipped kaolin was then added and thoroughly mixed to achieve a water content 1.7 times the liquid limit or 98%. Mixing the slurry at this water content allowed for the slurry to be readily poured. Once thoroughly mixed, the slurry was stored within sealed buckets for a minimum of 7 days to allow for full hydration of the kaolin. During the hydration period and prior to pouring into the test bed containers, the kaolin was agitated to minimize sedimentation or self-weight consolidation.

3.1.3 Test bed container

The kaolin 1-g model test bed containers were fabricated from PVC, an example of which is shown in Figure 3.6. The cylindrical portion of the container consisted of a 762 mm

long segment of a DR25 Potable Water AWWA C900/IB PVC Pressure Pipe of 24-inch size (not the true dimension) manufactured by North American Pipe Corporation. The base of the container consisted of a 914 mm square PVC plate that was 19 mm thick. A 6 mm channel was cut into the plate and filled with epoxy to connect the cylinder to the plate. This fabrication method resulted in a container inside diameter of 603 mm and height of 756 mm. The containers were equipped with drainage valves at the base to allow for double drained boundary conditions.

3.1.4 Consolidation

Prior to pouring the slurry into the containers, the bottom drainage layer was prepared. The bottom drainage layer consisted of compacted, poorly graded sand. The openings of the bottom drainage valves were first covered with filter paper. The play sand was then placed partially saturated and compacted by hand until above the height of the drainage valve openings. A geotextile serving as a filter fabric was then placed above the sand layer and tape was used to seal the gap between the container wall and the geotextile. After the bottom drainage layer was prepared, the fully hydrated slurry was poured into the container to a height of 610 mm. A geotextile layer was then placed over the slurry and consolidation was accomplished via surcharge. After end of primarily consolidation was reached based on the Taylor method, the surcharge, upper geotextile layer, and surficial water were removed and the bottom drainage valve was closed. The test bed was then complete for the load test. Between completion of consolidation and the start of the model test, the test bed container was covered and the surface was sprayed with water to prevent the desiccation of kaolin.

The consolidation via surcharging described above resulted in a final effective vertical stress at the mid depth of 4.6 kPa. The overconsolidation ratio (OCR) with depth of the test bed upon removal of the surcharge is shown in Figure 3.7. The OCR at the bottom of the tested was 2.6 and the OCR at a depth of 152 mm (the skirt length of the kaolin 1-g model foundation further discussed in Section 4.2.1) was 6.2. While these OCR values are relatively high, such OCR values are possible at tidal current sites due to the high potential for erosion from high current velocities (Hjulström 1935, Sundborg 1956, Georgia Tech Research Corporation 2011). Geotechnical investigations by Maynard et al. (2013) at the Cobscook tidal site have indicated the presence of up to 14.5 m of very soft to soft clay overlaying bedrock at such locations with current velocities indicating a high potential for erosion.

One test bed was consolidated for each of the kaolin 1-g model load tests for a total of fifteen test beds. The nomenclature for each of the kaolin 1-g model test beds is K-1G-TB# where # is the test bed number in chronological order. The surcharge applications and settlements with time for each of the test beds are shown in Figure 3.8 through Figure 3.22 along with the shear strength of each test bed as measured by laboratory vane shear. The final height of each test bed after consolidation is shown in Table 3.4. The average final test bed height was 487 mm.

3.2 Kaolin 90-g model test beds

3.2.1 General and geotechnical properties

The clay utilized in the eight kaolin 90-g model test beds was the same as that of the kaolin 1-g model test beds described in Section 3.1. The general and geotechnical properties of the kaolin are given in Table 3.1 while geotechnical properties specific to the kaolin 90-g model test beds are given in Table 3.3. Figure 3.1 through Figure 3.5 show the data obtained from a selection of these geotechnical laboratory tests including Atterberg limits, hydrometer, and incremental load consolidation.

3.2.2 Slurry preparation

The saltwater and kaolin slurry utilized for the kaolin 90-g model test beds was primarily prepared in the same manner as described in Section 3.1.2 for the kaolin 1-g model test bed. The only difference in the preparation method was that the kaolin was hydrated for a minimum of 2 days rather than 7 days due to facility-imposed time restrictions. This difference in hydration time will not have any significant effect on the behavior of the clay since hydration of kaolin typically occurs within 24 hours.

3.2.3 Test bed container

The kaolin 90-g model test bed containers were prefabricated and provided on site at the geotechnical centrifuge facility at the University of Colorado at Boulder (CU Boulder). An example of the container is shown in Figure 3.23. They were designed to fit on the payload side of the 15-g ton beam centrifuge as demonstrated in Figure 3.24. The beam centrifuge is discussed in further detail in Section 5.2.2. The overall design of the 1-g and the 90-g model test bed containers were similar with a cylindrical wall and a square base plate. However, the 90-g

model test bed containers were fabricated from aluminum. The inside diameter of the 90-g containers were 378 mm and the container heights were 305 mm. The containers were equipped with a porous stone and drainage line at the base to allow for double drained boundary conditions.

3.2.4 Consolidation

Two types of kaolin 90-g test beds were prepared distinguishable by the thickness of the clay layer. Having two thicknesses allowed for optimization of the finite test time on the geotechnical beam centrifuge by shortening the length of time needed to consolidate the thinner test bed. The different lengths of the two kaolin 90-g model foundations (described further in Section 5.2.1) allowed for the two test bed thicknesses. The bottom sand drain layer thickness and initial slurry thickness were determined to allow for a minimum of two foundation diameters between the tip of the foundation model and the bottom of the test bed when fully embedded and to position the top of both test beds at approximately the same distance from the center of rotation to ensure a matching g-level at the surface of the kaolin for both test bed types.

The general consolidation procedures for both types of the kaolin 90-g test beds were similar to their 1-g counterparts. A compacted play sand drainage layer was placed at the bottom of the container and covered with a geotextile filter fabric sealed to the sidewall of the container with tape. The two kaolin 90-g model foundations were of the same diameter but had different skirt lengths that required different thickness test beds to minimize boundary conditions effects (i.e. the shorter model foundation allowed for a thinner test bed). Due to this test bed thickness difference, the thickness of the bottom drainage layer was larger for the test beds of the shorter foundation to ensure that the kaolin test bed surfaces of the two types were at a similar g-level. The slurry was then poured over the prepared bottom drainage layer and filter fabric. The initial height of the slurry was 184 mm and 248 mm for K-90G-AR1's and K-90G-AR2's test beds respectively. These initial heights were based on calculated settlements using the data presented in Figure 3.3. A geotextile layer was then placed over the slurry and consolidation was accomplished via surcharge. After end of primarily consolidation was reached, the surcharge, and upper geotextile layer were removed. The test bed was then complete for the load test. Between completion of consolidation and the start of the model test, the test bed container was covered. A layer of water was left over the test bed in order to prevent desiccation both prior to and during centrifuge spinning.

The consolidation via surcharging described above resulted in a final effective vertical stress at the mid-depth of 37.1 kPa and 51.4 kPa for K-90G-AR1's and K-90G-AR2's test beds respectively. These final effective vertical stresses applied during the 1-g surcharge consolidation were chosen to match the prototype effective vertical stresses at the mid-depth of the test bed during spinning. The prototype OCR with depth of the test bed is shown in Figure 3.25 and Figure 3.26 for the K-90G-AR1 and K-90G-AR2 model foundations respectively. At the depth of the K-90G-AR1 and K-90G-AR2 foundation tips, the prototype OCR was 1.6 and 1.1 respectively. These are lower than those of the kaolin 1-g model test beds allowing for observation of foundation behavior in kaolin at varying levels of OCR.

Two kaolin 90-g model load tests were conducted in each of the kaolin 90-g model test beds. This was possible due to the offset of the loading actuator on the beam centrifuge described further in Section 5.2.2. The nomenclature for each of kaolin 90-g model test beds is K-90G-TB# where # is the test bed number in chronological order. The height of each test bed and the foundation that the test bed was prepared for are listed in Table 3.7. The surcharge applications and settlements with time for each of the test beds are shown in Figure 3.27 through Figure 3.34 along with the shear strength of each test bed as measured by laboratory vane shear. The average final test bed height after consolidation was 125 mm and 167 mm for the K-90G-AR1 and K-90G-AR2 test beds respectively in the model scale or 11.3 m and 15.0 m in the prototype scale.

3.3 Laponite 1-g model test beds

3.3.1 General and geotechnical properties

The transparent soil utilized in the four laponite 1-g model test beds was manufactured by BYK Additives & Instruments and known commercially as Laponite RD. Laponite is a 2:1 synthetic smectite comparable to the natural clay mineral hectorite. The reported geometry of an individual particle of laponite has a diameter of 25 nm and a height of 0.92 mm (BYK Additives and Instruments 2014) and is relatively uniform due to the manufacturing process (Ramsay 1986). General and geotechnical properties of the laponite are given in Table 3.6. The properties were obtained from geotechnical laboratory tests conducted by the author and reports from the manufacturer. Since the test beds were prepared at a specific concentration of 6%, properties at that given concentration are reported. Geotechnical properties of laponite at various

concentrations can be found in Appendix A (Wallace and Rutherford 2015) and Beemer et al. (2016).

3.3.2 Slurry preparation

Similar to the kaolin, the laponite was prepared in slurry form by mixing the as shipped, dry, powered laponite with a pore fluid. The pore fluid consisted of a sodium pyrophosphate decahydrate (SPP) and tap water pore fluid. The SPP was first dissolved in the tap water at a concentration of 0.135% based off of recommendations by Beemer et al. (2016) where the SPP concentration was defined as:

$$\boldsymbol{SPP_{con}}(\%) = \frac{\boldsymbol{m_{SPP}}}{\boldsymbol{m_{water}}} * \mathbf{100} \qquad \textbf{Equation 3.1}$$

where:

m_{SPP} = mass of sodium pyrophosphate decahydrate

m_water = mass of tap water

Once the SPP was fully dissolved, the retroreflective aluminum coated solid glass microspheres which served as the seeding particles were mixed into the pore fluid at a concentration of 0.022% of the total mass. The laponite powder was then added to the pore fluid under agitation over a time period of 2 to 3 minutes at a concentration of 6% where the laponite concentration was defined as follows:

$$\boldsymbol{Lap_{con}}(\%) = \frac{\boldsymbol{m_{laponite}}}{\boldsymbol{m_{total}}} * \mathbf{100} = \frac{\boldsymbol{m_{laponite}}}{\boldsymbol{m_{laponite}+m_{water}+m_{SPP}}} * \mathbf{100} \qquad \textbf{Equation 3.2}$$

where:

$m_{laponite}$ = mass of dry, as shipped laponite powder

The mixing was continued for an additional 5 to 10 minutes (i.e. until the laponite was fully hydrated based on manufacturer recommendations). Once the slurry was mixed, it was ready to be poured into the test bed container.

The slurry was prepared with the sodium pyrophosphate decahydrate and tap water pore fluid rather than the originally developed distilled water pore fluid because it was found to allow for higher concentrations of laponite to be mixed (Beemer et al. 2016). Higher concentrations result in higher shear strength of the material, but degrade the transparent nature of the final product due a non-perfect match of the pore fluid at the laponite particles. The inclusion of retroreflective aluminum coated solid glass microspheres also differs from the originally

developed procedures presented by Wallace and Rutherford (2015). These microspheres were an improvement presented by Killen (2016) that served as a seeding particle which increase the contrast and texture along the plane illuminated by the laser allowing for increased ability of optical deformation tracking. However, the increased contrast and texture could be counteracted if the concentration of laponite was too high. A trial and error method was utilized to determine the ideal location of the illuminated plane and concentration of laponite that would minimize boundary effects of the container wall, but still allow for substantial contrast to allow for optional deformation estimation techniques. The ideal laponite concentration was determined to be 6%. This concentration allowed for a distance to the illuminated plane of 60 mm to 65 mm as measured from the container wall to the plane.

3.3.3 Test bed container

The laponite 1-g model test bed containers were clear acrylic cubes with 5 mm thick walls. An example of the container is shown in Figure 3.35. Cubes were utilized, as a cylindrical sidewall would distort both the laser plane and the view within the container. Circular markers were placed on two parallel sidewalls to serve as reference points as required for some forms of optical deformation estimation. However, these reference points were not utilized for this study as the optical flow estimation analysis conducted did not require their use. The other two parallel sidewalls were left uncovered in order to allow free passage of laser light. The inside dimensions of the container were 295 mm by 295 mm in plan with heights varying from 171 mm to 203 mm.

3.3.4 Consolidation

Similar to the kaolin 90-g test beds, two types of laponite 1-g test beds were prepared distinguished by the thickness of the laponite layer. The two model foundations were the shorter L-1G-AR1 and the longer L-1G-AR2 (see Section 6.2.1 for nomenclature and detailed description). The thicker test beds were prepared for the L-1G-AR2 model foundations. The slurry was poured directly into the empty containers immediately after it was prepared. This was due to the slurry beginning to set after mixing was completed. The slurry was poured to a height of 123 mm to 131 mm for the L-1G-AR1 model foundation test beds and to a height of 161 mm to 163 mm for the L-1G-AR2 model foundation test beds. The containers were then covered and sealed and allowed to set over the course of 7 days prior to testing. No significant height change was measured over the course of 7 days.

Two laponite 1-g model load tests were conducted in each of the laponite 1-g model test beds. This was possible due to the offset of the loading actuator described further in Section 6.2.2 and of the illuminated laser plane discussed in Section 3.3.2. The nomenclature for each of the laponite 1-g model test beds is L-1G-TB# where # is the test bed number in chronological order. The height of each test bed and the foundation that the test bed was prepared for are listed in Table 3.7. The shear strength as measured by the laboratory vane shear is listed in Table 3.8. The average final test bed height after consolidation was 126 mm and 162 mm for the L-1G-AR1 and L-1G-AR2 test beds respectively.

3.4 Tables

Table 3.1: General and geotechnical properties of the kaolin used in kaolin 1-g model testing and the kaolin 90-g model testing

Parameter	Value
Composition – kaolinite[1] (%)	96 – 99.9
Composition – crystalline silica[1] (%)	0.1 – 4
Specific gravity[2], G_s	2.65
Liquid limit[2], LL (%)	59
Plastic limit[2], PL (%)	33
Plasticity index[2], PI (%)	26
Percent finer than 2 microns[2] (%)	71
Activity[2], A	0.37
Compression index[2], C_c	0.55
Swelling index[2], C_s	0.018
Secondary compression index[2], C_α	0.016
Permeability change index[2], C_k	0.94
Effective stress friction angle[3], φ'	33

[1]Reported by Edgar Minerals, Inc. (2013)
[2]Determined via laboratory tests
[3]Reported by Lin and Penumadu (2005)

Table 3.2: Geotechnical properties specific to the kaolin 1-g test beds

Parameter	Value
Coefficient of consolidation[1], c_v (m^2/yr)	0.68
Permeability[1], k (m/s)	$2.9*10^{-9}$
Undrained shear strength at surface[2], s_{uo} (kPa)	0.53
Undrained shear strength change with depth[2] (kPa/m)	2.3

[1]At the mid-depth of the test bed determined via laboratory tests
[2]Average of all kaolin 1-g model tests beds

Table 3.3: Geotechnical properties specific to the kaolin 90-g test beds

Parameter	Value[1]
Coefficient of consolidation[2], c_v (m^2/yr)	1.39, 1.55
Permeability[2], k (m/s)	$7.9*10^{-10}$, $6.7*10^{-10}$
Undrained shear strength at surface[3], s_{uo} (kPa)	5.0, 7.1
Undrained shear strength change with depth[3] (kPa/m)	0.060, 0.027

[1]First and second value applicable to test beds for K-90G-AR1 and K-90G-AR2 respectively
[2]At the mid-depth of the test bed determined via laboratory tests
[3]Average of all the applicable kaolin 90-g model tests beds and in prototype units

Table 3.4: Kaolin 1-g test bed heights

Test bed identifier	Test bed height (mm)
K-1G-TB1	491
K-1G-TB2	490
K-1G-TB3	490
K-1G-TB4	490
K-1G-TB5	490
K-1G-TB6	490
K-1G-TB7	491
K-1G-TB8	488
K-1G-TB9	490
K-1G-TB10	485
K-1G-TB11	489
K-1G-TB12	483
K-1G-TB13	482
K-1G-TB14	480
K-1G-TB15	481

Table 3.5: Kaolin 90-g test bed heights and the associated model foundations

Test bed identifier	Test bed height (mm)	Associated model test bed
K-90G-TB1	167	K-90G-AR2
K-90G-TB2	123	K-90G-AR1
K-90G-TB3	166	K-90G-AR2
K-90G-TB4	126	K-90G-AR1
K-90G-TB5	126	K-90G-AR1
K-90G-TB6	169	K-90G-AR2
K-90G-TB7	127	K-90G-AR1
K-90G-TB8	166	K-90G-AR2

Table 3.6: General and geotechnical properties of the laponite used in the laponite 1-g model testing

Parameter	Value
Composition – silicon dioxide[1] (%)	59.5
Composition – magnesium oxide[1] (%)	27.5
Composition – lithium oxide[1] (%)	0.8
Composition – sodium oxide[1] (%)	2.8
Composition – loss on ignition[1] (%)	8.2
Specific gravity[2], G_s	2.53
Liquid limit[2], LL (%)	1150
Plastic limit[2], PL (%)	240
Plasticity index[2], PI (%)	910
Compression index[2], C_c	21
Swelling index[2], C_s	9.1
Secondary compression index[2], C_α	0.72
Permeability change index[2], C_k	15
Coefficient of consolidation[2], c_v (m^2/yr)	0.009
Permeability[2], k (m/s)	$2*10^{-8}$

[1]Reported by BYK Additives and Instruments (2014)
[2]Determined via laboratory tests

Table 3.7: Laponite 1-g test bed heights and the associated model foundations

Test bed identifier	Test bed height (mm)	Associated model test bed
L-1G-TB1	125	L-1G-AR1
L-1G-TB2	163	L-1G-AR2
L-1G-TB3	126	L-1G-AR1
L-1G-TB4	161	L-1G-AR2

Table 3.8: Laponite 1-g test bed undrained shear strengths as measured by the laboratory vane shear

Test bed identifier	Depth (mm)	$s_{u,MV,peak}$ (kPa)	$s_{u,MV,residual}$ (kPa)
L-1G-TB1	38.1	0.47	0.13
	38.1	0.55	0.13
L-1G-TB2	76.2	0.51	0.13
	76.2	0.51	0.13
L-1G-TB3	38.1	0.51	0.13
	38.1	0.47	0.13
L-1G-TB4	76.2	0.47	0.13
	76.2	0.51	0.13

3.5 Figures

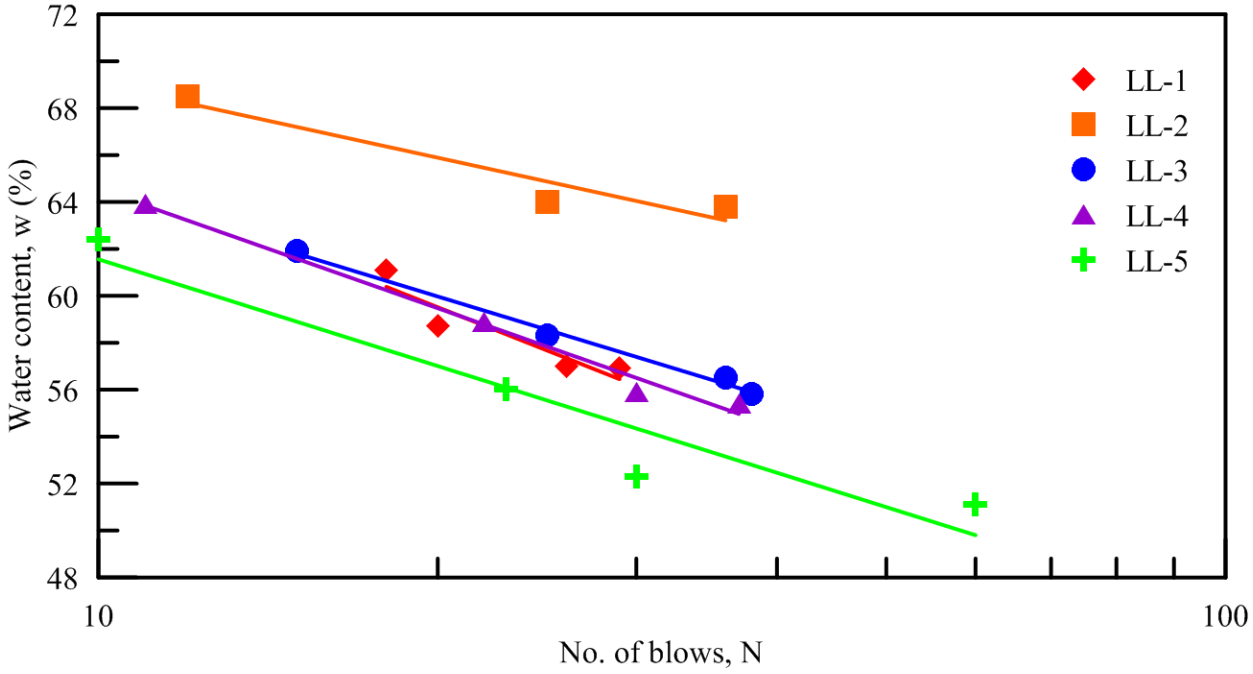

Figure 3.1: Liquid limit laboratory test data of the kaolin utilized in the kaolin 1-g model testing and kaolin 90-g model testing

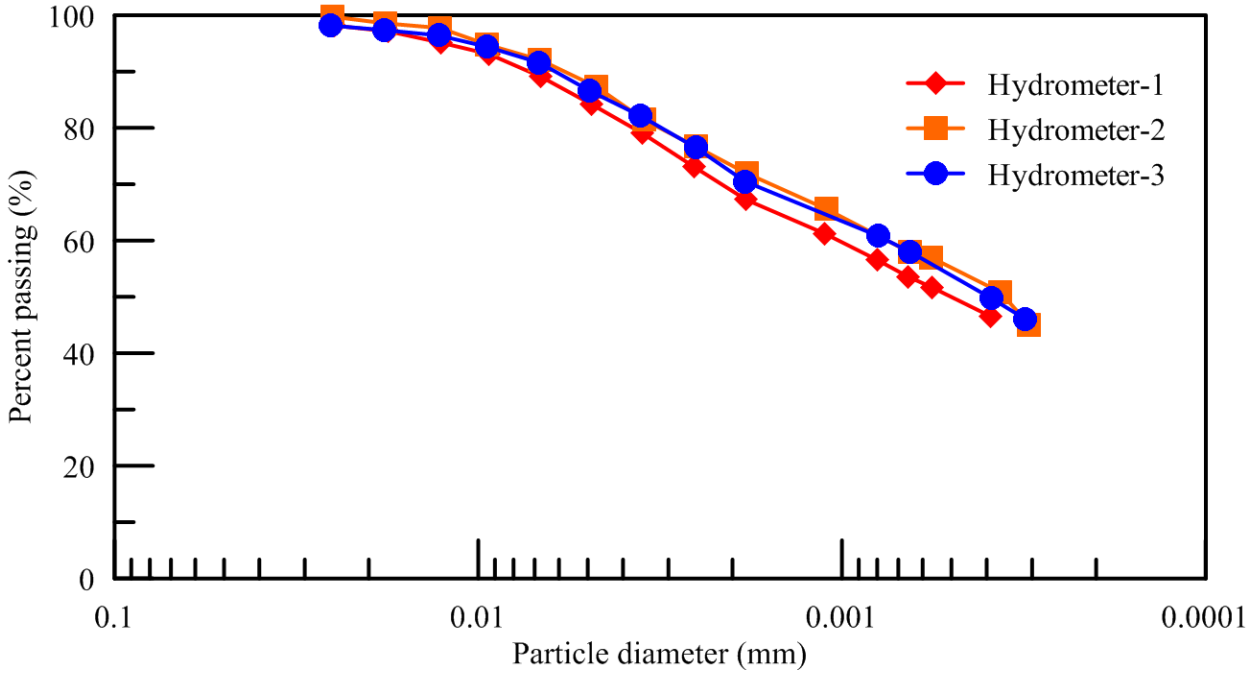

Figure 3.2: Hydrometer test data of the kaolin utilized in the kaolin 1-g model testing and kaolin 90-g model testing

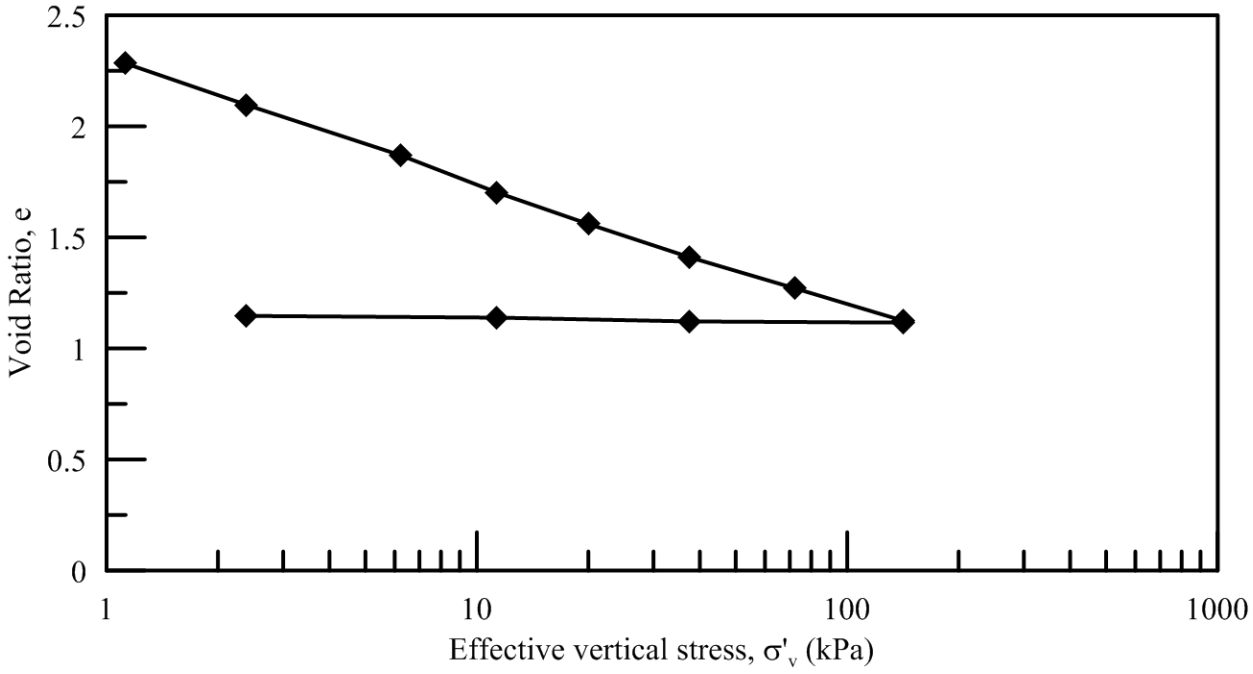

Figure 3.3: The void ratio versus log of effective vertical stress of the kaolin used in the kaolin 1-g model testing and kaolin 90-g model testing

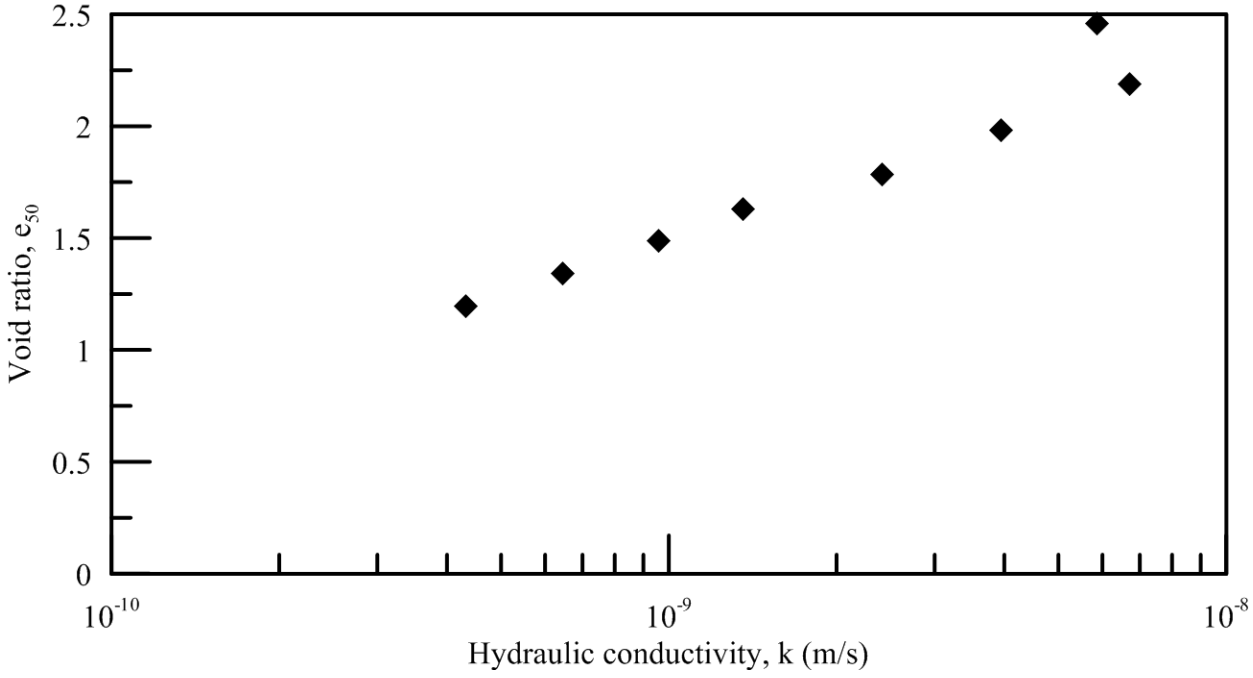

Figure 3.4: The void ratio versus the log of hydraulic conductivity of the kaolin used in the kaolin 1-g model testing and kaolin 90-g model testing

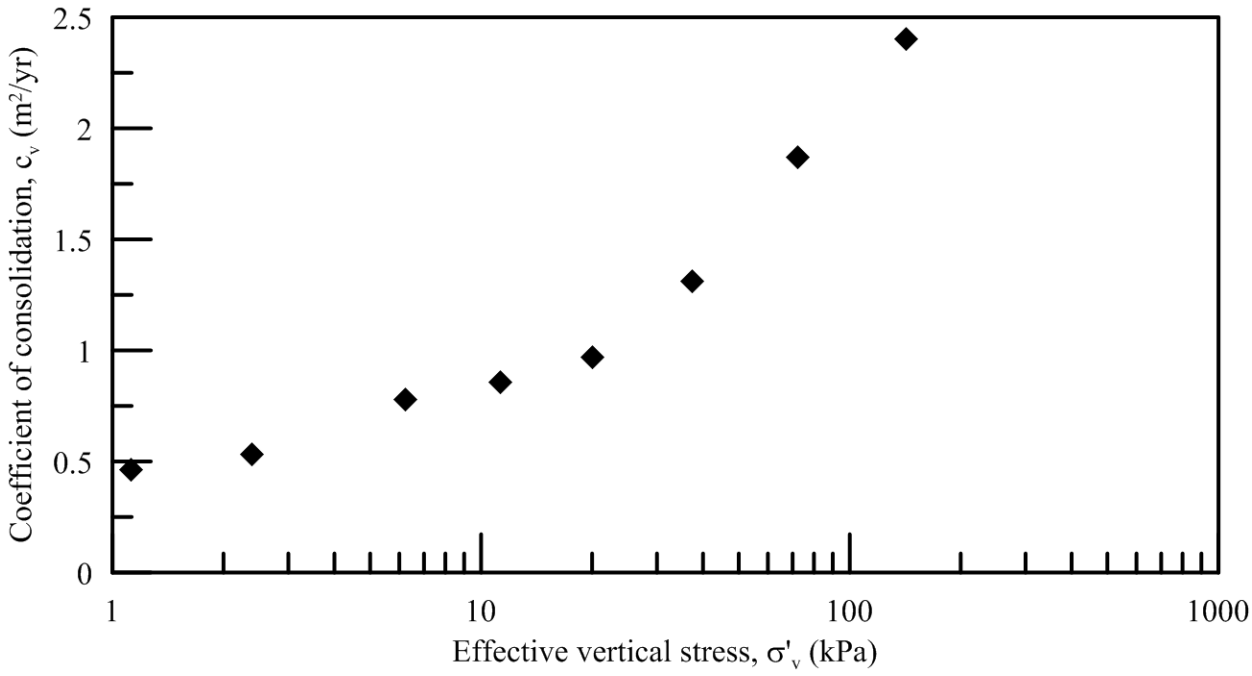

Figure 3.5: The coefficient of consolidation versus the log of effective vertical stress of the kaolin used in the kaolin 1-g model testing and kaolin 90-g model testing

Figure 3.6: Kaolin 1-g model test bed container

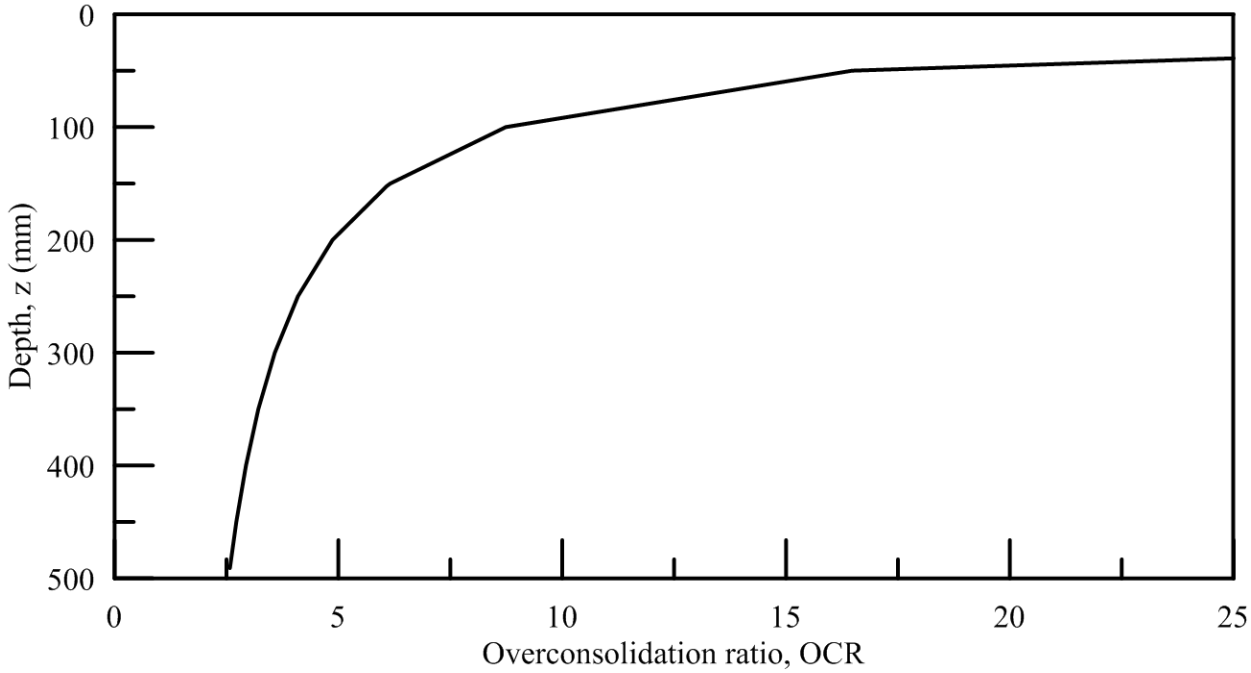

Figure 3.7: Overconsolidation ratio with depth of the Kaolin 1-g model test beds

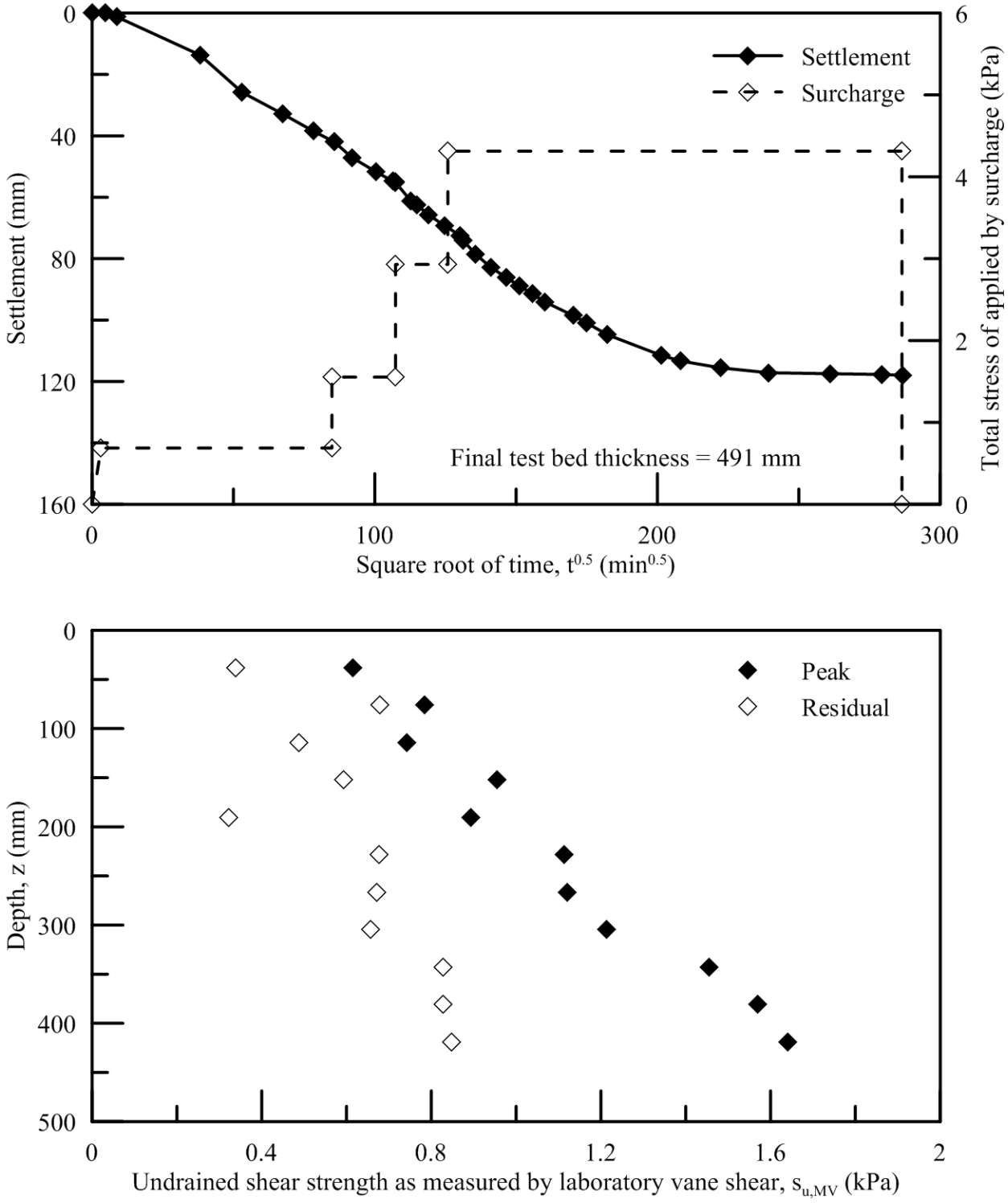

Figure 3.8: Consolidation surcharge with time, settlement with time and undrained shear strength as measured by laboratory vane shear post consolidation for K-1G-TB1

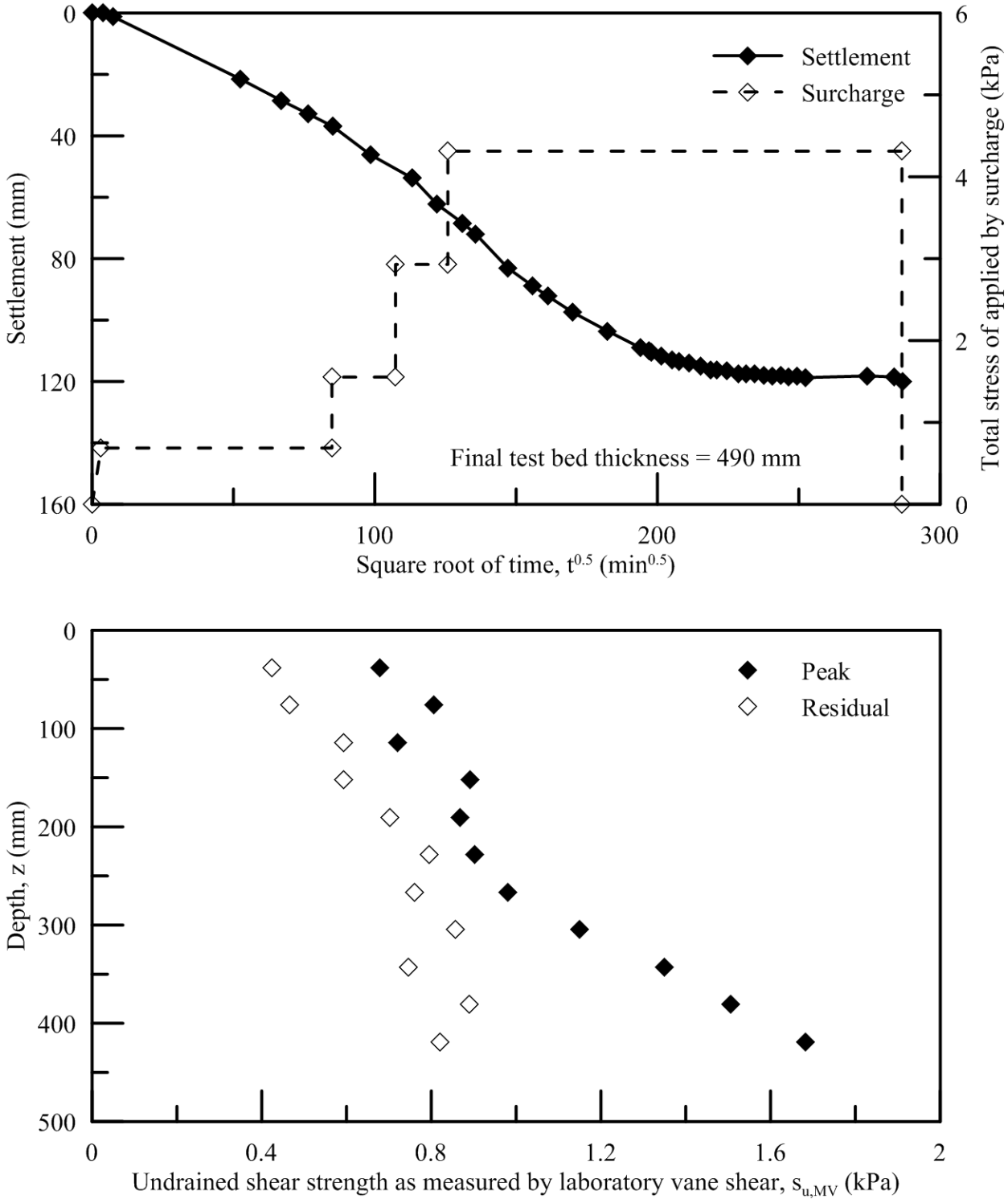

Figure 3.9: Consolidation surcharge with time, settlement with time and undrained shear strength as measured by laboratory vane shear post consolidation for K-1G-TB2

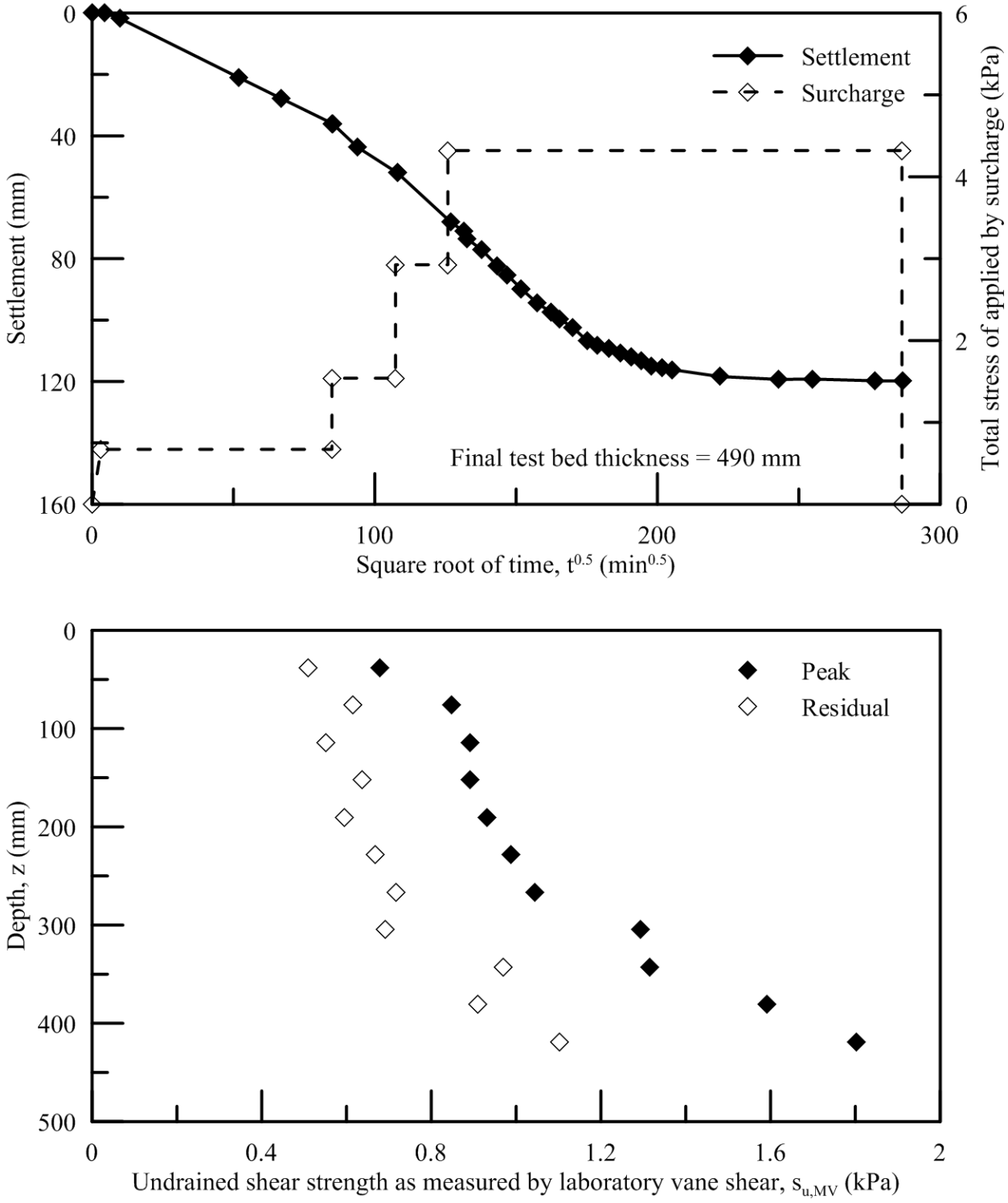

Figure 3.10: Consolidation surcharge with time, settlement with time and undrained shear strength as measured by laboratory vane shear post consolidation for K-1G-TB3

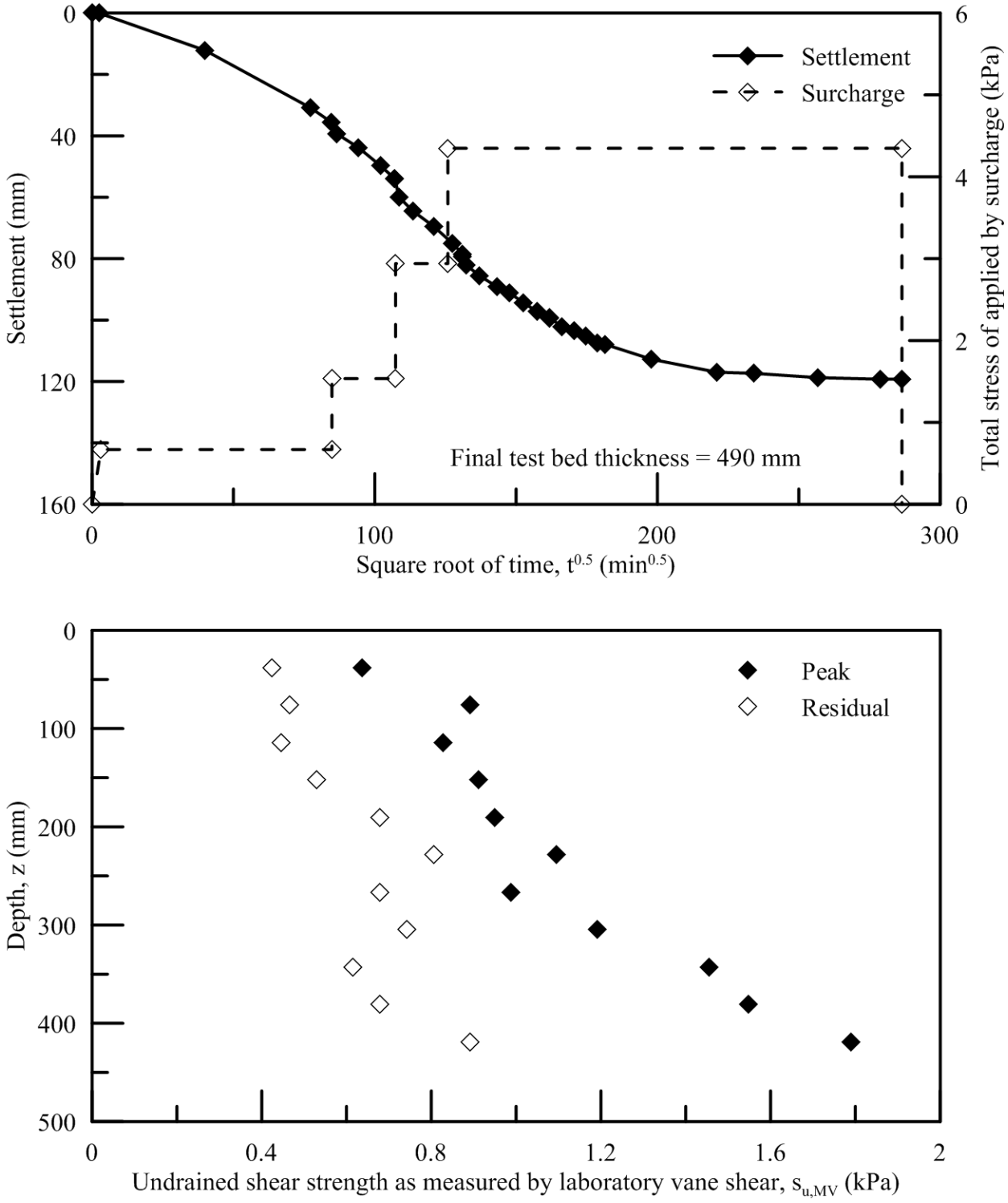

Figure 3.11: Consolidation surcharge with time, settlement with time and undrained shear strength as measured by laboratory vane shear post consolidation for K-1G-TB4

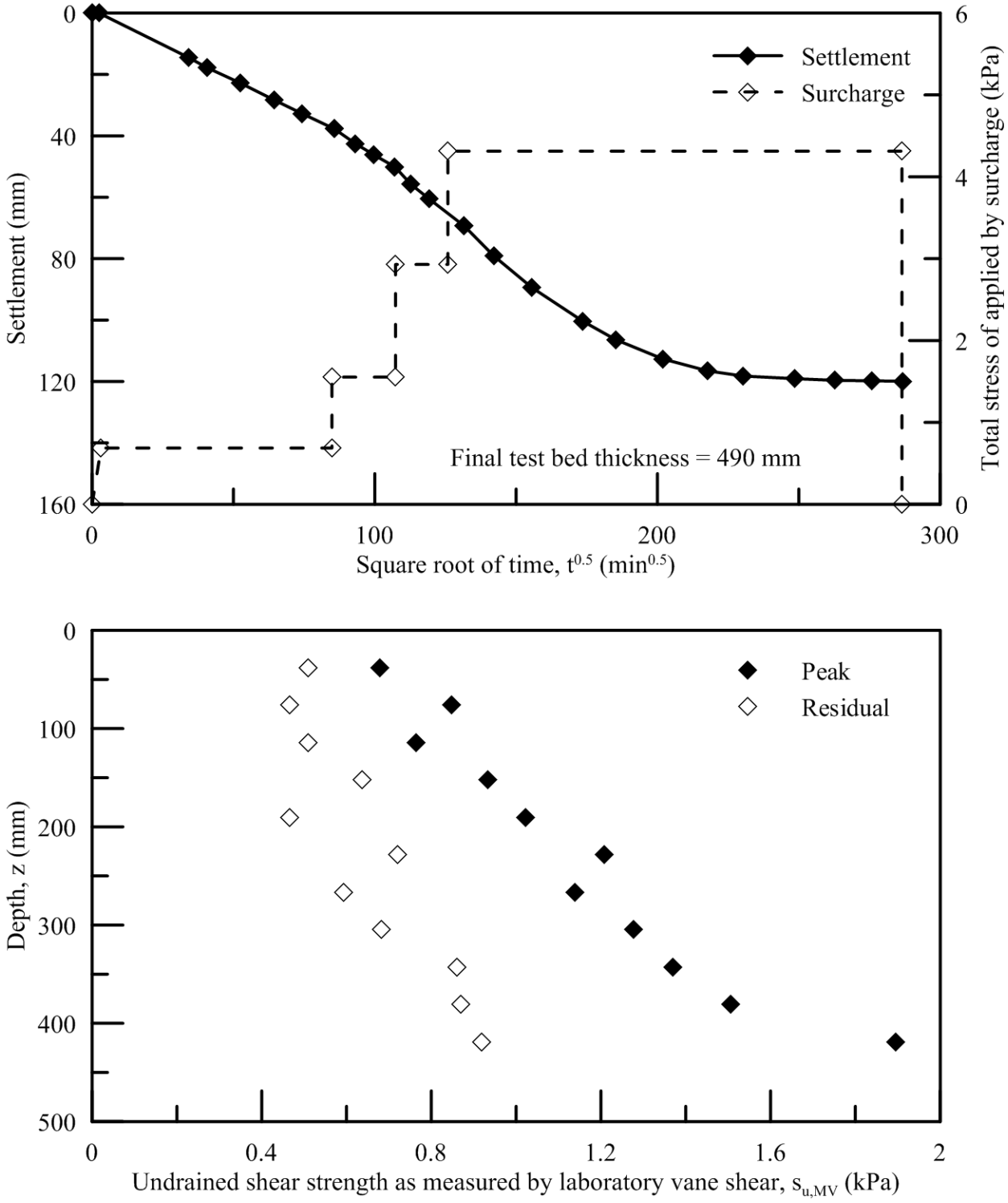

Figure 3.12: Consolidation surcharge with time, settlement with time and undrained shear strength as measured by laboratory vane shear post consolidation for K-1G-TB5

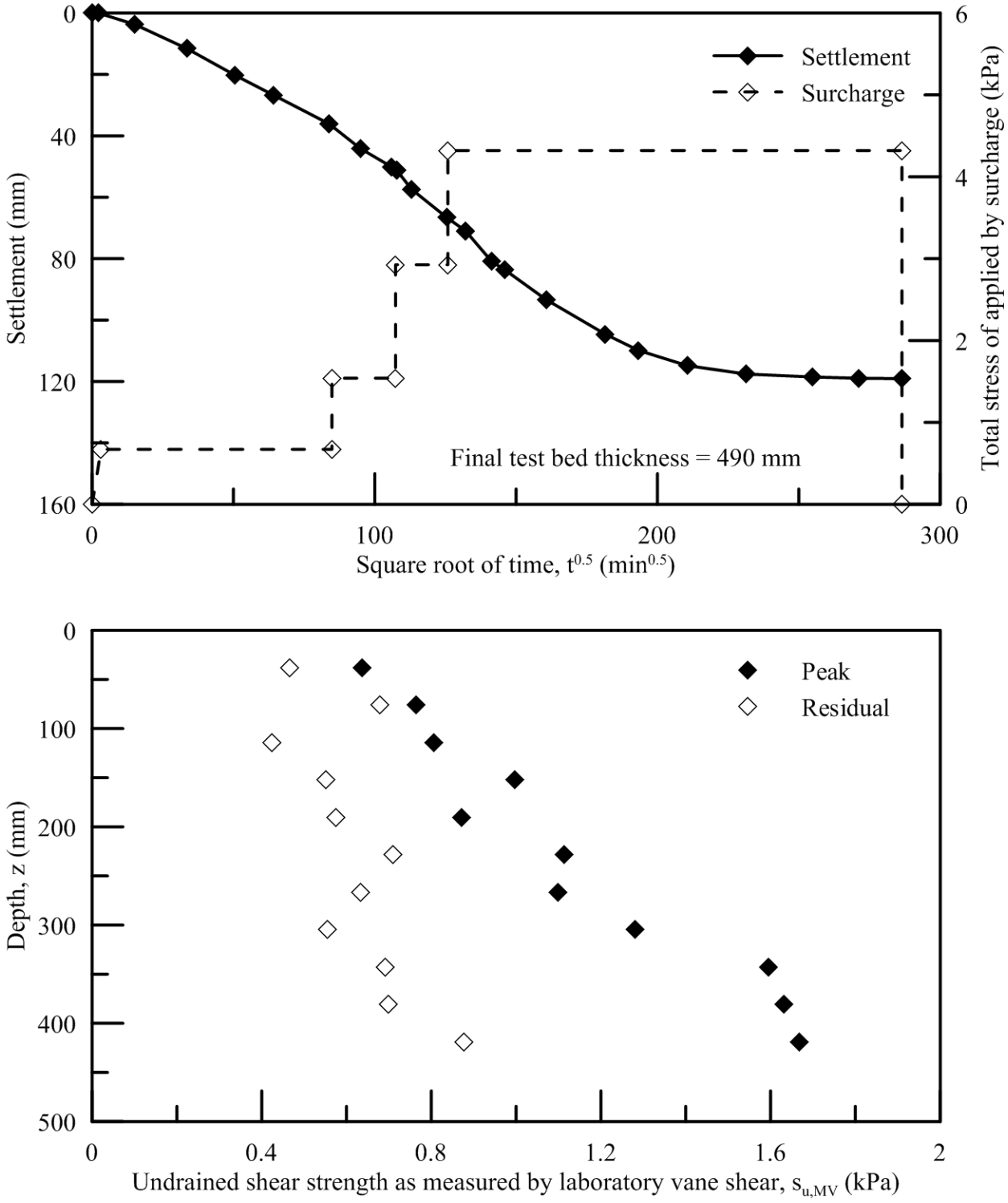

Figure 3.13: Consolidation surcharge with time, settlement with time and undrained shear strength as measured by laboratory vane shear post consolidation for K-1G-TB6

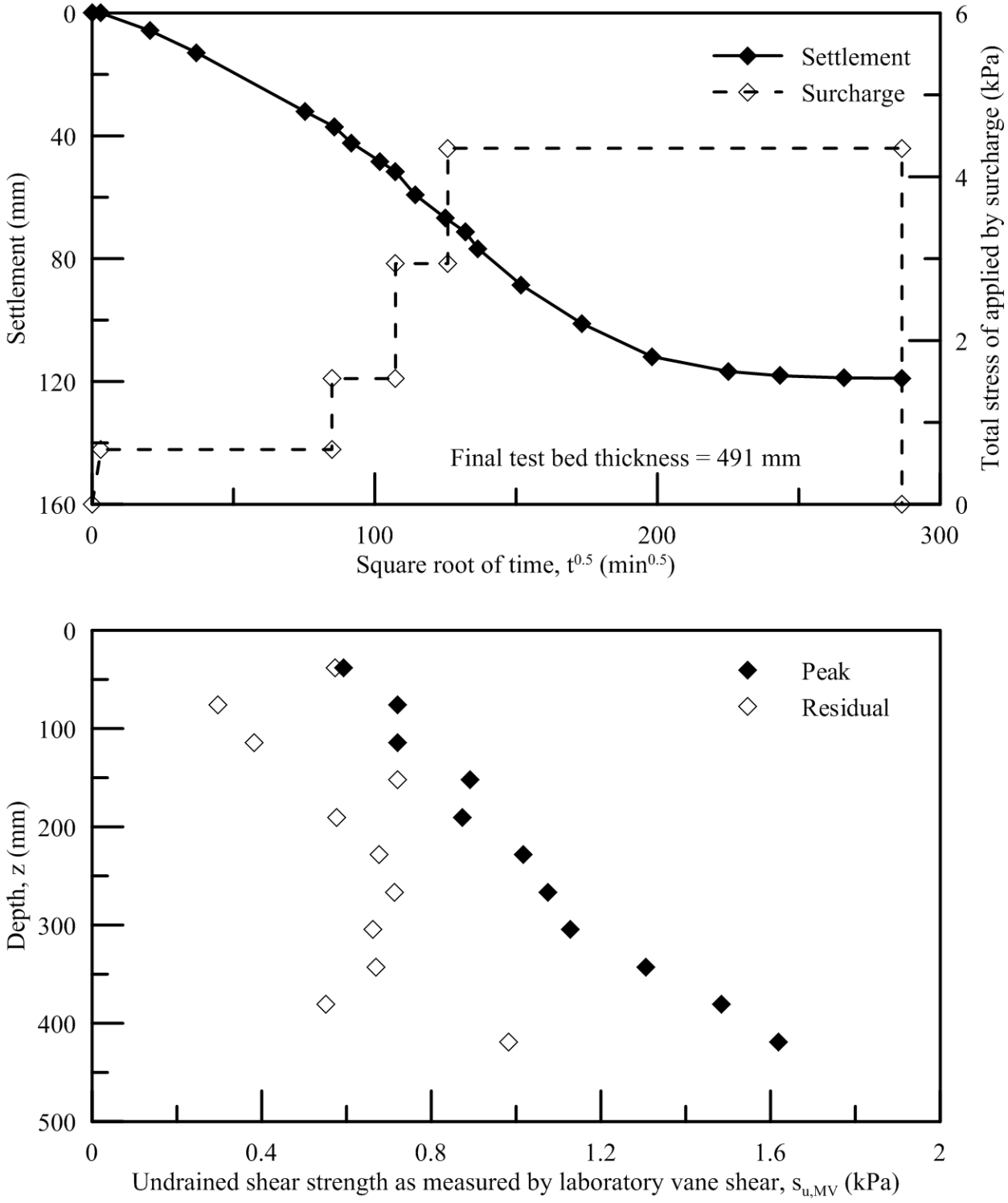

Figure 3.14: Consolidation surcharge with time, settlement with time and undrained shear strength as measured by laboratory vane shear post consolidation for K-1G-TB7

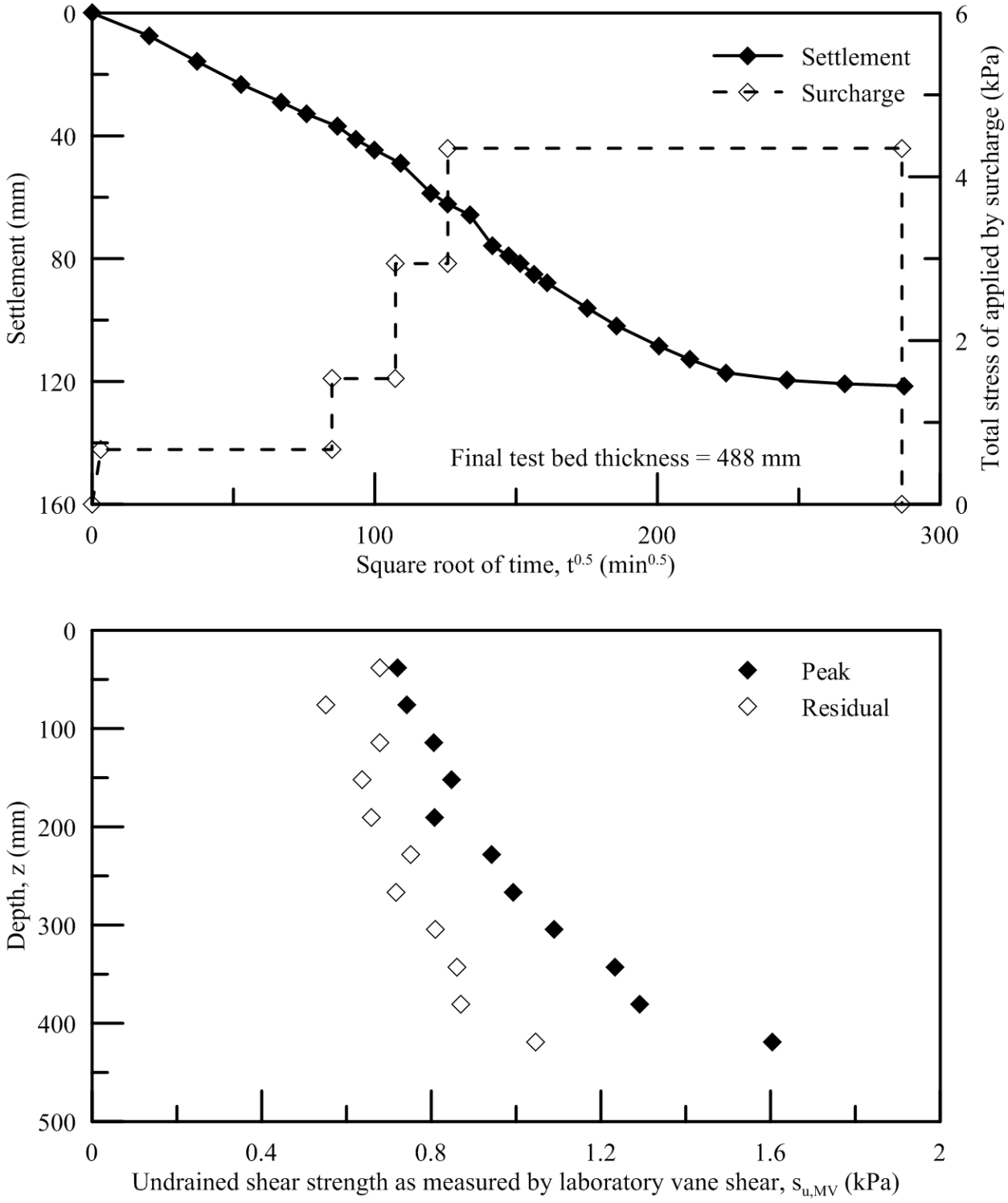

Figure 3.15: Consolidation surcharge with time, settlement with time and undrained shear strength as measured by laboratory vane shear post consolidation for K-1G-TB8

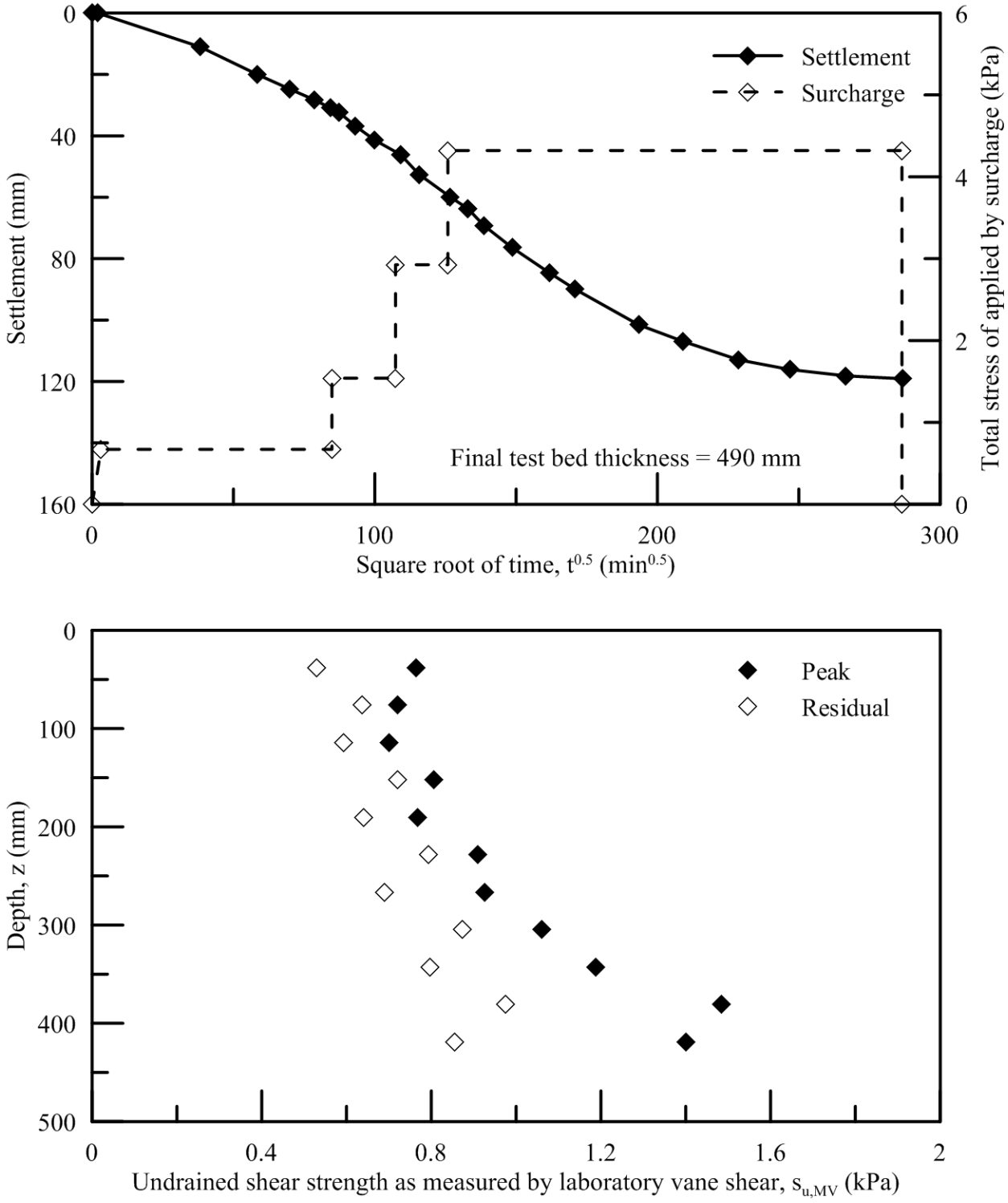

Figure 3.16: Consolidation surcharge with time, settlement with time and undrained shear strength as measured by laboratory vane shear post consolidation for K-1G-TB9

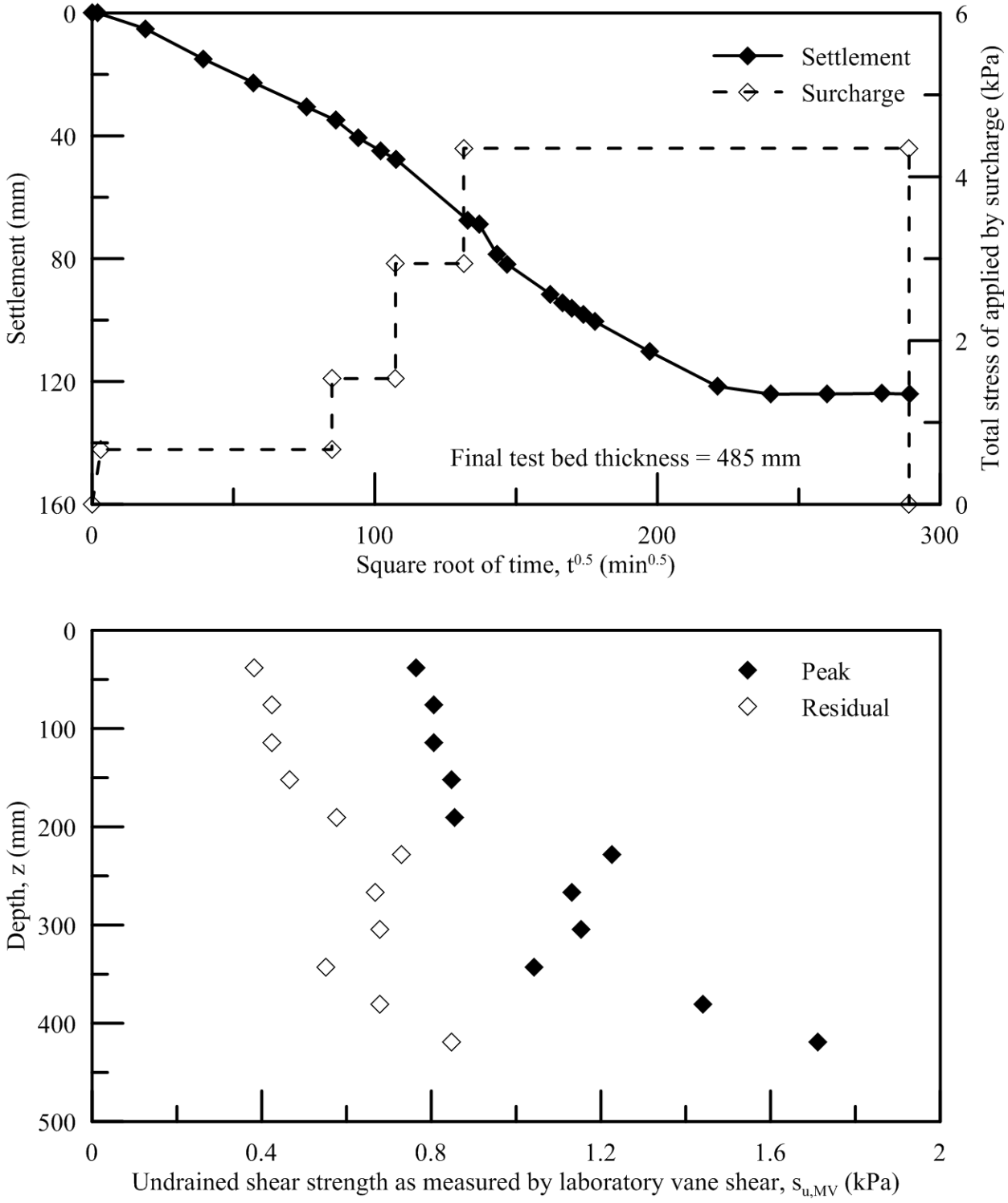

Figure 3.17: Consolidation surcharge with time, settlement with time and undrained shear strength as measured by laboratory vane shear post consolidation for K-1G-TB10

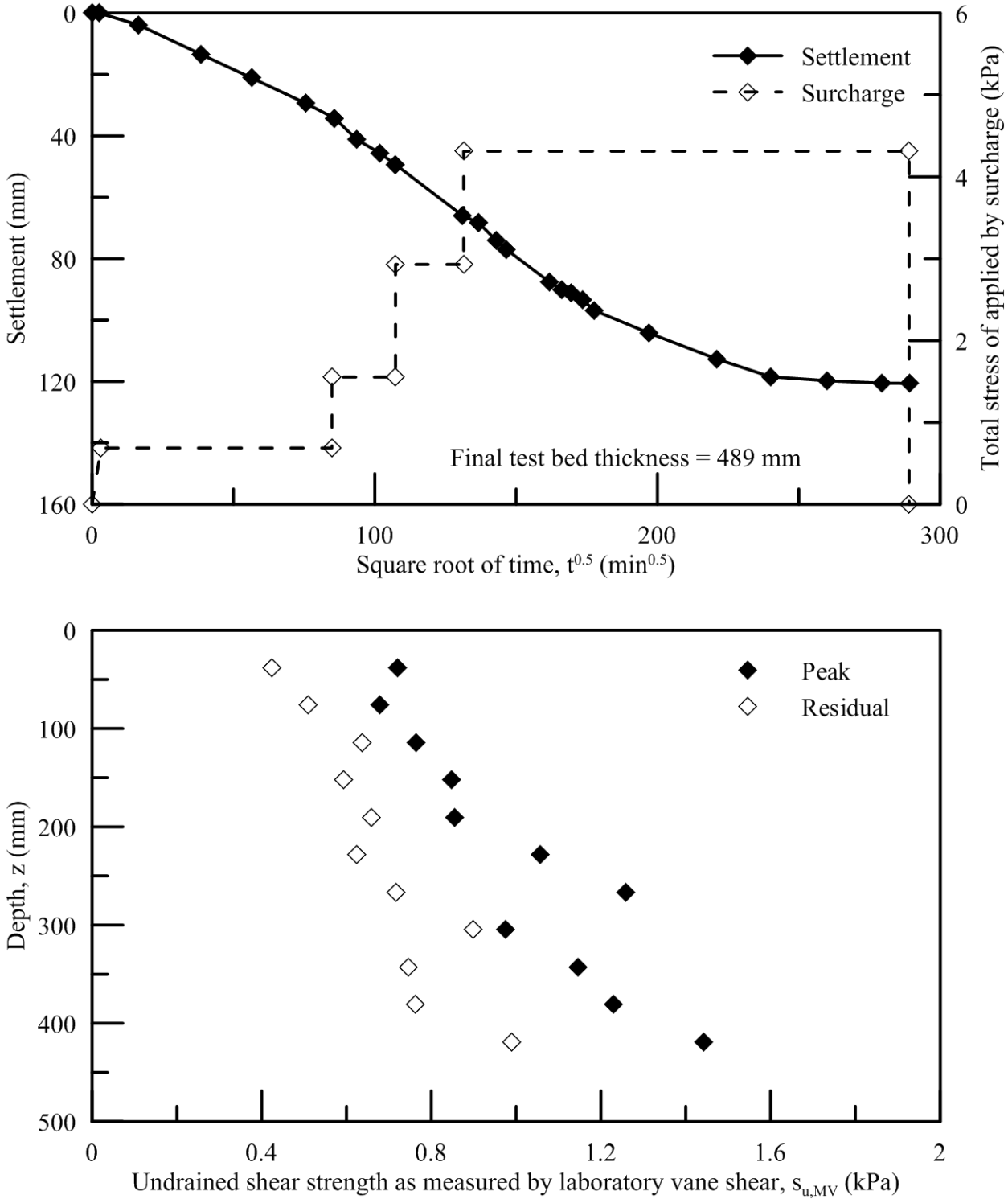

Figure 3.18: Consolidation surcharge with time, settlement with time and undrained shear strength as measured by laboratory vane shear post consolidation for K-1G-TB11

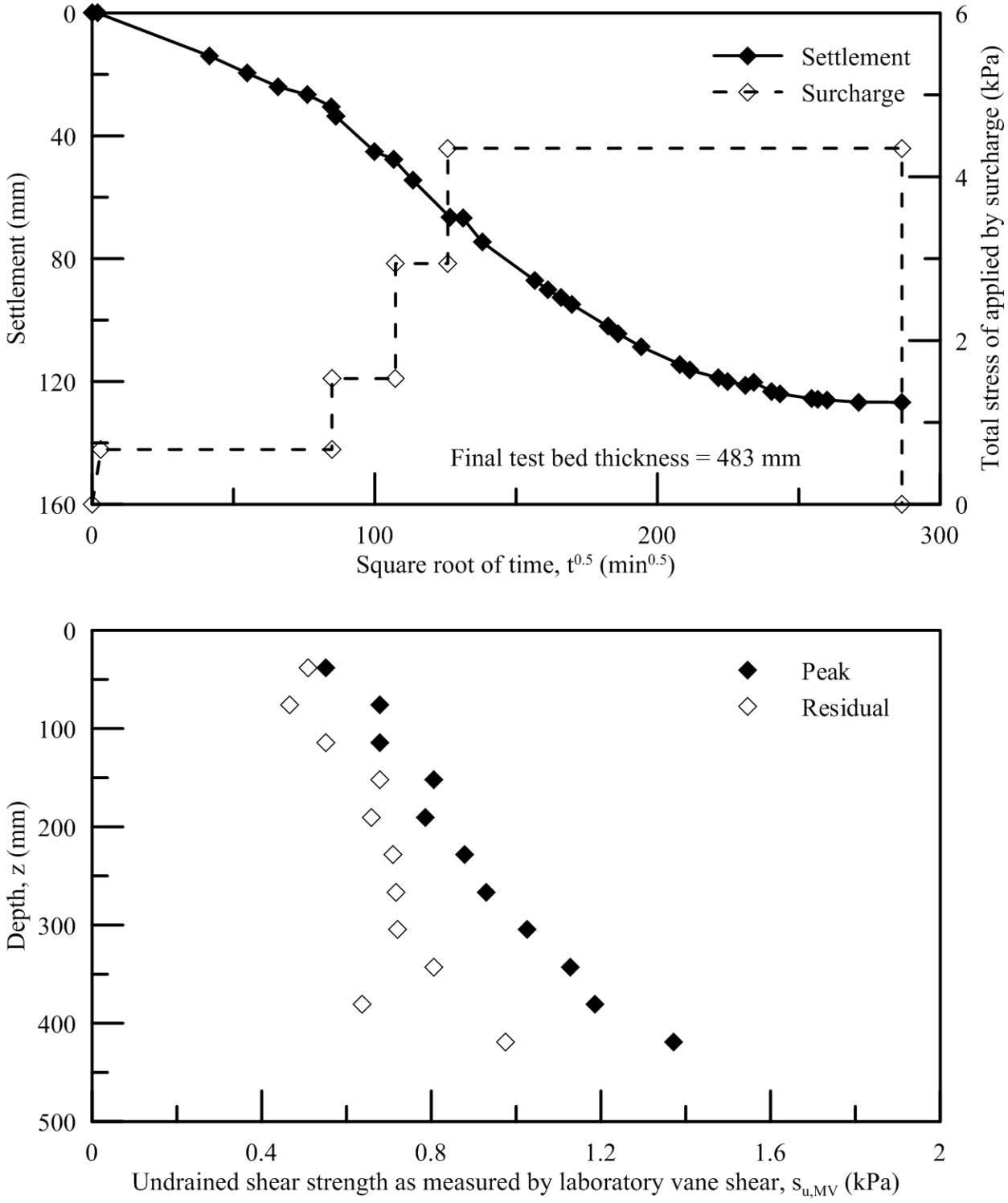

Figure 3.19: Consolidation surcharge with time, settlement with time and undrained shear strength as measured by laboratory vane shear post consolidation for K-1G-TB12

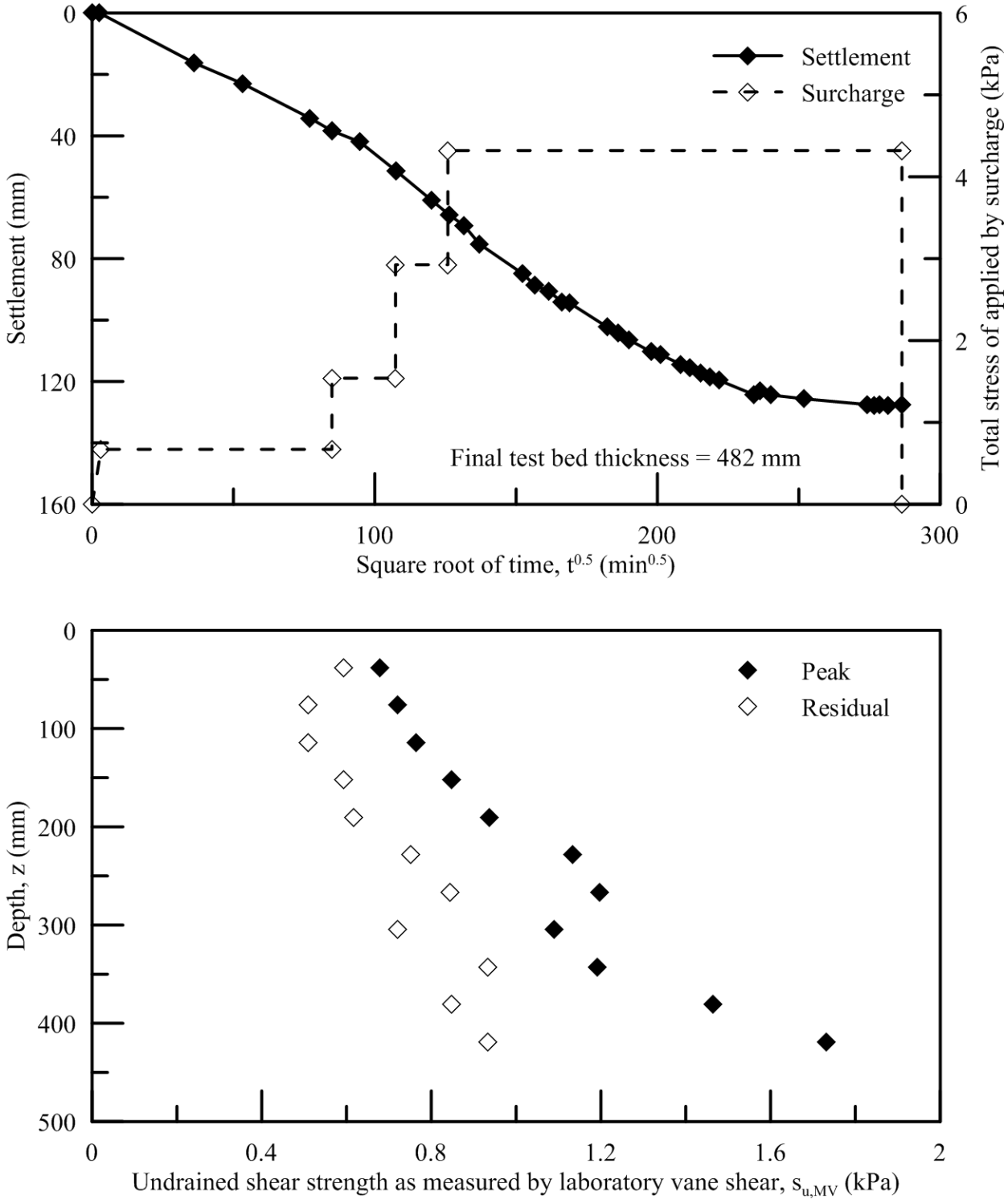

Figure 3.20: Consolidation surcharge with time, settlement with time and undrained shear strength as measured by laboratory vane shear post consolidation for K-1G-TB13

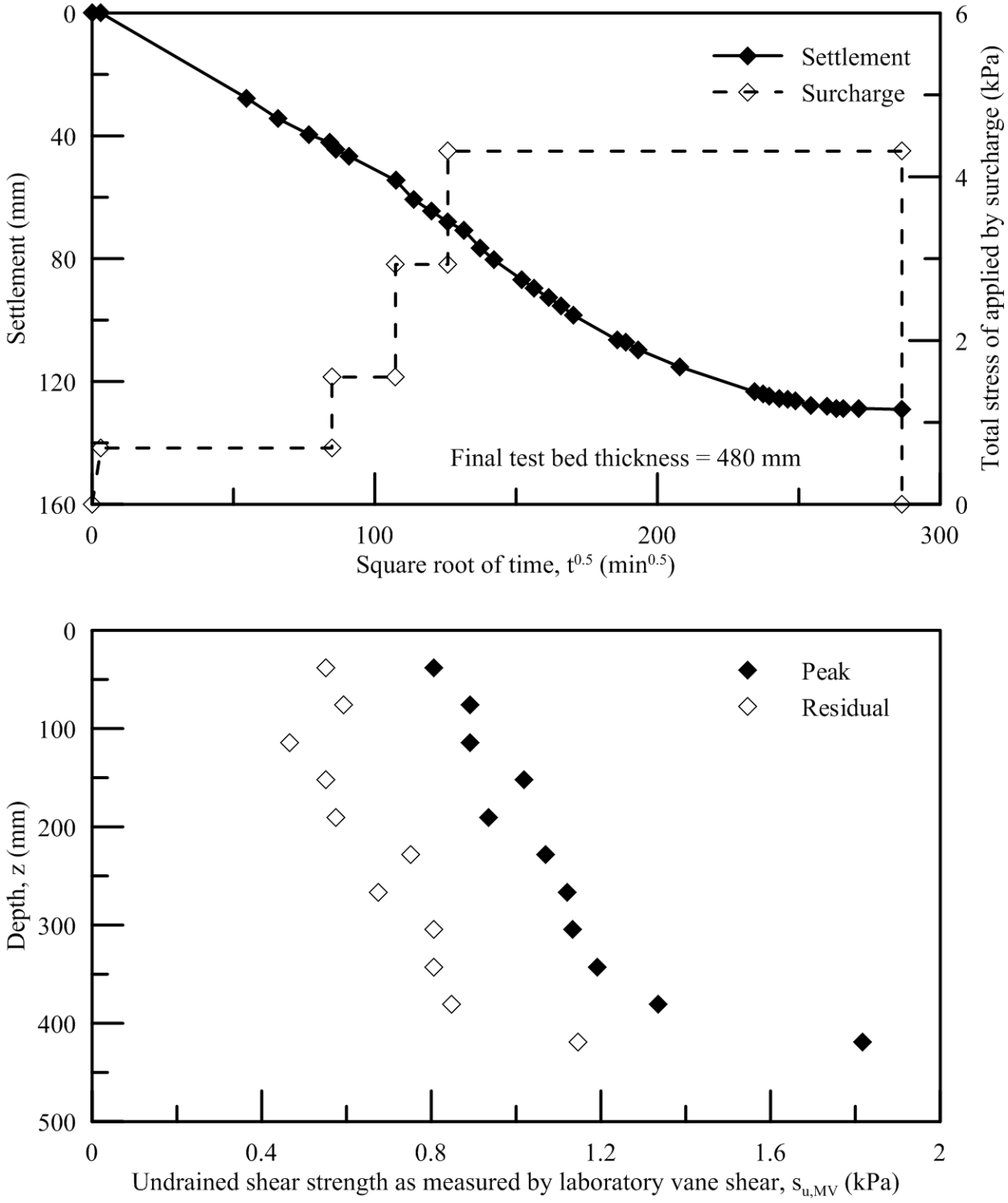

Figure 3.21: Consolidation surcharge with time, settlement with time and undrained shear strength as measured by laboratory vane shear post consolidation for K-1G-TB14

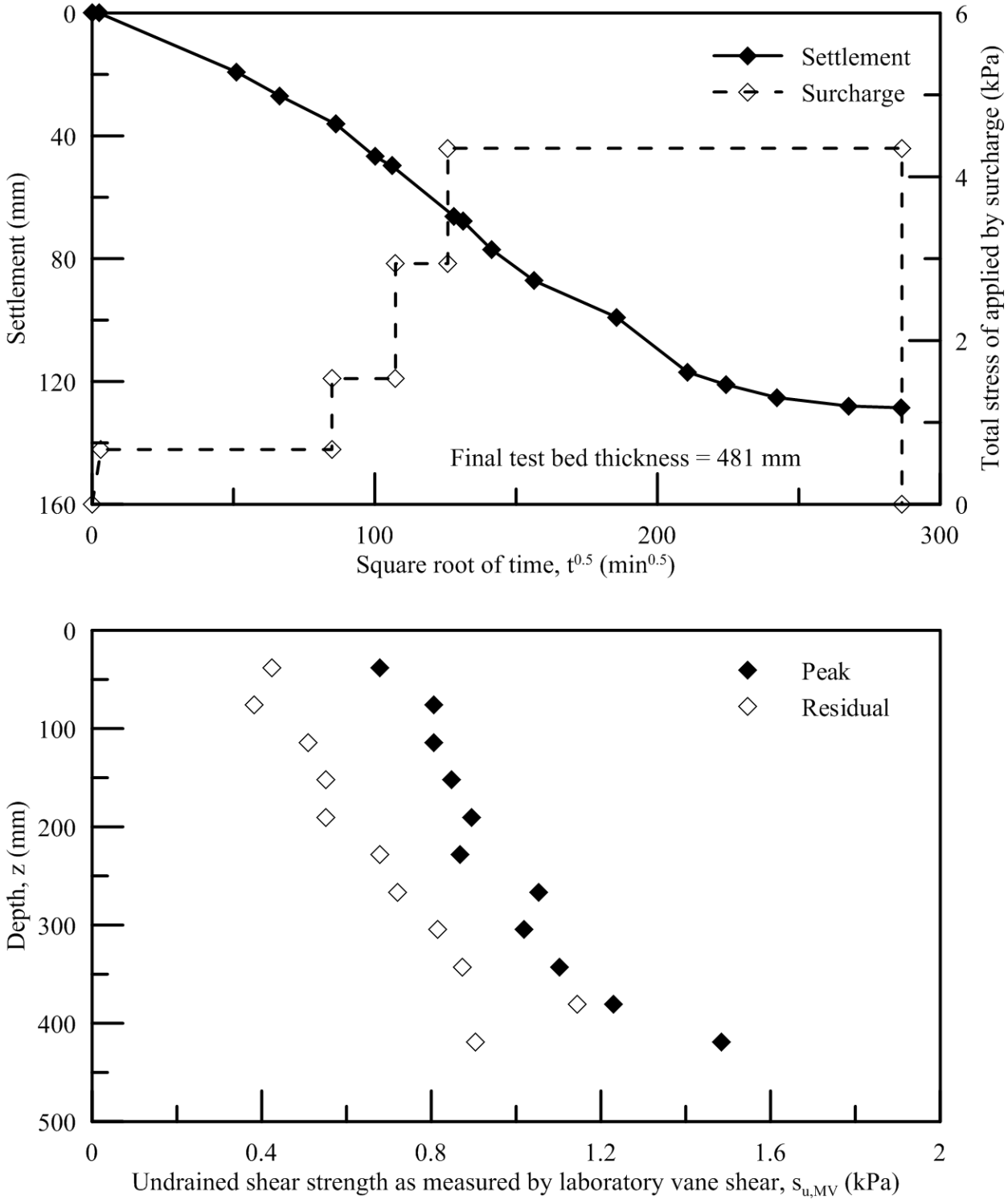

Figure 3.22: Consolidation surcharge with time, settlement with time and undrained shear strength as measured by laboratory vane shear post consolidation for K-1G-TB15

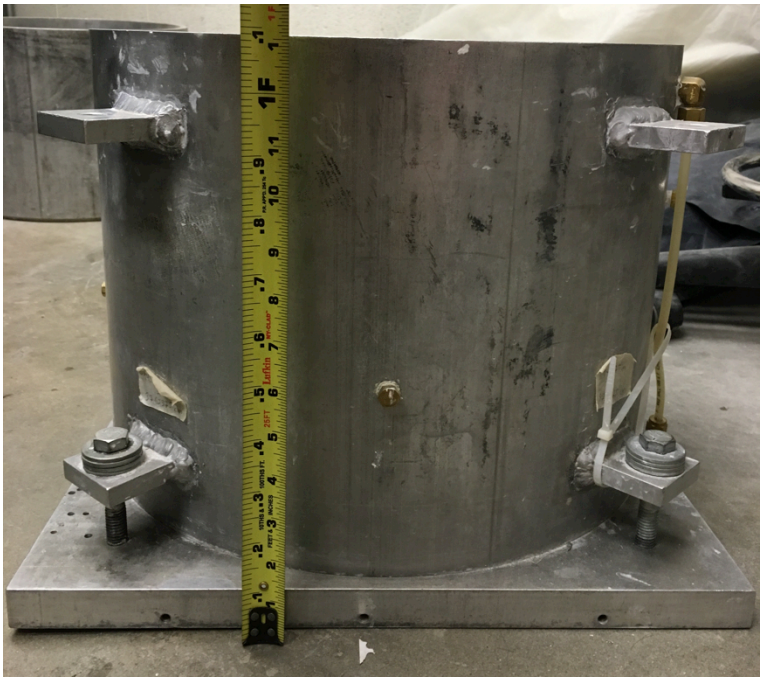

Figure 3.23: Kaolin 90-g model test bed container

Figure 3.24: Kaolin 90-g model test bed container on the loading basket of the 15 g-ton beam centrifuge at CU Boulder

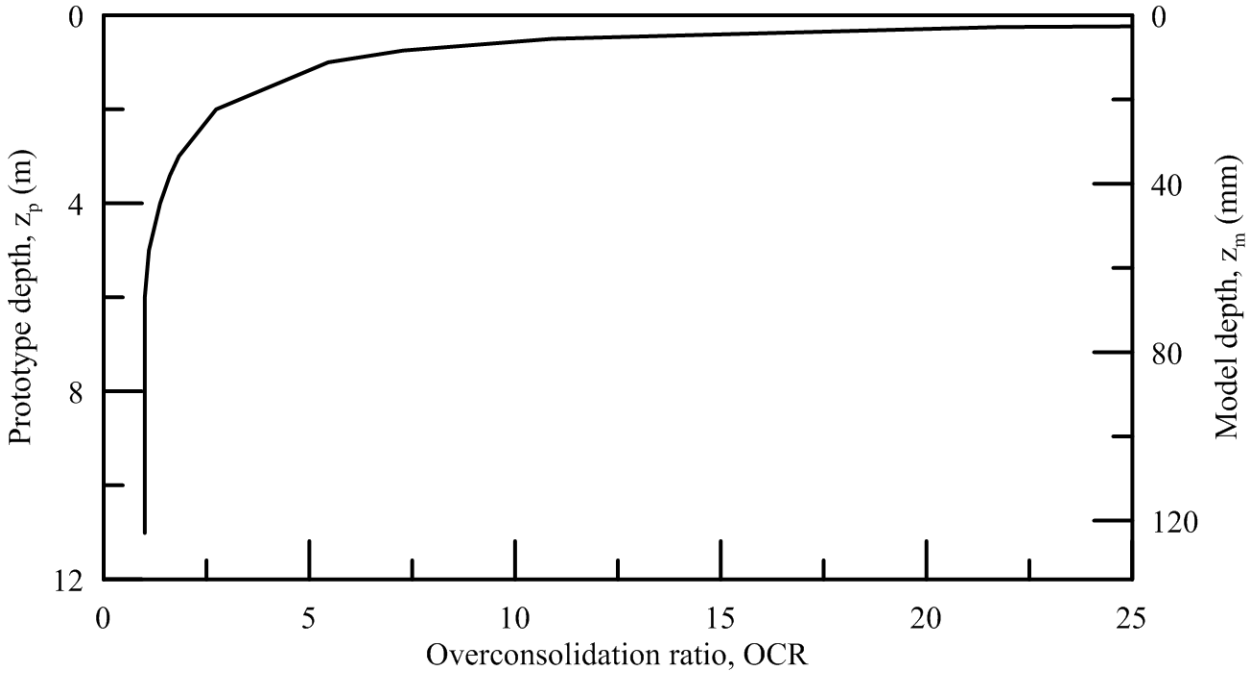

Figure 3.25: Prototype overconsolidation ratio with depth of the Kaolin 90-g model test beds for the K-90G-AR1 model foundation

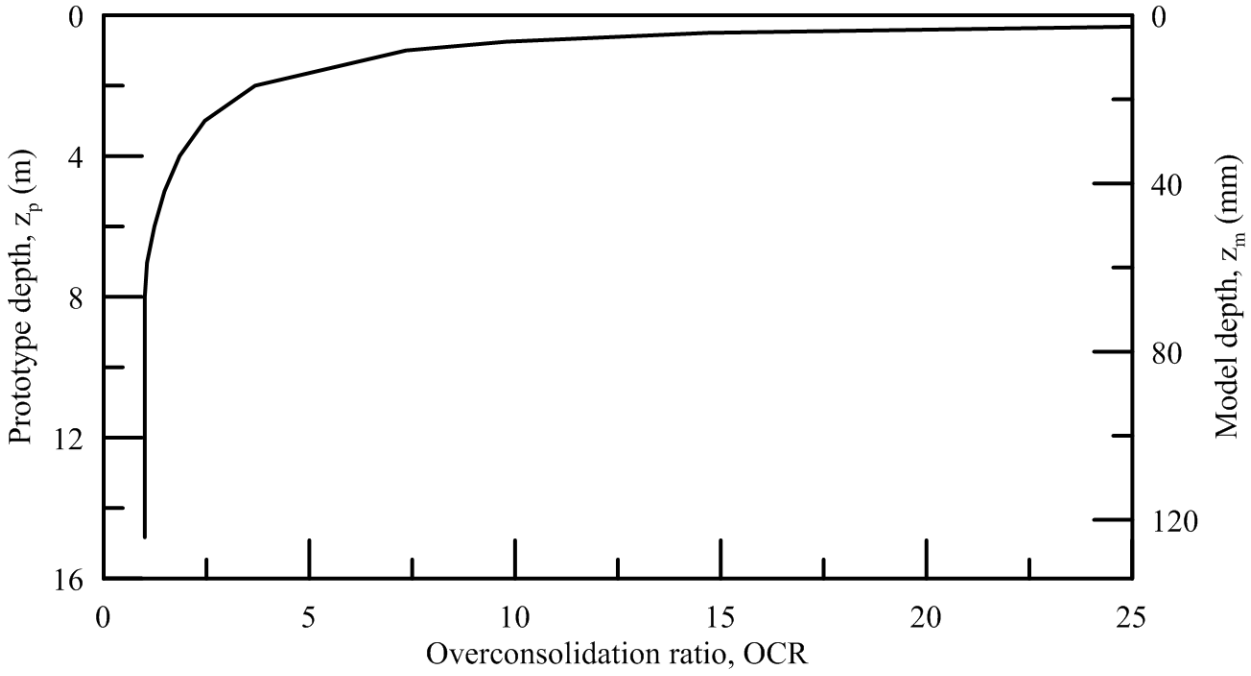

Figure 3.26: Prototype overconsolidation ratio with depth of the Kaolin 90-g model test beds for the K-90G-AR2 model foundation

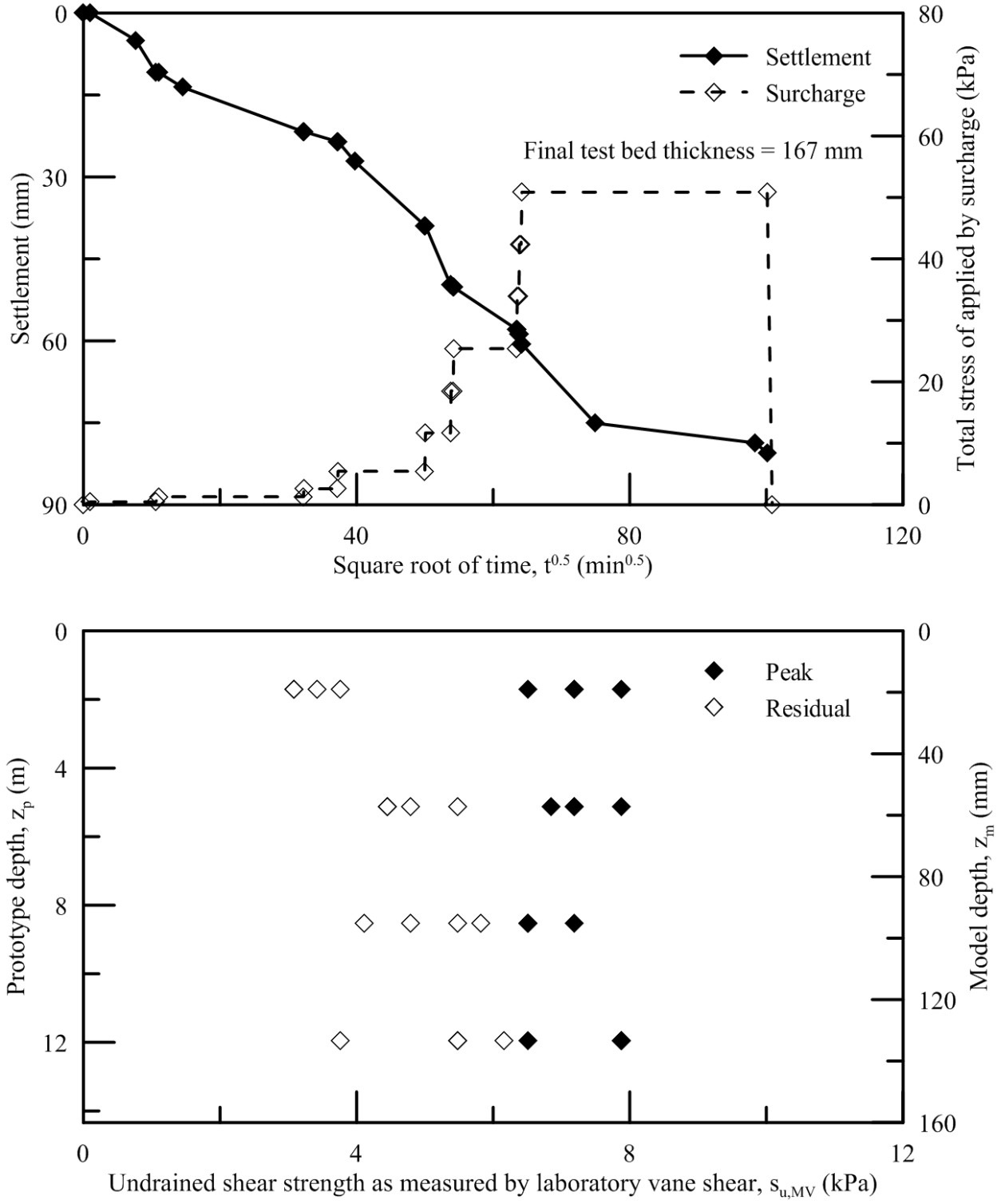

Figure 3.27: Consolidation surcharge with time, settlement with time and undrained shear strength as measured by laboratory vane shear post consolidation for K-90G-TB1

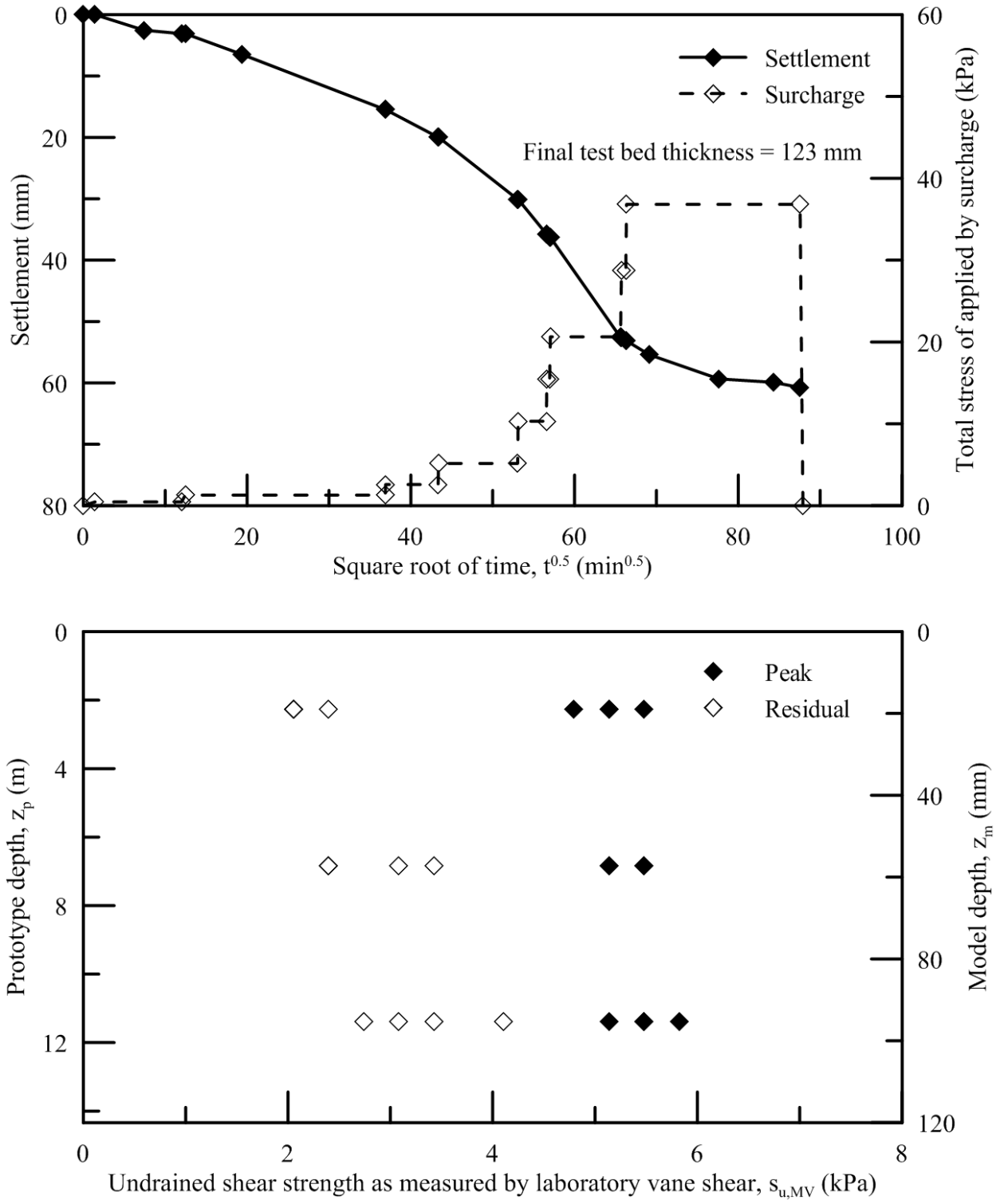

Figure 3.28: Consolidation surcharge with time, settlement with time and undrained shear strength as measured by laboratory vane shear post consolidation for K-90G-TB2

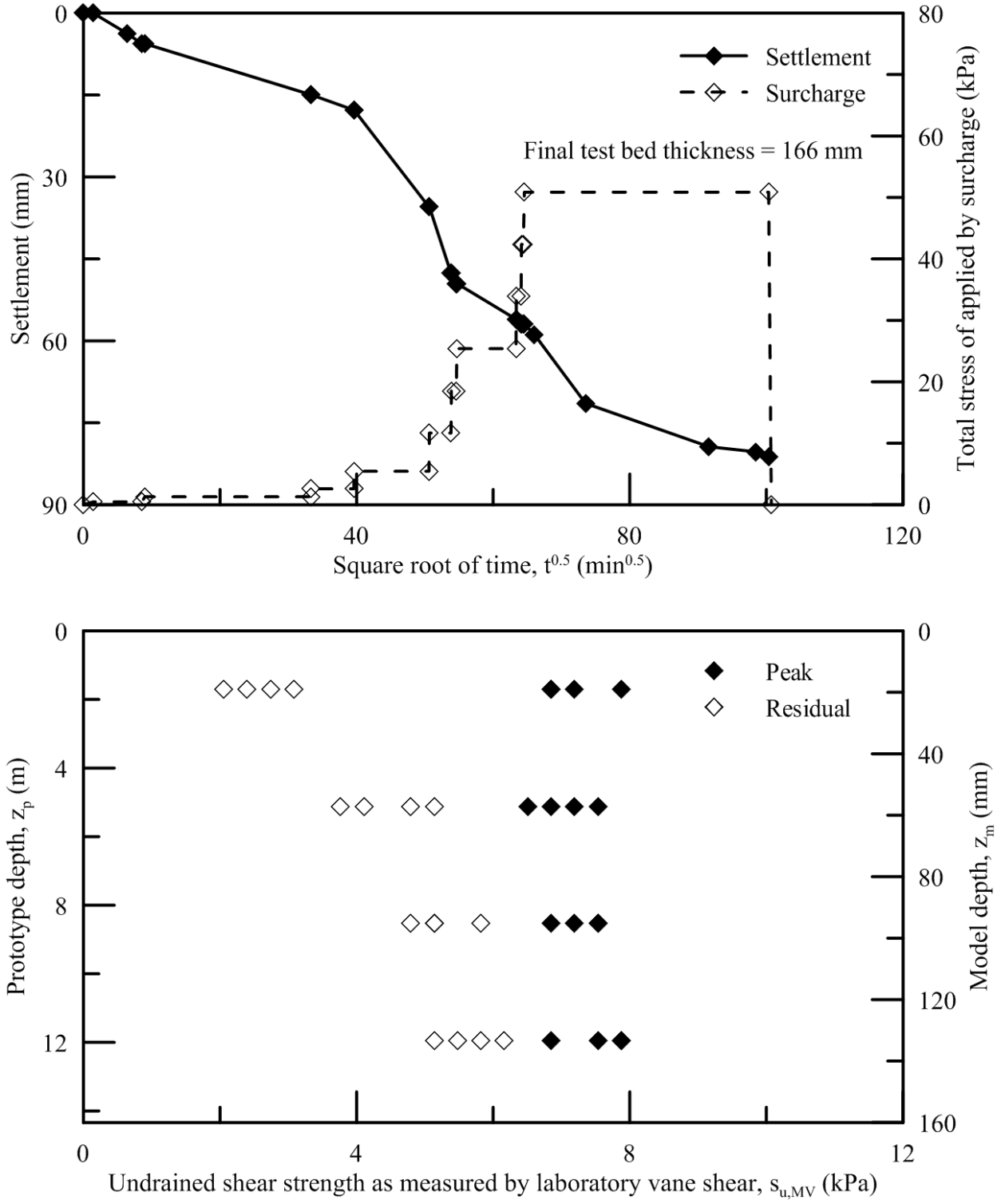

Figure 3.29: Consolidation surcharge with time, settlement with time and undrained shear strength as measured by laboratory vane shear post consolidation for K-90G-TB3

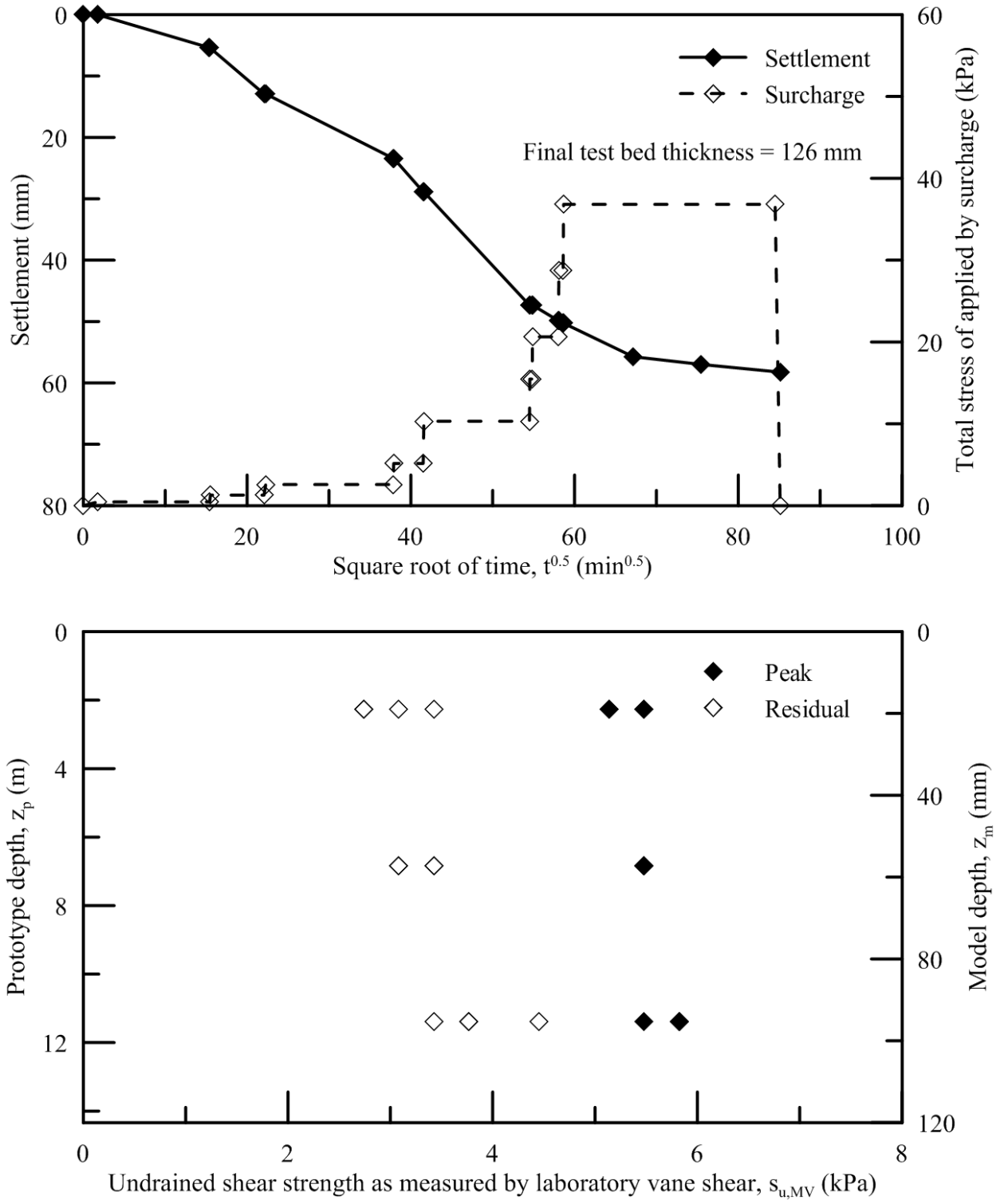

Figure 3.30: Consolidation surcharge with time, settlement with time and undrained shear strength as measured by laboratory vane shear post consolidation for K-90G-TB4

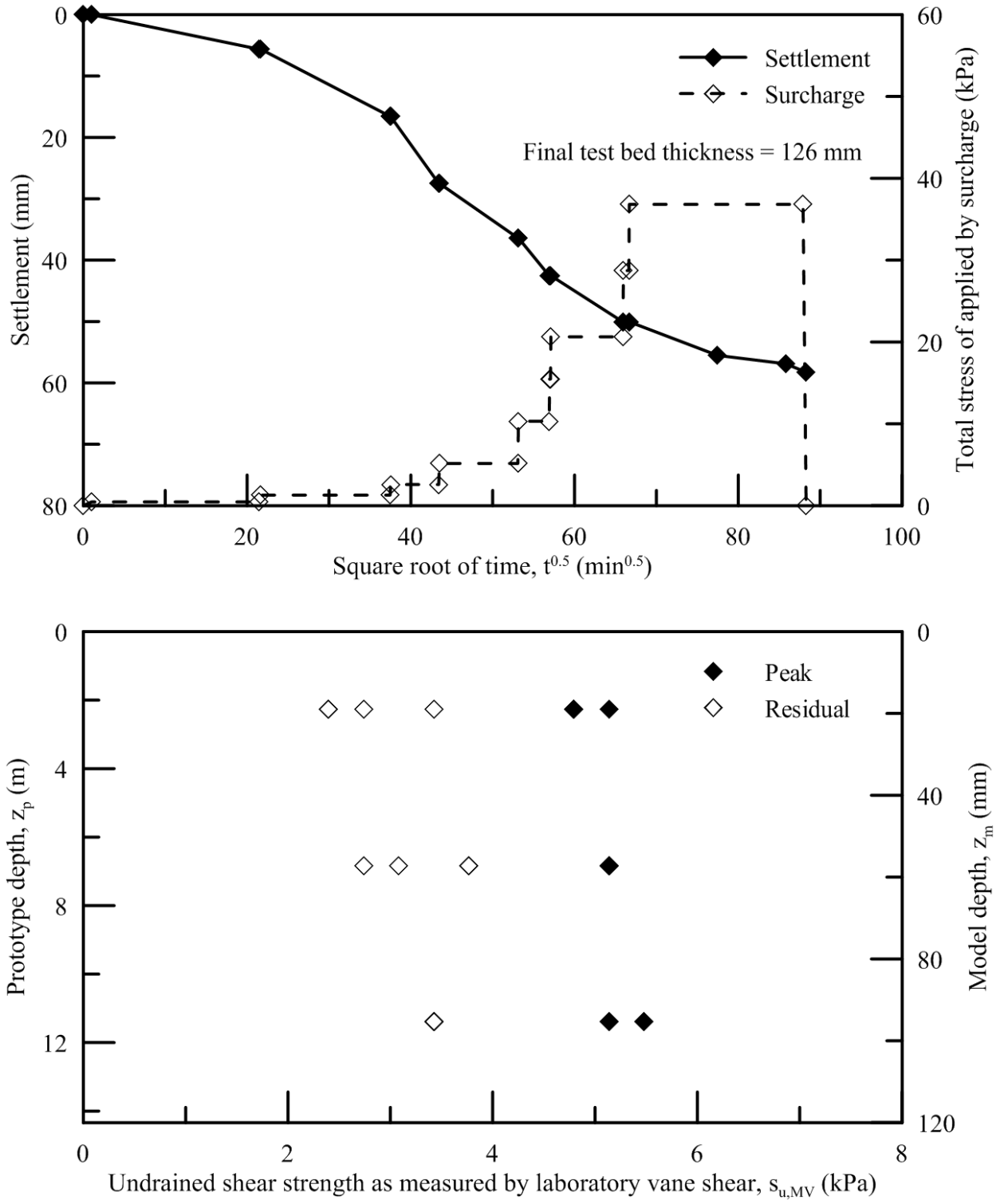

Figure 3.31: Consolidation surcharge with time, settlement with time and undrained shear strength as measured by laboratory vane shear post consolidation for K-90G-TB5

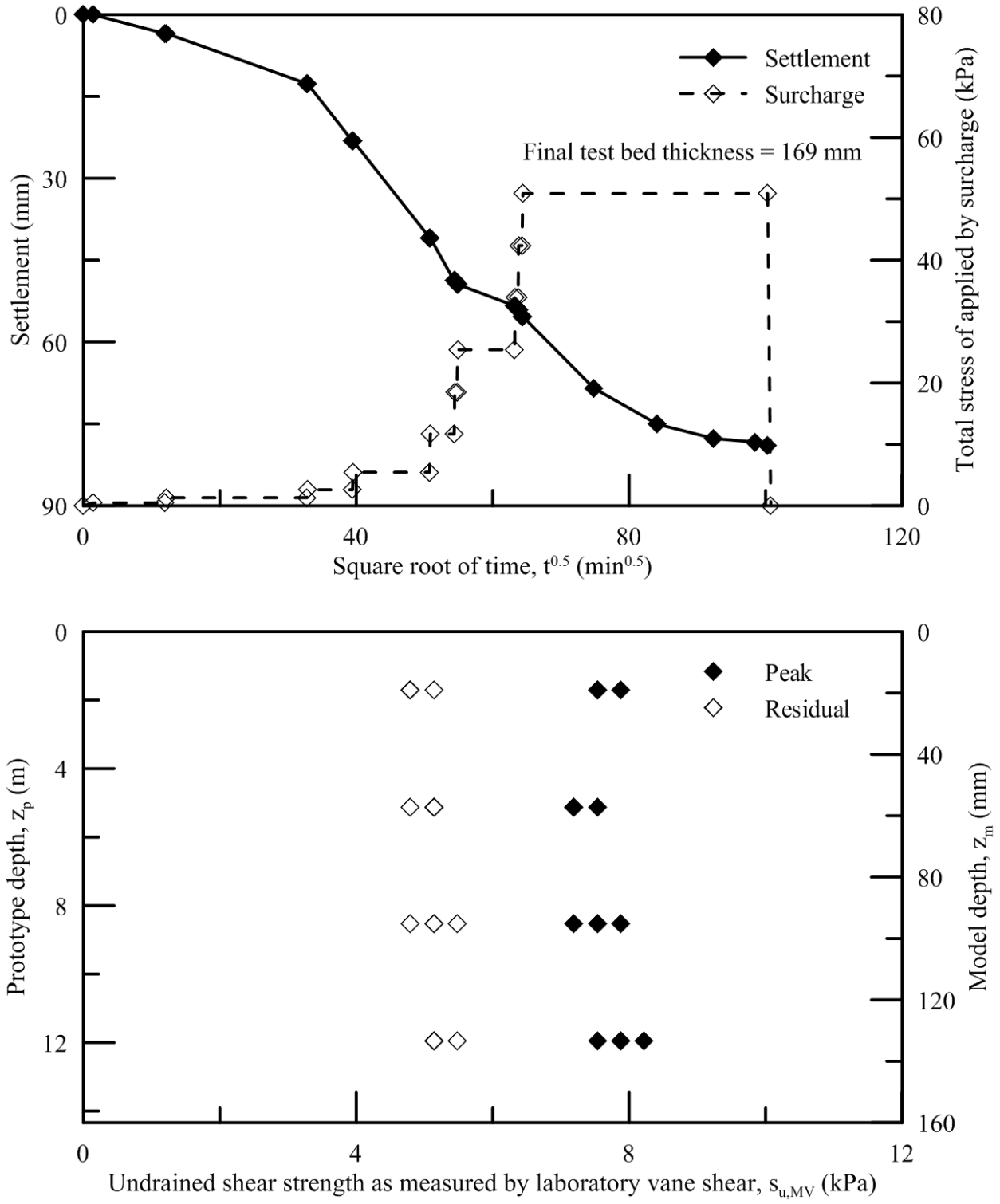

Figure 3.32: Consolidation surcharge with time, settlement with time and undrained shear strength as measured by laboratory vane shear post consolidation for K-90G-TB6

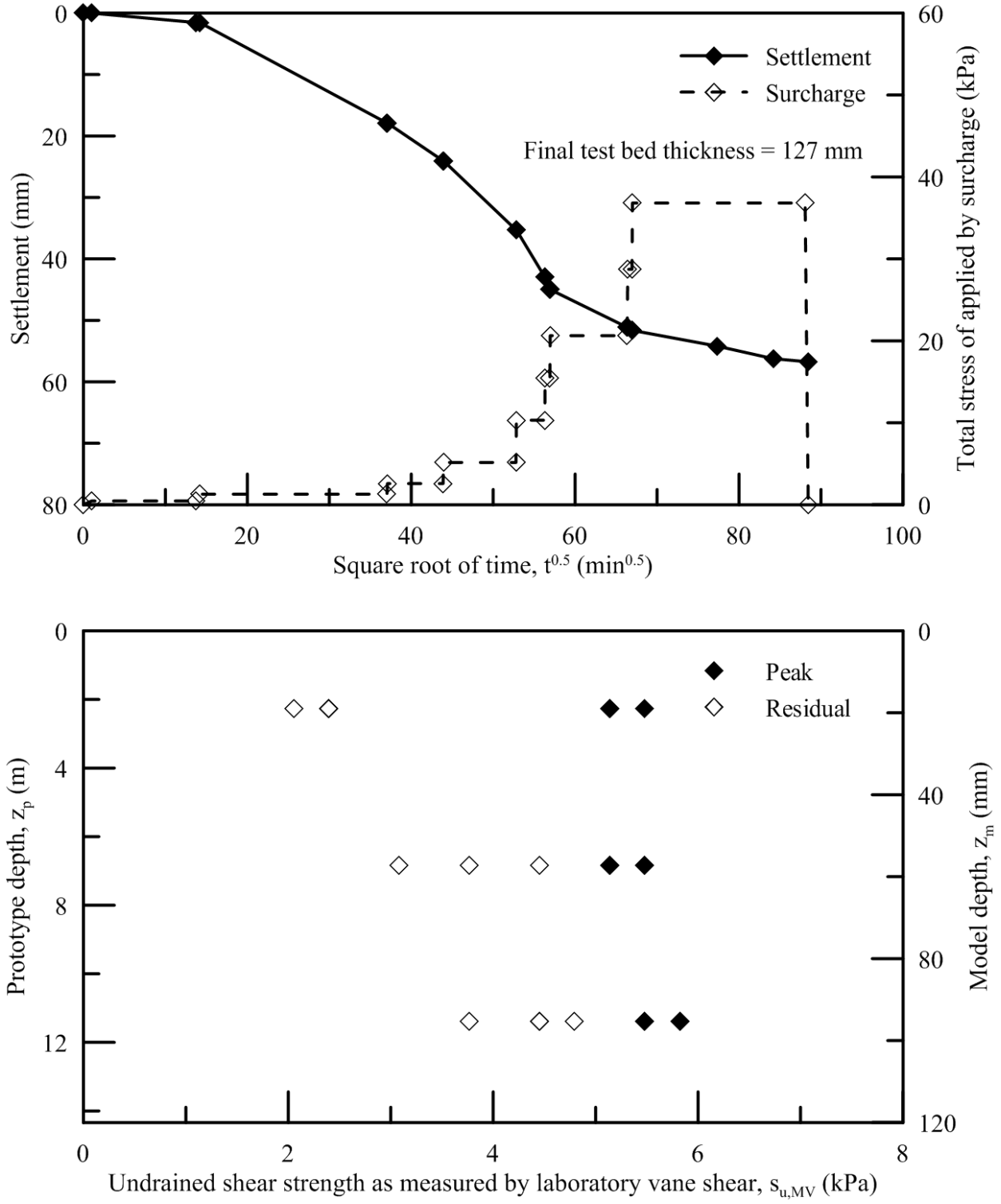

Figure 3.33: Consolidation surcharge with time, settlement with time and undrained shear strength as measured by laboratory vane shear post consolidation for K-90G-TB7

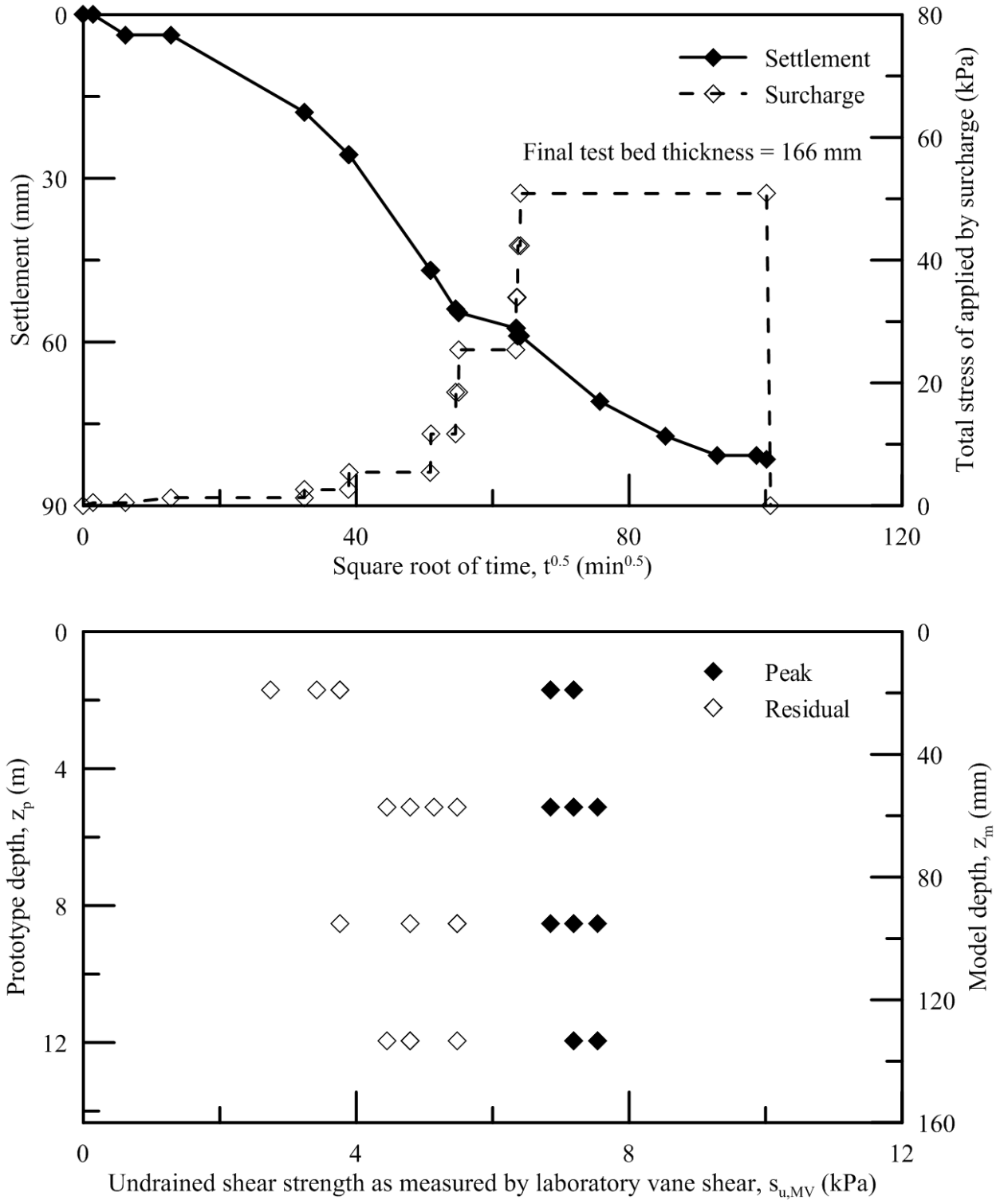

Figure 3.34: Consolidation surcharge with time, settlement with time and undrained shear strength as measured by laboratory vane shear post consolidation for K-90G-TB8

Figure 3.35: Two of the Laponite 1-g model test bed containers showing the 171 mm container height (left) and the 203 mm container height (right)

3.6 References

Beemer, R.D., Shaughnessy, E., Ewert, K.R., Boardman, N., Biscontin, G., Aubeny, C.P. & Grajales, F.J. (2016). "The Use of Sodium Pyrophosphate to Improve a Translucent Clay Simulate." Geo-Chicago 2016. Chicago, IL, USA.

BYK Additives and Instruments. (2014). "Technical Information B-RI 21-Laponite-Performance Additive." BYK Additives and Instruments. Geretsried, Germany.

Edgar Minerals, Inc. (2013). "Material Safety Data Sheet – Kaolin." Edgar Minerals, Inc., Edgar, Florida, USA.

Georgia Tech Research Corporation. (2011). "Assessment of energy Production Potential from Tidal Streams in the United States – Final Project Report." Georgia Tech Research Corporation, Atlanta, GA, USA.

Hjulström, F. (1935). "Studies of the morphological activity of rivers as illustrated by the river Fyris." *Bull. Geol. Inst. Uppsala*, 25: 221-527.

Killen, A. (2016). "Experimental Use of a Transparent Soil and Laser-Aided PIV – Visualizing the Failure Surface of the Laboratory Vane Shear Test." CIVL4660 – Final Year Project, University of Newcastle Australia.

Lin, H. & Penumadu, D. (2005). "Experimental Investigation on Principal Stress Rotation in Kaolin Clay." *J. Geotech. Geoenviron. Eng.*, 131(5): 633-642.

Maynard, M.L., Schneider, J.A., McEntee, J., & Newberg, E. (2013). "Suction caissons for cross-flow tidal power system." *Geotechnical Engineering*, 166(GE2): 99-110.

Ramsay, J.D.F. (1986). "Colloidal Properties of Synthetic Hectorite Clay Dispersions." *J. Coll. Interf. Sci.*, 109: 441-454.

Sundborg, A. (1956). "The River Klaralven: A study of fluvial processes." *Geograf. Ann.*, 38: 127-316.

Wallace, J.F. & Rutherford, C.J. (2015). "Geotechnical Properties of Laponite RD." *Geotech. Test. J.* 38(5):1-14.

CHAPTER 4. 1-G MODEL LOAD TESTS IN KAOLIN

4.1 General

A total of fifteen 1-g model load tests were conducted in the kaolin 1-g test beds (Section 3.1) to study the response of suction caissons under undrained loading conditions applicable to tidal current turbine applications. These tests were conducted on two model foundations with aspect ratios of 1 and 2. The types of undrained loading conditions investigated were monotonic vertical, cyclic vertical, monotonic horizontal, and cycling horizontal. A brief description of the 1-g model load tests including the test identifier and associated kaolin 1-g test bed is given in Table 4.1.

4.2 Experimental apparatus

4.2.1 Model foundations

Two model suction caissons fabricated from 6061-T6 aluminum were utilized for the 1-g model load tests in kaolin as shown in Figure 4.1. These two foundations were distinguished by their aspect ratios and were identified as K-1G-AR1 and K-1G-AR2. K-1G-AR1 had a diameter (D) of 152 mm, a skirt length (L) of 152 mm, and a wall thickness (t_{wall}) of 3.2 mm resulting in an aspect ratio of 1 and a diameter-to-wall thickness ratio of 48. K-1G-AR2 had a diameter of 76 mm, a skirt length of 152 mm, and a wall thickness of 1.6 mm resulting in an aspect ratio of 2 and a diameter-to-wall thickness ratio of 48. The diameter-to-wall thickness ratio of 48 was higher than typical values of suction caissons and more similar to that of open-ended pipe piles. However, the thicker walls allowed for jacking installation of the foundations and ensured that the response observed during testing was that of the soil rather than that of the aluminum. The skirt length of K-1G-AR1 and K-1G-AR2 were equivalent to mobilize soil resistance from approximately the same depth of clay under similar stress conditions.

The top cap of both foundations consisted of a 6.4 mm thick aluminum plate with the same diameter as the skirt of the suction caisson. The top cap was welded thoroughly with no gaps to ensure no water could permeate through the connection. A threaded valve was positioned in the top cap to allow for ventilation of the inside of the suction caisson during installation. This valve could be closed to prevent ventilation during any loading phases. A loading rod was positioned in the center of the top cap. Two load cells were positioned along the loading rod in

the vertical and horizontal orientation as shown in Figure 4.2 to measure the respectively oriented loads on the model foundation. A locking ball and socket joint also shown in Figure 4.2 was positioned at the top of the rod to allow for rotation of the foundation during horizontal load tests. The locking ball was positioned at a height of 324 mm and 170 mm (or 2.1 and 2.2 diameter heights) above the soil surface contact for K-1G-AR1 and K-1G-AR2 respectively. Flat platforms could be attached to the loading rod as shown in Figure 4.3 that allowed for additional area to place linear displacement transducers when the area of the top cap was not large enough. These linear displacement transducers allowed for calculation of vertical displacement, horizontal displacement, and rotation of the model foundation.

4.2.2 Loading apparatus

The loading apparatus utilized for the 1-g model load tests in kaolin, was built, designed, and programmed specifically for this study. The apparatus and its steel support frame are shown in Figure 4.4. The apparatus consisted of two screw driven linear slides with 305 mm of range. One of the slides was mounted horizontally on the steel support frame. The second slide was oriented vertically by means of a perpendicular mount to the horizontal slide. A cantilever arm that was fixed to the loading rod was mounted to the vertical slide. Both of the slides were controlled by integrated programmable servo motors in a direct drive configuration. The steel support frame allows the loading apparatus to position the model foundation over the center of the kaolin test bed container. The frame also holds the data acquisition system that feeds into a computer. This computer also allowed for programming and control of the motors.

4.3 Experimental methodology

One kaolin 1-g model test bed was consolidated for each of the 1-g model load tests conducted in kaolin. Each load test was conducted in the center of the kaolin 1-g test bed containers (610 mm in diameter) to minimize boundary effects of the container walls. The distance between the foundation and the edge of the container wall was 1.5D and 3.4D for K-1G-AR1 and K-1G-AR2 respectively. Based on visualizations of the failure mechanism in CHAPTER 6 this distance was found to not intersect with the mobilized failure mechanism. Each of the load tests generally consisted of an installation phase, a system reconfiguration phase, a loading phase, and an extraction phase.

4.3.1 Relationship of foundation velocity and drainage conditions during loading

Geotechnical laboratory element tests on saturated clays are typically characterized as undrained or drained. In laboratory element testing, these conditions are controlled by means of opening or closing drainage valves and by changing the strain rate. For foundations however, the drainage conditions surrounding the foundation cannot be controlled by means of drainage valves. Therefore the velocity of the foundation must be utilized to control the drainage conditions of the supporting soils. This study utilized the following non-dimensional velocity term to determine the loading conditions of the supporting soils:

$$\boldsymbol{v_n = \frac{vL}{c_v}} \qquad \textbf{Equation 4.1}$$

where:

v_n = non-dimensional foundation velocity

v = actual foundation velocity

L = relevant distance of drainage

c_v = coefficient of consolidation of the soil

This non-dimensional velocity was used by Finnie (1993) for spudcans in calcareous sands and by House (2002) for suction caissons in kaolin. House (2002) found that $v_n > 10$ corresponds to undrained conditions and $v_n < 0.1$ corresponds to drained conditions. These were based on L values corresponding to the wall thickness of the suction caisson and diameter of the suction caisson for conditions where the top cap was vented and not vented respectively (House 2002, Villalobos 2006). For all of the load tests in this study, the foundation loading conditions were characterized by v_n based on the above definition with the velocity defined as the velocity of the reference point defined as the center point of the top cap in contact with the soil surface. The c_v was defined at a distance of one skirt length below the test bed surface.

4.3.2 Installation

To install the model suction caissons, the foundation was first positioned vertically over the center of the test bed with the ball and socket joint locked and the vent valve open. The foundations were then installed under constant velocities of 0.075 mm/s and 0.15 mm/s for K-1G-AR1 and K-1G-AR2 respectively. These velocities result in a non-dimensional velocity of 13 based on a coefficient of consolidation of 0.0189 mm^2/s at the skirt tip that corresponds to undrained conditions. The installation phase was terminated when a rapid increase in the

penetration resistance was measured by means of the vertical load cell. This indicated that the top cap had made contact with the test bed. After the installation phase was completed, a period of 20 minutes was included to allow for reconfiguration of the loading apparatus and model foundation for the loading phase.

4.3.3 Undrained monotonic vertical loading

Undrained monotonic vertical load tests were conducted to provide a baseline response of the model suction caissons. During these phases the ball and socket joint was locked and the ventilation valve was closed. These load tests were conducted using the constant velocity method at velocities of 0.025 mm/s and 0.050 mm/s for K-1G-AR1 and K-1G-AR2 respectively. The velocity was determined at the foundation reference point that was defined as the center of the bottom side of the top cap that made contact with the soil surface. These velocities correspond to non-dimensional velocities of 201 and therefore undrained loading conditions. A total of four baseline tests were conducted as listed in Table 4.1. The four tests provided the baseline undrained monotonic deformation response and capacity both in compression and in uplift for K-1G-AR1 and K-1G-AR2. The baseline load test in monotonic compression on each foundation was followed by monotonic uplift until extraction.

While only four load tests were conducted that were solely monotonic, there were monotonic undrained loading phases in all 15 of the 1-g load tests in kaolin. These post-cyclic monotonic load tests served three purposes. The first was to allow for observation of the effects of various cyclic loads on future extreme loads such as ship collisions or large current loads that can be modeled as post-cyclic monotonic loads. The second was to provide a potential form of quantification of the amount of remolding or formation of the failure surface had occurred with cycling. The third was to extract the foundation from the test beds. These post-cyclic monotonic loads were applied either first in compression then followed by uplift to extraction or simply uplift to extraction as specified in Table 4.1 and were conducted after both the vertical and horizontal cyclic load tests.

4.3.4 Undrained cyclic vertical loading

The undrained cyclic vertical loading was applied to the suction caisson models by means of displacement-controlled sinusoids. The sinusoids were applied so that the mean displacement was the position at which the installation phase was terminated and with compression as the first

loading direction. The decision to use displacement control rather than load control was based on the following reasons. First, the 90-g model load tests in kaolin were conducted at a facility with equipment that functioned ideally under displacement control. Second, the displacement control allowed for the observation of a potential range of cyclic displacement amplitudes over which the foundation response shows little to no capacity degradation with cycling. This possibility of elastic behavior during cyclic exists due to the formation of an elastic zone beneath footings during foundation loading (Terzaghi 1943) and has been shown to exist at the element level under displacement controlled laboratory tests on clay undergoing cyclic shear strains below 0.012 to 0.014% (Mortezaie and Vucetic 2016). Third, displacement controlled tests allow for a more simplistic comparison to serviceability constraints during the design phase.

The period of the sinusoidal cycles was 5 seconds for all the 1-g kaolin cyclic load tests. This period was chosen as it represented the period of multiple cyclic loading types that are applicable to the tidal current turbine as discussed in Section 2.2. Two general types of cyclic load tests were conducted at 1-g in kaolin as described in Table 4.1. The first type consisted of applying constant displacement amplitude cycles over a time period of approximately 24 hours or 17,280 cycles. The three tests of this type were conducted at constant cyclic displacement amplitudes of 0.6% of the diameter (K-1G-AR1-V-Cyc-1), 0.47% of the diameter (K-1G-AR2-V-Cyc-1), and 0.04% of the diameter (K-1G-AR1-V-Cyc-3). The second type consisted of six 100-cycle packets. Each of the 100-cycle packets had constant cyclic displacement amplitudes. This displacement amplitude was increased with each successive packet. The two tests of this type were conducted at cyclic displacement amplitudes of 0.005%, 0.01%, 0.05%, 0.25%, 1.25%, and 3.5% of the diameter (K-1G-AR1-V-Cyc-2) and 0.0035%, 0.00425%, 0.0525%, 0.125%, 1.15%, and 3.25% (K-1G-AR2-V-Cyc-2). A period of 20 minutes was included in between each pack to allow for the same recalibration period that existed after the installation phase.

4.3.5 Undrained monotonic horizontal loading

Undrained monotonic horizontal load tests were conducted to provide a baseline response of the model suction caissons. These horizontal load tests were conducted with the vent valve closed and with the ball and socket joint unlocked to allow for rotation. The horizontal load tests were applied using the swipe mechanism. The swipe was conducted by holding the vertical slide at a constant position while applying motion along the horizontal slide. This mechanism was

utilized in order to ensure that the horizontal load was applied in the same direction as the horizontal displacement. If the swipe mechanism were not utilized, the exact rotation point of the model foundation would have needed to be predicted for each test to ensure that both slides are displaced in a way that did not apply compression loads to the foundation. Any compression could generate a resultant horizontal load that was in the opposite direction of horizontal displacement. Predicting this rotation point reliably requires a trial and error method and would be complicated by any slight variation in strength therefore making the process inefficient when considering the consolidation time of each test bed.

Determining a foundation velocity for the monotonic horizontal load tests involved more effort than the monotonic vertical load tests. This was due to the fact that in the vertical load tests the translation of the vertical slide with the ball and socket joint locked was directly correlated to vertical displacement of the foundation's reference point. However for the horizontal test conducted with the ball and socket joint unlocked, the displacement of the horizontal slide directly correlated to the displacement of the ball and socket joint but not the foundation's reference point. To determine the rate to displace the horizontal slide to achieve a similar non-dimensional velocity to the vertical tests of 201 for the foundation reference point, the following assumptions were made. First, it was assumed that the rotation point of the model foundation would occur at the same location as determined by a PLAXIS 3D model of the system loaded horizontally. Second, it was assumed that the velocity of the reference point was related to the velocity of the ball and socket joint in the same manner as a beam rotation around a fixed point. Based on these assumptions, the horizontal slide was displaced at a constant velocity of 0.078 and 0.123 mm/s for K-1G-AR1 and K-1G-AR2 respectively. The tests were conducted using an out and back motion where the foundation was swiped outward and then returned to the original position post-installation. Once the out and back swipe was completed, the foundation was extracted in monotonic uplift at a non-dimensional velocity of 201.

4.3.6 Undrained cyclic horizontal loading

The undrained cyclic horizontal loading was applied to the suction caisson models by means of displacement-controlled sinusoids with the vent valve closed and the ball and socket unlocked, similar to the vertical cyclic loading. The horizontal loading mechanism utilized was the swipe mechanism similar to the monotonic horizontal load tests. For all cycles, the horizontal servo motor was programmed to displace the slide from the origin or zero position to a position

double the amplitude of the cycle. The origin was defined as the location upon completion of the installation phase. The period of the cycles were 5 seconds similar to the undrained vertical cyclic load tests.

Two types of cyclic load tests were conducted. The first type consisted of four constant cyclic displacement amplitude packets. The packets were approximately 350 minutes long with 20-minute slack periods in between to match the loading apparatus re-configuration time after the installation phase. While the amplitude of the horizontal slide cycling was constant for each of the packets, the sign (+/-) of the mean slide displacement was alternated with each successive cycle. In other words, the slide was programmed to cycle from the origin to a given positive integer (double the cyclic amplitude) during the first packet and from the origin to a given negative integer during the second packet and so on. The second type of cyclic horizontal load tests consisted of two sets of six 100-cycle packets. For both sets, the amplitude of the horizontal slide cycling within each packet was kept constant. For the first set of six, the slide cycling was from the origin to a positive integer position. For the second set of six, the slide cycling was from the origin to a negative integer position. For K-1G-AR2-H-Cyc-2, within a set of packets, the successive packet the amplitude was increased and the mean was adjusted to maintain the origin to negative integer cycling. However for K-1G-AR1-H-Cyc-2, the increase in cyclic displacement amplitude was only applied for the first three packets. The cyclic displacement amplitude of packets three through six in each set had constant cyclic displacement amplitudes. A period of 20 minutes was present between each packet. Both types of horizontal cyclic load tests were followed by undrain monotonic uplift until extraction.

4.3.7 Extraction

As referenced in previous sections within this chapter, the extraction of the model suction caissons was combined with an uplift load test. The extractions were conduced monotonically at a constant non-dimensional velocity of 201. The extraction of the foundations via the monotonic undrained mechanism allowed for the possibility of sufficient displacement to occur in order to visualize the failure mechanism generated by the foundation loading at the surface of the test bed.

4.4 Experimental results

4.4.1 Non-dimensionalization of undrained results

All results of the model load tests conducted for this study were converted to non-dimensional units to allow for comparison between the models and for future application to prototype or field scale behavior prediction. The non-dimensionalization equations presented by Kelly et al. (2006) were utilized. The investigation conducted by Kelley et al. (2006), described in Section 2.3.5, was shown to achieve a satisfactory comparison of load and stiffness between a 1-g lab bench scale model and a field scale model suction caisson in clay. The nomenclature and orientation of the foundation loads and displacements are shown in Figure 4.5 while the non-dimensional loads, displacements, and rotations were defined as follows:

$$V'^{*} = \frac{V'}{s_u D^2} \qquad \textbf{Equation 4.2}$$

$$\Delta z^{*} = \frac{\Delta z}{D} \qquad \textbf{Equation 4.3}$$

$$H^{*} = \frac{H}{s_u D^2} \qquad \textbf{Equation 4.4}$$

$$\Delta x^{*} = \frac{\Delta x}{D} \qquad \textbf{Equation 4.5}$$

$$M^{*} = \frac{M}{s_u D^3} \qquad \textbf{Equation 4.6}$$

$$\theta' = \theta \qquad \textbf{Equation 4.7}$$

where:

V'^{*} = non-dimensional net vertical load (i.e. foundation weight not included in the load)

V' = net vertical load on the model suction caisson

s_u= undrained shear strength at the bottom of the skirt tips of the model suction caisson

D = diameter of the model suction caisson

Δz^{*} = non-dimensional vertical foundation displacement

Δz = vertical foundation displacement

H^{*} = non-dimensional horizontal load

H = horizontal load on the model suction caisson

Δx^{*} = non-dimensional horizontal foundation displacement

Δx = horizontal foundation displacement

M^* = non-dimensional moment on the model suction caisson

M = moment on the model suction caisson

$\theta^* = \theta$ = non-dimensional rotation and rotation (equivalent values)

For each of the cyclic load tests, the load response of the displacement-controlled cycles was separated into a positive cyclic amplitude component and negative cyclic amplitude component for each cycle as defined in Figure 4.6. For the vertical loading, compression was defined as positive and uplift was defined as negative. For the horizontal loading, the positive loading direction was arbitrarily defined as the initial horizontal direction of loading. These were the same sign convention as for the monotonic load tests.

4.4.2 Installation penetration resistance

The non-dimensional penetration resistances during the installation phases of all the 1-g model load tests conducted in kaolin are shown in Figure 4.7 through Figure 4.21 as labeled. The non-dimensional load required to install the foundations ranged from 1.3 to 1.9 and 3.0 to 3.5 for K-1G-AR1 and K-1G-AR2 respectively. Using these values, the α for the foundations was back-calculated based on the design recommendations for penetration resistance from API RP 2SK (2008) described in Section 2.3.1.1. The back-calculated α values were 0.14 to 0.26 and 0.22 to 0.30 for K-1G-AR1 and K-1G-AR2 respectively.

These back-calculated values, however, were less than half of the design recommendation from API RP 2SK (2008) based on the inverse of sensitivity (0.63 based on the average measured sensitivity of the 1-g kaolin test beds). Dendani (2003) has also reported lower back-calculated α values based on field measurements of installation penetration resistance of suction caissons in clay. The lower back-calculated α was most likely due to the failure surface occurring between the soil and the structure. While the use of the inverse of sensitivity accounts for the remolding of the soil, it does not account for any reduction of the unit side resistance due to the adhesion mechanism. This type of reduction of the adhesion mechanism cannot readily be accounted for with sensitivity alone, as it is an indicator of clay-clay interface strength. The very little to no clay remaining attached to the model foundations after extraction described later in Section 4.4 supports the soil-structure interface failure mechanism. A soil-soil interface would have resulted in a layer of clay left attached to the foundation upon extraction.

During the installation phase, a narrow and uniform gap formed around the model suction caissons at the soil surface as shown in Figure 4.22. For K-1G-AR1, the gap was no more than 2 mm wide at the surface and no more than 5 mm deep. For K-1G-AR2, the gap was no more than 1 mm at the surface and no more than 2 mm deep. The likely cause of the gap was the relatively high wall thickness to diameter ratio of the model foundations.

4.4.3 Baseline undrained vertical monotonic response

4.4.3.1 Compression followed by uplift

The undrained load responses of the baseline vertical monotonic load tests in compression on K-1G-AR1 and K-1G-AR2 are shown in Figure 4.7 and Figure 4.10 respectively. These tests both displayed a strain-softening behavior, K-1G-AR1 more so than K-1G-AR2, with non-dimensional ultimate compression capacities of 12.0 and 12.7 mobilized after non-dimensional vertical displacements of 0.021 and 0.022 for K-1G-AR1 and K-1G-AR2 respectively. The back-calculated N_c values based on these ultimate capacities, API RP 2GEO (2011) design equations, and α values back calculated from the installation phase (Section 4.4.2) were 14.6 for both K-1G-AR1 and K-1G-AR2. The API design equations recommend a N_c of 9 assuming the foundation will be deeply embedded (AR > 4). For the aspect ratios of the model foundations, Skempton (1951) recommends values of 7.6 and 8.4 for K-1G-AR1 and K-1G-AR2 respectively. The back-calculated values were higher than Skempton's and therefore API's recommendations. The N_c values back-calculated using both assumptions fall between values reported by previous studies by El-Sherbiny (2005) and Luke et al. (2005) for suction caissons in clay (6 to 16). An important note, the α values utilized in this analysis and the remainder of presented analyses were those back calculated during the installation phase. Since the unit adhesion resistance along a suction caisson was assumed to be the same regardless of installation or monotonic compression, a single value of α was determined to be reasonable. The only difference in terms of adhesion or side resistance would be the amount of surface area that the resistance was mobilized along (i.e. the outside and inside wall during installation and only the outside wall during monotonic loading). API however recommends differing α values for the installation and monotonic loading phases or 0.63 and 0.43 respectively. Having two different adhesion factors does not make intuitive sense for a similar loading mechanism. Additionally, having a lower design value during monotonic loading would indicate a loss of resistance rather

than an increase in resistance after installation (a.k.a. pile set-up) that has commonly been observed for offshore foundations.

The undrained load responses of the uplift load tests to extraction that followed the baseline vertical monotonic load tests in compression on K-1G-AR1 and K-1G-AR2 are shown in Figure 4.7 and Figure 4.10 respectively. These tests both displayed a very slight strain-softening behavior over the course of the large amounts of uplift displacement. Byrne and Cassidy (2002) and Gournevec et al. (2009) observed similar load responses. The non-dimensional peak uplift capacities of -8.2 and -9.1 were mobilized after non-dimensional vertical displacements of 0.148 and 0.384 for K-1G-AR1 and K-1G-AR2 respectively. For both tests, a plug was retained in the model suction caissons with very little to no clay clinging to the outside skirt of the foundation. A circular scarp formed around both foundations during extraction as shown in Figure 4.23 and Figure 4.24, however these were due to a Rankine type of wedge filling the void left behind by plug retention rather than the development of a general shear failure mechanism. Due to the lower mobilized resistance in the uplift that followed the compression phase, it was likely that the prior compression mobilized resistance along the same or similar mechanism. The detachment of the plugs from the clay test beds was marked by a rapid decrease in uplift resistance.

4.4.3.2 Uplift only

The undrained load responses of the baseline vertical monotonic load tests in uplift on K-1G-AR1 and K-1G-AR2 are shown in Figure 4.20 and Figure 4.21 respectively. These tests displayed a strain-softening behavior that was much more pronounced than that of the monotonic uplift tests conducted after monotonic compression described in Section 4.4.3.1 similar to observations by Allersma et al. (2000), Byrne and Cassidy (2002), Luke et al. (2005), Chen and Randolph (2007a) and Li et al. (2015). The non-dimensional ultimate uplift capacities of -12.5 and -12.7 were similar to the non-dimensional ultimate compression capacities and mobilized at non-dimensional vertical displacements of 0.013 and 0.031 for K-1G-AR1 and K-1G-AR2 respectively also similar to their compression counterpart. The back-calculated N_c values based on these ultimate capacities based on API RP 2GEO (2011) design equations and α values back-calculated during installation (Section 4.4.2) were 13.1 and 11.7 for K-1G-AR1 and K-1G-AR2 respectively. These values accounted for the weight of the clay within the suction caisson as contributing to the resistance as the full plug was retained upon extraction. As they were in

compression, these values were higher than the recommended design values from Skempton and API, but fall between values reported by previous studies by El-Sherbiny (2005) and Luke et al. (2005) for suction caissons in clay (6 to 16).

A circular scarp formed around both foundations during extraction as shown in Figure 4.23 and Figure 4.24, however these were due to a Rankine type of wedge filling the void left behind by plug retention rather than the development of a general shear failure mechanism. The plugs were retained in the foundation with very little to no clay clinging to the outside skirt. The detachment of the plugs from the clay test beds was marked by a rapid decrease in uplift resistance.

4.4.4 Undrained vertical cyclic response

The non-dimensional vertical cyclic capacity amplitude, $\pm V'^{*}_{cyc}$, of each cycle of the 100 packet cyclic load tests for K-1G-AR1 (K-1G-AR1-V-Cyc-2) and for K-1G-AR2 (K-1G-AR2-V-Cyc-2) are shown in Figure 4.25 and Figure 4.26 respectively. For K-1G-AR1-V-Cyc-2, the packets with non-dimensional cyclic displacement amplitude less than or equal to 0.05% of D did not exhibit capacity degradation over the course of the 100 cycles. Packets with amplitudes greater than or equal to 0.25% of D did exhibit capacity degradation over the 100 cycles, however the threshold was likely closer to that of 0.05% of D. For K-1G-AR2-V-Cyc-2, the thresholds were less than or equal to 0.0525% of D for no capacity degradation and greater than or equal to 0.125% of D for capacity degradation. These thresholds indicated that a range of displacements exist over which suction caisson foundation response was elastic or exhibits insignificant to no load degradation. This threshold has also been observed in load controlled cyclic model tests in clay conducted by Chen and Randolph (2007b), Gourvenec et al. (2007), and Villalobos et al. (2010), and in element level direct simple shear testing of clay conducted by Mortezaie and Vucetic (2016). This threshold likely coincides with the displacement required to exceed the threshold shear strains for cyclic degradation within the clay. The similar magnitude of V'^{*}_{cyc} in compression and in uplift indicate that the failure mechanism being mobilized was similar in both directions of loading.

The vertical cyclic capacity amplitude, $\pm V'^{*}_{cyc}$, of each cycle of the day long cyclic load tests on K-1G-AR1 (K-1G-AR1-V-Cyc-1 and K-1G-AR1-V-Cyc-3) and K-1G-AR2 (K-1G-AR2-V-Cyc-1) are shown in Figure 4.27, Figure 4.28, and Figure 4.29 respectively. The lowest

cyclic displacement amplitude test of 0.004% of D showed relatively constant V'^{*}_{cyc} over the day of cycling both in compression and uplift. The magnitude of the uplift mechanism was slightly higher than that of the compression. This cyclic displacement amplitude agrees with the elastic displacement range determined from K-1G-AR1-V-Cyc-2. Both K-1G-AR1-V-Cyc-1 and K-1G-AR2V-Cyc-2 were conducted at cyclic displacement amplitudes greater than the elastic displacement range and therefore exhibited cyclic degradation in the early cycles. However, V'^{*}_{cyc} began to increase after 1300 and 300 cycles respectively. This increase in capacity at higher cycles has been observed previously in model tests in clay conducted by Chen (2013) and was likely attributed to an increase in strength due to consolidation resulting from dissipation of accumulated pore pressure along the shear surface. For the two tests with cyclic displacement amplitudes outside of the elastic displacement range, the magnitude of V'^{*}_{cyc} were similar regardless of a compression or uplift mechanism.

4.4.5 Post-cyclic undrained vertical monotonic response

4.4.5.1 Compression followed by uplift

The following vertical cyclic load tests were followed by monotonic compression and uplift: K-1G-AR1-Cyc-1, K-1G-AR1-Cyc-2, and K-1G-AR2-Cyc-2. The post-cyclic monotonic compression portions of these three tests are shown in Figure 4.8, Figure 4.9, and Figure 4.12 respectively. The load responses did not display strain-softening behavior and mobilized their peak capacity at significantly larger non-dimensional displacements than their baseline counterparts. The peak capacities in compression were similar to or lower than the baseline monotonic ultimate capacity. The amount of reduction in the peak capacity was dependent on the cyclic displacement amplitude during the cyclic loading phase. In the case of K-1G-AR1-Cyc-1 where the cyclic displacement amplitude was less than the displacement required to mobilize the ultimate capacity in compression during the baseline test, the peak capacity similar to the baseline monotonic ultimate capacity. In the case of K-1G-AR1-Cyc-2 and K-1G-AR2-Cyc-2 where the cyclic displacement amplitude exceeded the displacement required to mobilize the ultimate capacity in compression during the base line test, the peak capacity decreased by 48% and 28% respectively. This likely indicates that the shear surface was completely formed and significant levels of remolding occurred along the vast majority of the shear surface during cycling that in turn significantly reduced the monotonic capacity post cycling. In the case of K-

1G-AR1-Cyc-1 with the lower cyclic displacement amplitude, the shear surface did not form completely and/or was not fully remolded resulting in a similar peak capacity while still requiring increased displacement to mobilize. These two responses show that the progression of the shear surface and the amount of remolding that occurs along the shear surface during cyclic loading were dependent on the amplitude of cycling.

The undrained load responses of the uplift load tests to extraction that followed the post-cyclic vertical monotonic load tests in compression just described are shown in Figure 4.8, Figure 4.9, and Figure 4.12 respectively. The general shape of the load response was similar to the uplift that followed the baseline compression load test. Similar to the post-cyclic compression response, the peak capacity in uplift was dependent on the cyclic displacement amplitude applied during cyclic loading. For K-1G-AR1-Cyc-2, the cyclic displacement amplitude was high enough to result in significant remolding along the shear surface resulting in significantly decreased uplift capacity. The other two tests did not show as significant degradation of monotonic uplift capacity due to cycling likely due to a lack of remolding along a significant portion of the shear surface.

Similar to the baseline tests, scarps formed around the foundations during the three post-cyclic monotonic load tests followed by compression as shown in Figure 4.23 and Figure 4.24. While K-1G-AR1-V-Cyc-1 and K-1G-AR1-V-Cyc-2 both showed a fully formed circular scarp, K-1G-AR2-V-Cyc-2 only formed a partial circular scarp. On one side of the foundation, the circle converged to intersect the foundation skirt. K-1G-AR1-V-Cyc-1 also contained an anomaly with a smaller secondary scarp that formed during the cyclic loading portion of the test. As with the baseline tests, the plug was retained within the foundation upon extraction with very little to no clay clinging to the outside skirt and the detachment of the plug was marked by a rapid decrease in capacity.

4.4.5.2 Uplift only

The following vertical cyclic load tests were followed by monotonic uplift only: K-1G-AR2-Cyc-1 and K-1G-AR1-Cyc-3. The post-cyclic monotonic uplift portions of these two tests are shown in Figure 4.11 and Figure 4.13 respectively. The load responses of these two tests were dependent on the cyclic displacement amplitude that occurred during the previous cyclic loading phase. For the low cyclic displacement amplitude of K-1G-AR1-Cyc-3, the strain softening behavior was very pronounced as it was for the baseline monotonic uplift load test of

K-1G-AR1-Mono-2. On the other hand, the strain-softening was less pronounced for K-1G-AR2-Cyc-1. The cyclic displacement amplitude of K-1G-AR2-Cyc-1 was larger than that of K-1G-AR1-Cyc-3 leading to increased remolding of the shear surface along which resistance was mobilized. This softening allows for additional displacement to occur prior to plug failure. The non-dimensional peak capacities of these tests were -16.6 and -13.4 mobilized after non-dimensional displacements of 0.024 and 0.030 for K-1G-AR2-Cyc-1 and K-1G-AR1-Cyc-3 respectively. These non-dimensional displacements are similar to the non-dimensional displacements required to mobilize the ultimate uplift and compression capacities from the respective baseline load tests. The non-dimensional peak capacities of the two tests were also relatively similar to the non-dimensional ultimate capacities of the respective baseline uplift load tests.

A circular scarp formed around K-1G-AR2-Cyc-1 as shown in Figure 4.24, however these were due to a Rankine type of wedge filling the void left behind by plug retention rather than the development of a general shear failure mechanism. A circular scarp did not form around K-1G-AR1-Cyc-3 as shown in Figure 4.23. This was likely due to the low cyclic displacement amplitude limiting the amount of remolding along the failure surface that forced the failure to occur at the plug. This early plug failure did not allow for significant movement along the failure mechanism at the tip that resulted in insignificant surface scarp formation. The plug was retained in the model foundation for both tests with very little to no clay clinging to the outside skirt.

4.4.6 Baseline undrained horizontal monotonic response

The undrained load responses of the baseline horizontal monotonic load tests on K-1G-AR1 and K-1G-AR2 are shown in Figure 4.30 and Figure 4.31 respectively. Both of these tests did not display a strain-softening behavior. The non-dimensional ultimate (maximum) horizontal capacities mobilized were 1.7 and 2.5 at non-dimensional horizontal displacements of 0.11 and 0.19 (i.e. the point of loading direction reversal or maximum horizontal displacement during the outward swipe) for K-1G-AR1-H-Mono-1 and K-1G-AR2-H-Mono-1 respectively. Both tests began with a load response that was concave up that was followed by a relatively linear segment. While K-1G-AR2-H-Mono-1 maintained this linear segment until the test was terminated, K-1G-AR1-H-Mono-1 proceeded into a third segment that was concave down. During the initial outward swipe, a scarp formed on the tailing side of the foundation for both tests as shown in Figure 4.32 and Figure 4.33 similar to results observed by Bransby and Young (2009), Barari

and Ibsen (2012), and Hung and Kim (2012). The scarps were formed as a result of the clay filling the gap that was left behind the foundation due to its rotation and horizontal displacement rather than due to a failure surface extension that contributes towards the capacity of the foundation.

4.4.7 Undrained horizontal cyclic response

The maximum and minimum mobilized horizontal cyclic capacity of each cycle of the 100 packet cyclic load tests on K-1G-AR1 (K-1G-AR1-H-Cyc-2) and K-1G-AR2 (K-1G-AR2-H-Cyc-2) are shown in Figure 4.36 and

Figure 4.37 respectively. As described in Section 4.3.6 for both tests, the first set of six packets was swiped out and back from the origin in the positive direction and the second set of six packets was swiped out and back from the origin in the negative direction.

For K-1G-AR1-H-Cyc-2, the return portion of the cyclic swipe mobilized a relatively constant load across the first set of packets with a slight step increase in the third packet of the positive set and in the third amplitude packet of the negative set. The cyclic degradation was more prevalent in the outward direction of the two sets when the foundation was pushing into the soil mass. In the positive set, the packets with non-dimensional cyclic displacement less than or equal to 0.74% of D did not exhibit significant capacity degradation over the course of the 100 cycles while those greater than of equal to 1.3% of D did exhibit capacity degradation. In the negative set, the packets with non-dimensional cyclic displacement less than or equal to 1.3% of D did not exhibit significant capacity degradation over the course of the 100 cycles while those greater than of equal to 2.0% of D did exhibit capacity degradation. The effect of pile setup was observed during the last four packets of each set where the cyclic displacement amplitude was constant. However, the pile setup due to the 20 minute slack period between packets was much more prominent on the positive set of packets. During the cyclic swipes, a scarp formed on the tailing side of the foundation for both tests as shown in Figure 4.32 and Figure 4.33. As in the monotonic horizontal load tests, the scarps were formed as a result of the clay filling the gap that was left behind the foundation due to its rotation and horizontal displacement rather than due to a failure surface extension that contributes to the capacity of the foundation. This scarp formation during the positive set of swipes significantly remolded the upper portion of clay that would provide horizontal capacity during the negative set of swipes. This resulted in lower horizontal

capacities during the negative set of packets along with less prominent pile setup between each packet.

For K-1G-AR2-V-Cyc-2, the return portion of the cyclic swipe mobilized a slightly increasing load over the course of each packet for both the positive and negative set of packets. Again, the cyclic degradation was more prevalent in the outward direction of the two sets. In the positive set, all the packets with non-dimensional cyclic displacement greater than or equal to 0.96% of D did exhibit capacity degradation. In the negative set, the packets with non-dimensional cyclic displacement less than or equal to 1.8% of D did not exhibit significant capacity degradation over the course of the 100 cycles while those greater than of equal to 3.0% of D did exhibit capacity degradation. During the cyclic swipes, a scarp formed on the tailing side of the foundation for both tests as shown in Figure 4.32 and Figure 4.33. As in the monotonic horizontal load tests, the scarps were formed as a result of the clay filling the gap that was left behind the foundation due to its rotation and horizontal displacement rather than due to a failure surface extension that contributes to the capacity of the foundation. This scarp formation during the positive set of swipes significantly remolded the upper portion of clay that would provide horizontal capacity during the negative set of swipes. This resulted in lower horizontal capacities during the negative set of packets.

The maximum and minimum mobilized horizontal cyclic capacity of each cycle of the day long cyclic load tests on K-1G-AR1 (K-1G-AR1-H-Cyc-1) and K-1G-AR2 (K-1G-AR2-H-Cyc-1) are shown in Figure 4.38 and Figure 4.39 respectively. As described in Section 4.3.6 for both tests, the first and third packets were swiped out and back from the origin in the positive direction and the second and fourth packets were swiped out and back from the origin in the negative direction. For K-1G-AR1-H-Cyc-1, cyclic capacity degradation was observed during all four packets on the outward portion of the swipe. During the return portion of the swipe, approximately the same capacity was mobilized regardless of the cycle number for all four packets. In general, the magnitudes of the first and third packets were greater than that of the second and fourth packets for their respective outward and return portions of the swipe due to the same softening and remolding of the soil due to gap formation on the tailing side of the foundation as seen in the previously described horizontal load tests. All four packets approached a stable capacity at the end of the ~4,320 cycle packet. While this stabilization was in agreement with results from Chen (2013), based on their results it was possible that the capacity would

increase slightly had the cycling been maintained. Very similar load responses were made during K-1G-AR2-H-Cyc-1, the only major difference being that the outward swipe portion of the second and fourth packets did not exhibit significant cyclic capacity degradation and rather mobilized a similar capacity with each passing cycle. During the cyclic swipes, a scarp formed on the tailing side of the foundation for both tests as shown in Figure 4.32 and Figure 4.33. As in the monotonic horizontal load tests and the 12 sets of packet-ed cyclic load tests, the scarps were formed as a result of the clay filling the gap that was left behind the foundation due to its rotation and horizontal displacement rather than due to a failure surface extension that contributes towards the capacity of the foundation.

4.4.8 Post-horizontal loading undrained vertical monotonic response

The load responses of the undrained vertical monotonic extraction processes conducted after the horizontal load tests are shown in Figure 4.14 through Figure 4.19. The shape of the uplift load response all displayed strain-softening behavior similar to that of the baseline undrained vertical monotonic uplift tests of K-1G-AR1-V-Mono-2 and K-1G-AR2-V-Mono-2. The non-dimensional peak uplift capacity mobilized for the six tests ranged from -11.2 to -13.8 after non-dimensional displacements of 0.018 to 0.025 for K-1G-AR1 and -13.2 to -18.5 after non-dimensional displacements of 0.033 to 0.060 for K-1G-AR2. These values were similar to K-1G-AR1-V-Mono-2 and K-1G-AR2-V-Mono-2 indicating that the swipe loading mechanism did not have a significant effect on the uplift capacity of the foundation. During extraction, a circular scarp formed around both foundations as shown in Figure 4.34 and Figure 4.35 similar in shape to the extraction scarps that formed around the foundations during the vertical load tests. Slight amounts of clay clung to the outside wall of the foundations. It was primarily concentrated on the uppermost portion of the sidewall facing the outward swipe motion. Additional clay that was remolded at the surface due to the horizontal loading clung to the bottommost portion of the external wall as it was completely extracted fro the test bed. Similar to the extraction phases following the vertical load tests, a plug was retained within the foundation upon extraction.

4.5 Conclusions

Based on the results of undrained 1-g model load tests in kaolin described in this chapter, the following conclusions were made as indicated for the installation penetration resistance, vertical loading, and horizontal loading:

1. Installation penetration resistance
    a. The back-calculated α values of 0.14 to 0.30 for both foundations was significantly lower than the API design recommendation of 0.63 that was determined from the sensitivity of the soil. This factor, in addition to the low amount of clay clinging to the outside wall of the caisson upon extraction, indicated that the side resistance of the suction caisson foundation was mobilized along the soil-structure interface rather than the soil-soil interface that was recommended by use of the sensitivity driven API design recommendation.
2. Undrained vertical loading
    a. The back-calculated N_c values for the K-AR1-1G baseline monotonic compression, K-AR1-1G baseline monotonic uplift, K-AR2-1G baseline monotonic compression, and K-AR2-1G baseline monotonic uplift were 14.6, 13.1, 14.6, and 11.7 when using the α values back-calculated from the installation phase. These back-calculated N_c values were greater than the API design N_c values of 7.6 and 8.4 based on Skempton (1951) for AR1 and AR2 circular foundations in clay. This indicates that the failure mechanism likely differed from the assumed plastic limit equilibrium theory failure surface presented by Skempton (1951). While limit equilibrium methods such as Skempton's have been commonly utilized in design of foundations in soft clay, they were not developed for use in such materials. The failure mechanism will be visualized and discussed in CHAPTER 6.
    b. The back-calculated bearing capacity factor, non-dimensional ultimate capacity, displacement required to mobilize the non-dimensional ultimate capacity, and surface scarp shape post-extraction of the compression and uplift baseline load tests on K-1G-AR1 and K-1G-AR2 indicated that the failure mechanism in compression and in uplift were likely similar in both their shape and the method of soil shearing. The major differences between the two were that the uplift mechanism added an additional potential failure at the plug, provided additional resistance due to the

weight of the soil plug retained in the caisson, and resulted in an additional driving force of surcharge soil. The failure scarps after extraction of the foundations indicated a circular type of failure similar to that assumed by Skempton (1951), but with enough differences to alter the back-calculated bearing capacity factor. This assumption was confirmed through the load testing described in CHAPTER 6.

c. During cyclic loading, a range of vertical non-dimensional displacements exists over which cyclic capacity was 'elastic' (i.e. the foundation capacity exhibits none to insignificant levels of degradation with each cycle). Mortezaie and Vucetic (2016) observed this type of behavior at the element level. Due to the inherently cyclic nature of TEC foundation loading and sensitivity of the energy production to the orientation of the blades in the tidal current profile, serviceability constraints of the foundation will be critical during design. Understanding the service loads and their relation to this elastic zone can provide additional insight into the potential displacements during operation. This limiting cyclic displacement threshold exists at a point between 0.05% and 0.25% of the diameter and 0.0525% and 0.125% of the diameter for K-1G-AR1 and K-1G-AR2 respectively.
d. The response of the model suction caissons to extreme loading events (modeled as undrained monotonic vertical loads) that occurred post-cycling was highly dependent on the cyclic displacement amplitude of the cycling.
    i. For post-cyclic monotonic compression loading, any strain softening behavior was no longer present after cycling and the non-dimensional displacement required to mobilize peak capacity was increased. The magnitude of the peak capacity, however, was dependent on the non-dimensional displacement amplitude during cycling. When the amplitude was greater than approximately 2% of D (the amplitude required to mobilize the ultimate capacity in the baseline tests), the peak capacity degraded significantly. For

cases when it was less than 2%, the peak capacity was similar to the baseline tests. This indicated that the failure mechanism was progressive and/or subject to remolding.

ii. For post-cyclic monotonic uplift loading, similar trends were observed as stated in 2.d.i. with additional criteria as a result of the potential for plug failure. For cases when the non-dimensional cyclic displacement amplitude was very low (i.e. 0.04% of D) and the extreme load was in the uplift direction, the plug failed at very low displacements resulting in a 'brittle' failure mechanism with a rapid loss of capacity upon reaching the peak capacity. If additional remolding of the soil occurred along the failure mechanism, the response was much more ductile with plug failure and rapid loss of capacity occurring at a point where the foundation was nearing the point of complete extraction. TEC foundations must therefore be designed to allow for sufficient deformations during standard operation to prevent an early plug failure during an extreme event or provide sufficient protection from events such as ship collisions from occurring.

3. Undrained horizontal loading
    a. The soil provides higher resistance in the initial direction of horizontal loading due to the softening of the clay that occurs on the tailing end of foundation motion due to clay filling the gap that was formed. The gapping decreased the resistance of the foundation in the opposing direction. Due to the nature of TEC loading involving a reversing of the loading direction two to four times a day, the design of the foundation should be designed assuming the softening due to gapping has occurred.
    b. During cyclic loading, a range of horizontal non-dimensional displacements exists over which cyclic capacity was 'elastic' (i.e. the foundation capacity exhibits none to insignificant levels of degradation with each cycle). Mortezaie and Vucetic (2016) observed this type of behavior at the element level. Due to the inherently cyclic nature of TEC

foundation loading and sensitivity of the energy production to the orientation of the blades in the tidal current profile, serviceability constraints of the foundation will be critical during design. Understanding the service loads and their relation to this elastic zone can provide additional insight into the potential displacements during operation. This limiting cyclic displacement threshold exists at a point between 0.74% and 1.3% of the diameter and 0.96% and 1.8% of the diameter for K-1G-AR1 and K-1G-AR2 respectively.

c. While the cyclic horizontal loading did soften the near surface soils due to the gapping discussed above, horizontal cycling did not have a significant effect of the uplift capacity or uplift load response of the foundation. The uplift conducted post horizontal cycling on the foundations resembled the load response of the baseline undrained monotonic uplift test conducted on the foundations. This indicated that the horizontal and vertical failure mechanisms were significantly different therefore the remolding of the soils providing horizontal resistance did not affect the strength of the soil providing vertical resistance.

d. The horizontal ultimate capacity of the intermediate aspect ratio foundations provided approximately 14% to 20% of the vertical ultimate capacity of the foundations. Additionally large non-dimensional horizontal displacements were required to mobilize these percentages of capacity. Therefore, for TECs suction caissons in the multi-pod configuration will provide a more economically feasible foundation design from a purely geotechnical perspective as the horizontal current loads can be resisted by the push-pull mechanism on opposing foundations.

4.6 Tables

Table 4.1: Brief description of 1-g model undrained load tests in kaolin

Identifier	Test bed	Type	Description
K-1G-AR1-V-Mono-1	K-1G-TB1	Vertical, monotonic	Compression followed by uplift until extraction.
K-1G-AR1-V-Cyc-1	K-1G-TB2	Vertical,	~17,280 constant displacement amplitude

Table 4.1: Brief description of 1-g model undrained load tests in kaolin (Continued)

Identifier	Test bed	Type	Description
		cyclic	of 0.6% diameter cycles with a period of 5 seconds followed by monotonic compression and monotonic uplift until extraction.
K-1G-AR1-V-Cyc-2	K-1G-TB3	Vertical, cyclic	Six 100 cycle packets with a period of 5 seconds followed by monotonic compression and monotonic uplift until extraction. Cycle packets were separated by 20 minutes of no loading and the displacement amplitude increased with each successive cycle as follows: 0.005%, 0.01%, 0.05%, 0.25%, 1.25%, and 3.5% of the diameter.
K-1G-AR2-V-Mono-1	K-1G-TB4	Vertical, monotonic	Compression followed by uplift until extraction
K-1G-AR2-V-Cyc-1	K-1G-TB5	Vertical, cyclic	~17,280 constant displacement amplitude of 0.47% diameter cycles with a period of 5 seconds followed by monotonic uplift until extraction.
K-1G-AR2-V-Cyc-2	K-1G-TB6	Vertical, cyclic	Six 100 cycle packets with a period of 5 seconds followed by monotonic compression and monotonic uplift until extraction. Cycle packets were separated by 20 minutes of no loading and the displacement amplitude increased with each successive cycle as follows: 0.0035%, 0.00425%, 0.0525%, 0.125%, 1.15%, and 3.25% of the diameter.
K-1G-AR1-V-Cyc-3	K-1G-TB7	Vertical, cyclic	~17,280 constant displacement amplitude of 0.04% diameter cycles with a period of 5 seconds followed by monotonic compression and monotonic uplift until extraction.
K-1G-AR1-H-Cyc-1	K-1G-TB8	Swipe, cyclic	Four ~4320 cycle packets with a period of 5 seconds followed by monotonic uplift until extraction. Cycle packets were separated by 20 minutes of no loading. First and third packets swiped from origin to a positive integer with constant displacement amplitude of 2.7% of the diameter. Second and fourth packets swiped from origin to a negative integer with constant displacement amplitude of

Table 4.1: Brief description of 1-g model undrained load tests in kaolin (Continued)

Identifier	Test bed	Type	Description
			2.7% of the diameter.
K-1G-AR1-H-Cyc-2	K-1G-TB9	Swipe, cyclic	Two sets of six 100 cycle packets with a period of 5 seconds followed by monotonic uplift until extraction. Cycle packets were separated by 20 minutes of no loading. First set of six packets swiped from origin to a positive integer with displacement amplitudes of each successive cycle as follows: 0.74%, 1.3%, 2.1%, 2.0%, 2.0%, and 2.0% of the diameter. Second set of six packets swiped from origin to a positive integer with displacement amplitudes of each successive cycle as follows: 0.0035%, 0.76%, 1.3%, 2.0%, 2.0%, and 2.0% of the diameter.
K-1G-AR1-H-Mono-1	K-1G-TB10	Swipe, monotonic	Monotonic swipe outwards followed by a swipe back to the centerline followed by vertical uplift until extraction
K-1G-AR2-H-Mono-1	K-1G-TB11	Swipe, monotonic	Monotonic swipe outwards followed by a swipe back to the centerline followed by vertical uplift until extraction
K-1G-AR2-H-Cyc-1	K-1G-TB12	Swipe, cyclic	Four ~4320 cycle packets with a period of 5 seconds followed by monotonic uplift until extraction. Cycle packets were separated by 20 minutes of no loading. First and third packets swiped from origin to a positive integer with constant displacement amplitude of 5.3% of the diameter. Second and fourth packets swiped from origin to a negative integer with constant displacement amplitude of 5.3% of the diameter.
K-1G-AR2-H-Cyc-2	K-1G-TB13	Swipe, cyclic	Two sets of six 100 cycle packets with a period of 5 seconds followed by monotonic uplift until extraction. Cycle packets were separated by 20 minutes of no loading. First set of six packets swiped from origin to a positive integer with displacement amplitudes of each successive cycle as follows: 0.96%, 1.7%, 3.1%, 4.9%, 6.2%, and 7.5% of the diameter. Second set of six packets swiped from origin to a positive integer with displacement amplitudes of

Table 4.1: Brief description of 1-g model undrained load tests in kaolin (Continued)

Identifier	Test bed	Type	Description
			each successive cycle as follows: 1.1%, 1.8%, 3.0%, 4.4%, 5.6%, and 7.0% of the diameter.
K-1G-AR1-V-Mono-2	K-1G-TB14	Vertical, monotonic	Uplift until extraction
K-1G-AR2-V-Mono-2	K-1G-TB15	Vertical, monotonic	Uplift until extraction

4.7 Figures

Figure 4.1: The two kaolin 1-g model suction caissons with K-1G-AR1 shown on the left and K-1G-AR2 shown on the right

Figure 4.2: The two load cells and locking ball and socket joint positioned along the loading rod of the two kaolin 1-g model suction caissons shown on K-1G-AR2

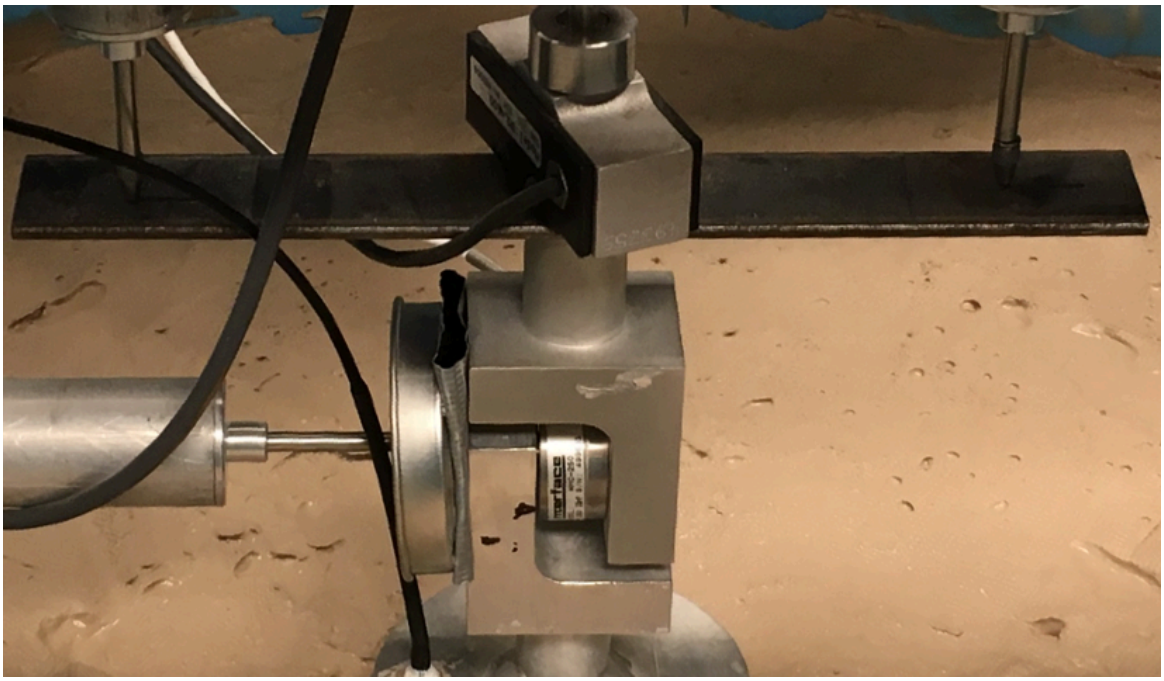

Figure 4.3: The platforms that could be placed along the loading rod to allow for additional area for linear displacement transducer placement

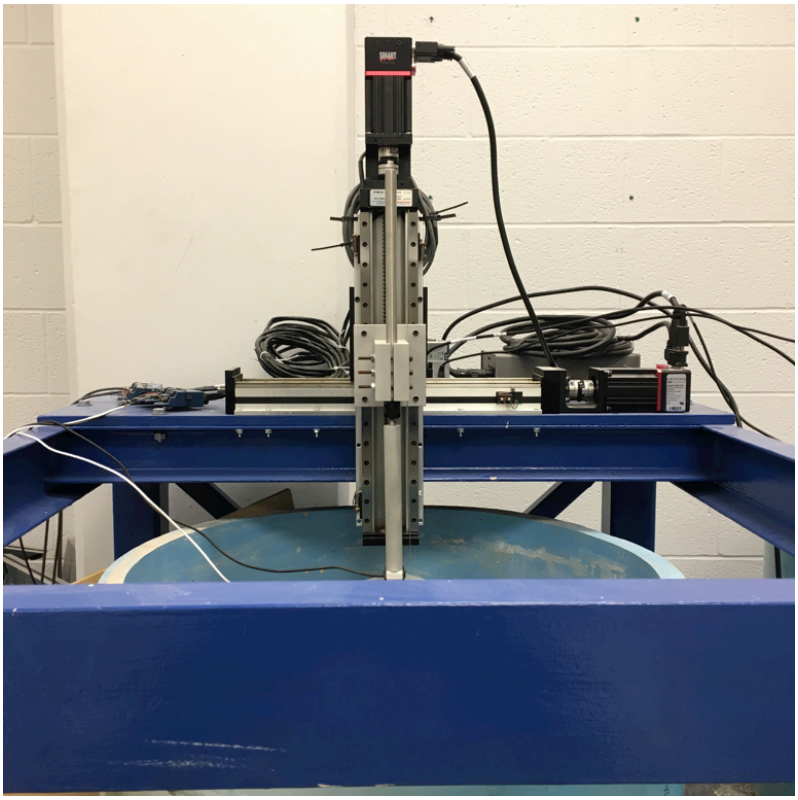

Figure 4.4: The loading apparatus and steel frame used to conduct the 1-g model load tests in kaolin

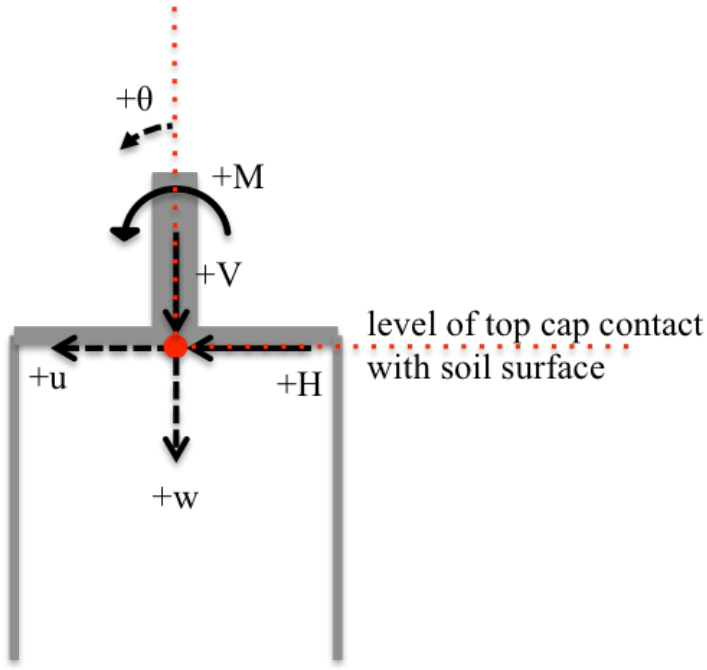

Figure 4.5: Nomenclature and orientation of model foundation loads and displacements along with the origin point of the model foundation

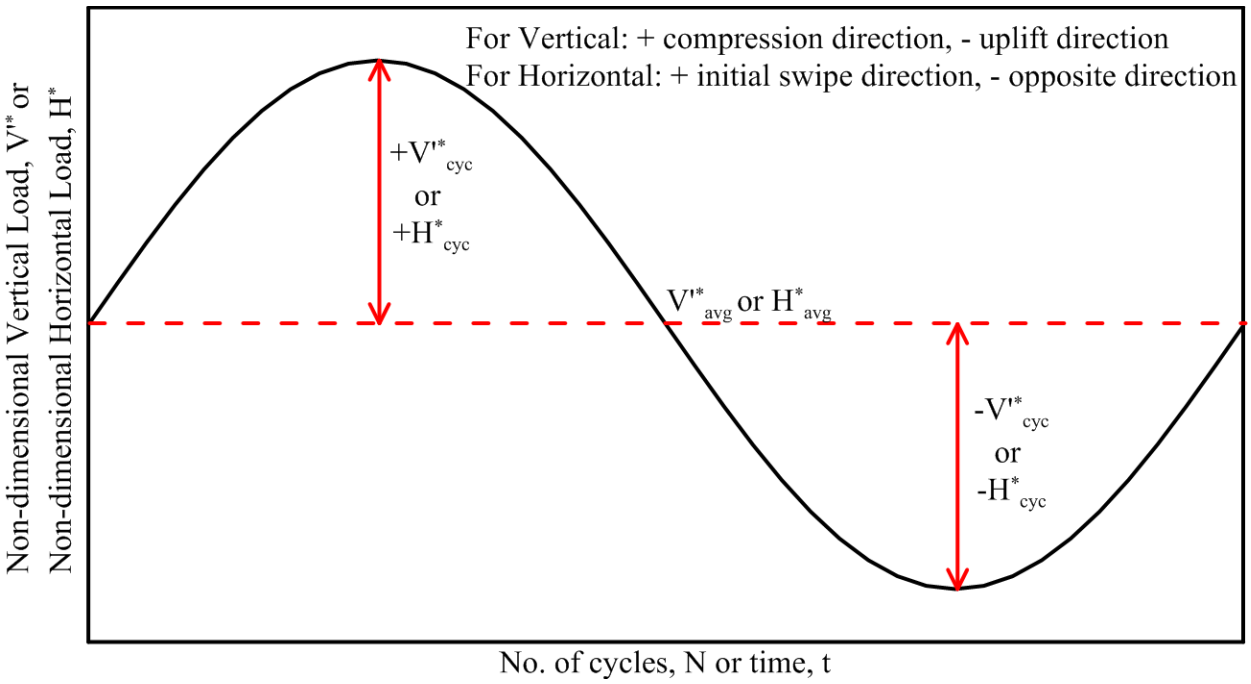

Figure 4.6: Nomenclature of the cyclic load response components

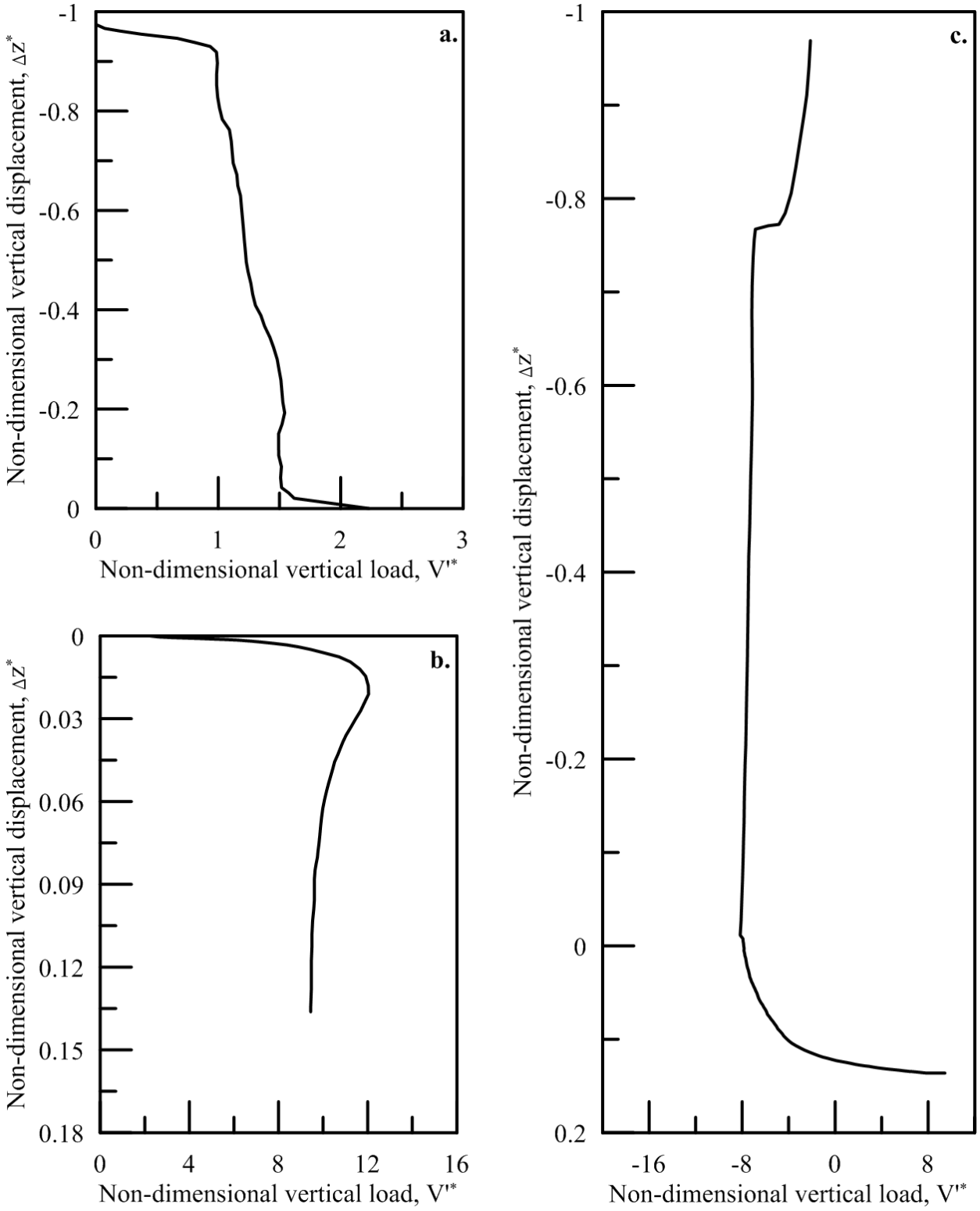

Figure 4.7: Load response of the vertical loading phases of K-1G-AR1-V-Mono-1 during a. installation, b. monotonic compression, and c. monotonic uplift as applicable

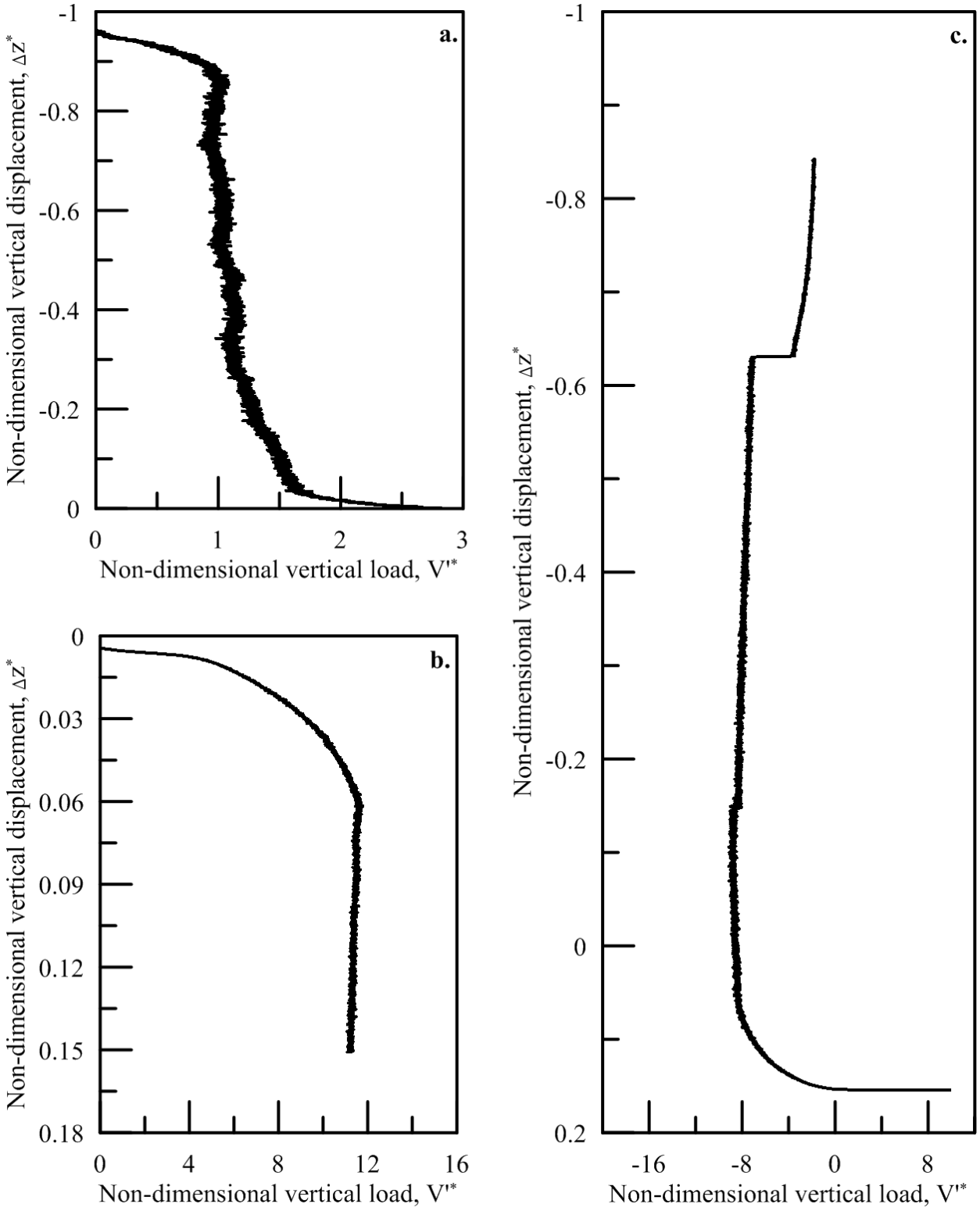

Figure 4.8: Load response of the vertical loading phases of K-1G-AR1-V-Cyc-1 during a. installation, b. monotonic compression, and c. monotonic uplift as applicable

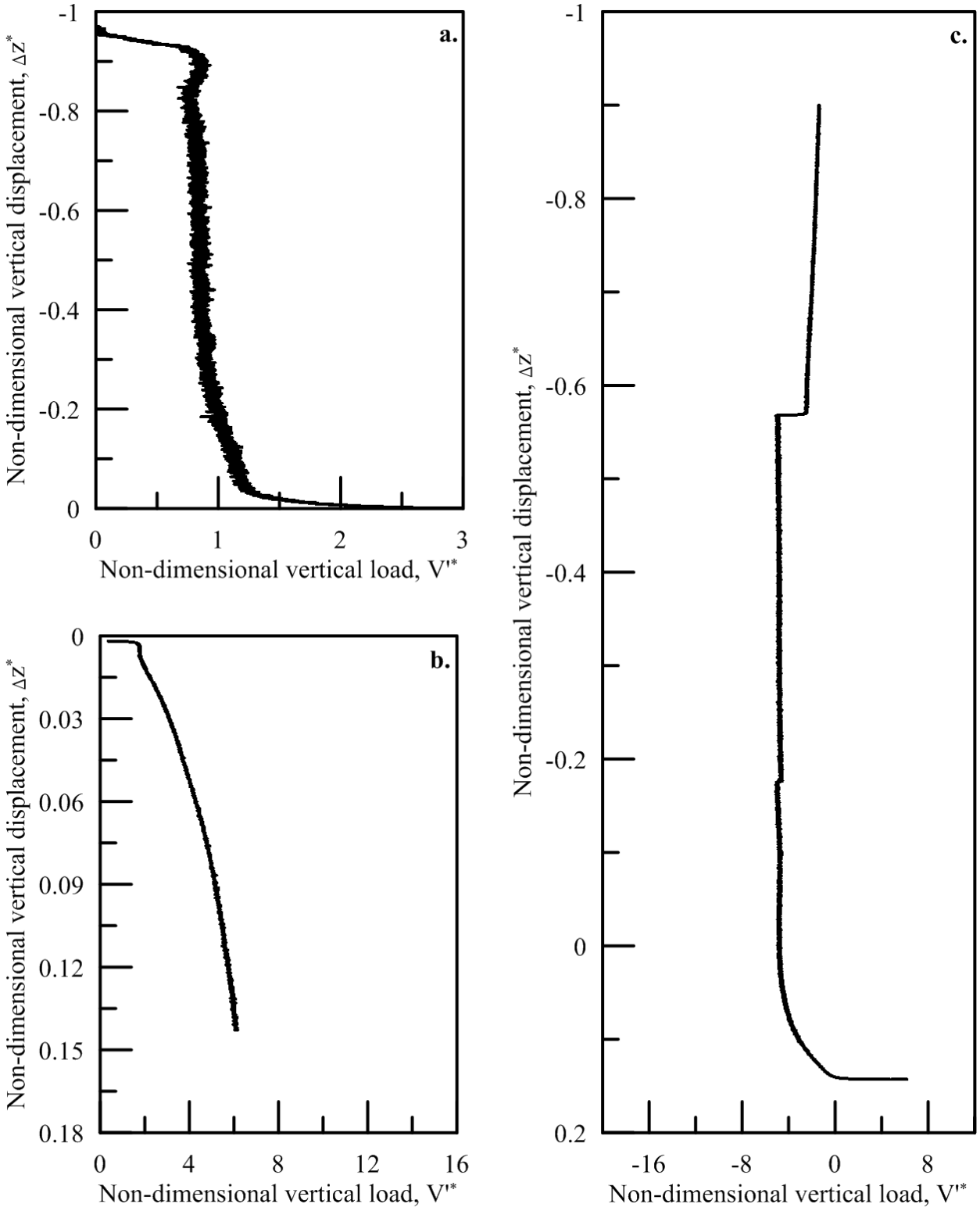

Figure 4.9: Load response of the vertical loading phases of K-1G-AR1-V-Cyc-2 during a. installation, b. monotonic compression, and c. monotonic uplift as applicable

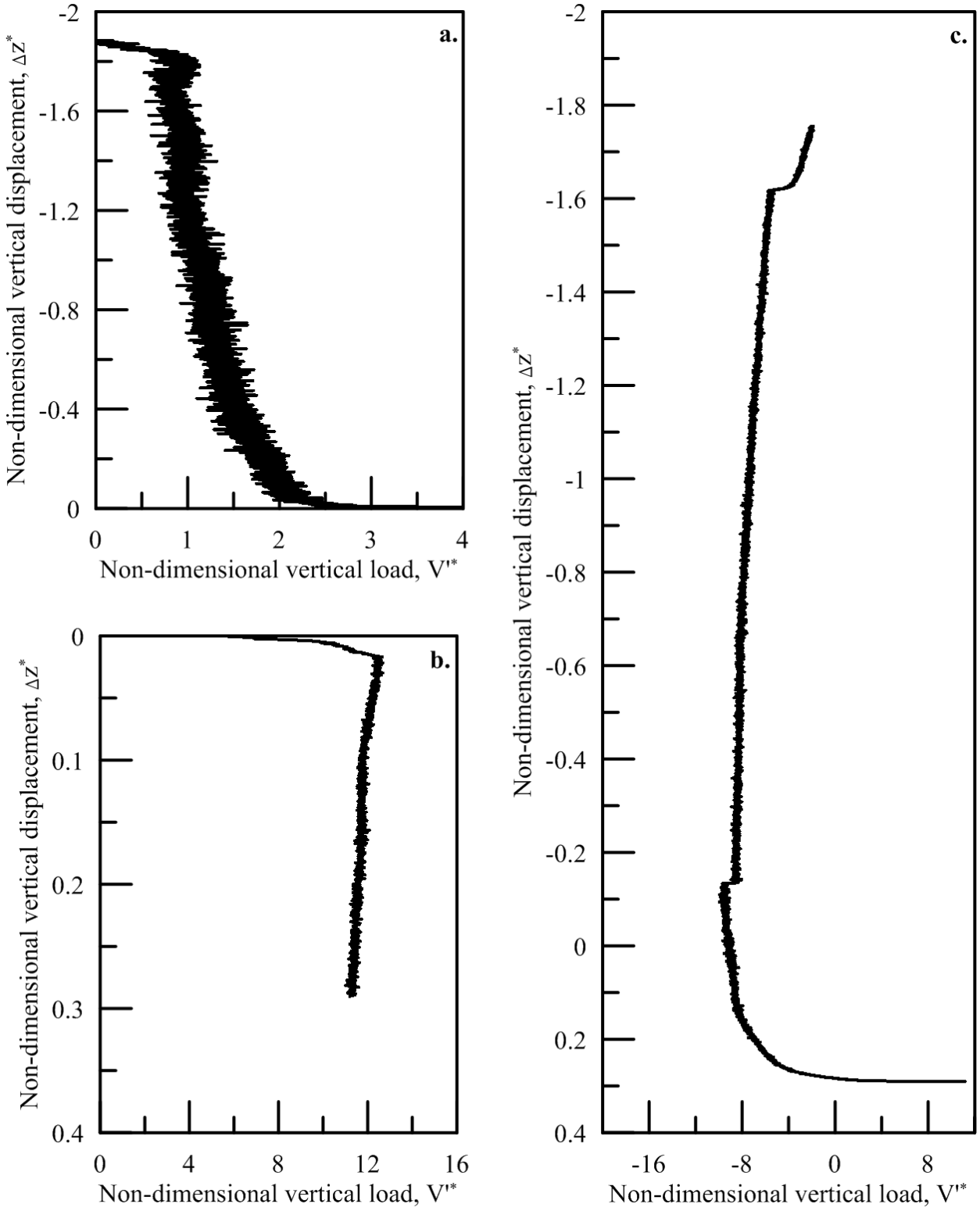

Figure 4.10: Load response of the vertical loading phases of K-1G-AR2-V-Mono-1 during a. installation, b. monotonic compression, and c. monotonic uplift as applicable

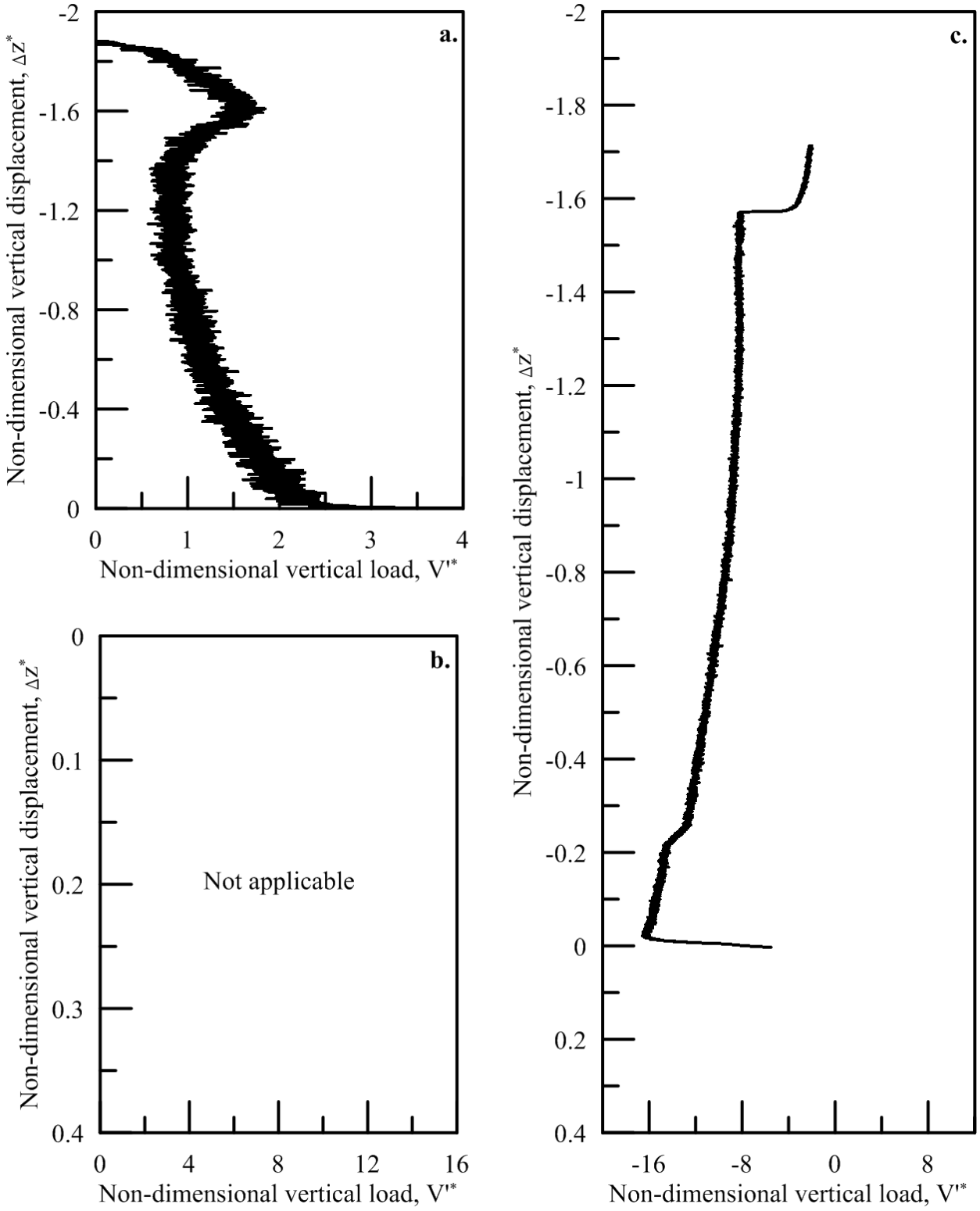

Figure 4.11: Load response of the vertical loading phases of K-1G-AR2-V-Cyc-1 during a. installation, b. monotonic compression, and c. monotonic uplift as applicable

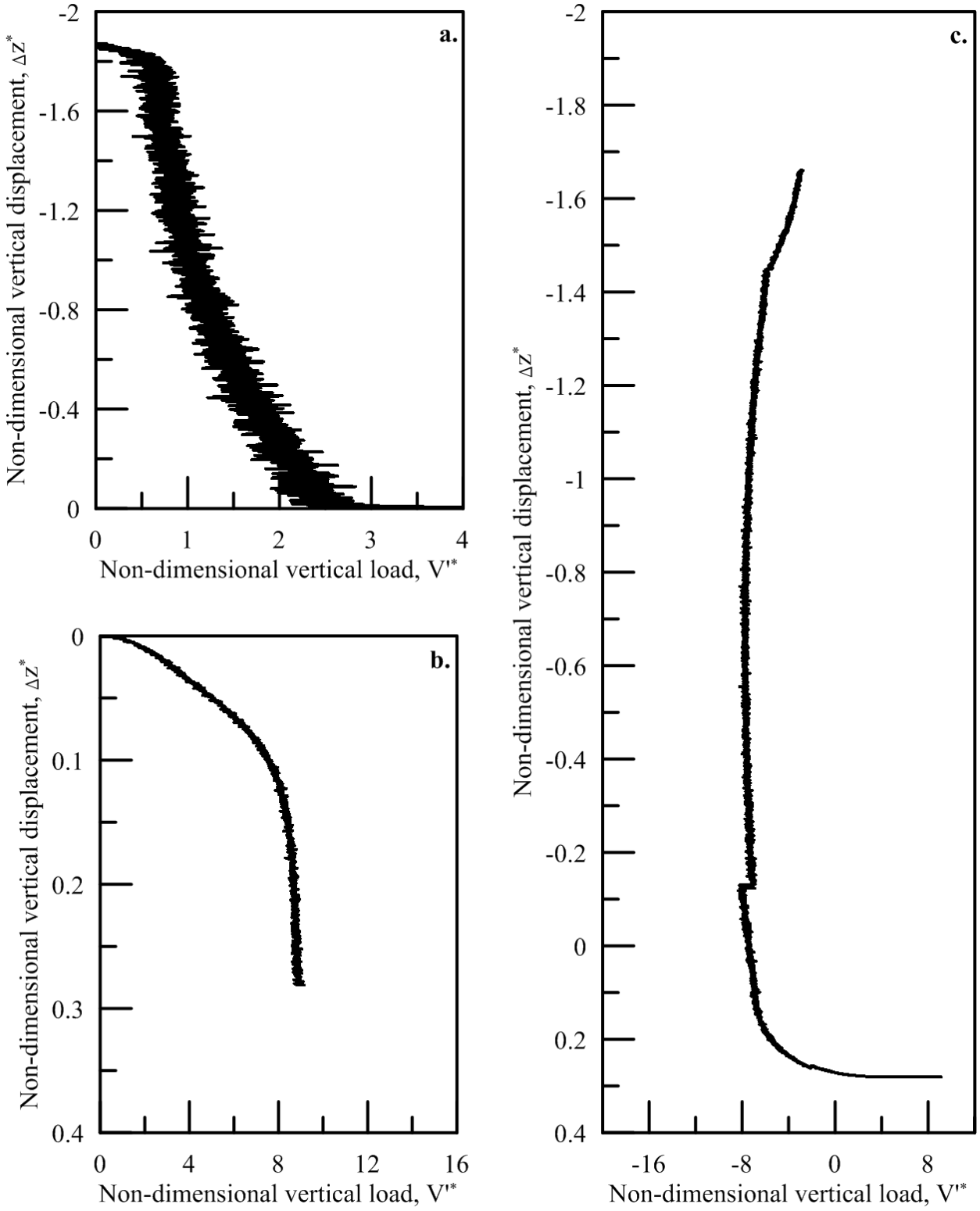

Figure 4.12: Load response of the vertical loading phases of K-1G-AR2-V-Cyc-2 during a. installation, b. monotonic compression, and c. monotonic uplift as applicable

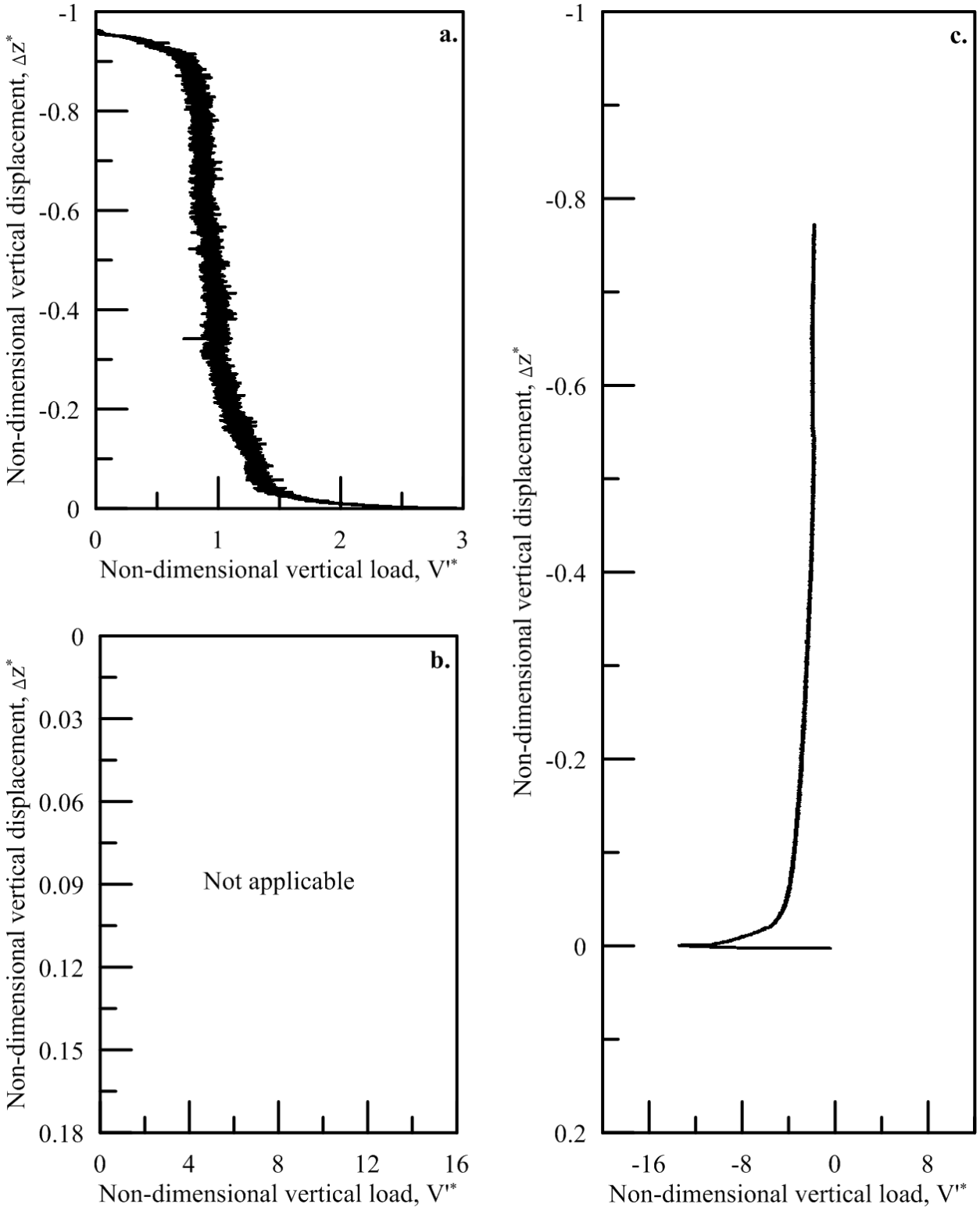

Figure 4.13: Load response of the vertical loading phases of K-1G-AR1-V-Cyc-3 during a. installation, b. monotonic compression, and c. monotonic uplift as applicable

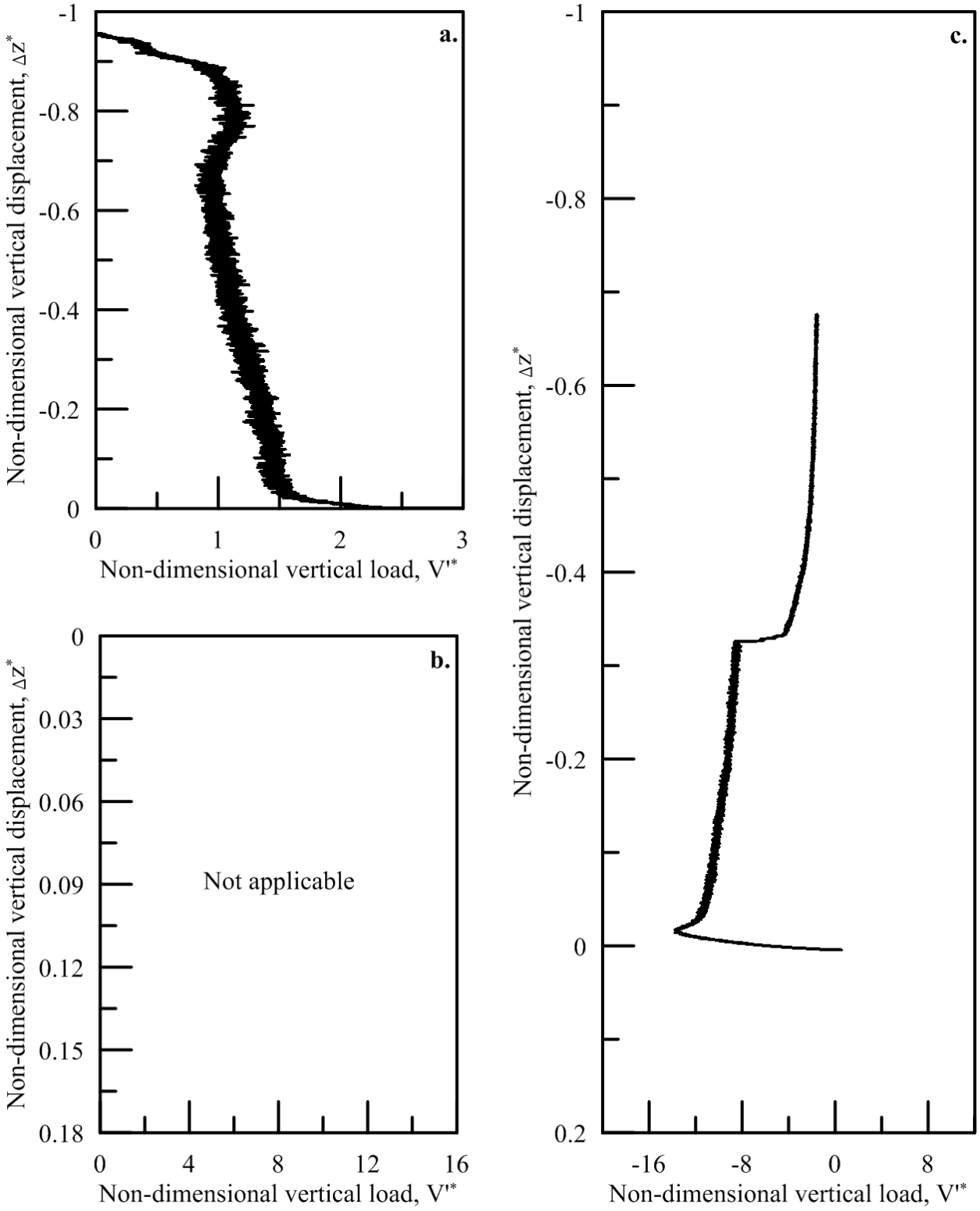

Figure 4.14: Load response of the vertical loading phases of K-1G-AR1-H-Cyc-1 during a. installation, b. monotonic compression, and c. monotonic uplift as applicable

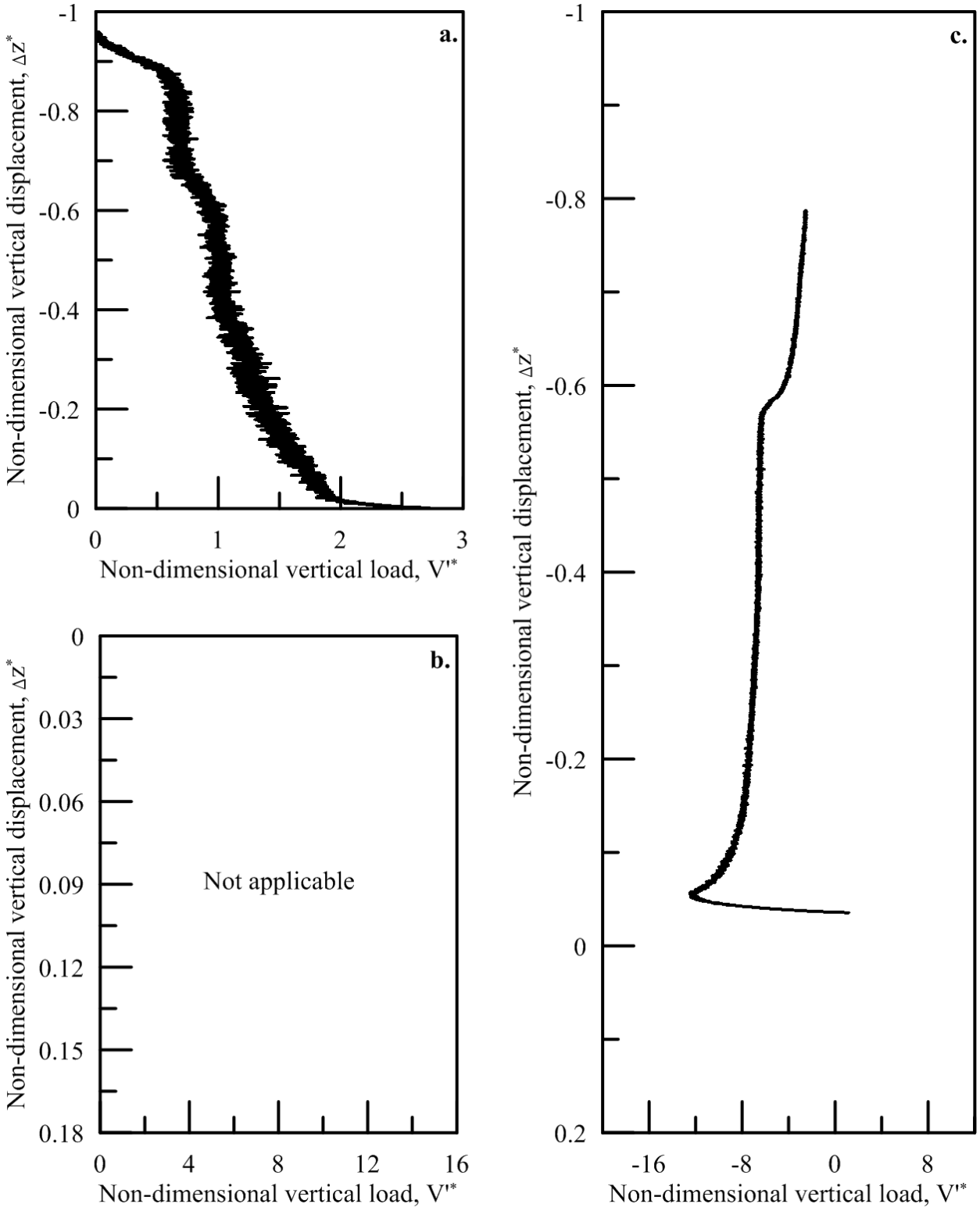

Figure 4.15: Load response of the vertical loading phases of K-1G-AR1-H-Cyc-2 during a. installation, b. monotonic compression, and c. monotonic uplift as applicable

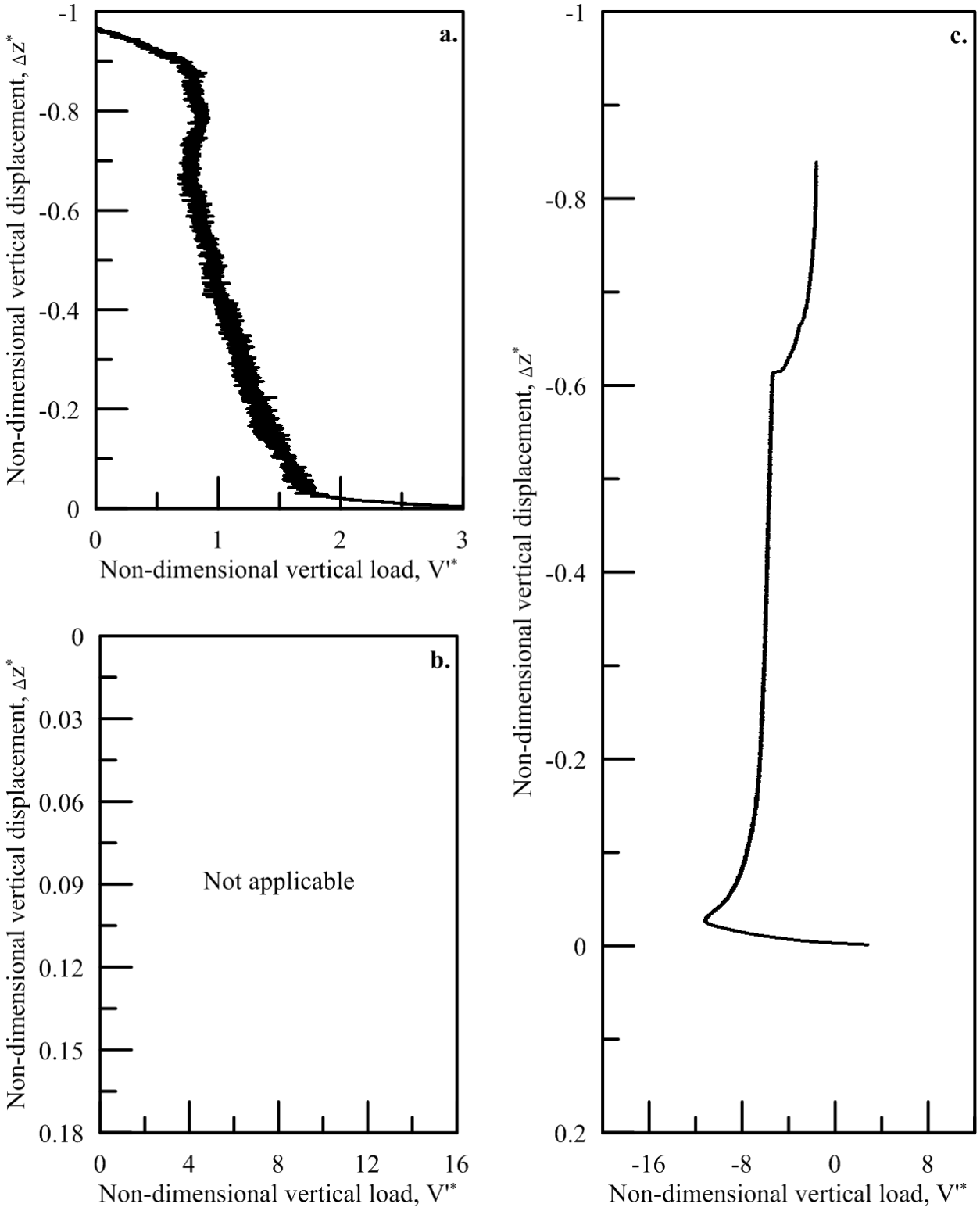

Figure 4.16: Load response of the vertical loading phases of K-1G-AR1-H-Mono-1 during a. installation, b. monotonic compression, and c. monotonic uplift as applicable

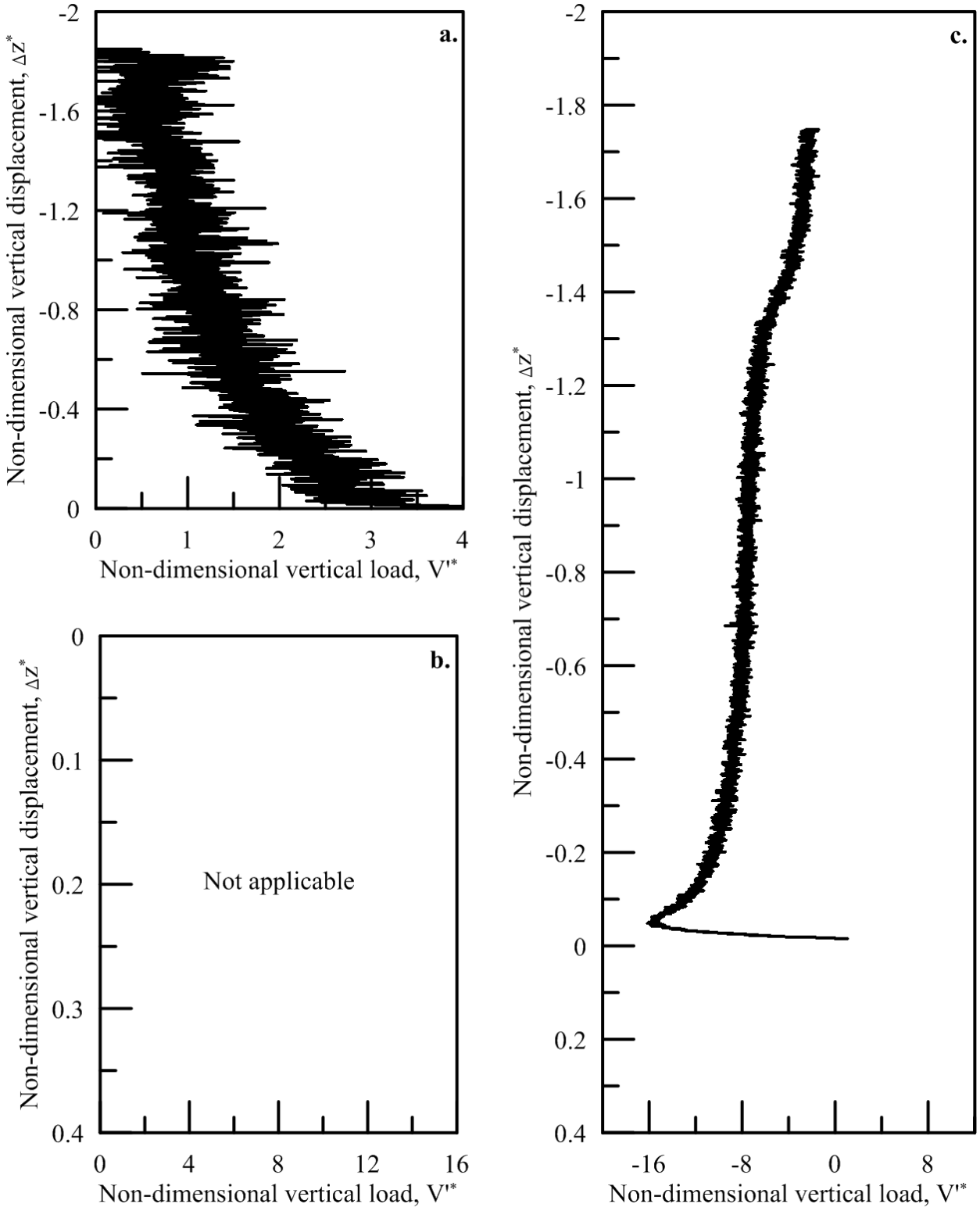

Figure 4.17: Load response of the vertical loading phases of K-1G-AR2-H-Mono-1 during a. installation, b. monotonic compression, and c. monotonic uplift as applicable

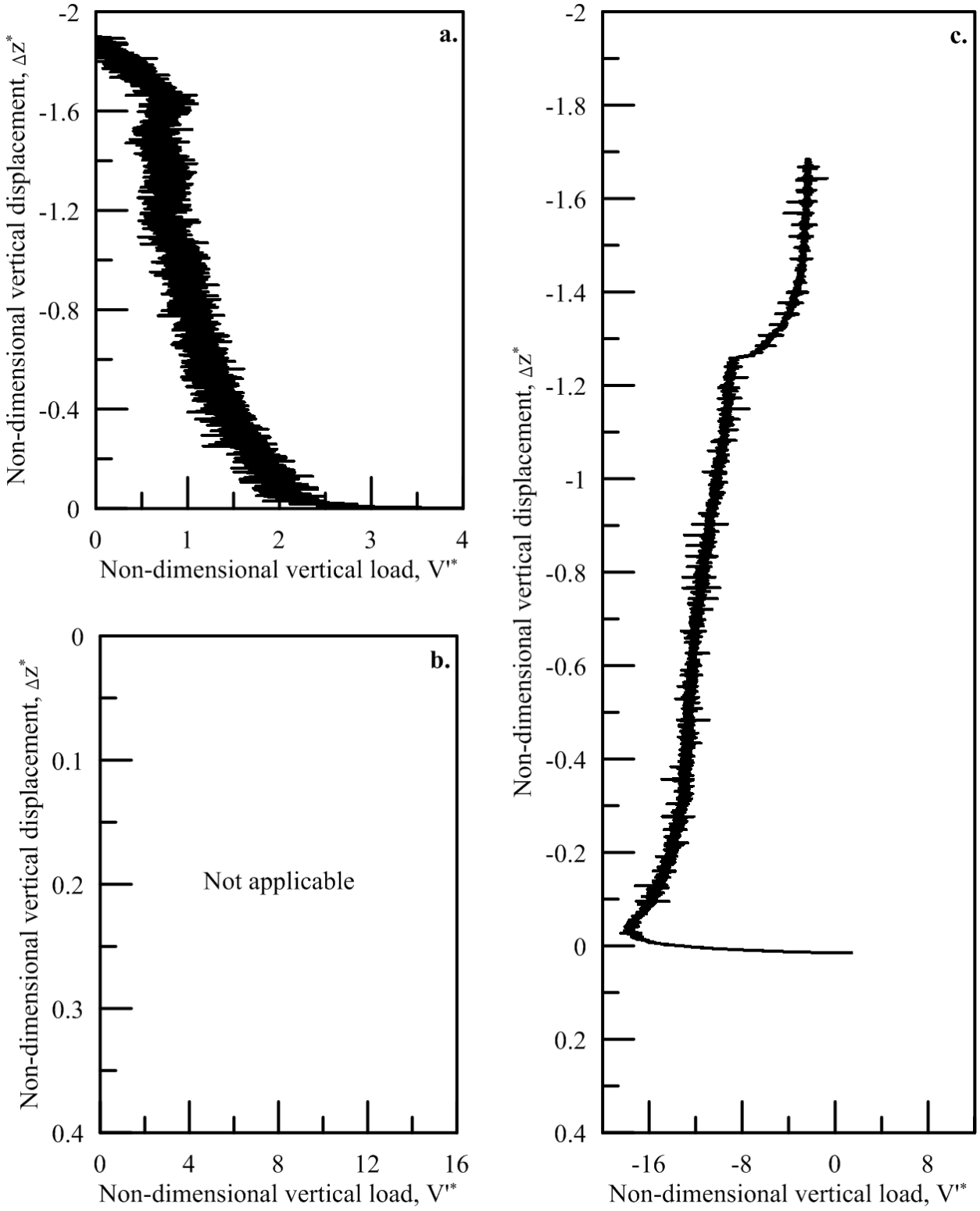

Figure 4.18: Load response of the vertical loading phases of K-1G-AR2-H-Cyc-1 during a. installation, b. monotonic compression, and c. monotonic uplift as applicable

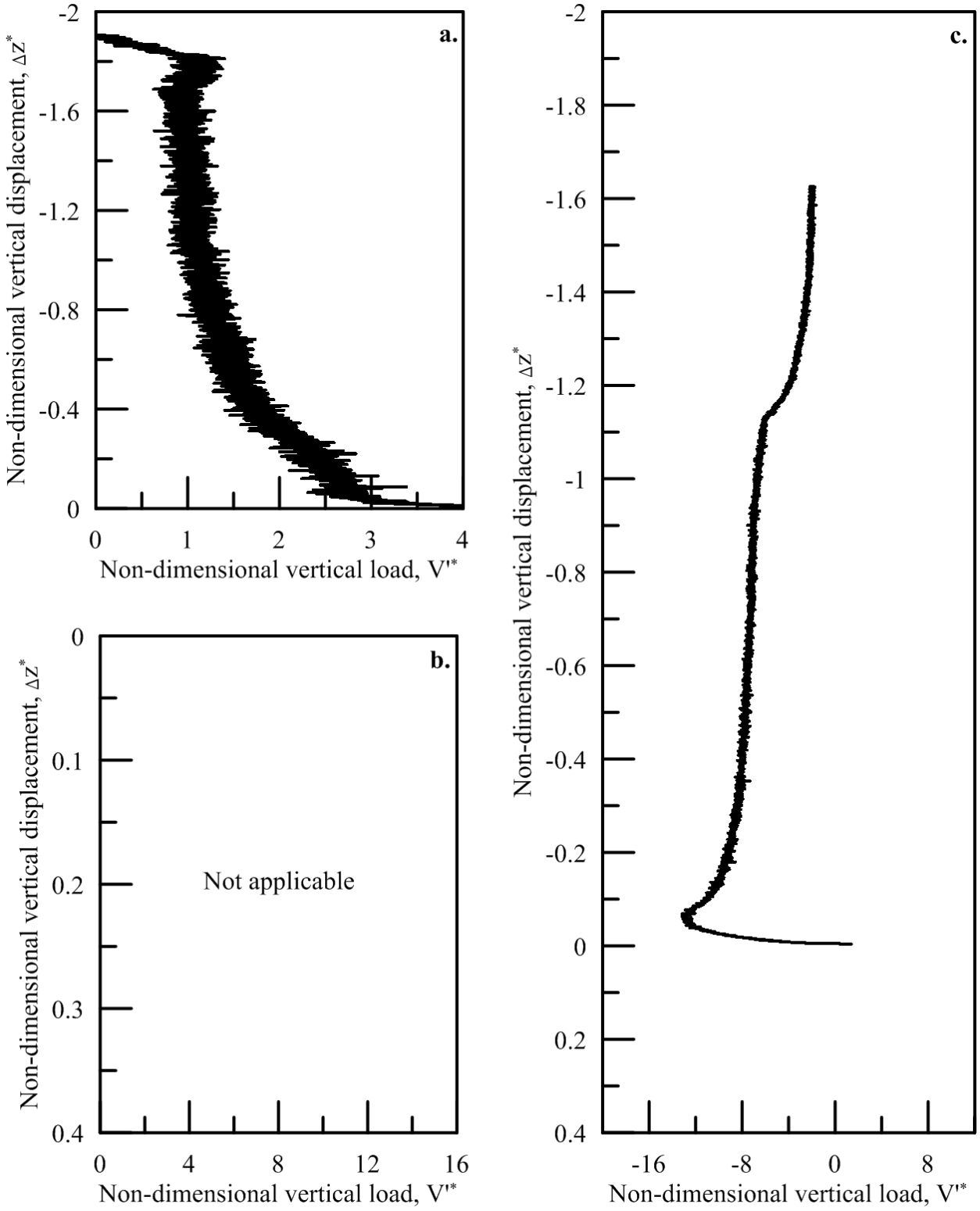

Figure 4.19: Load response of the vertical loading phases of K-1G-AR2-H-Cyc-2 during a. installation, b. monotonic compression, and c. monotonic uplift as applicable

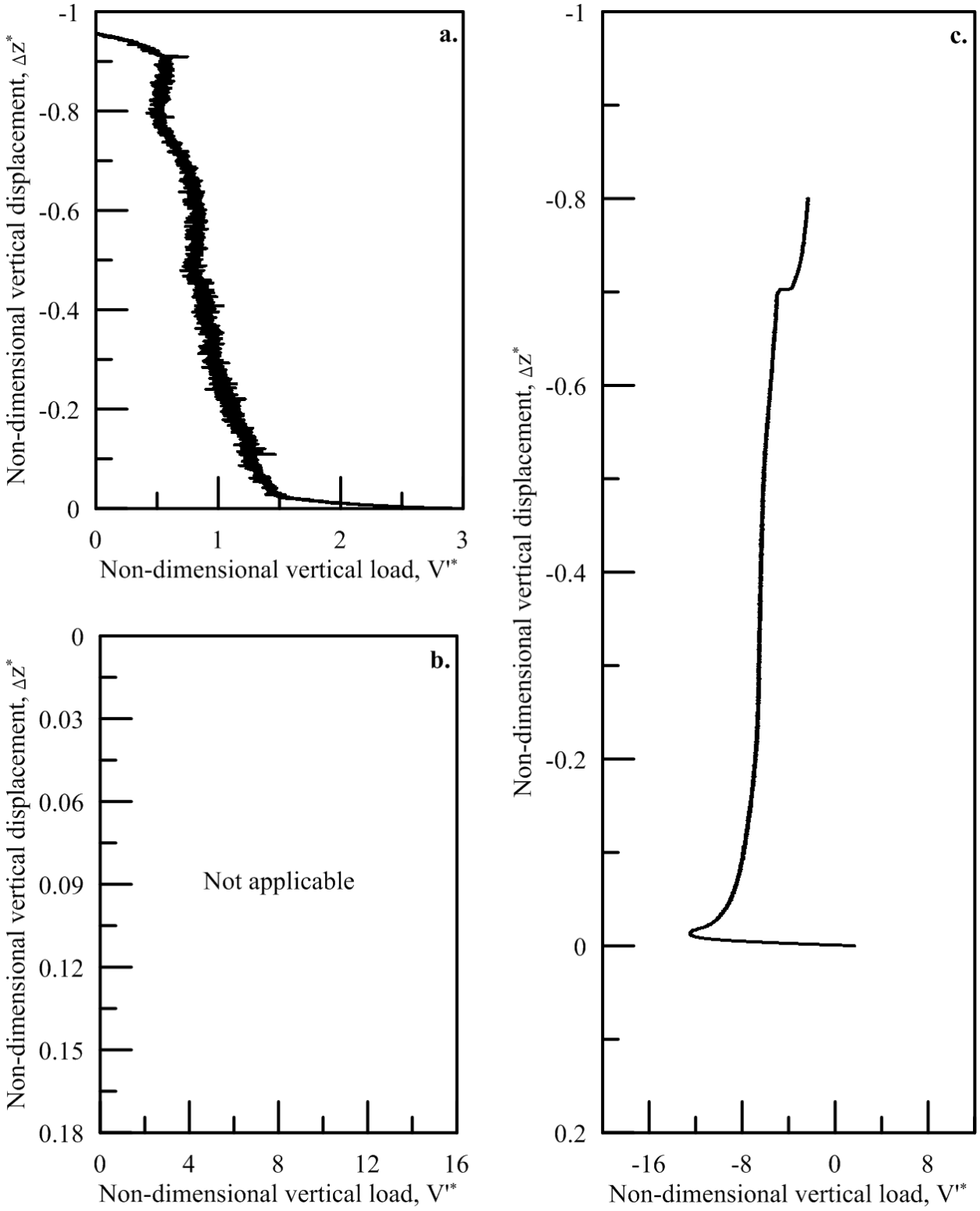

Figure 4.20: Load response of the vertical loading phases of K-1G-AR1-V-Mono-2 during a. installation, b. monotonic compression, and c. monotonic uplift as applicable

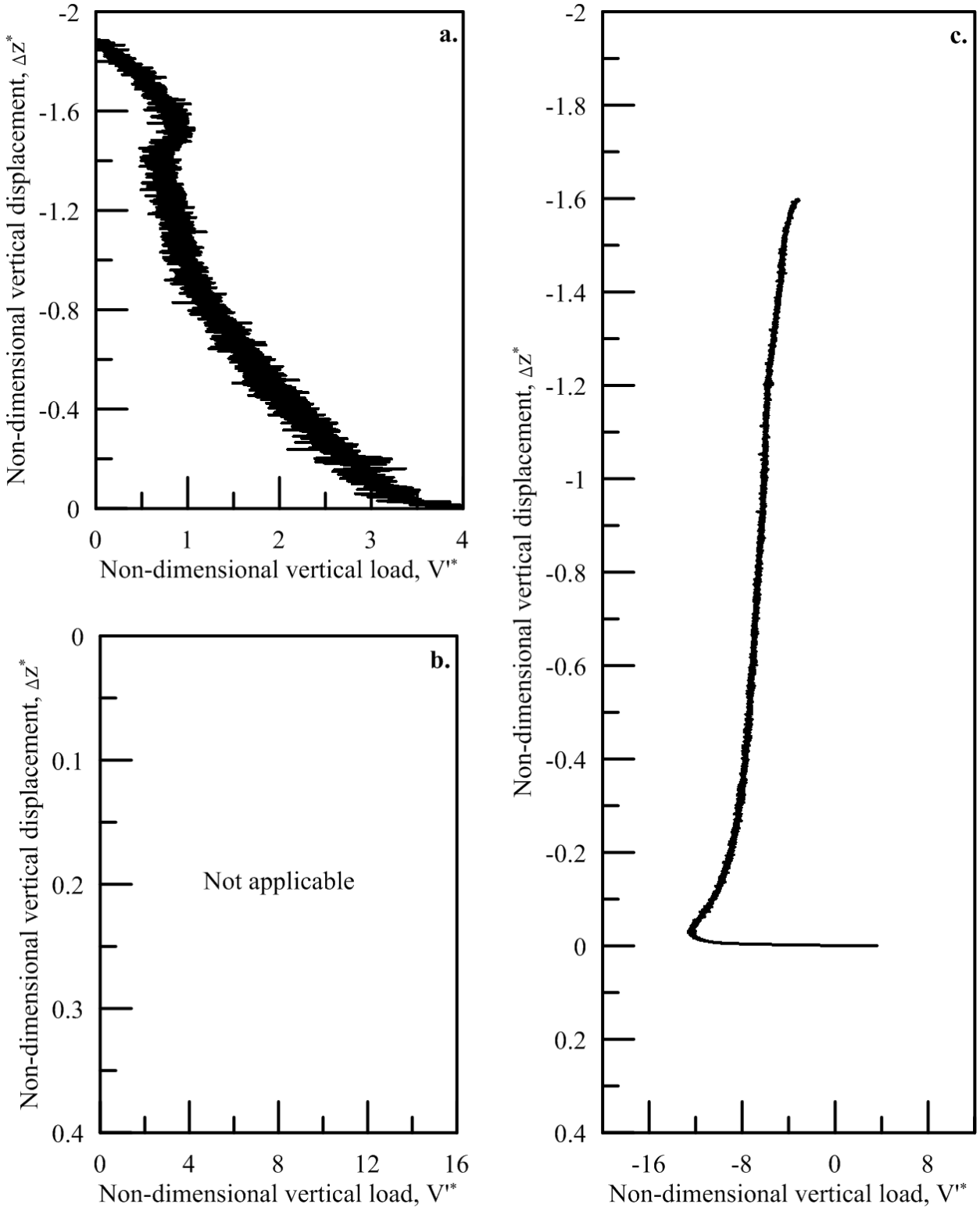

Figure 4.21: Load response of the vertical loading phases of K-1G-AR2-V-Mono-2 during a. installation, b. monotonic compression, and c. monotonic uplift as applicable

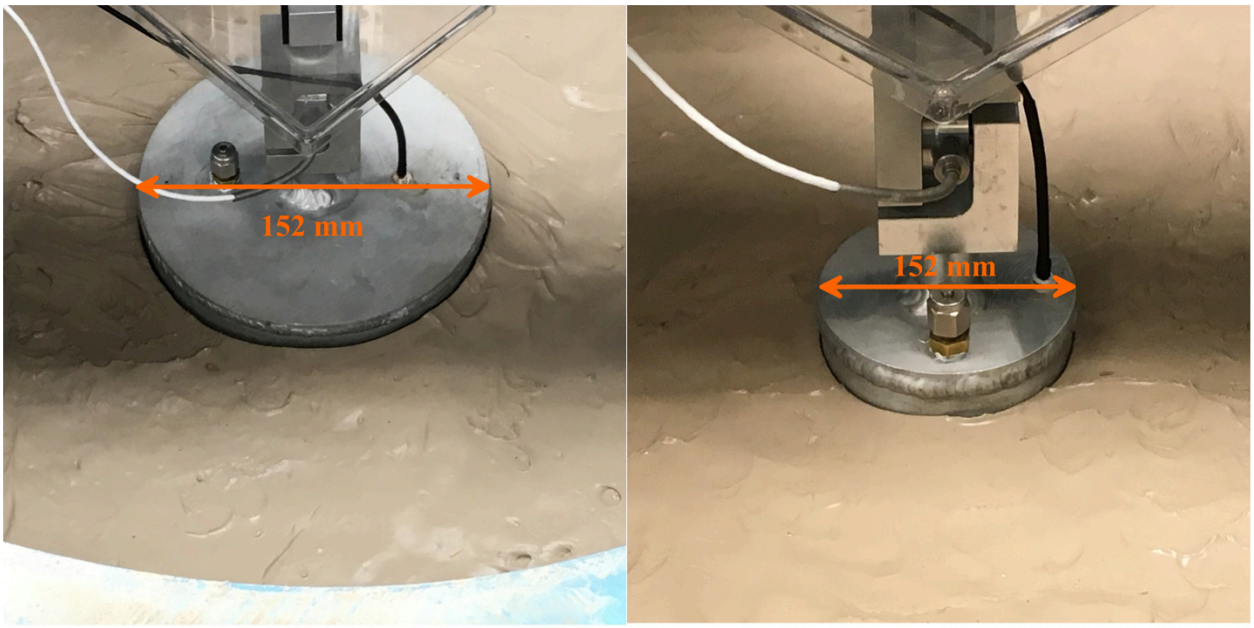

Figure 4.22: Slight gap that formed around K-1G-AR1 (left) and K-1G-AR2 (right) during the installation phase

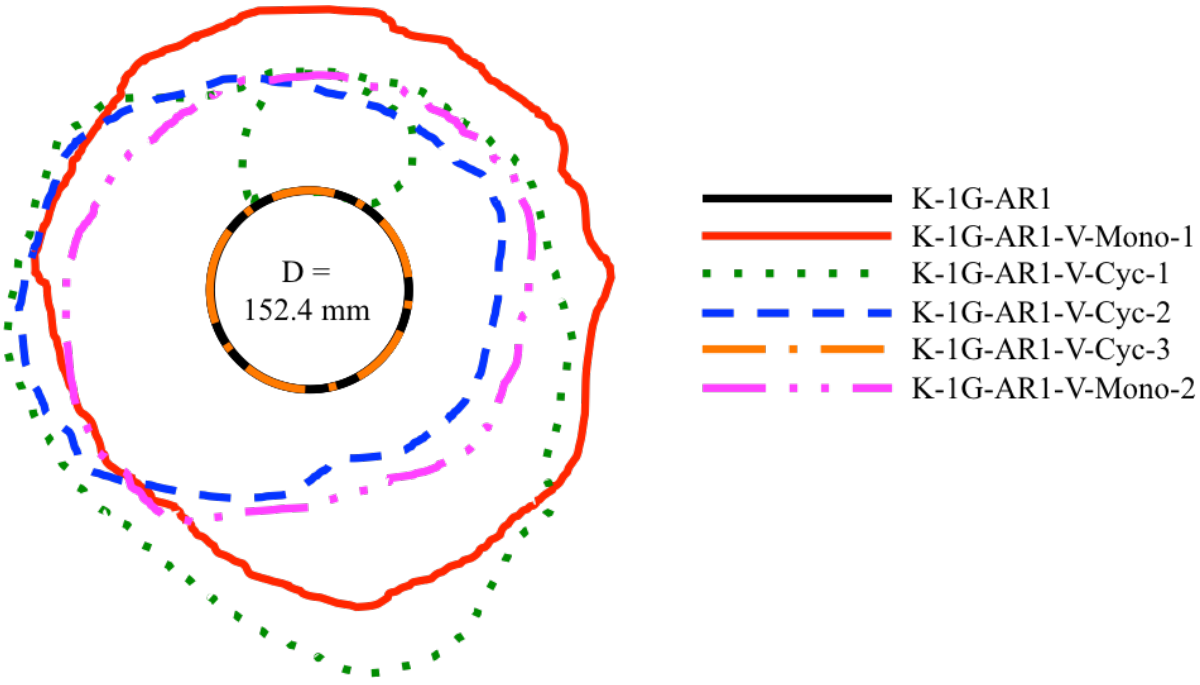

Figure 4.23: Surface scarp outlines post-extraction of the vertical load tests conducted on K-1G-AR1 for various indicated load tests

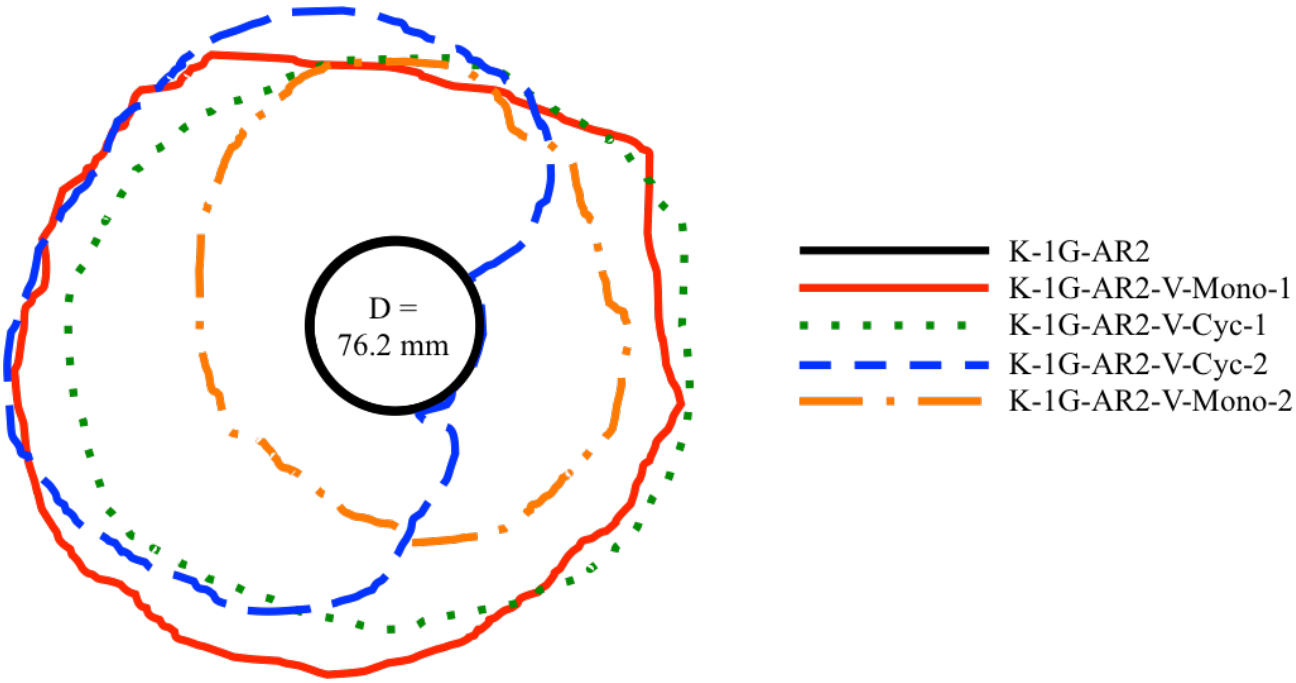

Figure 4.24: Surface scarp outlines post-extraction of the vertical load tests conducted on K-1G-AR2 for various indicated load tests

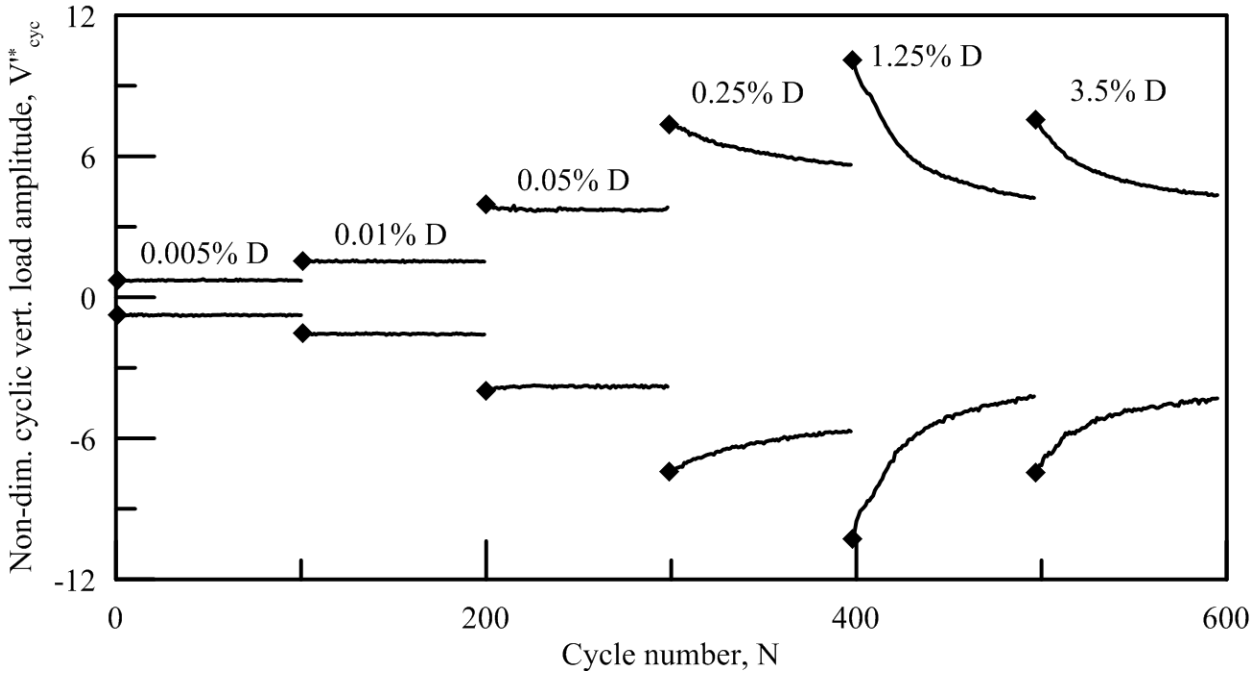

Figure 4.25: Vertical cyclic load amplitude, V'^{*}_{cyc}, versus number of cycles for K-1G-AR1-V-Cyc-2

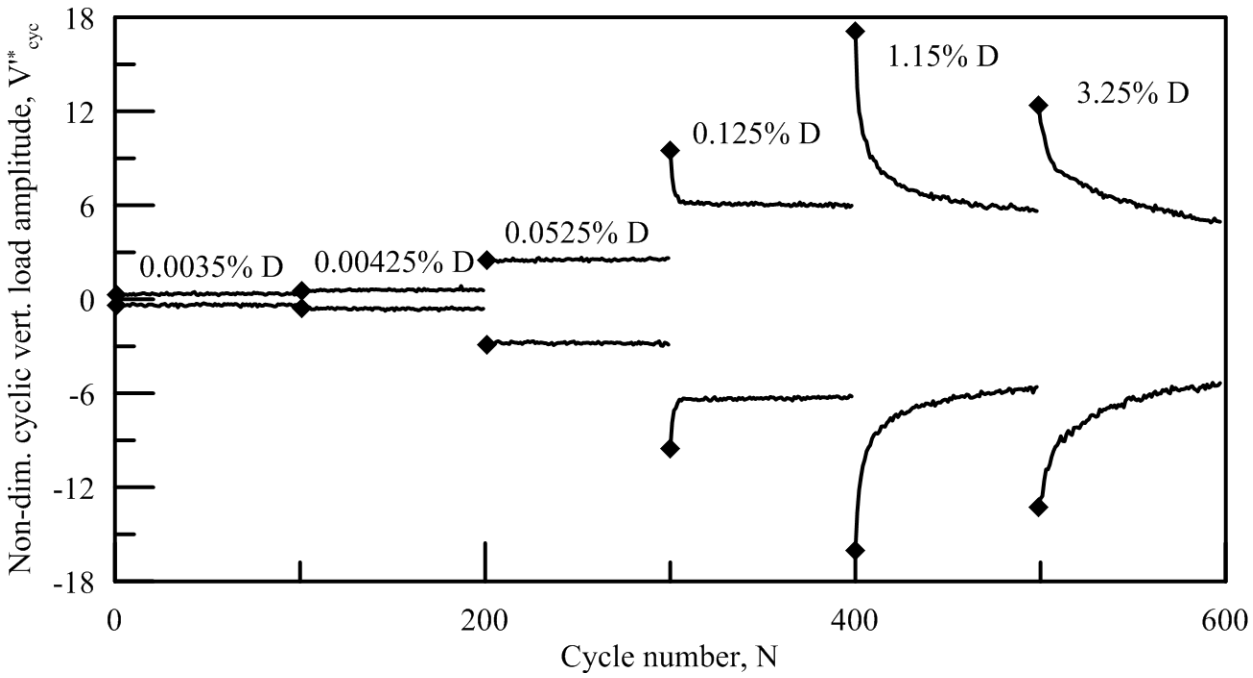

Figure 4.26: Vertical cyclic load amplitude, V'^{*}_{cyc}, versus number of cycles for K-1G-AR2-V-Cyc-2

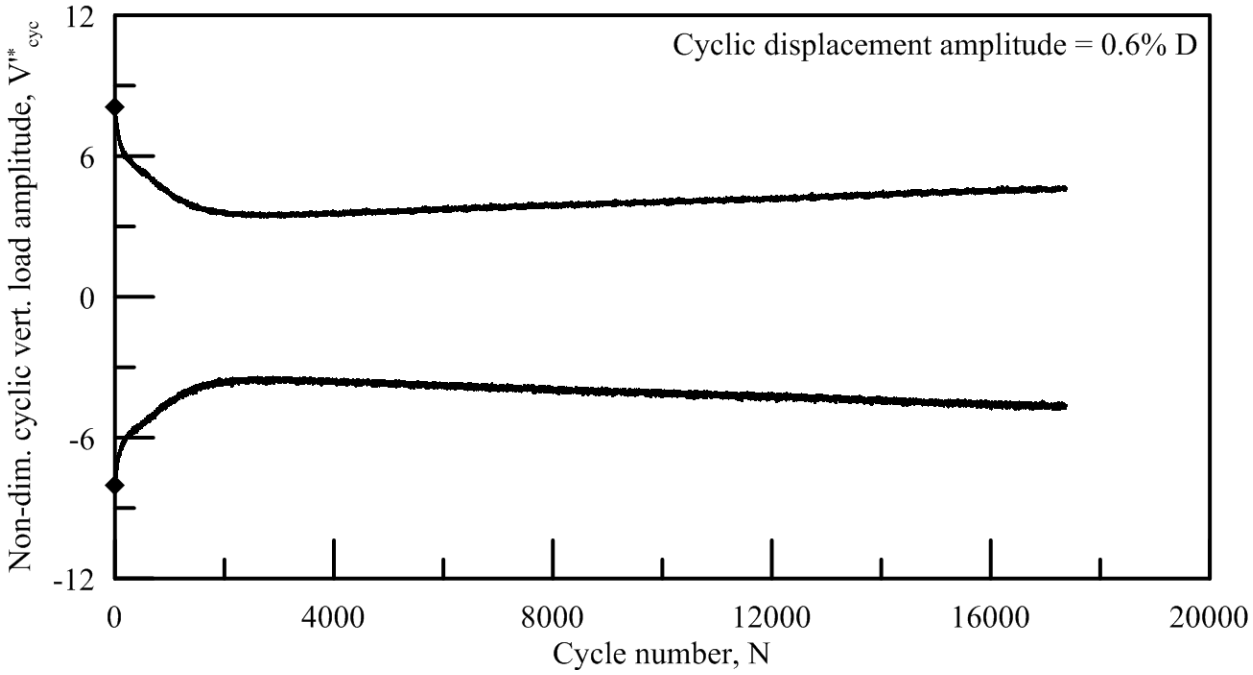

Figure 4.27: Vertical cyclic load amplitude, V'^{*}_{cyc}, versus number of cycles for K-1G-AR1-V-Cyc-1

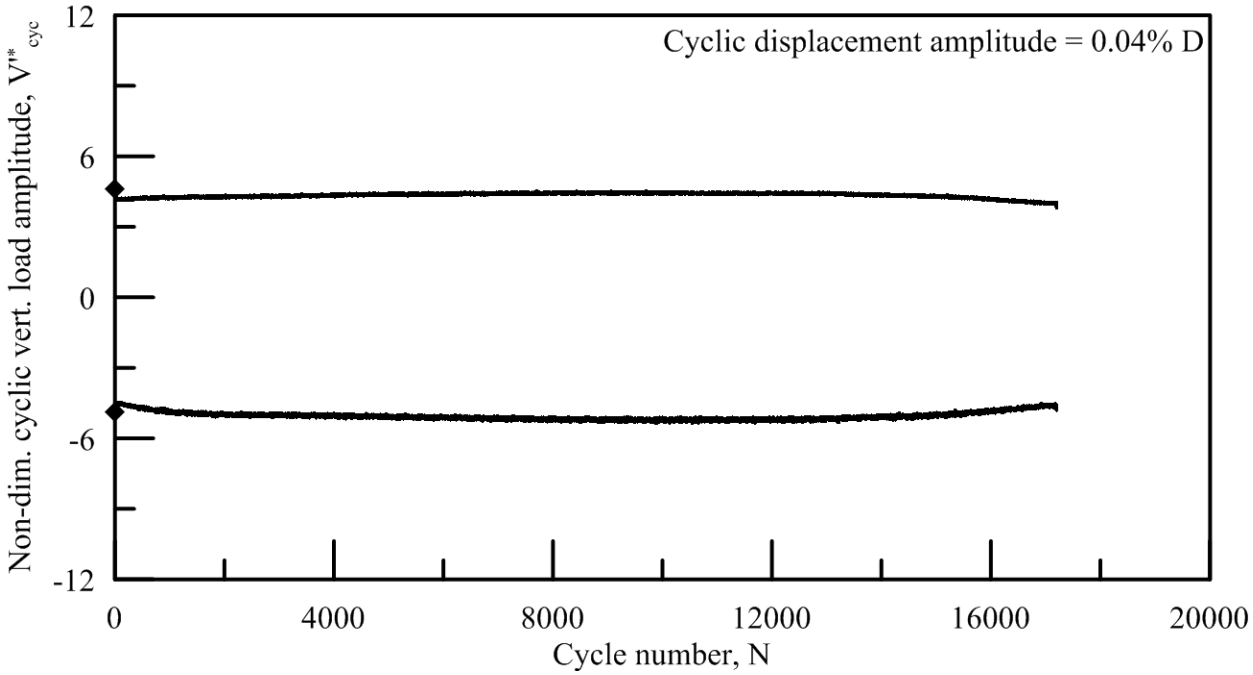

Figure 4.28: Vertical cyclic load amplitude, V'^{*}_{cyc}, versus number of cycles for K-1G-AR1-V-Cyc-3

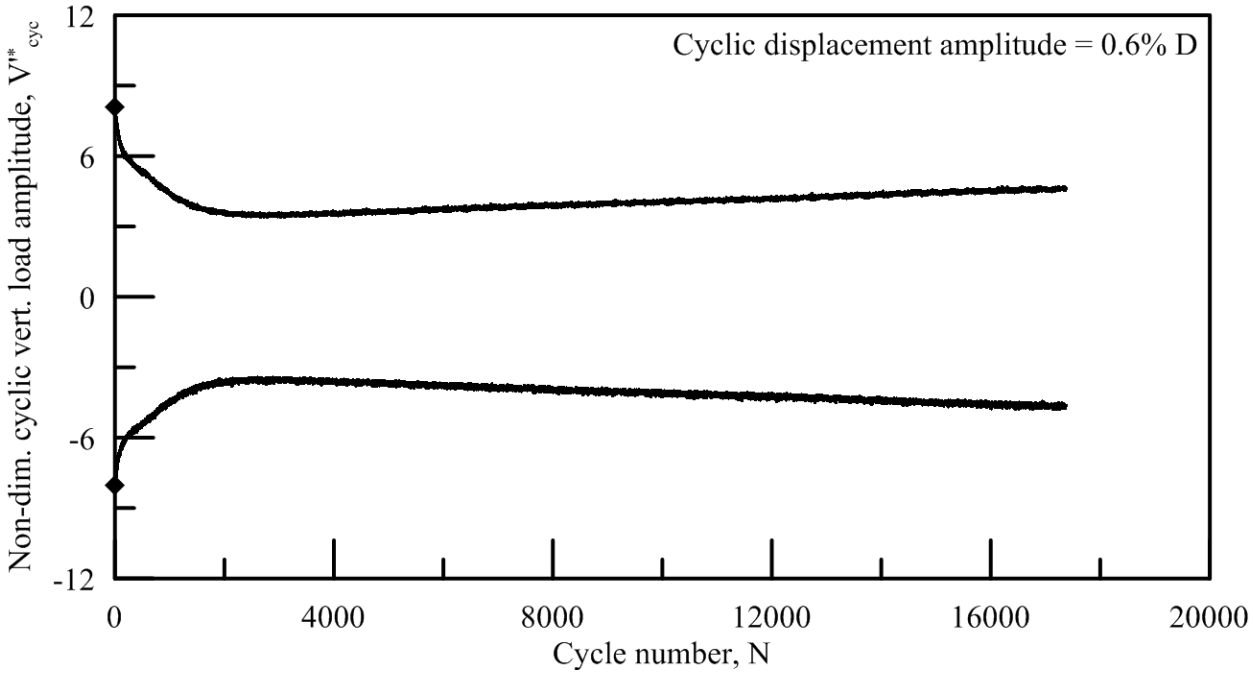

Figure 4.29: Vertical cyclic load amplitude, V'^{*}_{cyc}, versus number of cycles for K-1G-AR2-V-Cyc-1

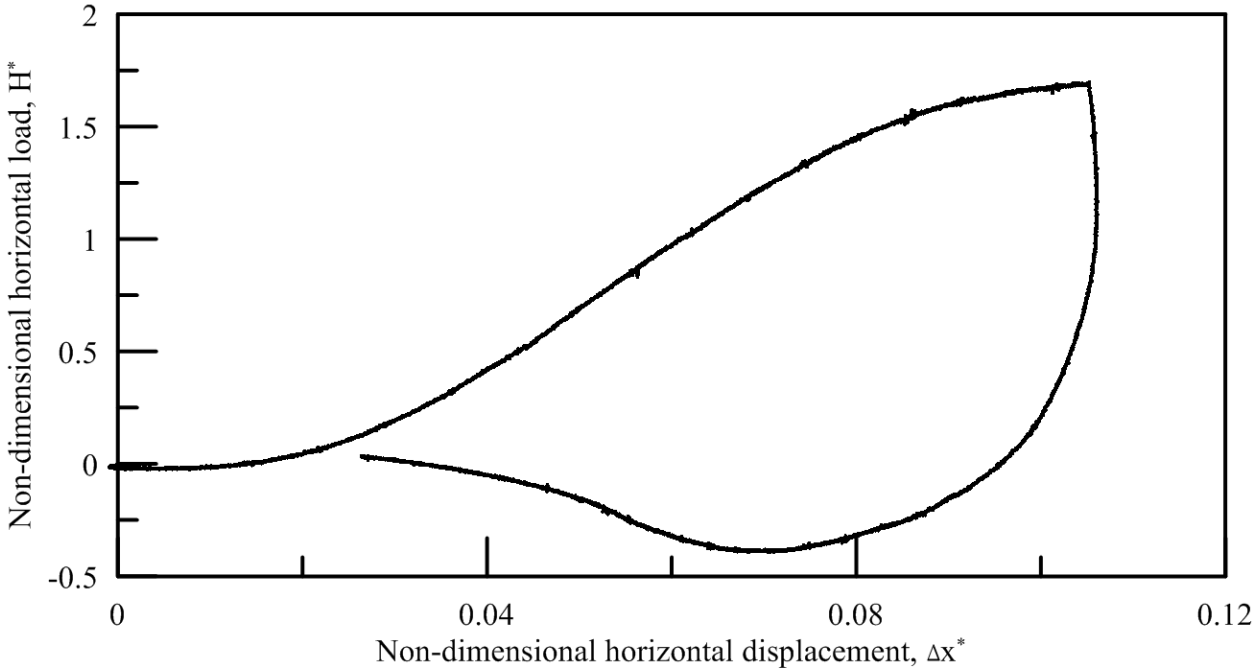

Figure 4.30: Horizontal load response of K-1G-AR1-H-Mono-1

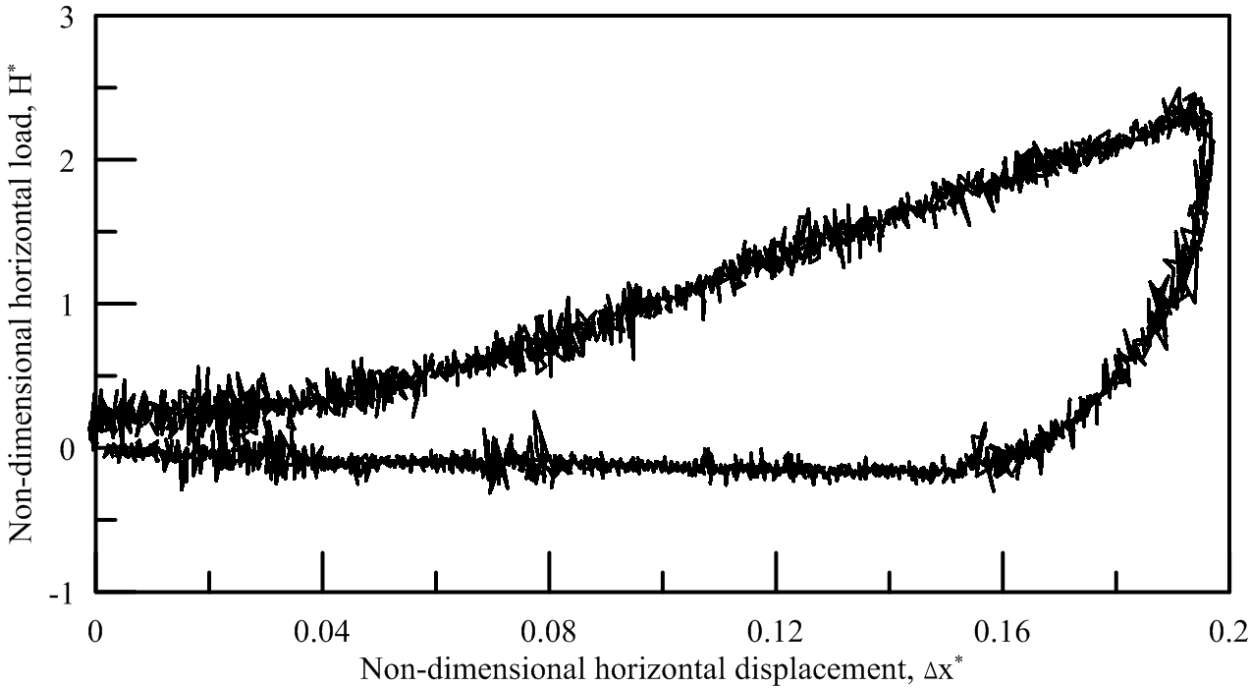

Figure 4.31: Horizontal load response of K-1G-AR2-H-Mono-1

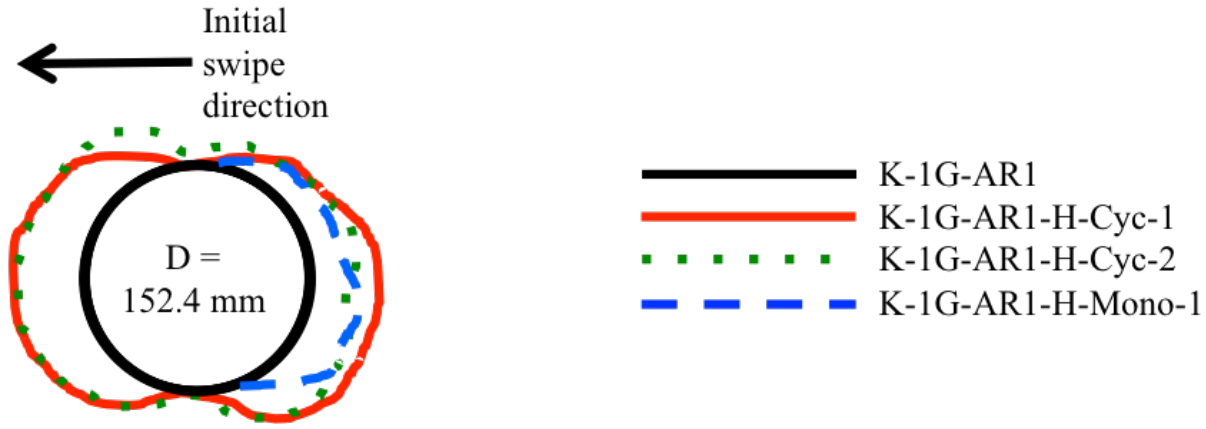

Figure 4.32: Surface scarp outlines after the horizontal loading portions of the horizontal load tests conducted on K-1G-AR1 for various indicated load tests

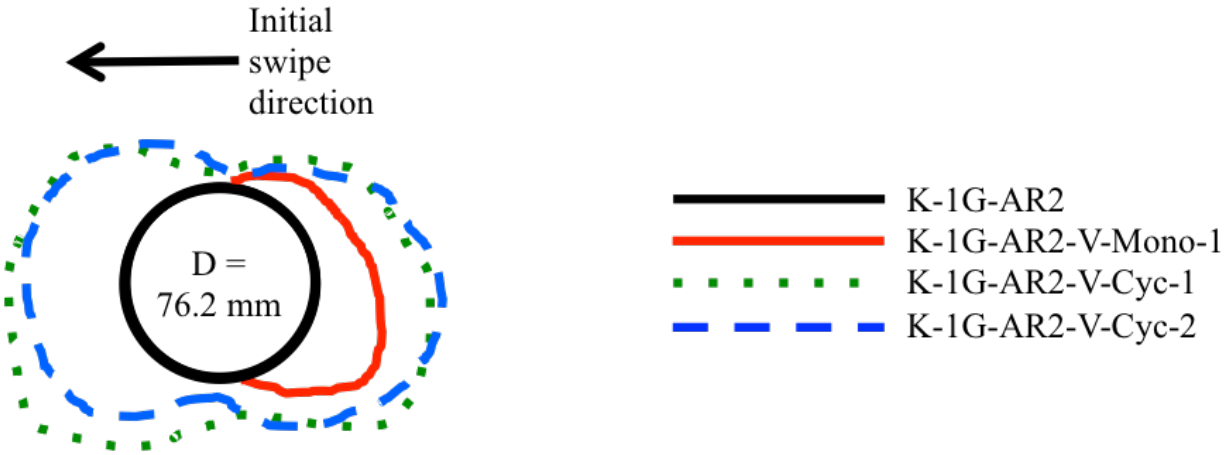

Figure 4.33: Surface scarp outlines after the horizontal loading portions of the horizontal load tests conducted on K-1G-AR2 for various indicated load tests

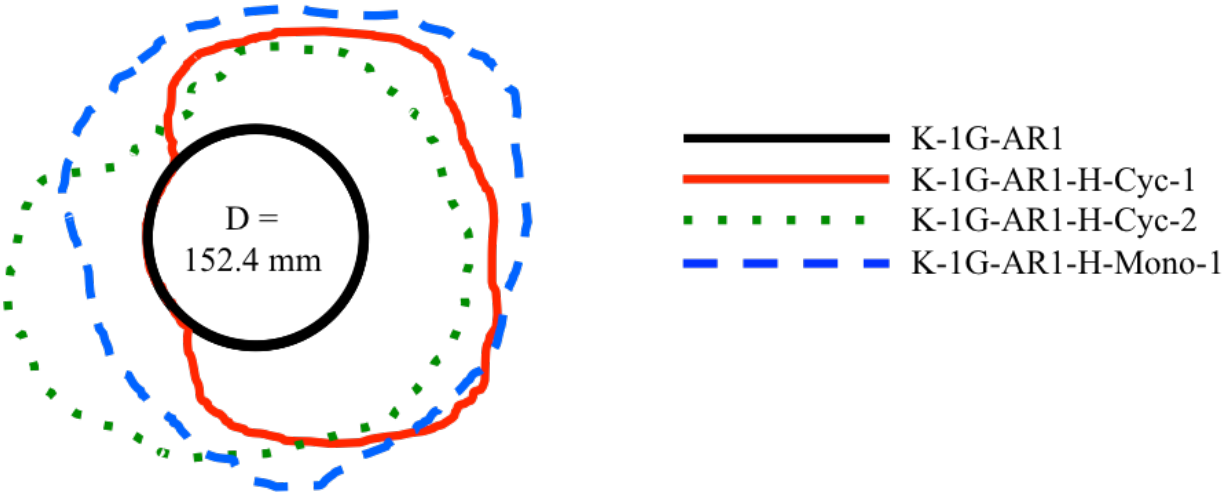

Figure 4.34: Surface scarp outlines post-extraction performed after the horizontal load tests conducted on K-1G-AR1 for various indicated load tests

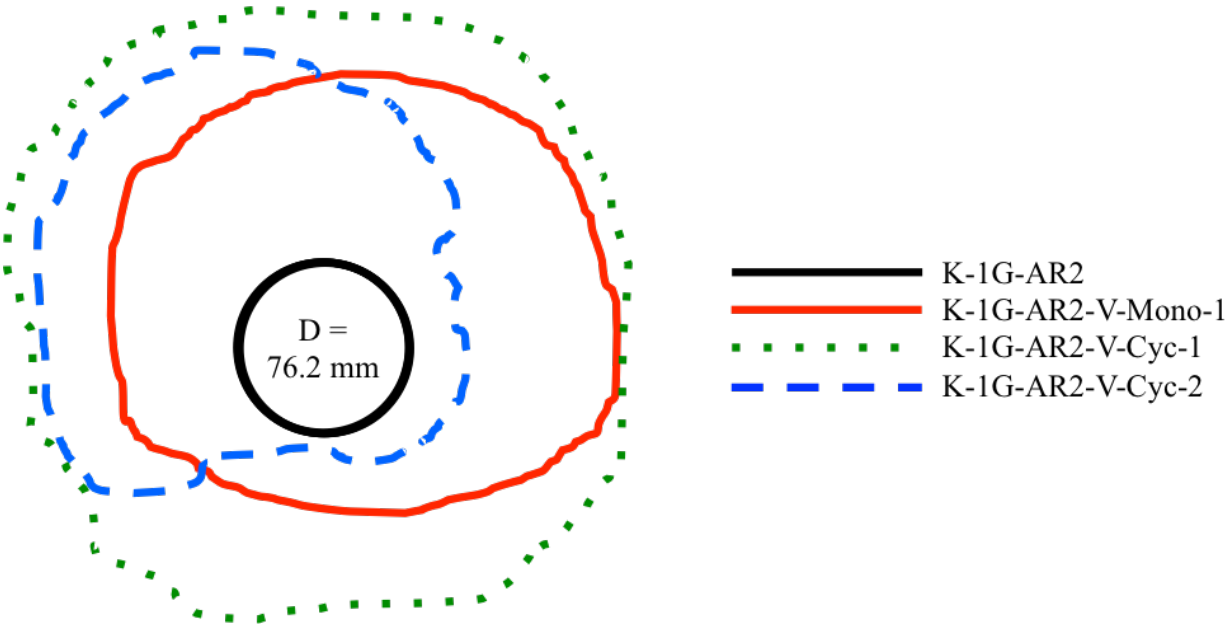

Figure 4.35: Surface scarp outlines post-extraction performed after the horizontal load tests conducted on K-1G-AR1 for various indicated load tests

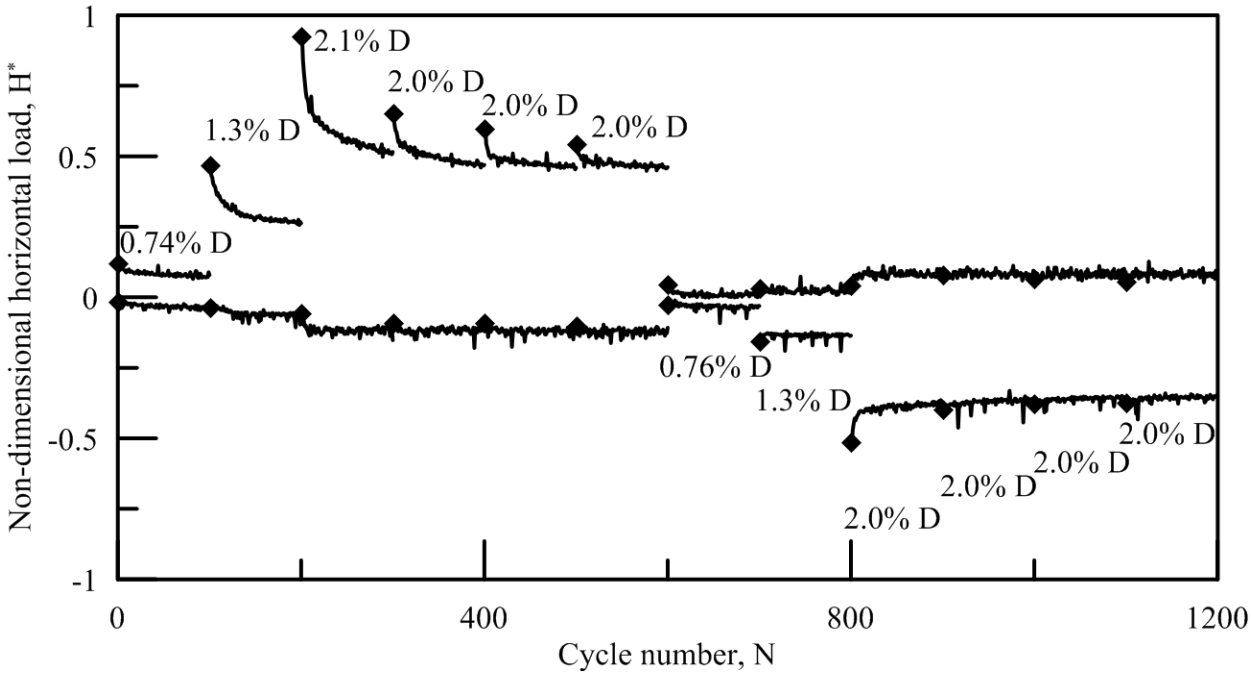

Figure 4.36: Maximum and minimum mobilized horizontal cyclic capacity versus number of cycles for K-1G-AR1-H-Cyc-2

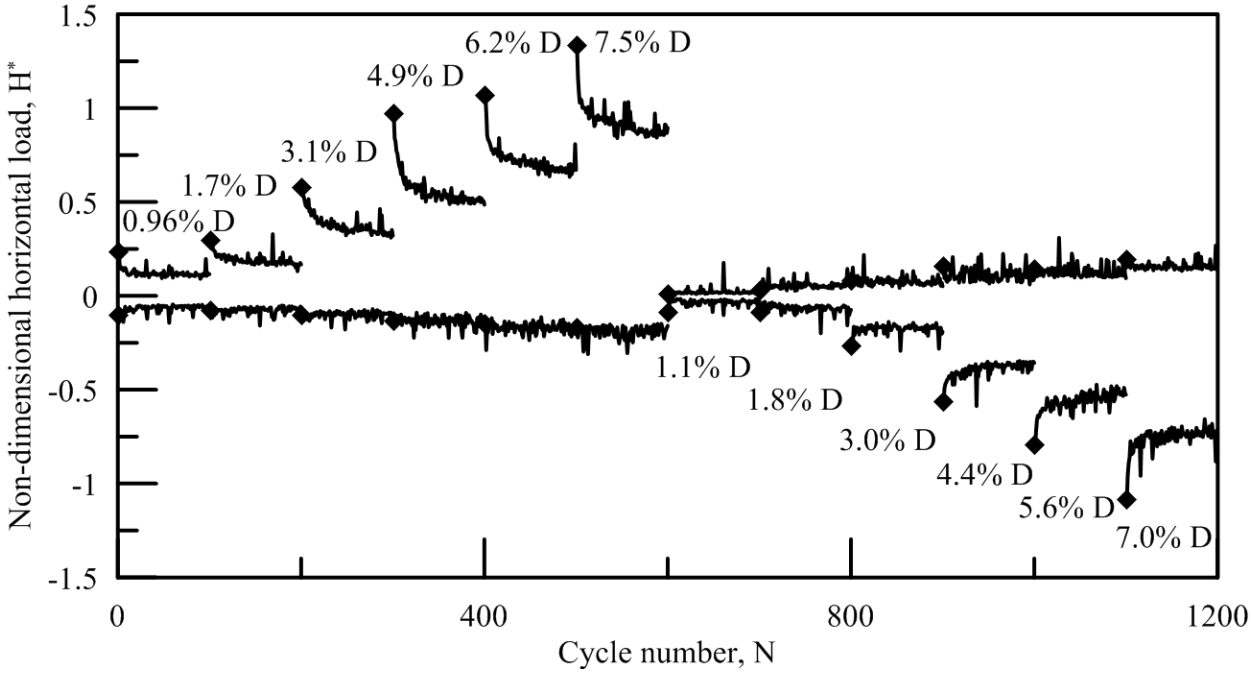

Figure 4.37: Maximum and minimum mobilized horizontal cyclic capacity versus number of cycles for K-1G-AR2-H-Cyc-2

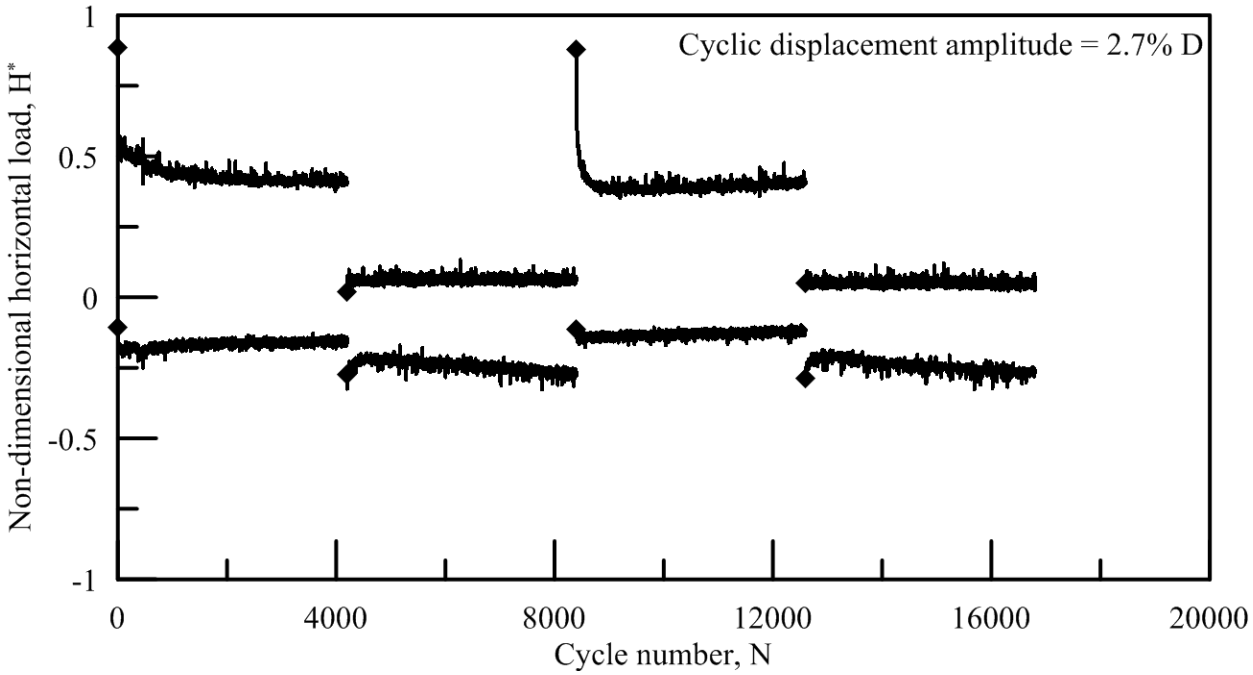

Figure 4.38: Maximum and minimum mobilized horizontal cyclic capacity versus number of cycles for K-1G-AR1-H-Cyc-1

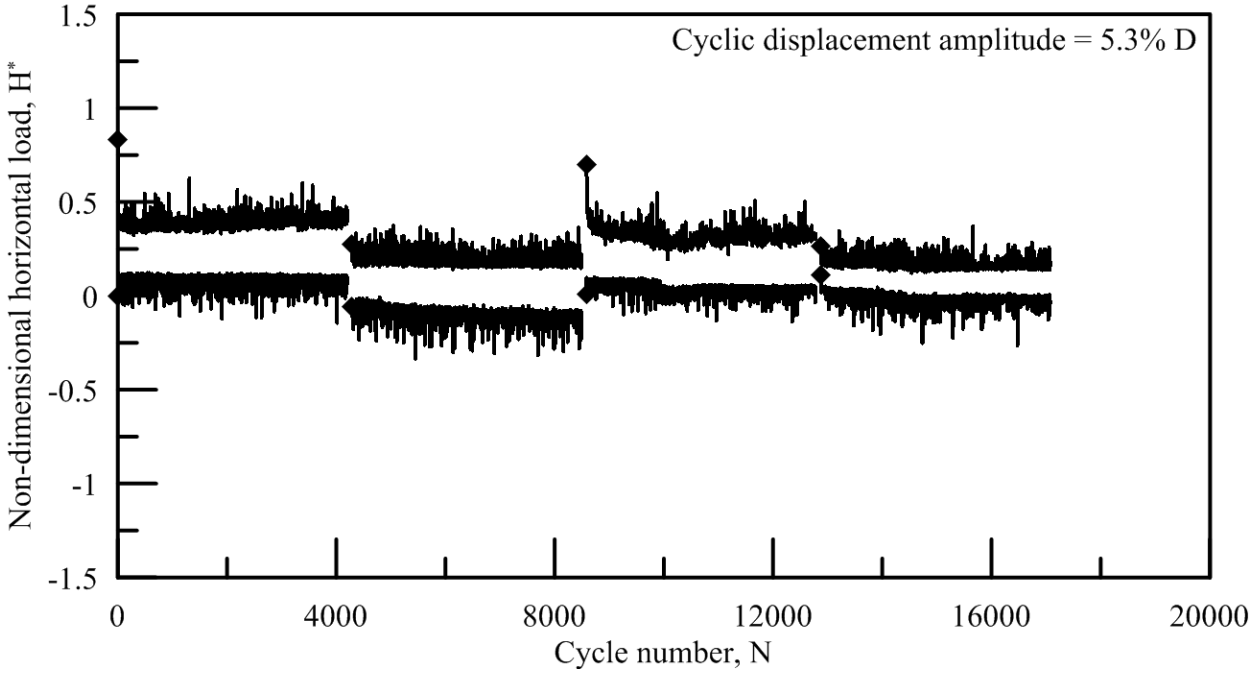

Figure 4.39: Maximum and minimum mobilized horizontal cyclic capacity versus number of cycles for K-1G-AR2-H-Cyc-1

4.8 References

Allersma, H.G.B., Kierstein, A.A. & Maes, D. (2000). "Centrifuge Modelling on Suction Piles Under Cyclic and Long Term Vertical Loading." *Proceedings of the Tenth (2000) International Offshore and Polar Engineering Conference*. Seattle, WA, USA.

API RP 2GEO. (2011). "Geotechnical and Foundation Design Considerations." ANSI/API Recommended Practice 2GEO, First Edition, American Petroleum Institute.

API RP 2SK. (2008). "Design and Analysis of Stationkeeping Systems for Floating Structures." API Recommended Practice 2SK, Third Edition, American Petroleum Institute.

Barari, A. & Ibsen, L.B. (2012). "Undrained Response of Bucket Foundations to Moment Loading." *Applied Ocean Research*. 36(2012):12-21.

Bransby, M.F. & Yun, G.J. (2009). "The Undrained Capacity of Skirted Strip Foundations under Combined Loading." *Geotechnique*. 59(2):115-125.

Byrne, B.W. & Cassidy, M.J. (2002). "Investigating the response of offshore foundations in soft clay soils." *Proceedings of OMAE'02 21st International conference of Offshore Mechanics and Arctic Engineering.* Oslo, Norway.

Chen, C.H. (2013). "Performance of Suction Caissons with a Small Aspect Ratio." Ph.D. thesis, The University of Texas at Austin.

Chen, W. & Randolph, M.F. (2007a). "External radial stress changes and axial capacity for suction caissons in soft clay." *Geotechnique*. 57(6):499-511.

Chen, W. & Randolph, M.F. (2007b). "Uplift Capacity of Suction Caissons under Sustained and Cyclic Loading in Soft Clay." *Journal of Geotechnical and Geoenvironmental Engineering.* 133(11):1352-1363.

Dendani, H. (2003). "Suction Anchors: Some critical aspects for their design and installation in clayey soils." Offshore Technology Conference. Houston, TX, USA.

El-Sherbiny, R. (2005). Performance of Suction Caisson Anchors in Normally Consolidated Clay. Ph.D. Dissertation, The University of Texas at Austin.

Finnie, I.M.S. (1993). "Performance of Shallow Foundations in Calcareous Soil." Ph.D. thesis. University of Western Australia.

Gourvenec, S., Acosta-Martinez, H. & Randolph, M.F. (2007). "Centrifuge Model Testing of Skirted Foundations for Offshore Oil and Gas Facilities." *In* Proc. 6th International

Offshore Sit Investigation and Geotechnics Conference, London, UK, 11-13 September 2007. pp. 479-484.

Gourvenec, S., Acosta-Martinez, H. & Randolph M.F. (2009). "Experimental study of uplift resistance of shallow skirted foundations in clay under transient and sustained concentric loading." *Geotechnique.* 59(6):525-537.

Georgia Tech Research Corporation. (2011). "Assessment of energy Production Potential from Tidal Streams in the United States – Final Project Report." Georgia Tech Research Corporation, Atlanta, GA, USA.

House, A. (2002). "Suction caisson foundations for buoyant offshore facilities." Ph.D. thesis, University of Western Australia.

Hung, L.C. & Kim, S.R. (2012). "Evaluation of Vertical and Horizontal Bearing Capacities of Bucket Foundations in Clay." *Ocean Engineering*. 52(2012):75-82.

Kelly, R.B., Houslby, G.T. & Byrne, B.W. (2006). "A comparison of field and laboratory tests of caisson foundations in sand and clay." *Geotechnique*. 56(9):617-626.

Li, X., Gaudin, C., Tian, Y. & Cassidy, M.J. (2015). :Effects of preloading and consolidation on the uplift capacity of skirted foundations." *Geotechnique*. 65(12):1010-1022.

Luke, A.M., Rauch, A.F. Olson, R.E. & Mecham, E.C. (2005). "Components of suction caisson capacity measured in axial pullout tests." *Ocean Engineering.* 32:878-898.

Mortezaie, A. & Vucetic, M. (2016). "Threshold Shear Strains for Cyclic Degradation and Cyclic Pore Water Pressure Generation in Two Clays." *Journal of Geotechnical and Geoenvironmental Engineering*. 142(5):1-14.

National Oceanic and Atmospheric Administration (2015). "National Oceanic and Atmospheric Administration's National Data Buoy Center." National Oceanic and Atmospheric Administration, Washington D.C., USA. Accessed June 2015.

Skempton, A.W. (1951). "The bearing capacity of clays." *Proceedings, Building Research Congress*. London, UK.

Terzaghi, K.T. (1943). *Theoretical Soil Mechanics.* Wiley and Sons, New York.

Villalobos, F.A. (2006). Model testing of foundations for offshore wind turbines. D.Phil. thesis, University of Oxford.

Villalobos, F.A., Byrne, B.W. & Houlsby, G.T. (2010). "Model testing of suction caissons in clay subjected to vertical loading." *Applied Ocean Research*. 32(2010):414-424.

CHAPTER 5. 90-G MODEL LOAD TESTS IN KAOLIN

5.1 General

A total of eighteen 90-g model load tests were conducted in the kaolin 90-g test beds (Section 3.2) to study the response of suction caissons under both undrained and partially drained loading conditions applicable to tidal current turbine applications. These tests were conducted on two model foundations with aspect ratios of 1 and 2. The types of loading conditions investigated were undrained monotonic vertical at two rates of loading (fast and slow), undrained cyclic vertical, and partially drained cyclic vertical. A brief description of the 90-g model load tests including the test identifier and associated kaolin 90-g test bed is given in Table 5.1.

5.2 Experimental apparatus

5.2.1 Model foundations

Two model suction caissons fabricated from 6061-T6 aluminum were utilized for the 90-g model load tests in kaolin as shown in Figure 5.1. These two foundations were distinguished by their aspect ratios and were identified as K-90G-AR1 and K-1G-AR2. K-90G-AR1 had a model diameter (D) of 38.1 mm, a skirt length (L) of 38.1 mm, and a wall thickness (t_{wall}) of 1.3 mm or prototype dimensions of 3.43 m, 3.43 m, and 0.12 m respectively. These measurements resulted in an aspect ratio of 1 and a diameter to wall thickness ratio of 29. K-90G-AR2 had a model diameter of 38.1 mm, a skirt length of 76.2 mm, and a wall thickness of 1.3 mm or prototype dimensions of 3.43 m, 6.86 m, and 0.12 m respectively. These measurements resulted in an aspect ratio of 2 and a diameter to wall thickness ratio of 29. The diameter to wall thickness ratio of 29 was again higher than typical values of suction caissons, however, they allowed for jacking installation of the foundations and ensured that the response observed during testing was that of the soil rather than the aluminum.

The top cap of both foundations consisted of a 6.4 mm thick aluminum plate with the same diameter as the skirt of the suction caisson. The top cap was welded thoroughly with no gaps to ensure no water could permeate through the connection. A threaded opening was positioned in the top cap to allow for ventilation of the inside of the suction caisson during installation. This threaded opening could be closed to prevent ventilation during any loading phases. A loading rod was positioned in the center of the top cap. One load cell was positioned

along the loading rod in the vertical orientation as shown in Figure 5.2 to measure the vertical loads on the model foundation. The loading rod was fixed directly to the loading mechanism by a rigid threaded connection as shown in Figure 5.2 in order to prevent rotation and maintain the foundation's verticality. Due to the space constraints in the centrifuge, vertical displacements were determined based on the displacement of the motor.

5.2.2 Loading apparatus

The loading apparatus utilized for the 90-g model load tests in kaolin was the prefabricated vertical foundation loading system that was available at the University of Colorado Boulder's 15 g-ton geotechnical centrifuge facility. The apparatus as positioned above the test bed basket is shown in Figure 5.3. The apparatus consisted of a hybrid stepper motor linear actuator with more than sufficient range to install, load, and extract the model foundations. The motor was attached to a platform positioned at the top of the test bed basket. The model foundation and vertical load cell was mounted directly onto the end of the linear actuator. The motor, sensors, and data acquisition system were accessed, controlled, and programmed via a computer positioned outside the protective housing of the 15 g-ton geotechnical centrifuge. The computer was hardwired into the electronic hardware positioned on the centrifuge arms.

5.3 Experimental methodology

One kaolin 90-g model test bed was consolidated for each pair of 90-g model load tests conducted in kaolin. Two model load tests could be conducted in each test bed due to the offset of the positioning of the hybrid stepper motor linear actuator. The offset was 83 mm from the center of the test bed along the centerline of the test bed that was oriented parallel to the facility's floor when the centrifuge was at its operating speeds. After conducting a load test in the first location, the test bed was rotated by 180^{o} to provide access to the second position. The position offset resulted in a minimum distance between the foundations and the container wall of 2.3D. The minimum distance between the load testing locations (skirt wall to skirt wall) was 3.3D. Each of the load tests generally consisted of an installation phase, a system configuration phase, a spin up phase, a loading phase, an extraction phase, and a spin down phase.

5.3.1 Installation

To install the model suction caissons, the foundation was first attached to the hybrid stepper motor linear actuator and positioned over one of the two load test locations within the test bed. With the vent valve open, the foundations were then installed under constant velocities of 0.27 mm/s and 0.30 mm/s for K-90G-AR1 and K-90G-AR2 respectively. Both of these velocities resulted in a non-dimensional velocity of 10 corresponding to undrained conditions based on coefficients of consolidation of 0.036 mm^2/s and 0.040 mm^2/s for the K-90G-AR1 and K-90G-AR2 test beds respectively. The installation phase was terminated when a rapid increase in the penetration resistance was measured by means of the vertical load cell. This indicated that the top cap had made contact with the test bed. After the installation phase was completed, a minimum period of 20 minutes was included to allow for reconfiguration of the loading apparatus and model foundation for the loading phase. The length of the time period was highly dependent on the centrifuge staff engineer and his various commitments at the facility. The installation phase was conducted at 1-g to minimize the amount of spin time on the centrifuge and therefore the cost of facility.

5.3.2 Undrained monotonic loading

Undrained monotonic vertical load tests were conducted to provide an undrained baseline response of the model suction caissons. These tests were conducted with the vent in the top cap closed at two non-dimensional velocities in order to determine the effects of load rate on the capacity of the foundation. The tests will be referred to as “rapid” and “slow” and are described in the following sections. The two velocities were also utilized due to potential unknowns in regards to the non-dimensional velocity in conjunction with the two centrifuge scaling factors in relation to time based on loading and pore pressure dissipation. It was ultimately determined that the non-dimensional velocity does not require significant modification in regards to the difference in scaling of time in regards to loading and pore pressure dissipation.

5.3.2.1 Rapid load tests

The rapid load tests were conducted using the constant velocity method at velocities of 2.78 mm/s and 3.08 mm/s for K-90G-AR1 and K-90G-AR2 respectively. The velocity was determined at the foundation reference point that was defined as the center of the bottom side of the top cap that made contact with the soil surface. These velocities correspond to non-

dimensional velocities of 3000 for both foundations and therefore undrained loading conditions. A total of four baseline rapid undrained load tests were conducted as listed in Table 5.1. The four tests provided the baseline undrained monotonic deformation response and capacity both in compression and in uplift for K-90G-AR1 and K-90G-AR2 under rapid loading conditions. The baseline rapid test in monotonic compression on each foundation was followed by monotonic rapid uplift until extraction. While only four rapid undrained load tests were conducted that were solely monotonic, there were monotonic rapid undrained loading phases in all sixteen of the 90-g load tests in kaolin. Similar to the 1-g load tests in kaolin, these post-cyclic rapid monotonic load tests served three purposes as outlined in Section 4.3.3.

5.3.2.2 Slow load tests

The slow load tests were conducted using the constant velocity method at velocities of 0.010 mm/s and 0.011 mm/s for K-90G-AR1 and K-90G-AR2 respectively. The velocity was determined at the foundation reference point that was defined as the center of the bottom side of the top cap that made contact with the soil surface. These velocities corresponded to non-dimensional velocities of 11 and therefore just above the threshold of undrained loading conditions. A total of four baseline tests were conducted as listed in Table 5.1. The four tests provided the baseline monotonic deformation response and capacity both in compression and in uplift for K-90G-AR1 and K-90G-AR2 at slow velocities still in the undrained loading range. The baseline slow undrained load test in monotonic compression on each foundation was followed by monotonic slow uplift and then monotonic rapid uplift until extraction.

5.3.3 Undrained and partially drained cyclic vertical loading

The undrained and partially drained cyclic vertical loading was applied to the suction caisson models by means of displacement-controlled sinusoids due to controller limitations at the CU Boulder 15 g-ton geotechnical centrifuge facilities and reasons outlined in Section 4.3.4. The sinusoids were applied so that the mean displacement was the position at which the installation phase was terminated and with compression as the first loading direction. The prototype periods of sinusoidal cycling varied depending on the load test as indicated in Table 5.1. These prototype periods were 15 minutes and 10.8 hours. These periods were chosen as they both represented relevant loading periods to tidal current turbines described in Section 2.2 while taking advantage of the scaling of time on the geotechnical centrifuge. The 15 minute prototype period coincides

with storm wave periods (Munk 1950) and the 10.8 hour prototype period coincides approximately with semi-diurnal tidal current direction reversal. The discrepancy between the 10.8 hour loading period and the true semi-diurnal tidal period was due to a discrepancy of the facility's spin calculation point (100-g) and the reference point at the base of the model foundation (approximately 90-g).

Two general types of cyclic load tests were conducted at 90-g in kaolin as described in Table 5.1. The first type consisted of applying 14 constant displacement amplitude cycles with a prototype cyclic period of 10.8 hours. The four tests of this time were conducted at constant cyclic displacement amplitudes of 0.46% of the diameter (K-90G-AR1-V-Cyc-1), 0.21% of the diameter (K-90G-AR1-V-Cyc-2), 2.5% of the diameter (K-90G-AR2-V-Cyc-1), and 0.60% of the diameter (K-90G-AR2-V-Cyc-2). The second type consisted of six or seven 30-cycle packets with prototype cyclic periods of 15 minutes. The displacement amplitude was increased with each successive packet. The four tests of this type were conducted at cyclic displacement amplitudes of 0.0072%, 0.025%, 0.074%, 0.25%, 0.74%, and 2.5% of the diameter (K-1G-AR1-V-Cyc-3), 0.0049%, 0.010%, 0.049%, 0.099%, 0.49%, 0.99%, and 5.0% of the diameter (K-1G-AR1-V-Cyc-4), 0.0073%, 0.025%, 0.074%, 0.25%, 0.75%, and 2.5% of the diameter (K-1G-AR2-V-Cyc-3), and 0.0049%, 0.010%, 0.050%, 0.099%, 0.49%, 0.98%, and 4.9% of the diameter (K-1G-AR2-V-Cyc-4). A minimum prototype period of 20 minutes was included between each packet to allow for recalibration of the control program. The period was highly dependent on the lag and processing speed of the data acquisition system at any given time.

5.3.4 Extraction

As referenced in previous sections within this chapter, the extraction of the model suction caissons was combined with an uplift load test. The complete extractions of the foundations were conducted monotonically at a constant non-dimensional velocity of 3000 similar to the rapid undrained load tests. For the baseline slow undrained monotonic uplift load tests conducted at a constant non-dimensional velocity of 11, sufficient displacement was allowed to occur in order to visualize the failure mechanism generated by the foundation loading before switching to the rapid load rate. The complete extractions of the foundations were always conducted at the rapid rate for time and cost efficiency of utilizing the geotechnical centrifuge.

5.4 Experimental results

5.4.1 Non-dimensionalization of undrained and partially drained results

All results of the model load tests conducted for this study were converted to non-dimensional units to allow for comparison between the models and for future application to prototype or field scale behavior prediction. Similar to the undrained non-dimensionalization described in Section 4.4.1, the 90-g load test results were non-dimensionalized using the same undrained equations presented by Kelly et al. (2006). While Kelly et al. (2006) only presented non-dimensionalization equations for undrained or drained loading conditions, it was assumed that due to the generation of pore water pressures that the undrained equations would be more applicable. The load response of the displacement-controlled cycling was separated into positive cyclic amplitude and negative cyclic amplitude component for each cycle as defined in Figure 5.5. For the vertical loading, compression was defined as positive and uplift was defined as negative. These were the same sign convention as for the monotonic load tests.

5.4.2 Installation penetration resistance

The non-dimensional penetration resistances during the installation phases of all the 90-g model load tests conducted in kaolin are shown in Figure 5.6 through Figure 5.21 as labeled. The non-dimensional load required to install the foundations ranged from 1.8 to 2.6 and 2.8 to 3.5 for K-90G-AR1 and K-90G-AR2 respectively. Using these values, the α for the foundations was back-calculated based on the design recommendations for penetration resistance from API RP 2SK (2008) described in Section 2.3.1.1. The back-calculated α values were 0.16 to 0.31 and 0.17 to 0.23 for K-90G-AR1 and K-90G-AR2 respectively. These values overlap with the ranges for the K-1G-AR1 and K-1G-AR2 foundations or 0.14 to 0.26 and 0.22 to 0.30 respectively.

These back-calculated values were less than 52% of the design recommendation from API RP 2SK (2008) based on the inverse of sensitivity (0.59 based on the average measured sensitivity of the 90-g kaolin test beds). This lower trend was similar to those from the 1-g load tests conducted in kaolin described in Section 4.3.2 and those reported by Dendani (2003) based on field measurements of suction caissons in clay. Again, the lower back-calculated α was most likely due to the failure surface occurring between the soil and the structure. While the use of the inverse of sensitivity accounts for the remolding of the soil, it does not account for any reduction of the unit side resistance due to the adhesion mechanism. This type of reduction of the adhesion

mechanism cannot readily be accounted for with sensitivity alone, as it is an indicator of clay-clay interface strength. The very little to no clay remaining attached to the model foundations after extraction described later in Section 5.3.4 supports the soil-structure interface failure mechanism. A soil-soil interface would have resulted in a layer of clay left attached to the foundation upon extraction.

5.4.3 Baseline rapid undrained vertical monotonic response

5.4.3.1 Compression followed by uplift (rapid)

The undrained load responses of the baseline rapid vertical monotonic load tests in compression on K-90G-AR1 and K-90G-AR2 are shown in Figure 5.8 and Figure 5.6 respectively. These tests both displayed a strain-hardening behavior with resistance continuing to increase with increasing strain. The two tests did show decreasing resistance towards the end of the monotonic load test, however this was due to the motor's functionality. As the motor approached the end of its programmed target displacement, the motor decreased its velocity gradually to zero rather than a sudden step resulting in a reduction in resistance. The non-dimensional ultimate compression capacities of 9.5 and 11.1 mobilized after non-dimensional vertical displacements of 0.14 and 0.14 for K-90G-AR1 and K90G-AR2 respectively. The back-calculated N_c values corresponding to these ultimate capacities based on API RP 2GEO (2011) design equations and α values back calculated during installation (Section 5.4.2) were 11.0 for K-90G-AR1 and 12.5 for K-90G-AR2. The API design recommendation of utilizing Skempton (1951) suggests N_c values of 7.6 and 8.4 for K-90G-AR1 and K-90G-AR2 respectively. The back-calculated values were both higher than the recommended values. All back-calculated N_c values fell within the range of values reported by previous studies by El-Sherbiny (2005) and Luke et al. (2005) for suction caissons in clay (6 to 16). The back-calculated N_c values reported above of 11.0 and 12.5 for the 90-g load tests were 14% to 25% lower than those back-calculated from their 1-g load test counterparts of 14.6 and 14.6.

The undrained load responses of the uplift load tests to extraction that followed the baseline vertical monotonic load tests in compression on K-90G-AR1 and K-90G-AR2 are shown in Figure 5.8 and Figure 5.6 respectively. K-90G-AR1-Mono-1 exhibited strain-hardening behavior throughout the extraction process until plug detachment occurred. K-90G-AR2-Mono-1 exhibited a very slight strain-softening behavior over the course of the large amount of uplift

displacement. Byrne and Cassidy (2002) and Gourvenec et al. (2009) observed similar load responses. The non-dimensional peak uplift capacity of -8.0 and -9.4 were mobilized after non-dimensional vertical displacements of 0.85 and 0.69 for K-90G-AR1 and K-90G-AR2 respectively. For both tests, a plug was retained in the model suction caissons during testing as was evidenced by the plug detachment load-response during extraction. The detachment of the plugs from the clay test beds was marked by a rapid decrease in uplift resistance. Due to the lower mobilized resistance in the uplift that followed the compression phase, it was likely that the prior compression mobilized resistance along the same or similar mechanism.

5.4.3.2 Uplift only (rapid)

The undrained load responses of the baseline vertical monotonic rapid load tests in uplift on K-90G-AR1 and K-90G-AR2 are shown in Figure 5.14 and Figure 5.16 respectively. Overall, these tests displayed a strain-hardening behavior similar to the 90-g kaolin monotonic undrained compression tests described in Section 4.4.3.2. K-90G-AR2-Mono-3 exhibited a small segment where the resistance leveled off with increasing displacement prior to increasing again. The non-dimensional ultimate uplift capacities of -8.5 and -13.6 for K-90G-AR1 and K-90G-AR2 respectively were within 11% to 23% of the 90-g kaolin non-dimensional ultimate compression capacities. These ultimate capacities were mobilized after non-dimensional vertical uplift displacements of 0.67 and 1.4 for K-90G-AR1 and K-90G-AR2 respectively and plug detachment occurred soon after. Due to the strain-hardening behavior of both the compression and uplift load response of the 90-g model foundations, a similar non-dimensional displacement to mobilize the ultimate uplift capacity was unlikely. The back-calculated N_c values based on these ultimate capacities, API RP 2GEO (2011) design equations, and α values back calculated during installation (Section 5.4.2) were 9.8 and 15.5 for K-90G-AR1 and K-90G-AR2 respectively. These values accounted for the weight of the clay within the suction caisson as contributing to the resistance as the plug was retained upon extraction. As they were in the 90-g baseline compression load tests, these values were higher than the recommended design values from Skempton and API. The N_c values back-calculated using both assumptions fall between values reported in previous studies by El-Sherbiny (2005) and Luke et al. (2005) for suction caissons in clay (6 to 16). The back-calculated N_c values reported above of 9.8 and 15.5 for the 90-g load tests were 25% lower to 40% higher than those back-calculated from their 1-g load test

counterparts of 13.1 and 11.7. For both tests, a plug was retained in the model suction caissons during testing as was evidenced by the plug detachment load-response during extraction. The detachment of the plugs from the clay test beds was marked by a rapid decrease in uplift resistance.

5.4.4 Baseline slow undrained vertical monotonic response

5.4.4.1 Compression followed by uplift (slow)

The undrained load responses of the baseline slow vertical monotonic load tests in compression on K-90G-AR1 and K-90G-AR2 are shown in Figure 5.9 and Figure 5.7 respectively. These tests both displayed a strain-hardening behavior with resistance continuing to increase with increasing strain. The non-dimensional ultimate compression capacities of 6.9 were mobilized after non-dimensional vertical displacements of 0.15 for both K-90G-AR1-Mono-2 and K90G-AR2-Mono-2. The back-calculated N_c values corresponding to these ultimate capacities based on API RP 2GEO (2011) design equations and α values back calculated during installation (Section 5.4.2) were 7.8 for K-90G-AR1 and 7.2 for K-90G-AR2. The API design recommendation of utilizing Skempton (1951) results in N_c values of 7.6 and 8.4 for K-90G-AR1 and K-90G-AR2 respectively. The back-calculated value for K-90G-AR1 was very similar to the Skempton (1951) recommended value of 7.6 while the back-calculated value for K-90G-AR2 was slightly lower than the recommended value of 8.4. These back-calculated values do not follow the same trend of significantly larger back-calculated N_c values from the rapid undrained monotonic tests conducted at 90-g in kaolin or the undrained monotonic tests conducted at 1-g in kaolin. However, these values do still fall within the range of values reported by previous studies by El-Sherbiny (2005) and Luke et al. (2005) for suction caissons in clay (6 to 16). The primary reason for the lower back-calculated N_c values was the lower mobilized resistance of the foundation. This lower mobilized resistance was likely a result of three items both related to the foundation velocity during loading. The first being the effect of rate of loading (time to failure) of the clay corresponding to a 7% increase in undrained shear strength for each tenfold increase in the rate of loading (Mesri 2001). In this case, this would correspond to a 14% decrease in the mobilized undrained strength and the corresponding capacity. This 14% decrease alone however does not fully account for the difference in the trend. The second item potentially contributing to the lower resistance was the potential for partially drained loading due to how close the

foundation velocity was to the undrained-partially drained threshold. Evidence of this second item was apparent during the uplift load test that followed compression that will be discussed in the next paragraph. The third item was that the loading lasted for a sufficient amount of time that compression (primary or secondary) occurred over the course of the time period.

The undrained load responses of the uplift load tests that followed the baseline vertical monotonic load tests in compression both at the slow loading rate on K-90G-AR1 and K-90G-AR2 are shown in Figure 5.9 and Figure 5.7 respectively. K-90G-AR1-Mono-2 exhibited strain-hardening behavior throughout the uplift loading with a non-dimensional peak uplift capacity of -2.5 mobilized after displacement of 0.20. K-90G-AR2-Mono-2 exhibited strain-softening behavior with a minimum non-dimensional capacity of 0.49 after a displacement of 0.052. This indicates that the capacity did not transition into the uplift mechanism. This was likely due to the potential for partially drained loading conditions due to the non-dimensional velocity having been near the threshold of undrained-partially drained behavior. Not developing fully undrained pore pressure generation resulted in the lack of suction within the caisson that would cause the plug to move in unison with the foundation and mobilize tip resistance across the entire diameter of the foundation.

After the slow undrained monotonic uplift load test, the model foundations were extracted at the rapid velocity until fully extracted. The load responses of these load tests on K-90G-AR1 and K-90G-AR2 are shown in Figure 5.9 and Figure 5.7 respectively. For K-90G-AR1-Mono-2, the behavior was strain-hardening throughout the extraction process until plug detachment occurred. For K-90G-AR2-Mono-2, the load response exhibited a very slight strain-softening behavior over the course of the large amount of uplift displacement similar to previous results reported by Byrne and Cassidy (2002) and Gourvenec et al. (2009). The non-dimensional peak uplift capacities of -8.3 and -8.8 were mobilized after non-dimensional vertical displacements of 0.66 and 0.75 for K-90G-AR1 and K-90G-AR2 respectively. These capacities were significantly greater than that of the slow monotonic undrained load tests conducted prior to the rapid uplift to extraction. This indicated that the uplift capacity was largely contingent on the development of negative pore water pressures developing in the suction caisson cavity during undrained loading. For both tests, a plug was retained in the model suction caissons during testing as was evidenced by the plug detachment load-response during extraction. The

detachment of the plugs from the clay test beds was marked by a rapid decrease in uplift resistance.

5.4.4.2 Uplift only (slow)

The undrained load responses of the baseline vertical monotonic slow load tests in uplift on K-90G-AR1 and K-90G-AR2 are shown in Figure 5.15 and Figure 5.17 respectively. For K-90G-AR1-V-Mono-4, the load response displayed a strain-hardening behavior with a non-dimensional ultimate uplift capacity of -2.5 mobilized after a non-dimensional displacement of 0.20. For K-90G-AR2-V-Mono-4, the load response displayed a strain-hardening behavior until a non-dimensional displacement of 0.11 at which the non-dimensional ultimate uplift capacity of -3.5 was mobilized after which the uplift capacity began to decrease as if a loss of suction had occurred. These capacities resulted in back-calculated N_c values of 1.0 and 2.8 based on API RP 2GEO (2011) design equations and α values back calculated during installation (Section 5.4.2) for K-90G-AR1 and K-90G-AR2 respectively. These values accounted for the weight of the clay within the suction caisson as contributing to the resistance as the plug was retained upon extraction and were much lower than the design recommendations based on Skempton (1951) of 7.6 and 8.4 for AR1 and AR2 foundations respectively. This was again likely due to the possibility of partially drained loading occurring as described in previous sections.

After the slow undrained monotonic uplift load test, the model foundations were extracted at the rapid velocity until fully extracted. The load responses of these load tests on K-90G-AR1 and K-90G-AR2 are shown in Figure 5.15 and Figure 5.17 respectively. For K-90G-AR1-Mono-4, the behavior was strain-hardening throughout the extraction process until plug detachment occurred. For K-90G-AR2-Mono-4, the load response exhibited a very slight strain-softening behavior over the course of the large amount of uplift displacement similar to previous results reported by Byrne and Cassidy (2002) and Gourvenec et al. (2009). The non-dimensional peak uplift capacities of -7.5 and -9.9 were mobilized after non-dimensional vertical displacements of 0.61 and 1.1 for K-90G-AR1 and K-90G-AR2 respectively. These capacities were significantly greater than that of the slow monotonic undrained load tests conducted prior to the rapid uplift to extraction. Indicating that the uplift capacity was largely contingent on the development of negative pore water pressures developing in the suction caisson cavity during undrained loading. For both tests, a plug was retained in the model suction caissons during testing as was evidenced by the plug detachment load-response during extraction. The

detachment of the plugs from the clay test beds was marked by a rapid decrease in uplift resistance.

5.4.5 Undrained and partially drained vertical cyclic response

The non-dimensional vertical cyclic capacity amplitude, $\pm V'^{*}_{cyc}$, of each cycle of the six to seven 30-packet cyclic load tests on K-90G-AR1 (K-90G-AR1-V-Cyc-3 and K-90G-AR1-V-Cyc-4) and on K-90G-AR2 (K-90G-AR2-V-Cyc-3 and K-90G-AR2-V-Cyc-4) are shown in Figure 5.26, Figure 5.27, Figure 5.28, and Figure 5.29 respectively. The drainage condition during the cycles was classified based on the cyclic displacement and the period of the cycling. Anytime the amplitude of the cycling was 0.05% of the diameter or below for both foundations the loading was partially drained. For all other amplitudes the loading was undrained for both model foundations. Similar to the packet-ed cyclic load tests conducted at 1-g in kaolin described in Section 4.4, the magnitude of V'^{*}_{cyc} was similar in compression and in uplift indicating that the failure mechanism being mobilized was similar in both directions of loading. Unlike the 1-g load tests in kaolin, a threshold cyclic displacement of elastic foundation response was not observed for these four tests. However, it does appear that the cyclic capacity degradation occurs more rapidly in the partially drained loading packets than in the undrained loading packets. Additionally, the packets with low displacement amplitudes combined with undrained loading conditions do exhibit much less capacity degradation with cycling than those of higher displacement amplitudes. This indicated that the elastic cyclic displacement thresholds were significantly different for the undrained case and the partially drained case. For the undrained case that was investigated at 1-g as well, the 90-g load tests indicate that the threshold amplitude for undrained elastic foundation response during cycling was below 0.075 and 0.074% of the diameter for K-90G-AR1 and K-90G-AR2 respectively. For the partially drained case, the threshold amplitude for partially drained elastic foundation response during cycling was below 0.0049% of the diameter for both K-90G-AR1 and K-90G-AR2. This displacement threshold value was approximately one order of magnitude less than that observed during the undrained cycling of both the 1-g and 90-g model suction caissons. The major reason for such a difference was the relationship between foundation displacement and soil strain for differing failure mechanism. In this case, a differing failure mechanism beneath and around the foundation results in differing soil strains at given reference foundation displacements (i.e. the soil strains resulting

in elastic behavior occur at larger foundation displacement in the undrained case than in the partially drained case).

The partially drained vertical cyclic capacity amplitude, $\pm V'^{*}_{cyc}$, of each cycle of the 7 day long cyclic load tests on K-90G-AR1 (K-90G-AR1-V-Cyc-1 and K-90G-AR1-V-Cyc-2) and K-90G-AR2 (K-90G-AR2-V-Cyc-1 and K-90G-AR2-V-Cyc-2) are shown in Figure 5.24, Figure 5.25, Figure 5.22, and Figure 5.23 respectively. The vertical cyclic capacity amplitude of K-90G-AR2-V-Cyc-1 and K-90G-AR2-V-Cyc-2 both showed degradation over the first four to five cycles before an increase in amplitude was observed. However, the vertical cyclic capacity amplitude of K-90G-AR1-V-Cyc-1 and K-90G-AR1-V-Cyc-2 only showed an increase in amplitude with cycling. The major difference between the load tests on the foundations with the two different aspect ratios was the cyclic displacement amplitude. The cyclic displacement amplitude of the tests on the K-90G-AR1 foundation was 0.21%D and 0.46%D while those of the tests on K-90G-AR2 foundation was 0.60%D and 2.5%D. The reason for these differences was that they corresponded to the displacements at which one third and one half of the ultimate monotonic undrained capacity were mobilized during K-90G-AR1-Mono-1 and K-90G-AR2-Mono-1. However, these differences may have led to the response of cyclic capacity degradation or lack thereof between the two aspect ratios. The eventual increase in capacity over the course of the relatively long time period observed across all four tests was also observed during the 24 hour cyclic tests conducted at 1-g in kaolin on both K-1G-AR1 and K-1G-AR2 similar to results reported by Chen (2013). While the cycling was not undrained for these tests, the partially drained nature do correspond to the generation of pore water pressures which would dissipate over time resulting in an increase in strength. The magnitude of V'^{*}_{cyc} were similar regardless of the compression or uplift mechanism. This observation was similar to the six to seven 30 cycle packet load tests at 90-g and all but one cyclic load test conducted at 1-g in kaolin indicating that the shear surface in compression and uplift were similar.

5.4.6 Post-cyclic undrained vertical monotonic response

5.4.6.1 Compression followed by uplift

The following vertical cyclic load tests were followed by an undrained rapid monotonic compression and then rapid monotonic uplift: K-90G-AR1-V-Cyc-1, K-90G-AR1-V-Cyc-2, K-90G-AR1-V-Cyc-3, K-90G-AR2-V-Cyc-1, K-90G-AR2-V-Cyc-2, and K-90G-AR3-V-Cyc-3.

The post-cyclic monotonic compression portions of these six tests are shown in Figure 5.12, Figure 5.13, Figure 5.18, Figure 5.10, Figure 5.11, and Figure 5.20 respectively. The load responses of these six tests all displayed strain-hardening behavior until the end of the load tests at which the motor velocity ramped down. The peak monotonic capacities therefore were mobilized at approximately the same displacement as the baseline counterpart load test for all six tests. The peak monotonic capacity in compression following the lowest cyclic displacement amplitude of cycling of 0.21%D on K-90G-AR1 (K-90G-AR1-V-Cyc-2) was approximately the same as the baseline ultimate monotonic capacity determined in K-90G-AR1-V-Mono-1. This indicates that either the cycling did not result in significant degradation of the failure surface and/or the failure surface did not completely form. The peak monotonic capacity in compression of the tests on K-90G-AR1 with cyclic displacement amplitudes greater than 0.21%D were 37% to 41% lower than the baseline ultimate monotonic capacity determined in K-90G-AR1-V-Mono-1. This indicates that the cyclic displacement of the remaining AR1 tests was sufficiently large enough to remold the failure surface resulting in a lower foundation capacity. The peak monotonic capacities in compression following all cyclic load tests on K-90G-AR2 were 9% to 24% lower than the baseline ultimate monotonic capacity determined in K-90G-AR2-V-Mono-1 indicating remolding along the failure surface. The post cyclic monotonic compression load tests on both K-90G-AR1 and K-90G-AR2 also indicate that the capacity degradation was dependent on the level of displacement that occurred during cycling.

The undrained load responses of the monotonic uplift load tests to extraction that followed the post-cyclic vertical monotonic load tests in compression just described are shown in Figure 5.12, Figure 5.13, Figure 5.18, Figure 5.10, Figure 5.11, and Figure 5.20 respectively. The general shape of the load response was similar to the uplift that followed the baseline compression load test for both the K-90G-AR1 and K-90G-AR2. All six of these monotonic uplift load tests exhibited strain hardening behavior over the course of the large uplift displacement. The peak post cyclic uplift capacity of all but one of the six tests (K-90G-AR1-V-Cyc-3) was higher than that of the peak uplift capacity mobilized during the baseline test (K-90G-AR1-V-Mono-1). However, these capacities were mobilized after displacements of 0.58 and 0.73 for K-90G-AR1 and 1.4 to 1.7 for K-90G-AR2. These displacements were near the point of nearly complete extraction and would likely fail serviceability constraints. This does indicate, however, that much more significant cyclic displacements may be required to

thoroughly remold the failure surface mobilized in the uplift case than in the compression case. This result was also observed during respective cyclic load tests and associated post-cyclic monotonic tests conducted at 1-g in kaolin. For all tests, a plug was retained in the model suction caissons during testing as was evidenced by the plug detachment load-response during extraction. The detachment of the plugs from the clay test beds was marked by a rapid decrease in uplift resistance.

5.4.6.2 Uplift only

The following vertical cyclic load tests were followed by undrained rapid monotonic uplift only: K-90G-AR1-Cyc-4 and K-90G-AR2-Cyc-4. The post-cyclic monotonic rapid uplift portions of these two tests are shown in Figure 5.19 and Figure 5.21 respectively. The test corresponding to K-90G-AR1-V-Cyc-4 showed strain-hardening behavior with a peak uplift capacity 36% lower than the baseline ultimate uplift capacity determined in K-90G-AR1-V-Mono-3. However, the non-dimensional displacements required to mobilize both capacities were similar. K-90G-AR2-V-Cyc-4 showed a load response that was very slightly strain-softening over the course of the large amount of uplift displacement. The peak uplift capacity and displacement required to mobilize the capacity were similar to the respective values of the baseline ultimate uplift load test (K-90G-AR2-V-Mono-3). These results further confirm that the cyclic displacement amplitude has an effect on the post-cyclic monotonic response, however it also indicates that the aspect ratio of the foundation also provides a contributing role. For both tests, a plug was retained in the model suction caissons during testing as was evidenced by the plug detachment load-response during extraction. The detachment of the plugs from the clay test beds was marked by a rapid decrease in uplift resistance.

5.4.7 Visual observation of test bed surface after spin down

As described at multiple points earlier in this chapter, all load responses during rapid undrained extraction indicated a plug detachment after relatively large amounts of uplift displacement. This plug detachment was indicated by a rapid decrease in the vertical load cell readings. After the foundation had been fully extracted from the soil and plug detachment had occurred, the load cell readings showed an additional relatively rapid decrease in vertical load cell readings. These final readings corresponded to approximately the weight of the load cell and the foundation that were positioned under the sensor element. Once spin down of the centrifuge

was completed, visual inspection of the foundation showed that the plug had fallen back into the test bed. In most cases the plug fell back into the cavity it left behind, but was positioned higher than the surrounding test bed surface. A very small amount of trace kaolin clung to the model suction caisson, both on the inner and outer wall. Unlike the 1-g tests, a clear circular scarp was not observed around all the foundation load test points as shown in Figure 5.30 through Figure 5.37 for the indicated load tests. However, those that did display scarping exhibited a scarp distance similar to that of the 1-g tests. The load responses of the tests also indicate that a similar failure mechanism did occur as in the 1-g cases. The lack of a clear scarping or circular cracking at the test bed surface upon spin down may have been a result of the scaling to 90-g, but also due to the sloshing of water during spin down that potentially filled or smeared the cracks with kaolin particles that dislodged from the test bed over the course of testing. The cracks that were observable after spin down do evidence a circular failure surface around the foundation similar to the 1-g load tests described in CHAPTER 4.

5.5 Conclusions

The results of the undrained and partially drained 90-g model load tests in kaolin described in this chapter led to the following conclusions as indicated for the installation penetration resistance and vertical loading. Some of the conclusions further verify those based on the undrained 1-g model load tests in kaolin described in CHAPTER 4 and are listed as such. Conclusions that differ or were not observed in the 1-g model load tests in kaolin are also indicated. The major difference between the two scales of load tests were the OCRs of the two test beds largely due to different in stress state at the two different gravity levels. The 90-g kaolin ted beds were heavily overconsolidated while the 1-g kaolin test beds were lightly overconsolidated.

1. Installation penetration resistance
    a. The back-calculated α values of 0.16 to 0.31 for both foundations was significantly lower than the API design recommendation of 0.59 that was determined from the sensitivity of the soil. This factor, in addition to the low amount of clay clinging to the outside wall of the caisson upon extraction, indicated that the side resistance of the suction caisson foundation was mobilized along the soil-structure interface rather than the soil-soil interface that was recommended by use of the sensitivity driven

API design recommendation. (Observation matches 1-g model load tests in kaolin)

2. Undrained vertical loading
    a. The 90-g monotonic undrained vertical load response in compression regardless of whether it occurred without or with prior cyclic loading displayed strain-hardening response for all load tests. This behavior was not consistent with the 1-g monotonic undrained vertical load response during which the baseline compression load tests displayed strain-softening behavior. This difference in behavior was a result of the different in OCR of the two test beds. Strain-softening behavior is typically a trait of highly overconsolidated soils while strain-hardening behavior is typically a trait of normally to light overconsolidated soils. The OCR of the soil will therefore be a critical factor for serviceability constraints due to the significant different in mobilized load for a given displacement.
    b. The 90-g monotonic undrained vertical load response in uplift regardless of whether it occurred without or with prior cyclic loading displayed a strain-hardening response or a very slightly strain-softening response. However, at no point was plug failure observed to occur at very low non-dimensional displacements as they were for the selection of 1-g tests preceded by insignificant remolding of the failure surface. This difference however was due to the change in critical failure condition based on the different ratios of strength to foundation dimensions.
    c. The back-calculated N_c values for the K-90G-AR1 baseline rapid monotonic compression, K-90G-AR1 baseline rapid monotonic uplift, K-90G-AR2 baseline rapid monotonic compression, and K-90G-AR2 baseline rapid monotonic uplift were 11.0, 12.5, 9.8, and 15.5 when using the α values back-calculated from the installation phase. The back-calculated N_c values were all greater than the API design N_c values of 7.6 and 8.4 based on Skempton (1951) for AR1 and AR2 circular foundations in clay. This indicates that the failure mechanism was likely not the

assumed plastic limit equilibrium theory failure surface presented by Skempton (1951). While limit equilibrium methods such as Skempton's have been commonly utilized in design of foundations in soft clay, they were not developed for use in such materials. The failure mechanism will be visualized and discussed in CHAPTER 6 (Observation matches 1-g model load tests in kaolin).

d. While the 90-g undrained baseline load tests conducted at a rapid rate resulted in similar behavior to the 1-g undrained baseline load tests, those conducted at the slow rate did not. These load tests were characterized by lower resistances that could not fully be account for by the decrease in load rate resulting in a 7% decrease in resistance per tenfold decrease in load rate (Mesri 2001). The back-calculated N_c values of the K-90G-AR1 baseline slow monotonic compression and K-90G-AR2 baseline slow monotonic compression were 7.8 and 7.2 or similar to slightly lower than those recommended by Skempton (1951) when using α values back-calculated from the installation phase. However, when loaded in uplift, the baseline tests for both foundations mobilized significantly lower capacities indicating that a reverse bearing capacity type of failure did not occur. This indicated that partial drainage had occurred within the suction caisson cavity resulting in the plug not moving upwards with the foundation. Rapid load test conducted after both tests confirmed that plug movement with the foundation was a function of loading rate. This indicated that careful consideration of design loads and conditions must be made in order to ensure that pore pressure generation or fully undrained conditions will be generated during loading, particularly during uplift.

e. The back-calculated bearing capacity factor, predominantly strain-hardening behavior, non-dimensional ultimate capacity, and surface scarp shape post-extraction of the compression and uplift baseline load tests on K-90G-AR1 and K-90G-AR2 indicated that the failure mechanism in compression and in uplift were likely similar in both their shape and the method of soil shearing. The major differences between the two were that

the uplift mechanism added an additional potential failure at the plug and provided additional resistance due to the weight of the soil plug retained in the caisson. This formation of a form of the general shear surface was based on the circular nature of the scarp around the foundation and the variation from the design assumptions based on Skempton (1951). The assumption was confirmed through the load testing described in CHAPTER 6. (Observation matches 1-g model load tests in kaolin)

f. The 'elastic' range of cyclic loading was not observed during the 90-g cyclic load tests. However, this was due to the fact that the cycling at lower amplitudes results in foundation velocities in the partially drained loading condition due to the longer period. This indicated that the elastic behavior cyclic displacement threshold for the undrained and drained mechanism were different. For the undrained cycling, capacity degradation was exhibited for all packets with cyclic displacement amplitudes greater than 0.075% and 0.074% of the diameter for K-90G-AR1 and K-90G-AR2 respectively. When combined with the results of the 1-g cyclic tests, this narrows the range of the cyclic displacement threshold to a point between 0.05% and 0.075% of the diameter and 0.0525% and 0.074% of the diameter for AR1 and AR2 suction caissons respectively. For the partially drained cycling, capacity degradation was exhibited for all packets with cyclic displacement amplitudes greater than 0.0049% of the diameter for both model foundations. This order of magnitude difference was due to the disparity of foundation displacement in regards to the soil strains. For the undrained condition, the threshold strain at the element level were mobilized at much larger foundation displacements than those for the partially drained condition. (Observations provide additional insight into conclusions from 1-g model load tests in kaolin)

g. The response of the model suction caissons to extreme loading events (modeled as undrained monotonic vertical loads) that occurred post-cycling was highly dependent on the cyclic displacement amplitude of the

cycling. However, the 90-g load tests confirmed that the aspect ratio and direction of loading were factors as well. (Observation matches 1-g model load tests in kaolin with addition of other parameters)

i. For post-cyclic monotonic compression loading, the strain-hardening behavior existed regardless of being preceded by cycling or not. This led to the displacement at which the peak capacity was mobilized to always be near the end of the monotonic compression motor push. The magnitude of the peak capacity, however, was dependent on the non-dimensional displacement amplitude during cycling. The cyclic displacement amplitudes for which post-cyclic monotonic compression peak capacity degradation was evident were those greater than or equal to 0.46% and 0.60% of the diameter for K-90G-AR1 and K-90G-AR2 respectively. These thresholds were smaller than those in the 1-g tests, but are likely a result of the differing load response due to OCR of the test bed. The degradation of capacity still indicates that the failure mechanism was progressive and/or subject to remolding. (Observation matches 1-g model load tests in kaolin)

ii. For post-cyclic monotonic uplift loading, similar trends were observed as stated in 2.f.i. However, the threshold cyclic displacement amplitudes were found to be significantly different than those in compression and also between suction caisson aspect ratios. The cyclic displacement amplitudes for which post-cyclic monotonic uplift peak capacity degradation was evident were those greater than or equal to 2.5% for the diameter for K-90G-AR1. However, K-90G-AR2 did not exhibit post-cyclic monotonic uplift peak capacity degradation even with cycles with displacement amplitudes up to 5% of the diameter. This indicates that while the failure mechanism was progressive and/or subject to remolding, both foundation aspect ratios and the loading mechanism will influence the effect of the progression and remolding.

(Observations matches 1-g model load tests in kaolin with additional information gained)

5.6 Tables

Table 5.1: Brief description of 90-g model vertical load tests in kaolin

Identifier	Test bed	Type	Description
K-90G-AR2-V-Mono-1	K-90G-TB1	Undrained (rapid), monotonic	Compression followed by uplift until extraction.
K-90G-AR2-V-Mono-2	K-90G-TB1	Undrained (slow), monotonic	Compression followed by uplift; rapid uplift conducted to extraction after slow uplift terminated.
K-90G-AR1-V-Mono-1	K-90G-TB2	Undrained (rapid), monotonic	Compression followed by uplift until extraction.
K-90G-AR1-V-Mono-2	K-90G-TB2	Undrained (slow), monotonic	Compression followed by uplift; rapid uplift conducted to extraction after slow uplift terminated.
K-90G-AR2-V-Cyc-1	K-90G-TB3	Partially drained, cyclic	14 constant displacement amplitude of 2.5% diameter cycles with a period of 10.8 hours followed by undrained monotonic compression and then uplift until extraction.
K-90G-AR2-V-Cyc-2	K-90G-TB3	Partially drained, cyclic	14 constant displacement amplitude of 0.60% diameter cycles with a period of 10.8 hours followed by undrained monotonic compression and then undrained monotonic uplift until extraction.
K-90G-AR1-V-Cyc-1	K-90G-TB4	Partially drained, cyclic	14 constant displacement amplitude of 0.46% diameter cycles with a period of 10.8 hours followed by undrained monotonic compression and then monotonic uplift until extraction.
K-90G-AR1-V-Cyc-2	K-90G-TB4	Partially drained, cyclic	14 constant displacement amplitude of 0.21% diameter cycles with a period of 10.8 hours followed by undrained monotonic compression and then undrained monotonic compression and then monotonic uplift until extraction.
K-90G-AR1-V-Mono-3	K-90G-TB5	Undrained (rapid), monotonic	Uplift until extraction.

Table 5.1: Brief description of 90-g model vertical load tests in kaolin (Continued)

Identifier	Test bed	Type	Description
K-90G-AR1-V-Mono-4	K-90G-TB5	Undrained (slow), monotonic	Uplift; rapid uplift conducted to extraction after slow uplift terminated.
K-90G-AR2-V-Mono-3	K-90G-TB6	Undrained (rapid), monotonic	Uplift until extraction.
K-90G-AR2-V-Mono-4	K-90G-TB6	Undrained (slow), monotonic	Uplift; rapid uplift conducted to extraction after slow uplift terminated.
K-90G-AR1-V-Cyc-3	K-90G-TB7	Undrained and partially drained, cyclic	Six 30 cycle packets with a period of 15 minutes followed by undrained monotonic compression and then monotonic uplift until extraction. Cycle packets were separated by a minimum of 20 minutes of no loading and the displacement amplitude increased with each successive cycle as follows: 0.0072%, 0.025%, 0.074%, 0.25%, 0.74%, and 2.5% of the diameter.
K-90G-AR1-V-Cyc-4	K-90G-TB7	Undrained and partially drained, cyclic	Six 30 cycle packets with a period of 15 minutes followed by undrained monotonic uplift until extraction. Cycle packets were separated by a minimum of 20 minutes of no loading and the displacement amplitude increased with each successive cycle as follows: 0.0049%, 0.010%, 0.049%, 0.099%, 0.49%, 0.99%, and 5.0% of the diameter.
K-90G-AR2-V-Cyc-3	K-90G-TB8	Undrained and partially drained, cyclic	Six 30 cycle packets with a period of 15 minutes followed by undrained monotonic compression and then monotonic uplift until extraction. Cycle packets were separated by a minimum of 20 minutes of no loading and the displacement amplitude increased with each successive cycle as follows: 0.0073%, 0.025%, 0.074%, 0.25%, 0.75%, and 2.5% of the diameter.
K-90G-AR2 -V-Cyc-4	K-90G-TB8	Undrained and partially drained, cyclic	Six 30 cycle packets with a period of 15 minutes followed by undrained monotonic uplift until extraction. Cycle packets were separated by a minimum of 20 minutes of no loading and the displacement amplitude increased with each successive cycle as follows: 0.0049%, 0.010%, 0.050%,

Table 5.1: Brief description of 90-g model vertical load tests in kaolin (Continued)

Identifier	Test bed	Type	Description
			0.099%, 0.49%, 0.98%, and 4.9% of the diameter.

5.7 Figures

Figure 5.1: The two kaolin 90-g model suction caissons with K-90G-AR1 shown on the left and K-90G-AR2 shown on the right

Figure 5.2: The load cell directly connecting the hybrid stepper motor linear actuator to the loading rod of the two kaolin 90-g model suction caissons

Figure 5.3: The loading apparatus as shown positioned above the test bed basket of the 15 g-ton geotechnical centrifuge within its protective housing

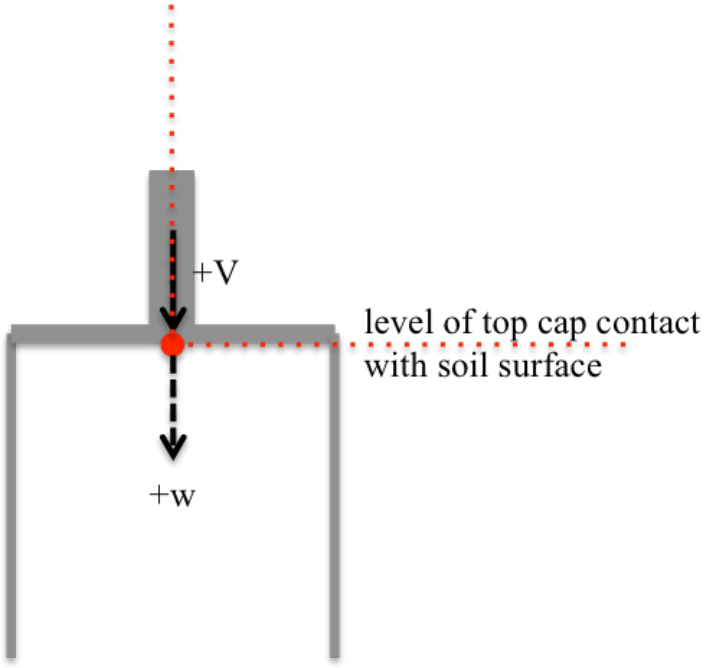

Figure 5.4: Nomenclature and orientation of model foundation loads and displacements along with the origin point of the model foundation

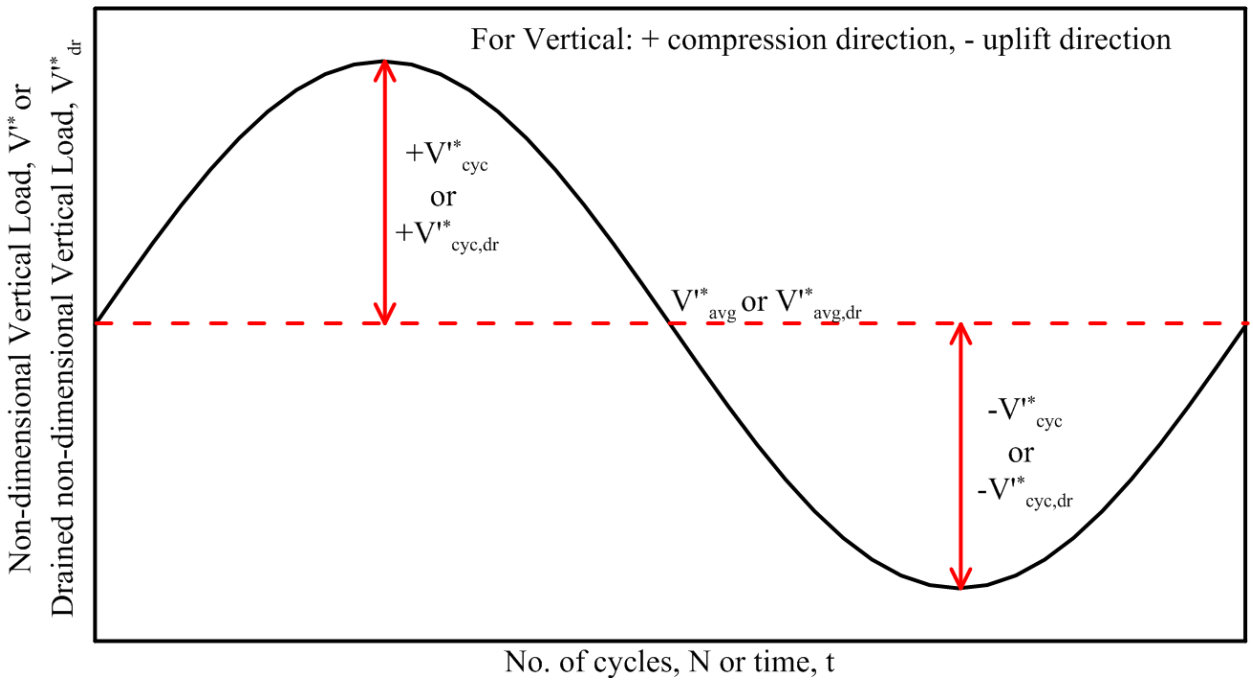

Figure 5.5: Nomenclature of the cyclic load response components

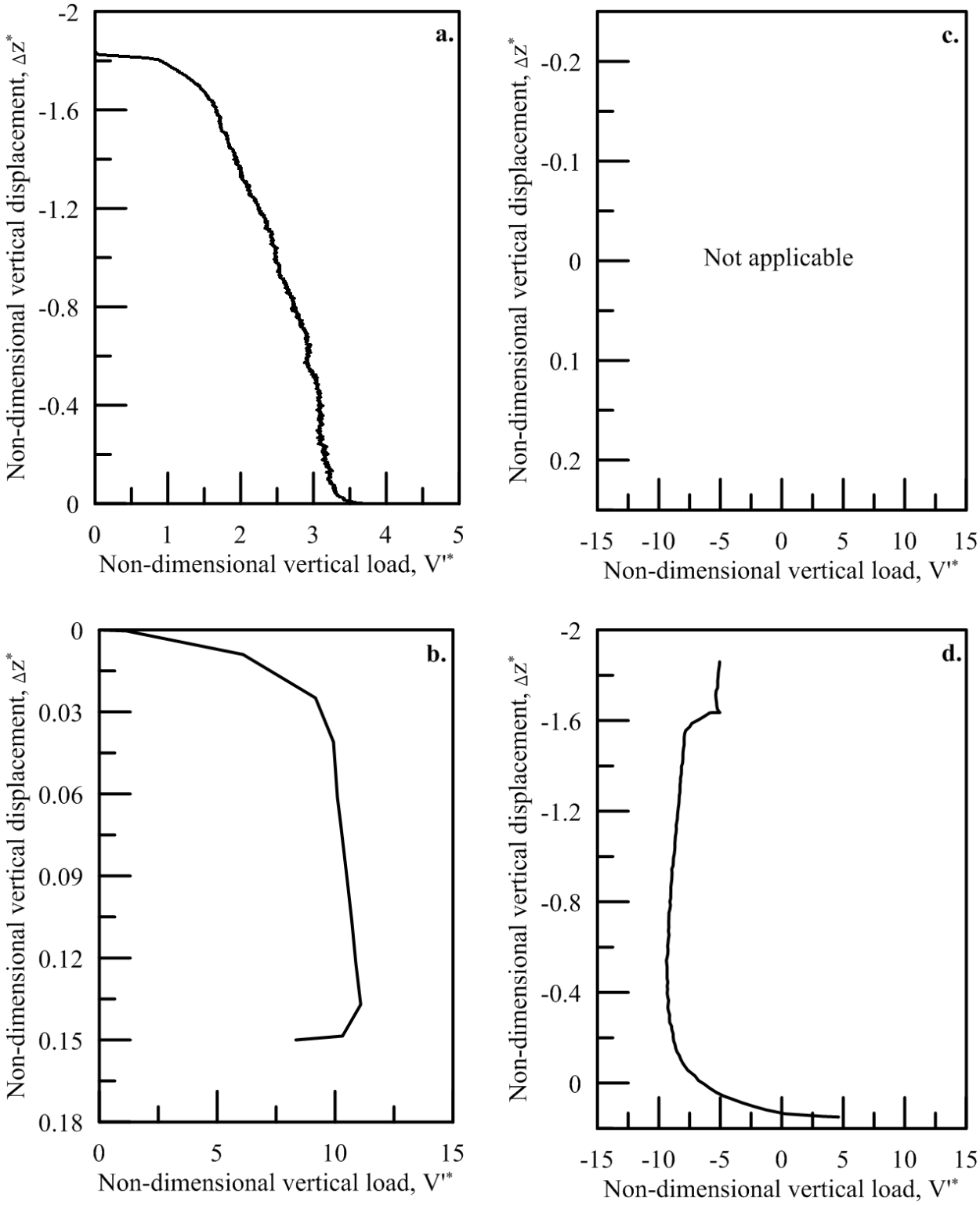

Figure 5.6: Load response of the vertical loading phases of K-90G-AR2-V-Mono-1 during a. installation, b. monotonic compression (drained or undrained as noted), c. monotonic drained uplift, and d. monotonic undrained uplift as applicable

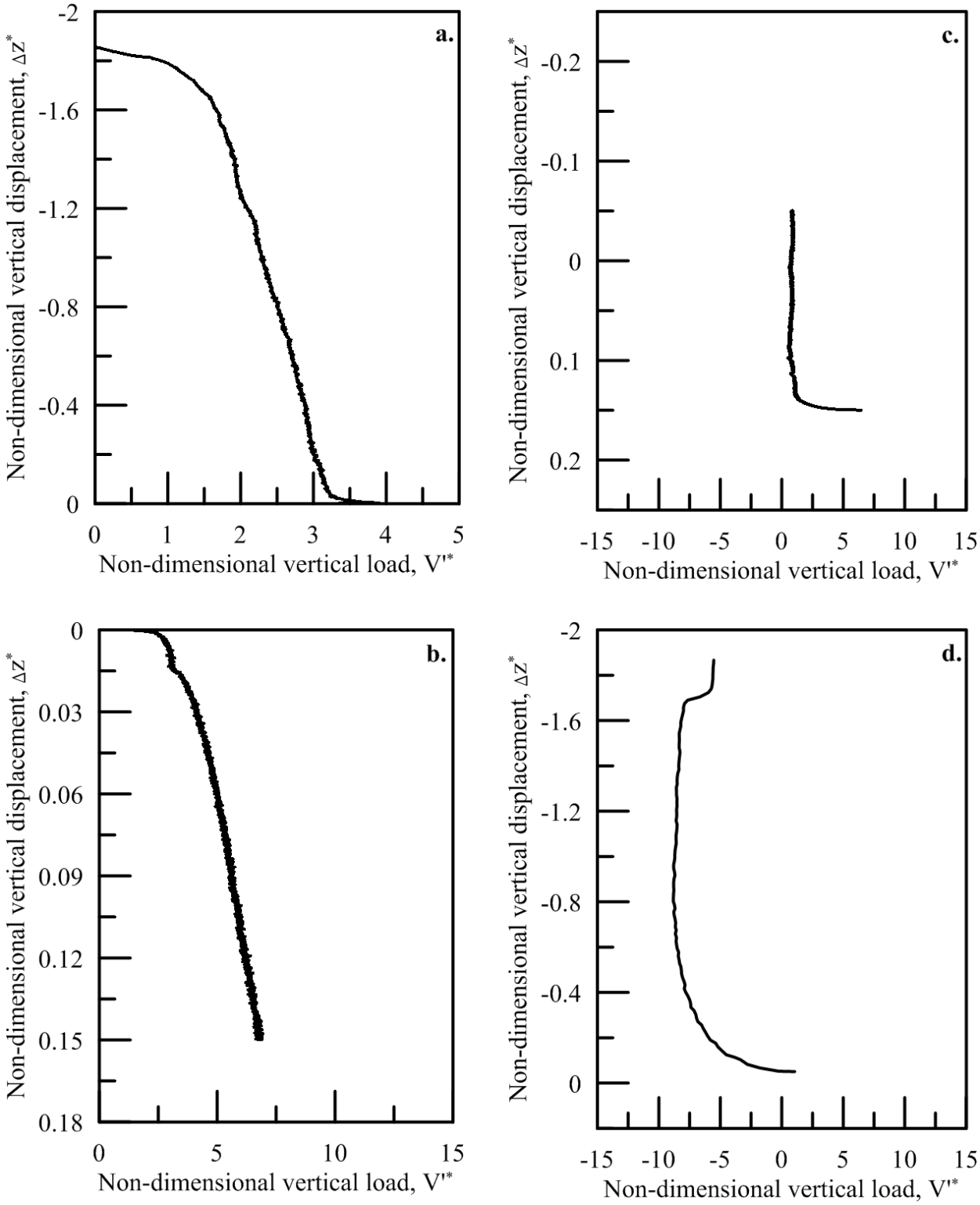

Figure 5.7: Load response of the vertical loading phases of K-90G-AR2-V-Mono-2 during a. installation, b. monotonic compression (drained or undrained as noted), c. monotonic drained uplift, and d. monotonic undrained uplift as applicable

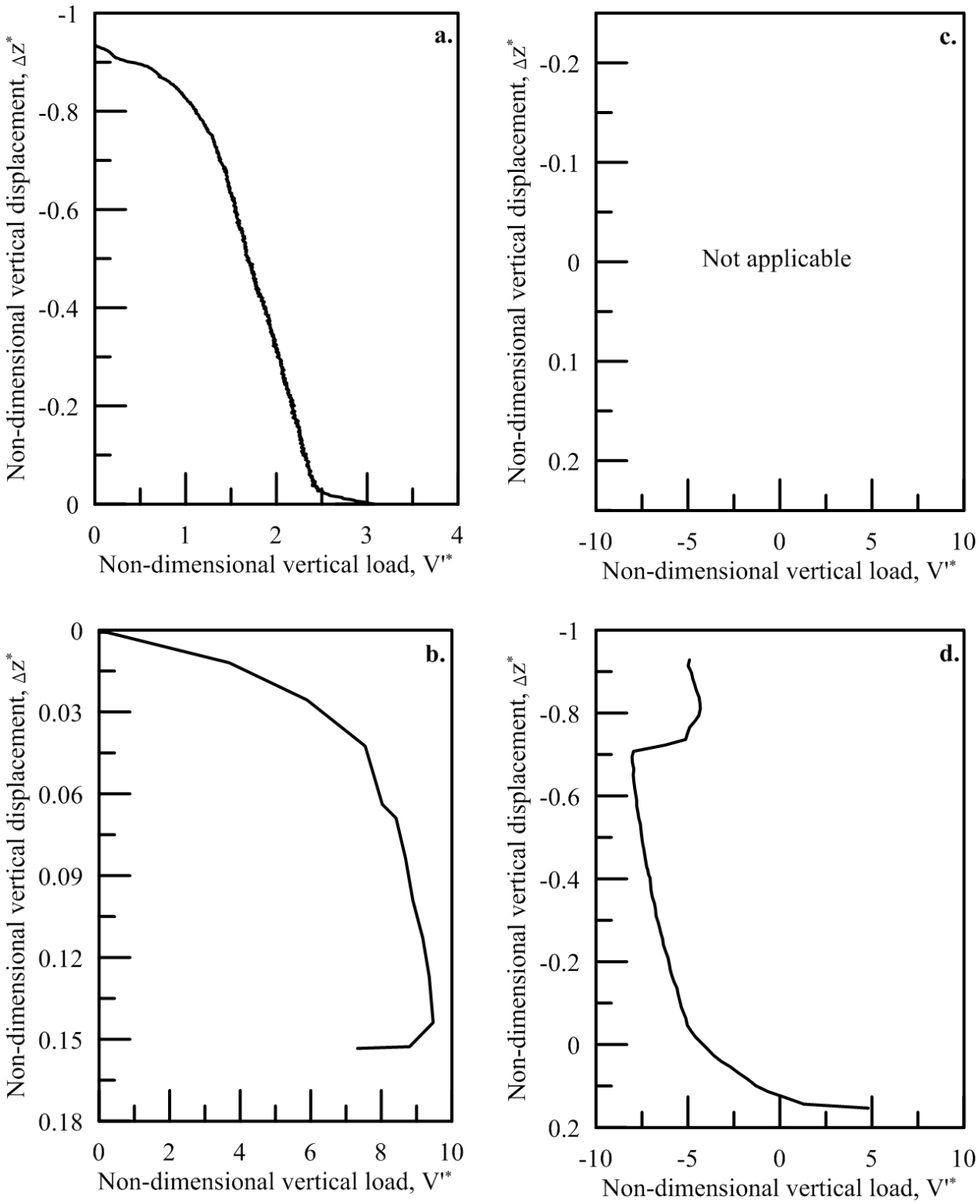

Figure 5.8: Load response of the vertical loading phases of K-90G-AR1-V-Mono-1 during a. installation, b. monotonic compression (drained or undrained as noted), c. monotonic drained uplift, and d. monotonic undrained uplift as applicable

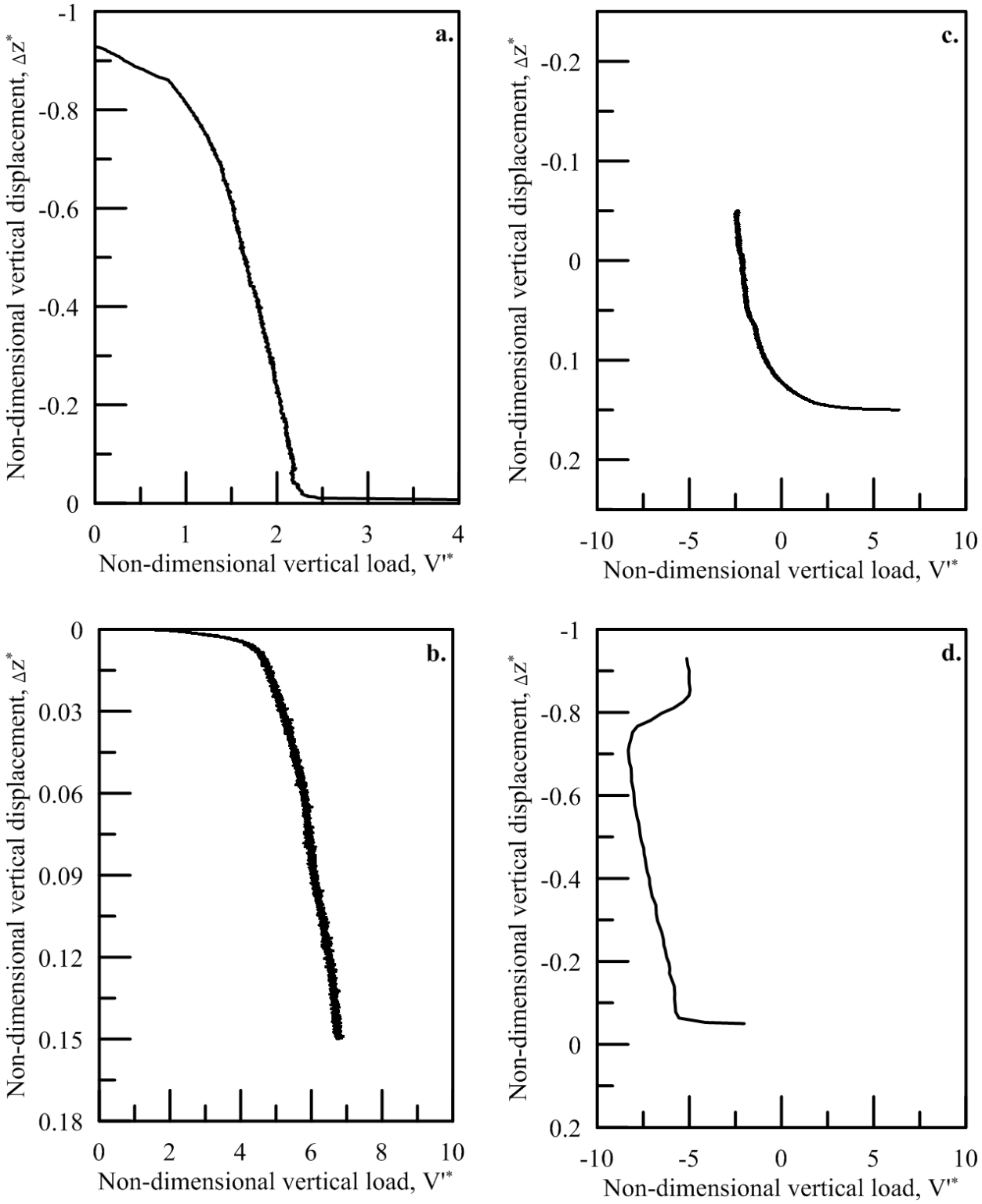

Figure 5.9: Load response of the vertical loading phases of K-90G-AR1-V-Mono-2 during a. installation, b. monotonic compression (drained or undrained as noted), c. monotonic drained uplift, and d. monotonic undrained uplift as applicable

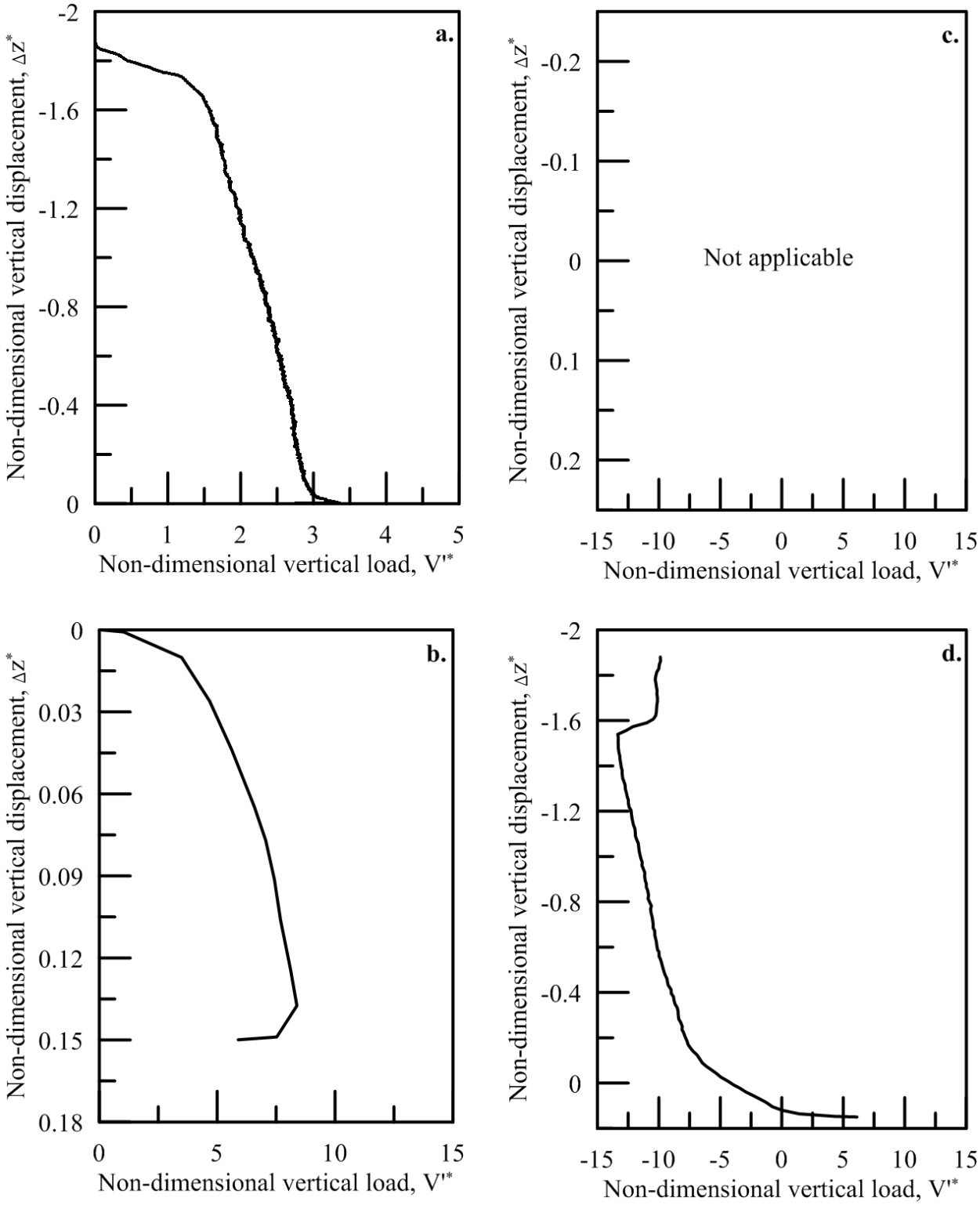

Figure 5.10: Load response of the vertical loading phases of K-90G-AR2-V-Cyc-1 during a. installation, b. monotonic compression (drained or undrained as noted), c. monotonic drained uplift, and d. monotonic undrained uplift as applicable

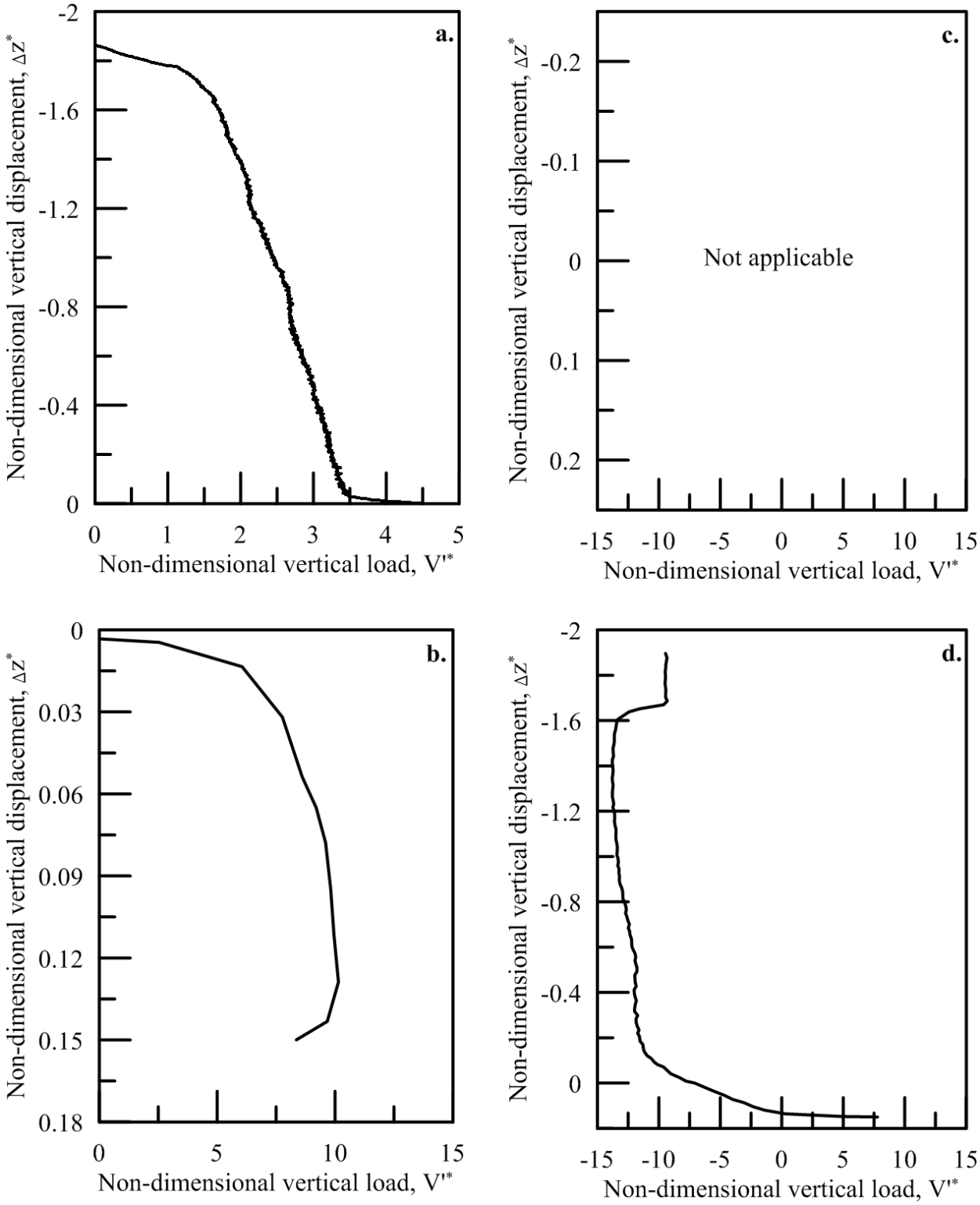

Figure 5.11: Load response of the vertical loading phases of K-90G-AR2-V-Cyc-2 during a. installation, b. monotonic compression (drained or undrained as noted), c. monotonic drained uplift, and d. monotonic undrained uplift as applicable

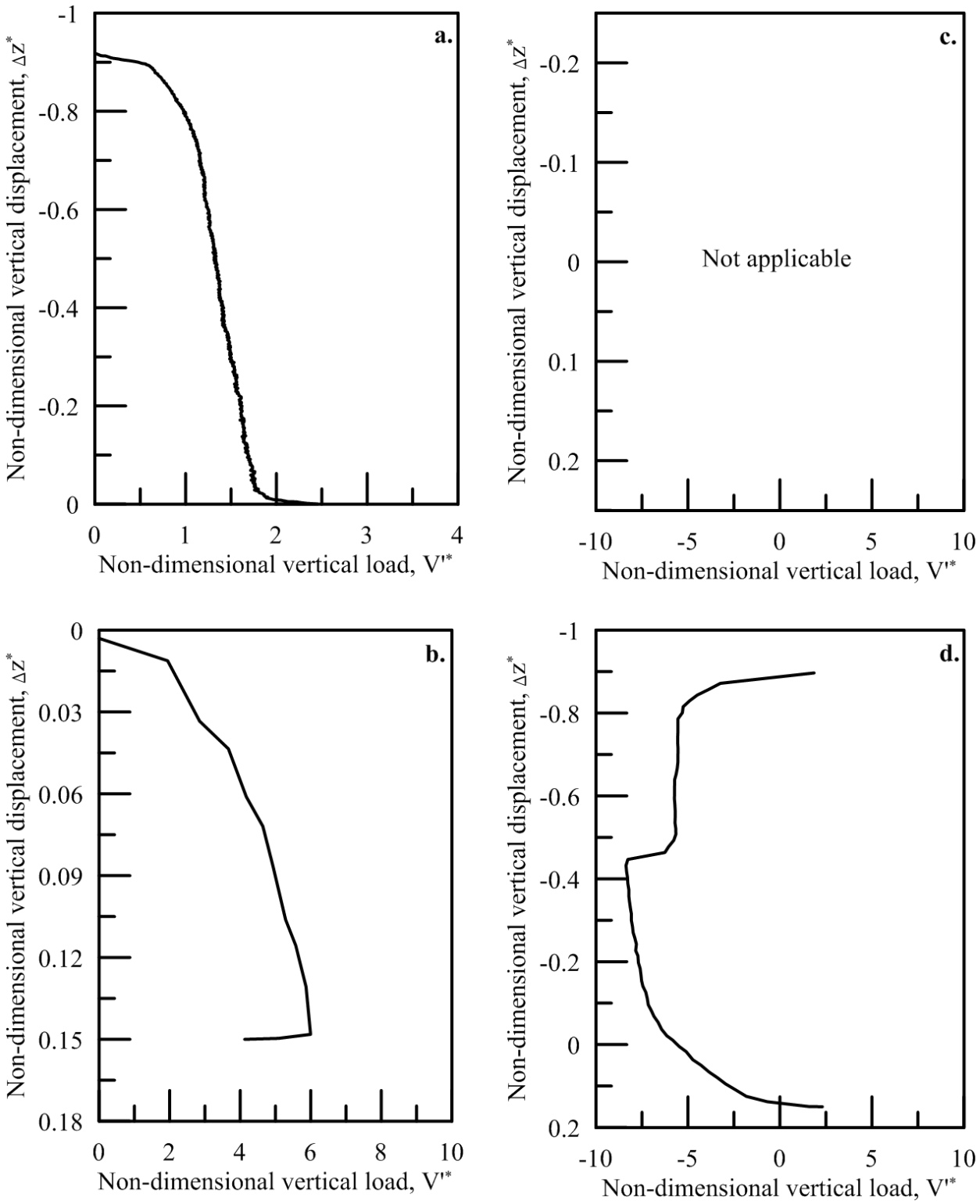

Figure 5.12: Load response of the vertical loading phases of K-90G-AR1-V-Cyc-1 during a. installation, b. monotonic compression (drained or undrained as noted), c. monotonic drained uplift, and d. monotonic undrained uplift as applicable

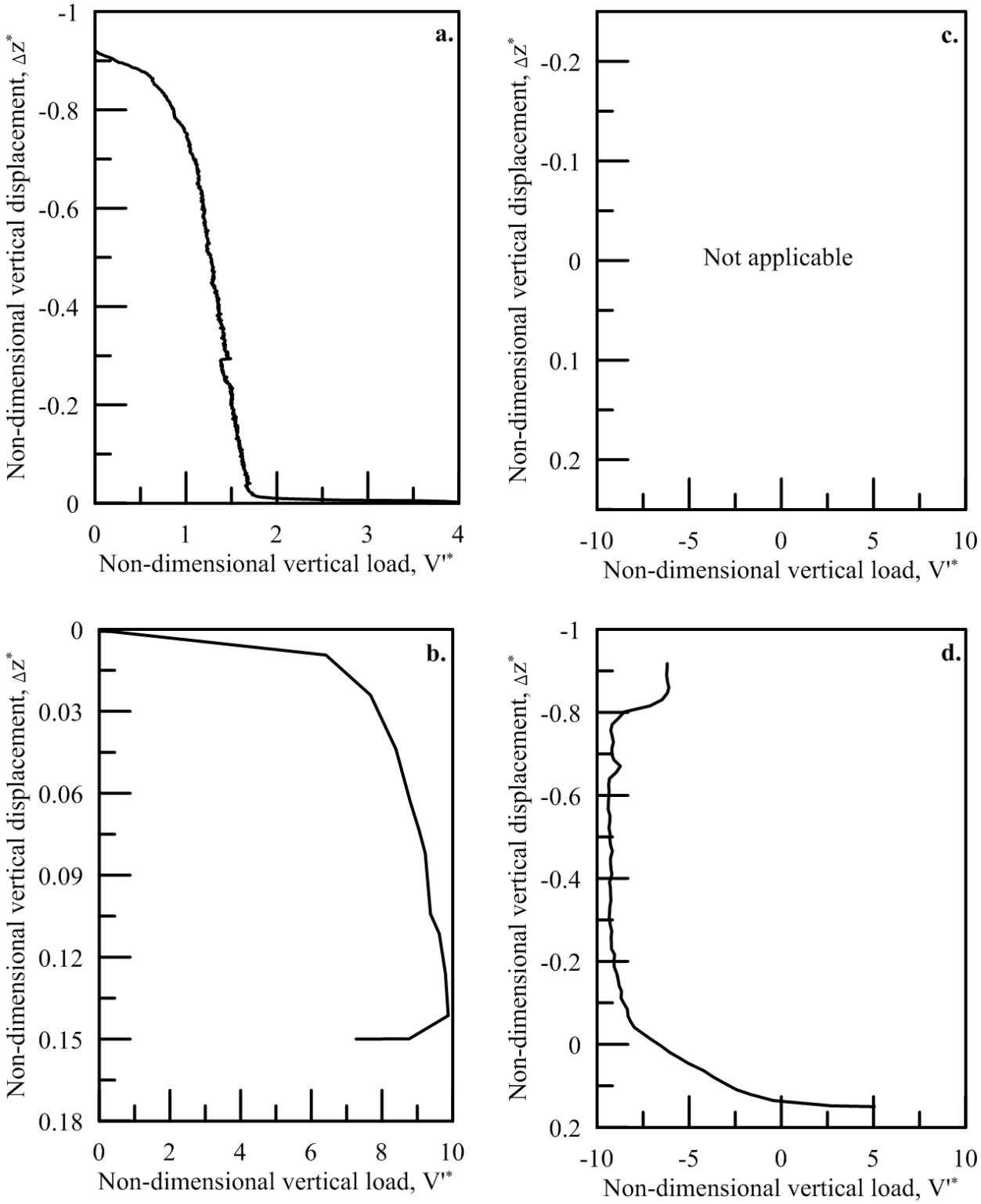

Figure 5.13: Load response of the vertical loading phases of K-90G-AR1-V-Cyc-2 during a. installation, b. monotonic compression (drained or undrained as noted), c. monotonic drained uplift, and d. monotonic undrained uplift as applicable

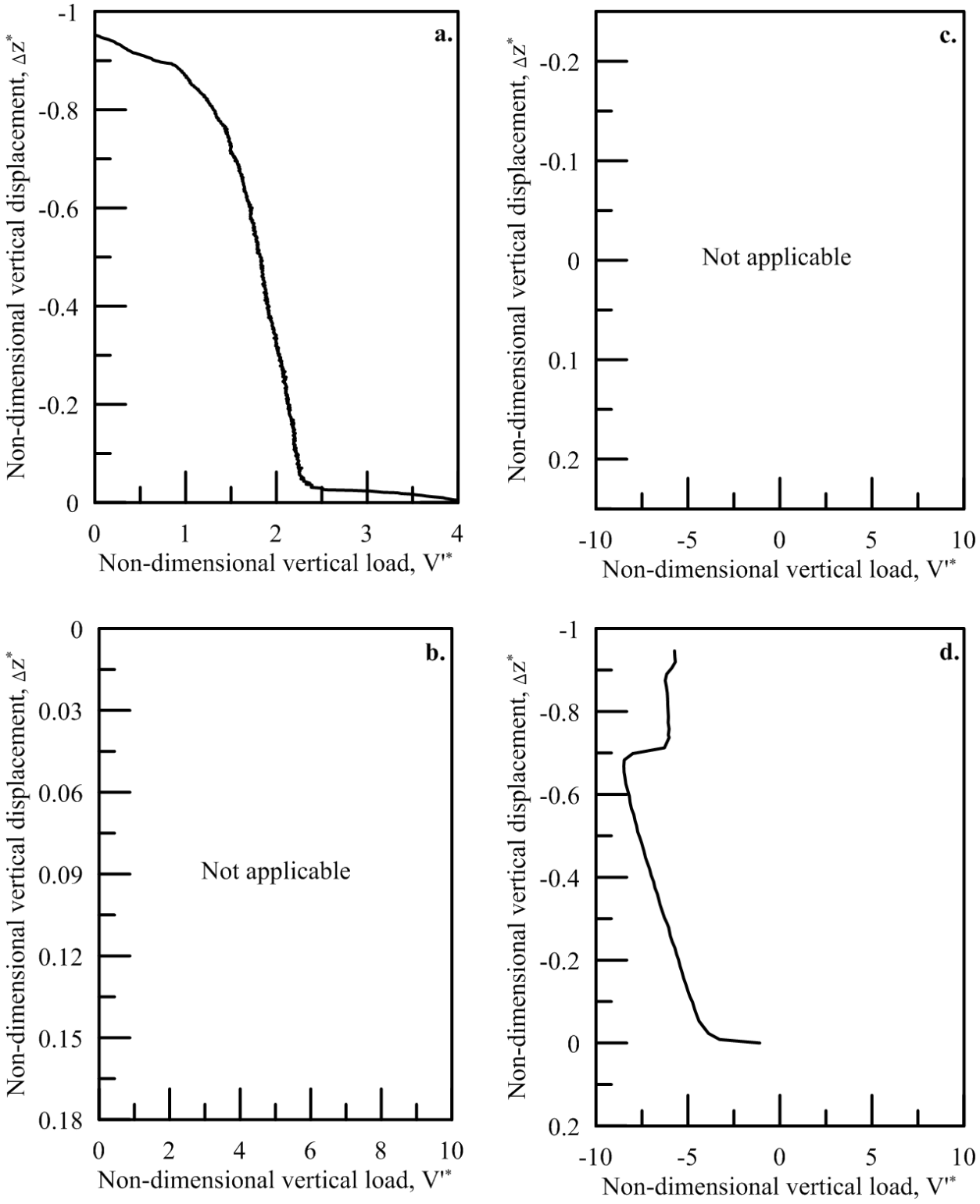

Figure 5.14: Load response of the vertical loading phases of K-90G-AR1-V-Mono-3 during a. installation, b. monotonic compression (drained or undrained as noted), c. monotonic drained uplift, and d. monotonic undrained uplift as applicable

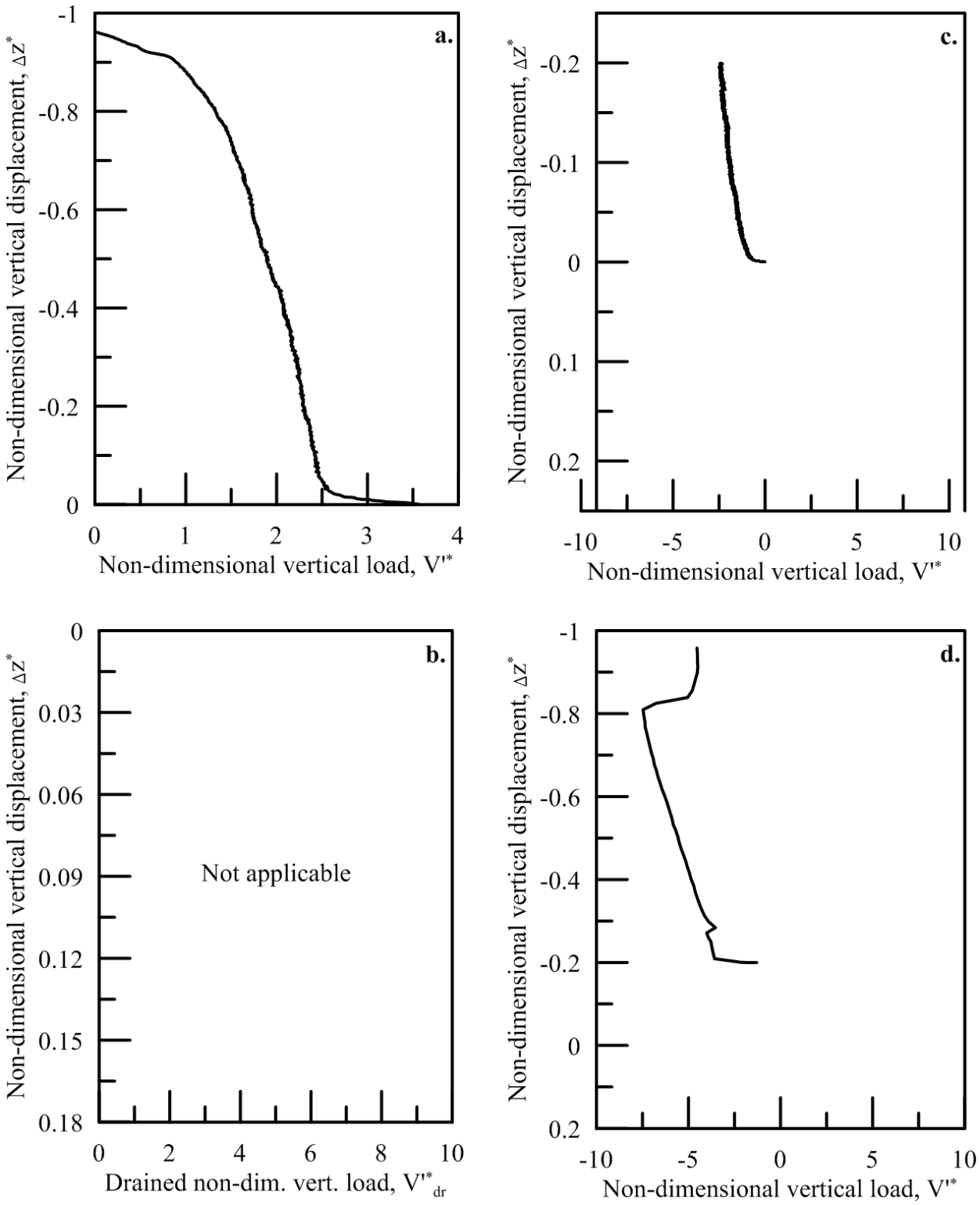

Figure 5.15: Load response of the vertical loading phases of K-90G-AR1-V-Mono-4 during a. installation, b. monotonic compression (drained or undrained as noted), c. monotonic drained uplift, and d. monotonic undrained uplift as applicable

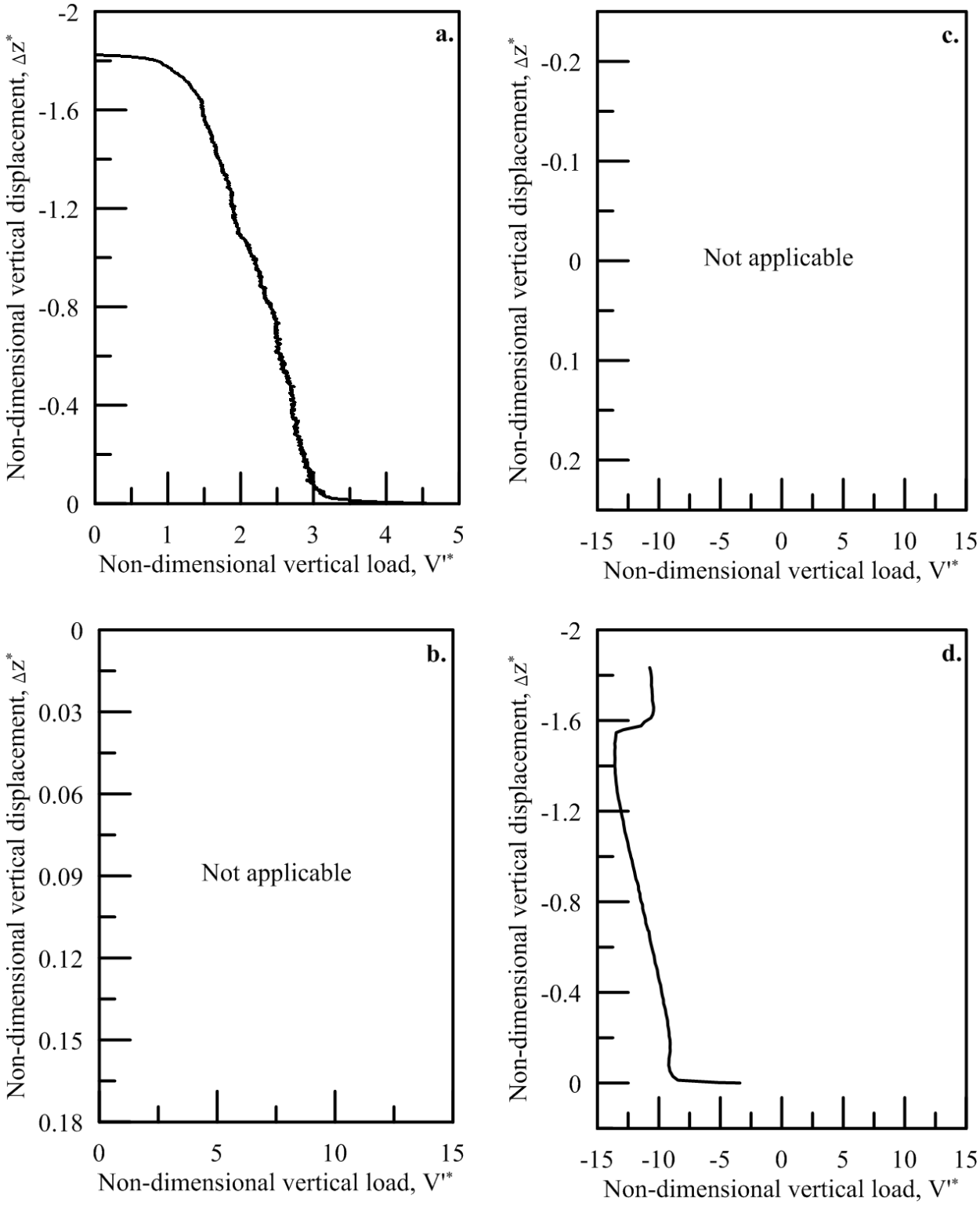

Figure 5.16: Load response of the vertical loading phases of K-90G-AR2-V-Mono-3 during a. installation, b. monotonic compression (drained or undrained as noted), c. monotonic drained uplift, and d. monotonic undrained uplift as applicable

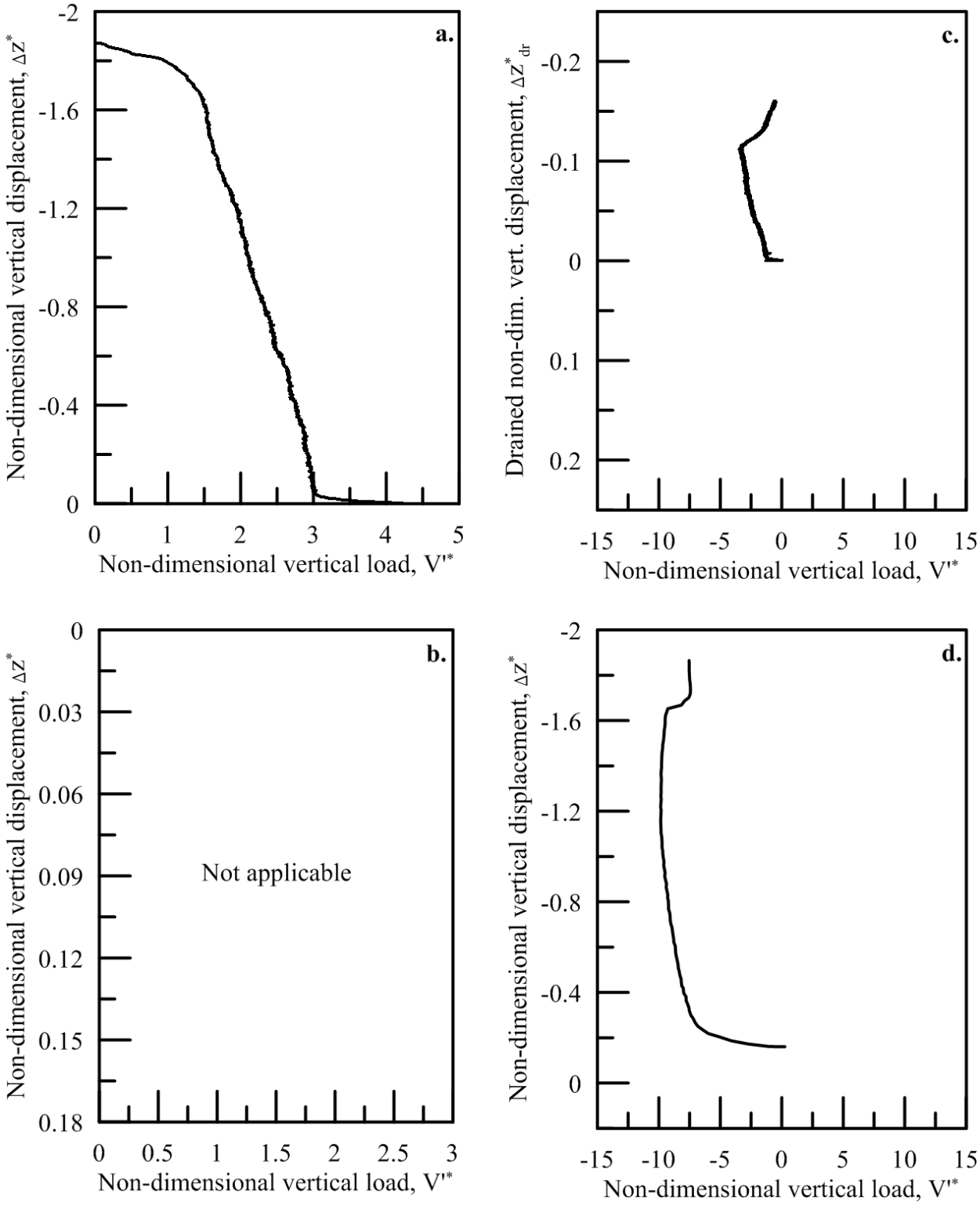

Figure 5.17: Load response of the vertical loading phases of K-90G-AR2-V-Mono-4 during a. installation, b. monotonic compression (drained or undrained as noted), c. monotonic drained uplift, and d. monotonic undrained uplift as applicable

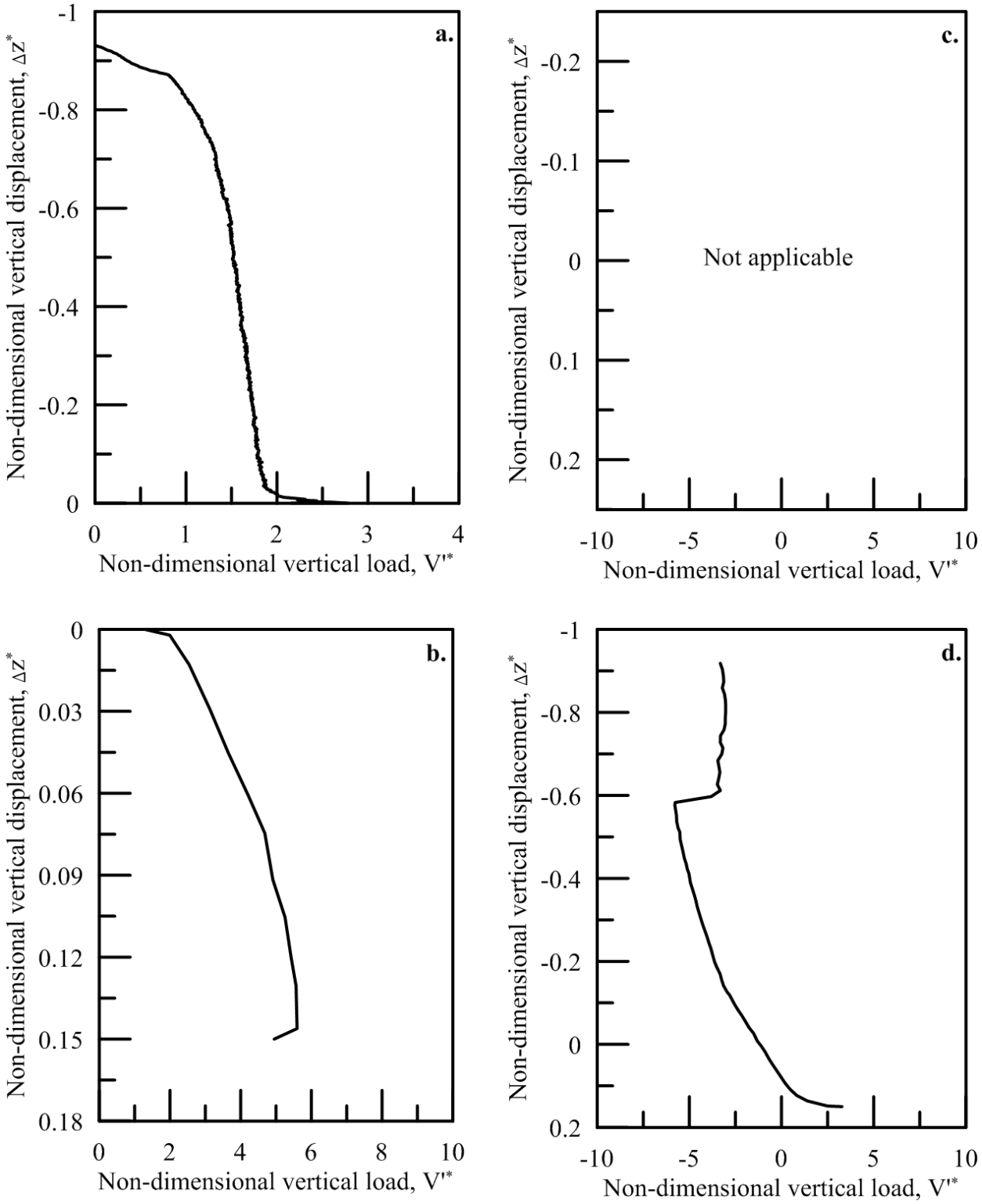

Figure 5.18: Load response of the vertical loading phases of K-90G-AR1-V-Cyc-3 during a. installation, b. monotonic compression (drained or undrained as noted), c. monotonic drained uplift, and d. monotonic undrained uplift as applicable

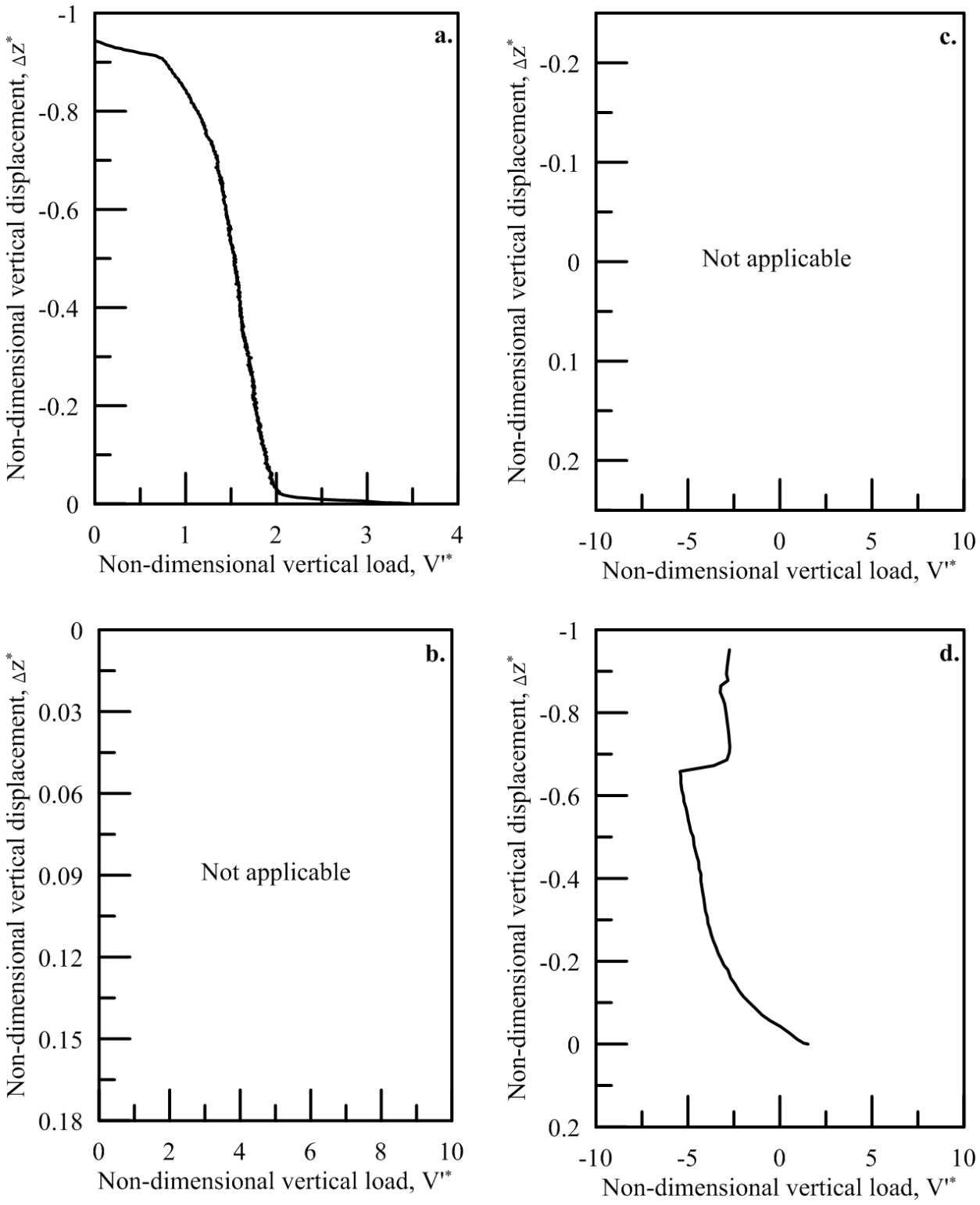

Figure 5.19: Load response of the vertical loading phases of K-90G-AR1-V-Cyc-4 during a. installation, b. monotonic compression (drained or undrained as noted), c. monotonic drained uplift, and d. monotonic undrained uplift as applicable

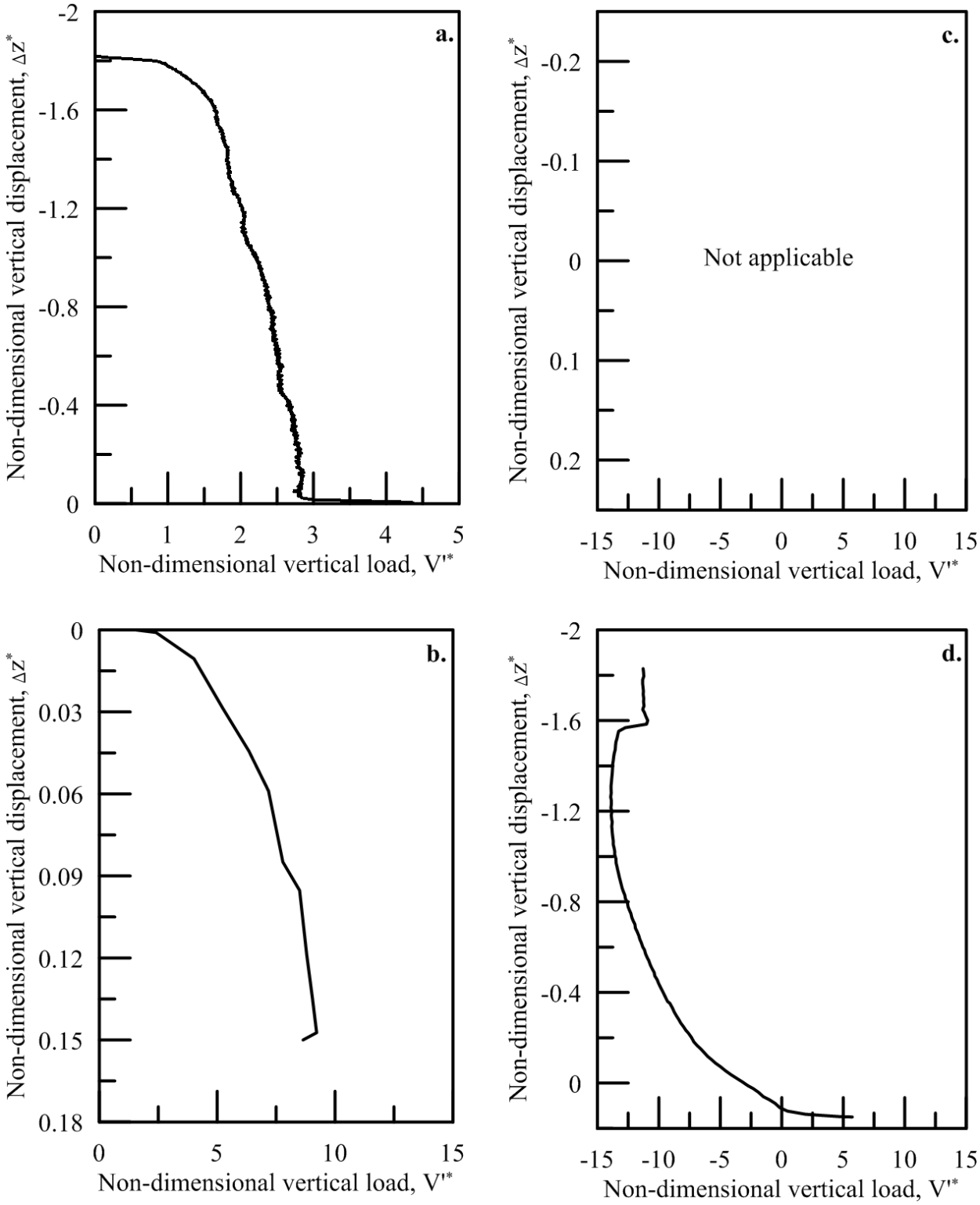

Figure 5.20: Load response of the vertical loading phases of K-90G-AR2-V-Cyc-3 during a. installation, b. monotonic compression (drained or undrained as noted), c. monotonic drained uplift, and d. monotonic undrained uplift as applicable

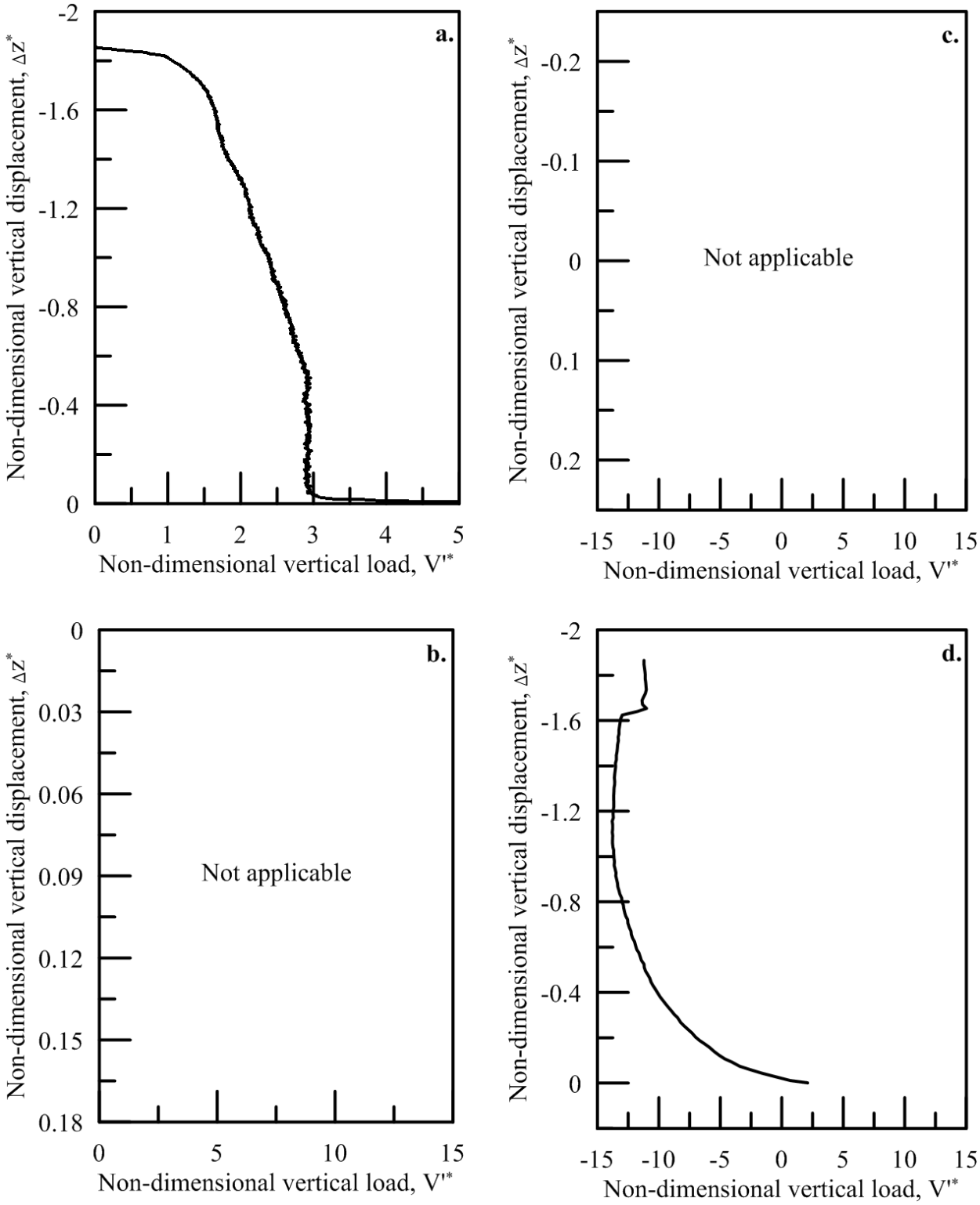

Figure 5.21: Load response of the vertical loading phases of K-90G-AR2-V-Cyc-4 during a. installation, b. monotonic compression (drained or undrained as noted), c. monotonic drained uplift, and d. monotonic undrained uplift as applicable

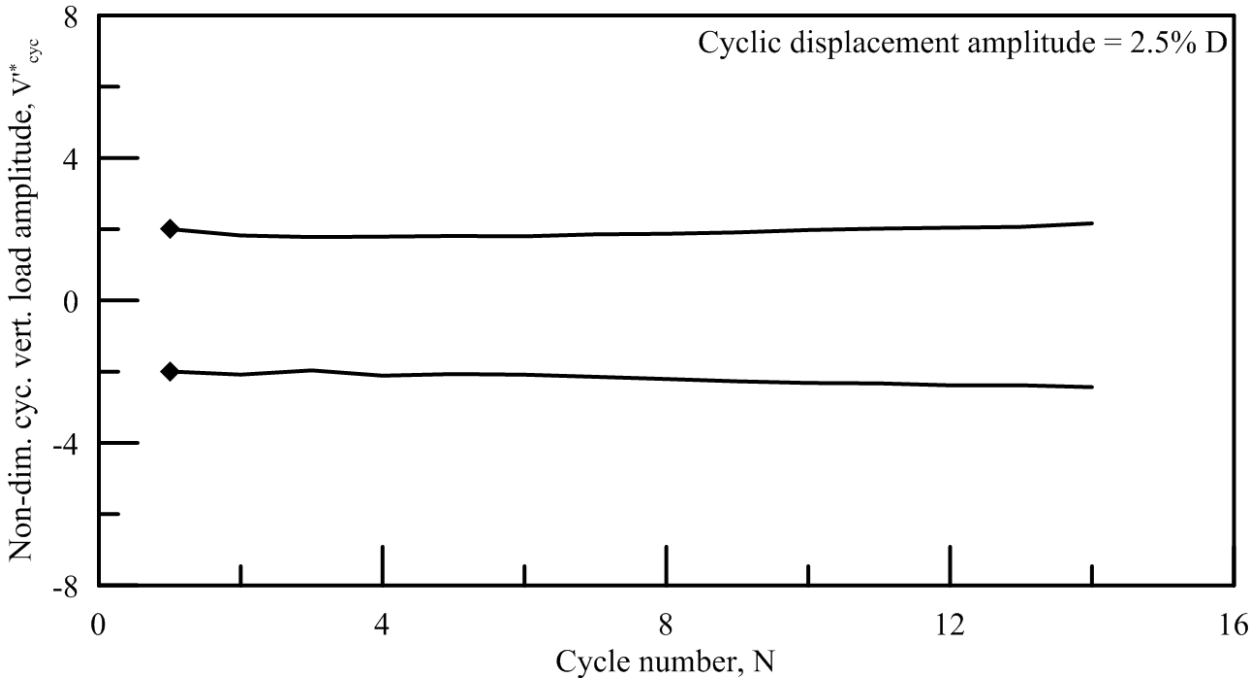

Figure 5.22: Drained vertical cyclic load amplitude, $V'^{*}_{cyc,dr}$, versus number of cycles for K-90G-AR2-V-Cyc-1

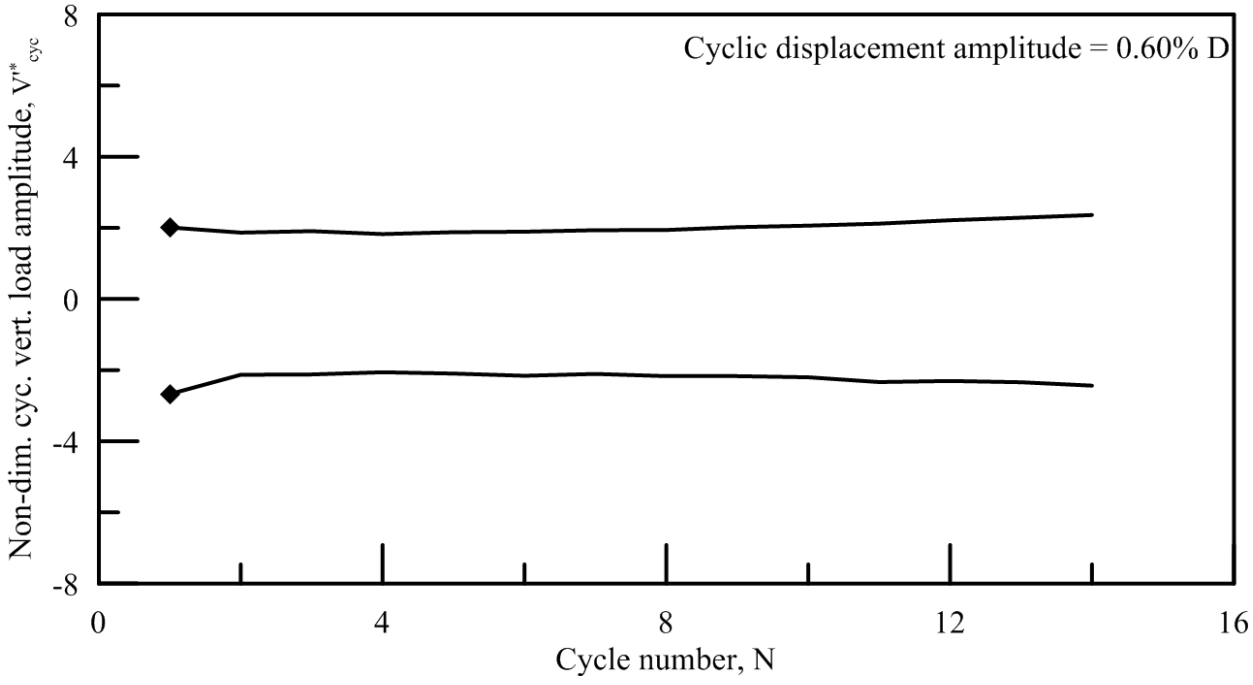

Figure 5.23: Drained vertical cyclic load amplitude, $V'^{*}_{cyc,dr}$, versus number of cycles for K-90G-AR2-V-Cyc-2

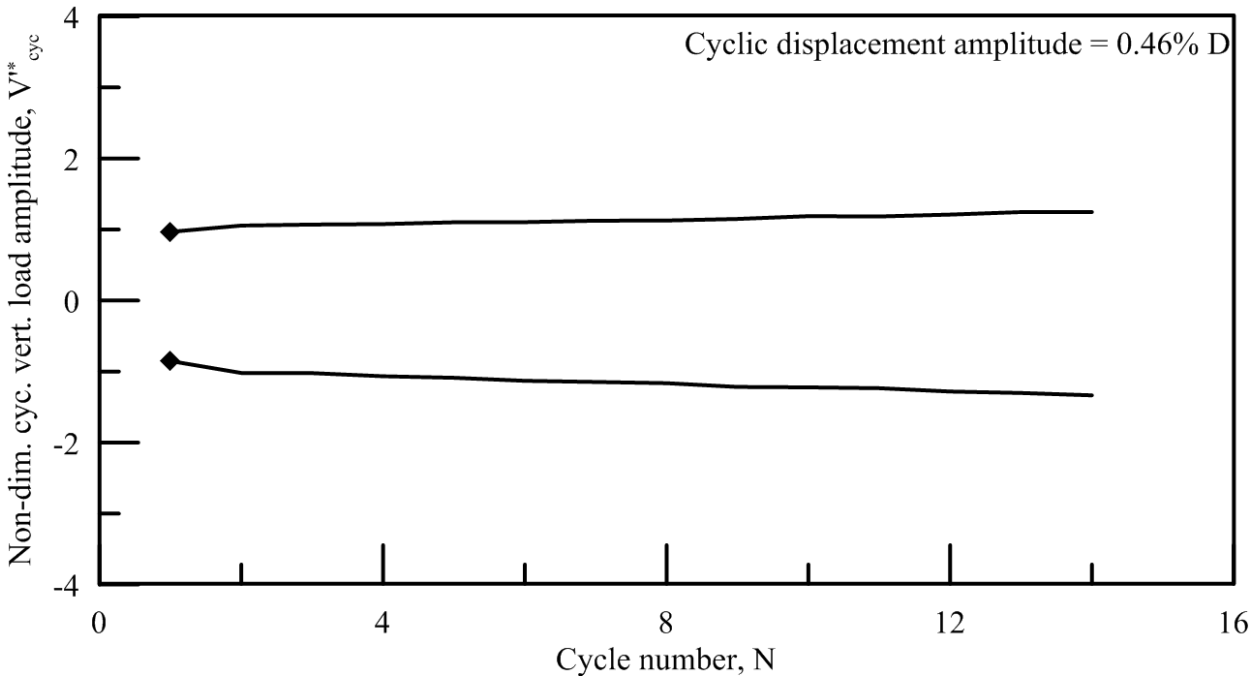

Figure 5.24: Drained vertical cyclic load amplitude, $V'^{*}_{cyc,dr}$, versus number of cycles for K-90G-AR1-V-Cyc-1

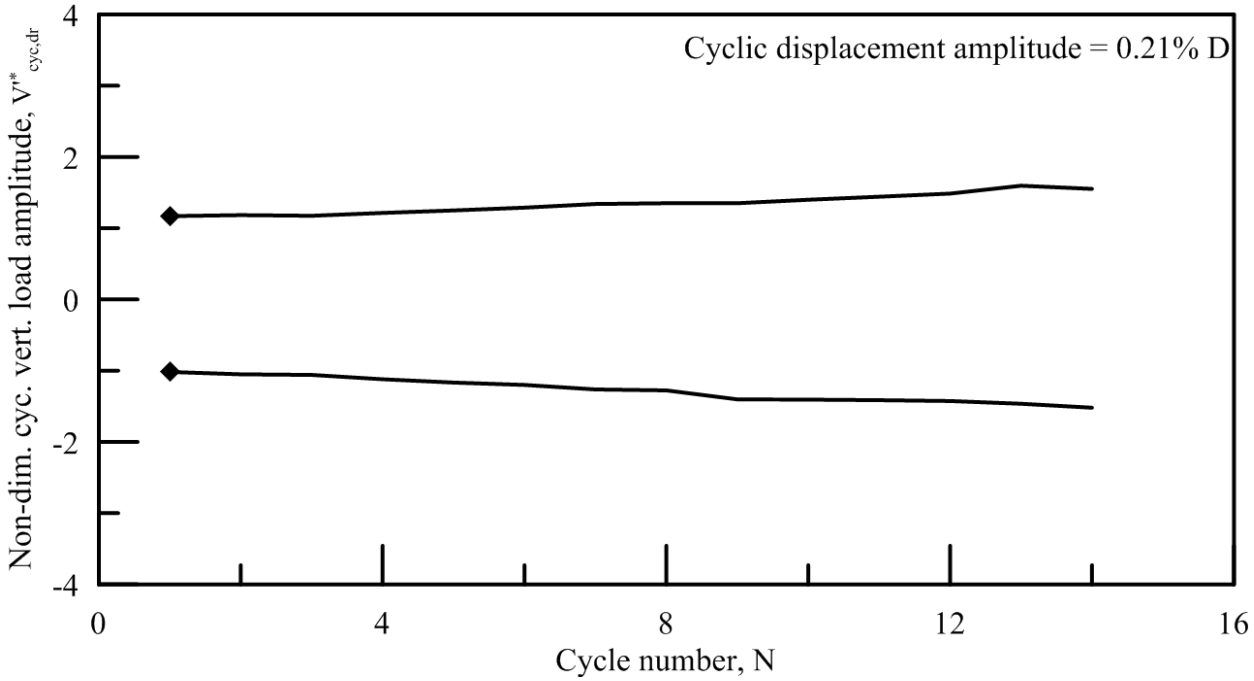

Figure 5.25: Drained vertical cyclic load amplitude, $V'^{*}_{cyc,dr}$, versus number of cycles for K-90G-AR1-V-Cyc-2

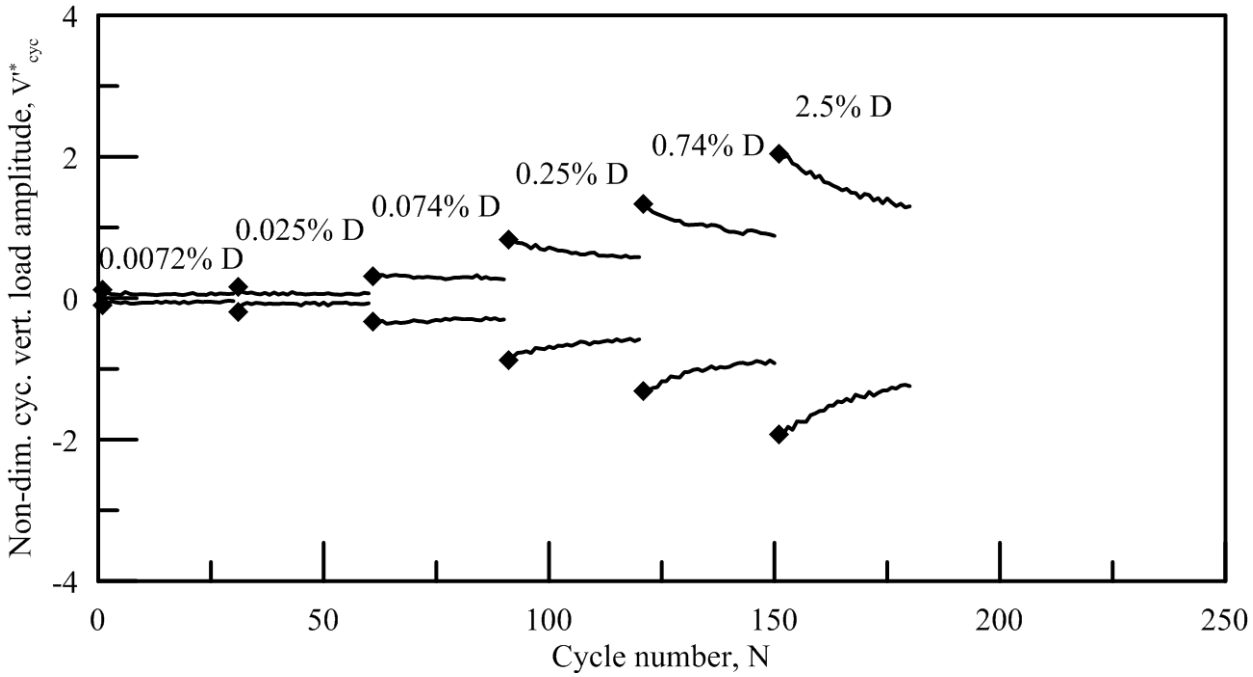

Figure 5.26: Drained vertical cyclic load amplitude, $V'^{*}_{cyc,dr}$, versus number of cycles for K-90G-AR1-V-Cyc-3

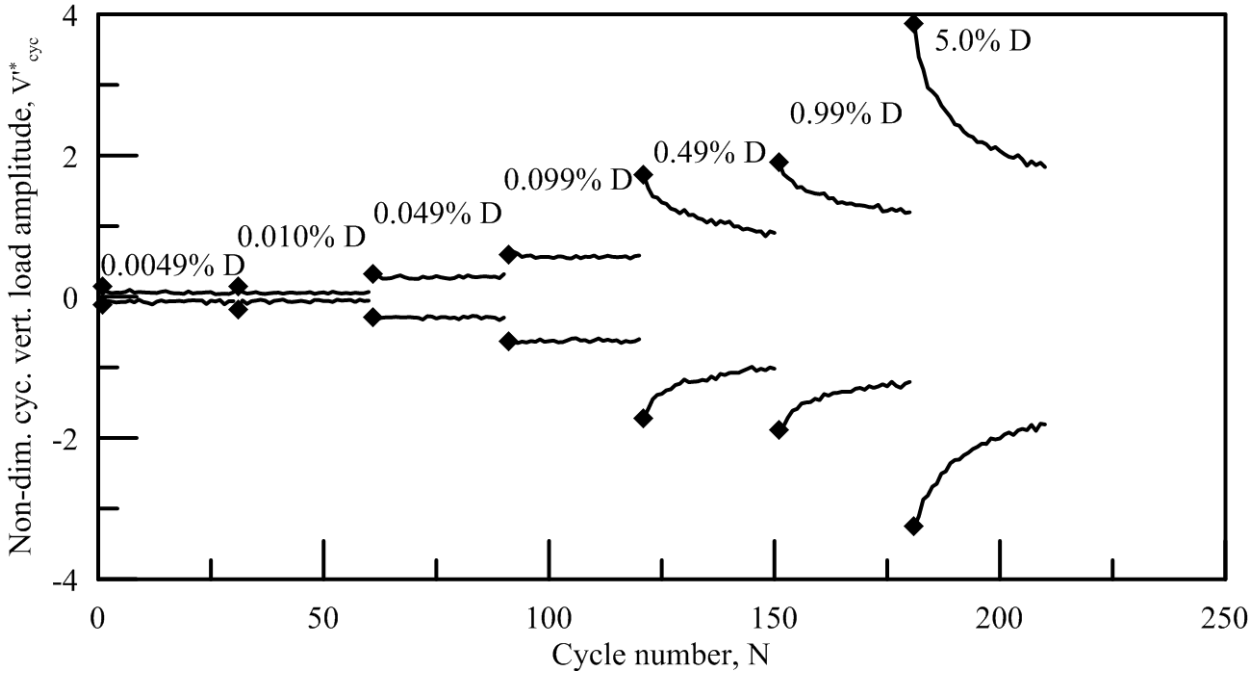

Figure 5.27: Drained vertical cyclic load amplitude, $V'^{*}_{cyc,dr}$, versus number of cycles for K-90G-AR1-V-Cyc-4

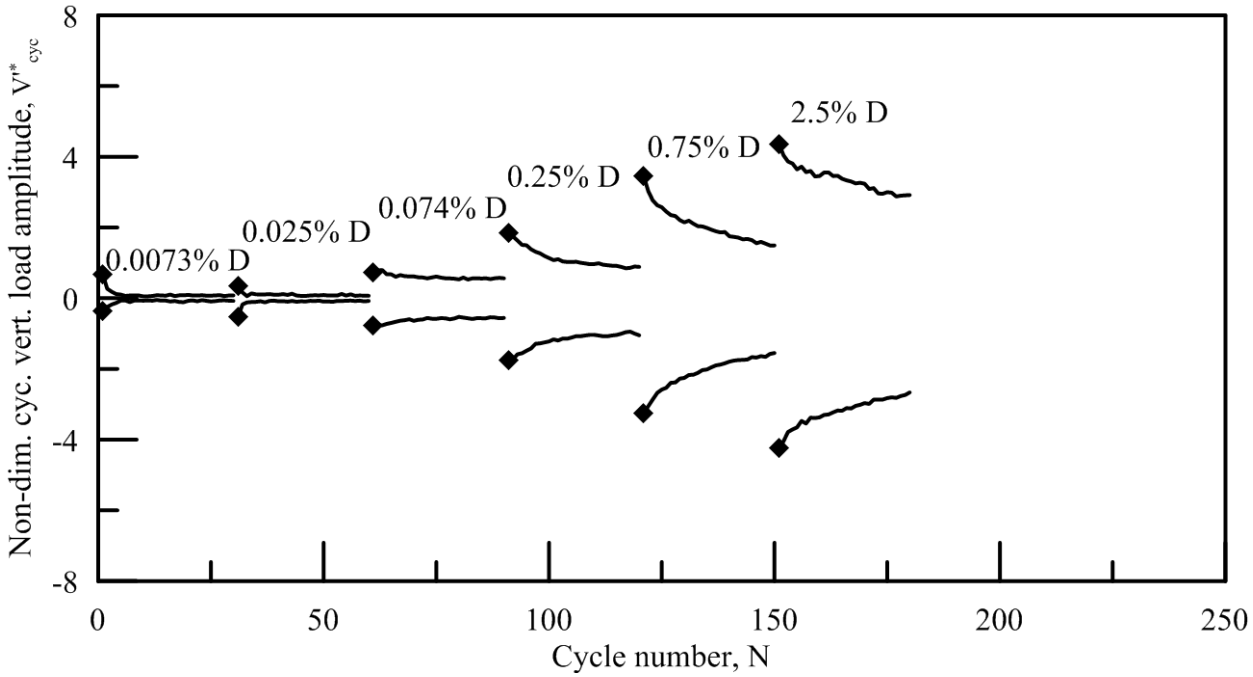

Figure 5.28: Drained vertical cyclic load amplitude, $V'^{*}_{cyc,dr}$, versus number of cycles for K-90G-AR2-V-Cyc-3

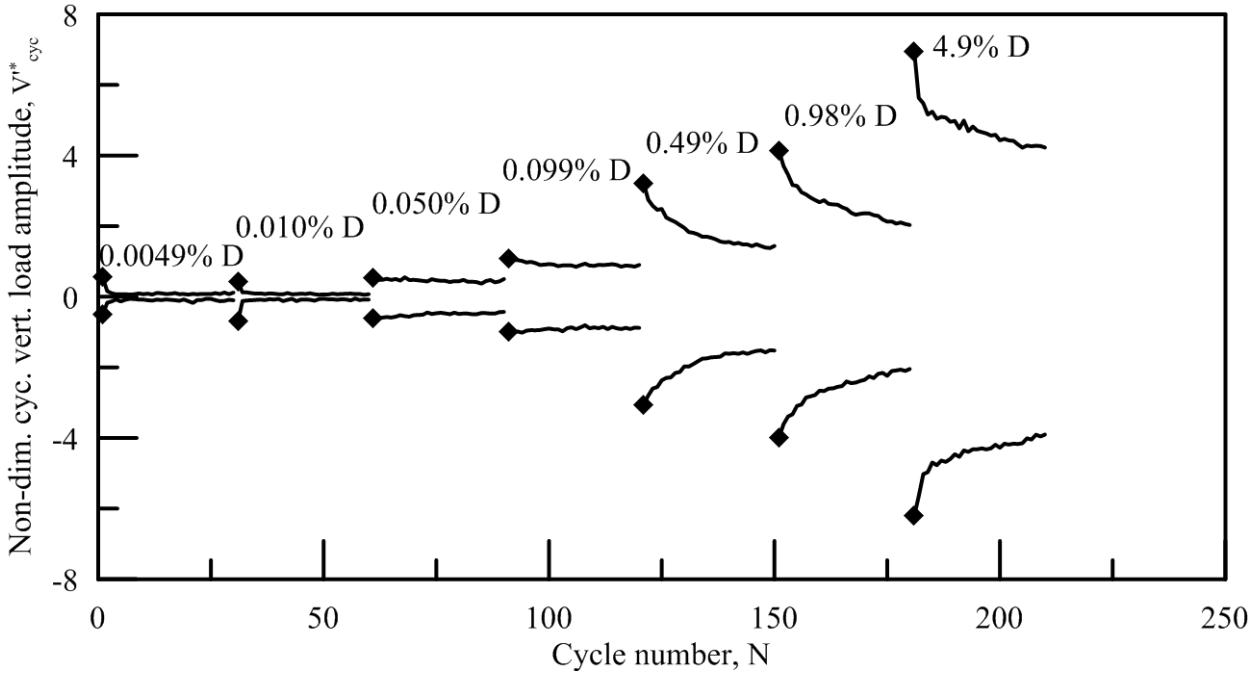

Figure 5.29: Drained vertical cyclic load amplitude, $V'^{*}_{cyc,dr}$, versus number of cycles for K-90G-AR2-V-Cyc-4

Figure 5.30: The 90-g kaolin test bed surface of K-90G-TB1, 377 mm in model scale diameter, showing the testing locations of K-90G-AR2-V-Mono-1 (left) and K-90G-AR2-V-Mono-2 (right) after being removed from the geotechnical centrifuge

Figure 5.31: The 90-g kaolin test bed surface of K-90G-TB2, 377 mm in model scale diameter, showing the testing locations of K-90G-AR1-V-Mono-1 (top) and K-90G-AR1-V-Mono-2 (bottom) after being removed from the geotechnical centrifuge

Figure 5.32: The 90-g kaolin test bed surface of K-90G-TB3, 377 mm in model scale diameter, showing the testing locations of K-90G-AR2-V-Cyc-2 (top) and K-90G-AR2-V-Cyc-1 (bottom) after being removed from the geotechnical centrifuge

Figure 5.33: The 90-g kaolin test bed surface of K-90G-TB4, 377 mm in model scale diameter, showing the testing locations of K-90G-AR1-V-Cyc-1 (top) and K-90G-AR1-V-Cyc-2 (bottom) after being removed from the geotechnical centrifuge

Figure 5.34: The 90-g kaolin test bed surface of K-90G-TB5, 377 mm in model scale diameter, showing the testing locations of K-90G-AR1-V-Mono-3 (top) and K-90G-AR1-V-Mono-4 (bottom) after being removed from the geotechnical centrifuge

Figure 5.35: The 90-g kaolin test bed surface of K-90G-TB6, 377 mm in model scale diameter, showing the testing locations of K-90G-AR2-V-Mono-3 (top) and K-90G-AR2-V-Mono-4 (bottom) after being removed from the geotechnical centrifuge

Figure 5.36: The 90-g kaolin test bed surface of K-90G-TB7, 377 mm in model scale diameter, showing the testing locations of K-90G-AR1-V-Cyc-3 (top) and K-90G-AR1-V-Cyc-4 (bottom) after being removed from the geotechnical centrifuge

Figure 5.37: The 90-g kaolin test bed surface of K-90G-TB8, 377 mm in model scale diameter, showing the testing locations of K-90G-AR2-V-Cyc-3 (top) and K-90G-AR2-V-Cyc-4 (bottom) after being removed from the geotechnical centrifuge

5.8 References

API RP 2GEO. (2011). "Geotechnical and Foundation Design Considerations." ANSI/API Recommended Practice 2GEO, First Edition, American Petroleum Institute.

API RP 2SK. (2008). "Design and Analysis of Stationkeeping Systems for Floating Structures." API Recommended Practice 2SK, Third Edition, American Petroleum Institute.

Byrne, B.W. & Cassidy, M.J. (2002). "Investigating the response of offshore foundations in soft clay soils." *Proceedings of OMAE'02 21st International conference of Offshore Mechanics and Arctic Engineering.* Oslo, Norway.

Chen, C.H. (2013). "Performance of Suction Caissons with a Small Aspect Ratio." Ph.D. thesis, The University of Texas at Austin.

Dendani, H. (2003). "Suction Anchors: Some critical aspects for their design and installation in clayey soils." Offshore Technology Conference. Houston, TX, USA.

El-Sherbiny, R. (2005). Performance of Suction Caisson Anchors in Normally Consolidated Clay. Ph.D. Dissertation, The University of Texas at Austin.

Gourvenec, S., Acosta-Martinez, H. & Randolph M.F. (2009). "Experimental study of uplift resistance of shallow skirted foundations in clay under transient and sustained concentric loading." *Geotechnique.* 59(6):525-537.

Kelly, R.B., Houslby, G.T. & Byrne, B.W. (2006). "A comparison of field and laboratory tests of caisson foundations in sand and clay." *Geotechnique*. 56(9):617-626.

Luke, A.M., Rauch, A.F. Olson, R.E. & Mecham, E.C. (2005). "Components of suction caisson capacity measured in axial pullout tests." *Ocean Engineering.* 32:878-898.

Mesri, G. (2001). "Undrained shear strength of soft clays from push cone penetration test." *Géotechnique*. 51(2):167-168.

Munk, W.H. (1950). "Origin and generation of waves." *Proc. 1st International Conference on Coastal Engineering*. Long Beach, CA, USA.

Skempton, A.W. (1951). "The bearing capacity of clays." *Proceedings, Building Research Congress*. London, UK.

CHAPTER 6. 1-G MODEL LOAD TESTS IN LAPONITE

6.1 General

A total of eight 1-g model load tests were conducted in the laponite 1-g test beds (Section 3.3) to study the response of suction caissons under monotonic undrained loading conditions in order to visualize the failure mechanism beneath the foundation. These tests were conducted on two model foundations with aspect ratios of 1 and 2. The types of loading conditions investigated were undrained monotonic vertical. A brief description of the 1-g model load tests including the test identifier and associated laponite 1-g test bed is given in Table 6.1. As indicated in Table 6.1, the total of eight tests were comprised of two sets of four load tests in order to verify the repeatability of the results.

6.2 Experimental apparatus

6.2.1 Model foundations

The two 6061-T6 aluminum model suction caisson foundations utilized in the 1-g model load tests in laponite were the same as those utilized for the 90-g model load tests in kaolin described in Section 5.2.1. The two model foundations were coated with matte black paint as shown in Figure 6.1 to minimize the reflection of the laser off of the model foundations. These two black-coated foundations were again distinguished by their aspect ratios and were identified as L-1G-AR1 and L-1G-AR2. L-1G-AR1 had a diameter (D) of 38.1 mm, a skirt length (L) of 38.1 mm, and a wall thickness (t_{wall}) of 1.3 mm resulting in an aspect ratio of 1 and a diameter to wall thickness ratio of 29. L-1G-AR2 had a diameter (D) of 38.1 mm, a skirt length (L) of 76.2 mm, and a wall thickness (t_{wall}) of 1.3 mm resulting in an aspect ratio of 1 and a diameter to wall thickness ratio of 29. The diameter to wall thickness ratio was higher than typical values of suction caissons, however, they allowed for jacking installation of the foundations and ensured that the response observed during testing was that of the soil rather than the aluminum.

The top cap of both foundations consisted of a 6.4 mm thick aluminum plate with the same diameter as the skirt of the suction caisson. The top cap was welded thoroughly with no gaps to ensure no water could permeate through the connection. A threaded opening was positioned in the top cap to allow for ventilation of the inside of the suction caisson during installation. This threaded opening could be closed to prevent ventilation during any loading

phases. A loading rod was positioned in the center of the top cap. Two load cells were positioned along the loading rod in the vertical and horizontal orientation as shown in Figure 6.2 to measure the respectively oriented loads on the model foundation. Two ball and socket joints were also positioned along the loading rod. These were both left locked in order to prevent rotation of the model foundations as the loading under investigation was vertical. A flat platform and accelerometers were also positioned along the loading rod. The flat platform, accelerometers, locking ball and socket joints, and load cells were present because the loading rod was originally designed to accommodate vertical and horizontal loading of very small models in kaolin. These functions, however, were not utilized during the investigated vertical load tests in laponite as the deformations of the laponite rather than the load response of the laponite were the focus of the investigation. Due to space and soil strength constraints, vertical displacements were determined based on the displacement of the motor.

6.2.2 Loading apparatus

The loading apparatus utilized for the 1-g model load tests in laponite was the same as that of the 1-g model load tests in kaolin described in Section 4.2.2 with modifications made to account for the differences in foundation and test bed size. The apparatus modifications are shown in Figure 5.3. The first modification consisted of a 19 mm thick PVC plate positioned on the steel support frame that would allow for the test beds to be positioned closer the linear slides. The second modification was an extension of the cantilever arm to position the model foundation closer to the edge of the container sidewall to minimize transparency degradation. The third was the changes to the loading rod attachment point and loading rod as described in Section 6.2.1.

6.3 Experimental methodology

One laponite 1-g model test bed was prepared for each pair of 1-g model load tests conducted in laponite. Two model load tests could be conducted in each test bed due to the offset of the positioning of the foundation over the test bed. The offset was 85 mm from the center of the test bed along one of the horizontal centerlines of the container. After conducting the first load test in one of the locations, the test bed was rotated by 180^{o} to test in the second position. The position offset resulted in a minimum distance between the foundations and the edge of the container wall of 1.1D. This distance was primarily a function of laponite transparency in that an increase thickness of laponite between the digital camera and the plane of laser light resulted in a

decrease in transparency. A distance of 61 mm between the container wall and the laser plane was determined to be the ideal location that still allowed for displacement visualization while minimizing boundary effects. The minimum distance between the load test locations (skirt wall to skirt wall) was 3.5D. Each of the load tests generally consisted of an installation phase, a system configuration phase, a loading phase, and a vented extraction phase.

6.3.1 Installation

To install the model suction caissons, the foundation was first attached to the loading apparatus and positioned over one of the two load test locations within the test bed. With the vent valve open, the foundations were then installed under constant velocities of 0.05 mm/s for both L-1G-AR1 and L-1G-AR2. Both of these velocities resulted in non-dimensional velocities of 196 corresponding to undrained conditions based on a coefficient of consolidation of 0.00032 mm^2/s. The installation phase was terminated by means of visual observation as the noise in the data acquisition system, load cell resolution, and undrained strength of the laponite did not lend to accurate indication of top cap contact via load cell readings. After the installation phase was completed, a minimum period of 20 minutes was included to allow for reconfiguration of the loading apparatus and model foundation for the loading phase.

6.3.2 Undrained monotonic vertical loading

Undrained monotonic vertical load tests were conducted on the model foundation to load the laponite under undrained conditions. During this phase, all the ball and socket joints on the loading rod were left locked and prevented all rotations of the model foundations. The top cap vent valve was also closed during loading. These loading phases were conducted at a constant velocity of 0.008 mm/s for both L-1G-AR1 and L-1G-AR2 similar to the load tests conducted in kaolin. The velocity was determined at the foundation reference point that was defined as the center of the bottom side of the top cap that made contact with the soil surface. These velocities correspond to the non-dimensional velocities of 961 and therefore undrained conditions. A total of eight undrained monotonic vertical load tests were conducted as listed in Table 6.1. The eight tests allowed for digital images to be taken during undrained monotonic vertical compression and undrained monotonic vertical uplift on L-1G-AR1 and L-1G-AR2. Each load test type on each foundation was repeated twice for a total of eight. Regardless of the direction of loading, the displacement of the loading phase was 15% of the diameter of the foundation.

The digital images were taken every 30 seconds over the course of the undrained monotonic compression or uplift load test. The first image corresponded to the initial position and was captured just before the constant velocity loading begun. The final image corresponded to a foundation position corresponding to the final displacement of 15% of the diameter or 5.7 mm and was captured just after the loading phase was terminated. This resulted in 24 to 25 digital images for each load test taken over a period of approximately 12 minutes. The DSLR digital camera used to capture these images was positioned perpendicular to the face of the acrylic container positioned closest to the model suction caisson. This position of the camera allowed for the capture of the entirety of the vertical cross section of the laponite test bed illuminated by the laser. The dimensions of this cross section were the test bed height given in Table 3.7 and a width of 292 mm. A HeNe laser was passed through a line lens to create a plane of laser light along which deformations were tracked. This plane of laser light was oriented vertically and positioned parallel to the vertical container wall facing the camera while also passing through the vertical centerline of the model suction caisson. All lights in the room other than the laser light were turned off during testing.

6.3.3 Extraction

The extractions of the model suction caissons were conducted after the completion of the investigated load test described in Section 6.3.2. These extractions were not conducted under undrained loading in order to prevent detachment and subsequent retention of laponite in the model suction caisson. The model suction caissons were vented and extracted under constant velocity at 0.05 mm/s or the same as the installation velocity. Plug failure was avoided to minimize the potential of laser reflection and refraction due to a plug of air in the test bed and to minimize potential slope stability failures into the gap left behind. Images were not obtained during the extraction process.

6.4 Experimental results

6.4.1 Optical flow estimation of digital images

The digital images obtained during the load tests were analyzed using a computer program that conducted optical flow estimation in the extended coarse to fine refinement framework as outlined by Xu et al. (2012). This framework overcomes the major issue of optical

flow estimation where fine motion structures could not be accurately determined in regions with drastically abrupt displacement changes. Dr. Junxing Zheng at Iowa State University initially developed the program and verified its applicability for use in geotechnical applications Zheng and Hryciw (2014). The program analyzed the series of 24 to 25 pictures from the first image taken prior to displacement and final image taken shortly after displacement ends and produces a vector field of displacements. For the analysis, the images were cropped down to minimize the portions that did not incorporate the vertical cross section of the laponite illuminated by the laser light. These generated vector fields of displacement images provide the total displacement at each point in the image over the course of the entire series of images or the entire load test. Zone I of the three-zone Rankine failure wedge as shown in Figure 2.7 was overlaid over all vector plots for comparison with design manual assumptions. All three zones were not overlain, as only the full development of Zone I was observed. Although plastic equilibrium theory resulting in the three-zone failure mechanism has been well documented to not be applicable to soft soils such as laponite, the bearing capacity design equations based on the theory are still utilized today for soft clays. It has been commonly assumed that soft soils will mobilize a partial mobilization of the three-zone Rankine failure wedge mechanism. It was important to note that the vectors were overlaid over the final analyzed images. The vectors of displacement however were accumulations at a specific point in space over the course of the entire image set resulting in distortion of the analysis in relation to the position of the model foundation as shown in the image.

In addition to this distortion, errors in the optical flow estimation existed due to the following: noise in the digital images due to the dark lighting conditions, degradation of the transparency of laponite with increasing thickness of laponite between the laser plane and the camera, shadowing of the laser due to the foundation, and refraction of the laser within the sample due to the seeding particles and laponite particles. The noise in the digital image was accounted for by conducting tests with relatively large displacement in order to overcome the minute displacements resulting from noise in the images. The degradation of the transparency of laponite was overcome by positioning the plane of laser light at an average distance of 61 mm from the container wall through which images were captured. The shadowing and refraction resulted in potential for minor inconsistencies between displacements on opposing sides of the

central vertical axis of the foundation. Due to these inconsistencies, the displacements on the laser side of the centerline were more accurate than those on the far side.

6.4.2 Monotonic undrained compression failure visualization

The results of the optical flow estimation analysis for the monotonic undrained compression load tests are shown in Figure 6.5, Figure 6.7, Figure 6.9, and Figure 6.11 for L-1G-AR1-Mono-1, L-1G-AR2-Mono-1, L-1G-AR1-Mono-3, and L-1G-AR2-Mono-3 respectively. These figures are cropped down versions of the vector fields resulting from the analyses described in Section 6.4.1 as the displacements occurring at locations larger than two diameters from the suction caisson model were insignificant. All four of the compression load tests showed the formation of a triangular wedge of soil immediately below the foundation. This triangular wedge displaced approximately the same magnitude of displacement as the foundation in the downward direction. This triangular wedge displacing with the foundation corresponds to Zone I of the plastic equilibrium theory assumed by Skempton (1951) as sketched in Figure 2.7. The triangular wedges drawn in Figure 6.5, Figure 6.7, Figure 6.9, and Figure 6.11 are all 45^o-45^o-90^o right triangles as theory suggests for a plastic equilibrium bearing capacity failure mechanism.

While there was clear development of Zone I, the clear developments of Zone II or Zone III of the three-zone failure mechanism were not observed. The displacement magnitude outside of Zone I increased with decreasing distance from the triangular Zone I. This indicates that there was relative displacement of the soil outside of Zone I where displacements. The displacements outside of Zone I were indicative of a radial shear zone that arced back towards the foundation skirt walls. The transition of a radial shear zone (Zone II) to a Rankine shear zone (Zone III) was not observed. The triangular Zone I combined with the radial displacements arcing back towards the foundation displayed similarities of the displacement fields surrounding a cone penetrometer or CPT by Chini et al. (2015). The CPT bearing capacity factor ranges from 10 to 20 with an average of 14 (Robertson 2009). The triangular Zone I resembles the CPT's cone tip albeit with a 90^o triangular wedge of soil rather a 60^o cone tip and a foundation skirt rather than a loading rod. However, the similarities of the deformation field to the CPT and the CPT's higher bearing capacity factors provide an explanation for the higher bearing capacity factors back-calculated in the 1-g and 90-g load tests in kaolin.

6.4.3 Monotonic undrained uplift failure visualization

The results of the optical flow estimation analysis for the monotonic undrained uplift load tests are shown in Figure 6.6, Figure 6.8, Figure 6.10, and Figure 6.12 for L-1G-AR1-Mono-2, L-1G-AR2-Mono-2, L-1G-AR1-Mono-4, and L-1G-AR2-Mono-4 respectively. All four of the uplift load tests showed the formation of a triangular wedge of soil immediately below the foundation. This triangular wedge displaced approximately the same magnitude as the foundation in the upward direction. This triangular wedge displacing with the foundation corresponded to Zone I of the plastic equilibrium theory assumed by Skempton (1951) as sketched in Figure 2.7. The triangular wedges drawn in Figure 6.5, Figure 6.7, Figure 6.9, and Figure 6.11 are all 45^o-45^o-90^o right triangles as theory suggests for a plastic equilibrium bearing capacity failure mechanism. These observations were similar to those in monotonic compression with the displacement occurring in the opposite direction due to the uplift rather than compression loading mechanism.

While there was clear development of Zone I, the clear developments of Zone II or Zone III of the three-zone failure mechanism were not observed. The displacement magnitude outside of Zone I increased with decreasing distance from the triangular Zone I. This indicated that there was relative displacement of the soil outside of Zone I where displacements. The displacements outside of Zone I were indicative of a radial shear zone that arced back towards the foundation skirt walls. The transition of a radial shear zone (Zone II) to a Rankine shear zone (Zone III) was not observed. The triangular Zone I combined with the radial displacements arcing back towards the foundation displayed similarities of the displacement fields surrounding a cone penetrometer or CPT by Chini et al. (2015). The CPT bearing capacity factor ranges from 10 to 20 with an average of 14 (Robertson 2009). The triangular Zone I resembles the CPT's cone tip albeit with a 90^o triangular wedge of soil rather a 60^o cone tip and a foundation skirt rather than a loading rod. However, the similarities of the deformation field to the CPT and the CPT's higher bearing capacity factors provide an explanation for the higher bearing capacity factors back-calculated in the 1-g and 90-g load tests in kaolin. These observations were similar to those in monotonic compression, but in the opposing direction.

6.4.4 Vented extraction

The vented extraction that occurred after the load tests did not result in plug detachment. This was the ideal extraction condition as it minimized the potential for deformations across the

entire test bed with time and reflection of the laser light if a large cavity was introduced via the plug being retained in the model suction caisson. However, due to the vented extraction and lack of plug retention a clear scarp was not observable after extraction.

6.5 Conclusions

The results of the visualization of the undrained 1-g model load tests in laponite described in this chapter led to the following conclusions for monotonic undrained vertical loading of suction caisson foundations:

1. The failure mechanism mobilized during undrained monotonic vertical loading resembles a partial formation of the commonly assumed plastic equilibrium theory based failure mechanism. This partial formation of the three-zone Rankine type failure mechanism was mobilized in both compression and in uplift.
2. The triangular zone or Zone I of the plastic equilibrium theory displayed full development and displaced approximately the same magnitude of displacement as the foundation in both compression and uplift. This triangular zone was well approximated by a 45^{o}-45^{o}-90^{o} right triangle as assumed by theory. This triangular wedge functioned similarly to the cone tip of a CPT.
3. The deformations outside of Zone I showed relative deformation based on proximity to Zone I. Partial formations of these zones has been predicted for softer soils such as laponite as stated by Terzaghi et al. (1996) as plastic equilibrium theory predictions were developed for ideal, hard materials. The displacements outside of Zone I were radial displacements arcing back towards the foundation and displayed similarities of the displacement fields surrounding a cone penetrometer or CPT by Chini et al. (2015).
4. Items listed in 2 and 3 above indicate a deviation from the plastic equilibrium theory assumed in Skempton (1951) and therefore the design equations of API RP 2GEO (2011) while also showing similarities to deformations resulting from a CPT. These deviations in conjunction with the lower than predicted side shear mobilization account for the larger than recommended bearing capacity factors across both 1-g and 90-g kaolin load tests. The bearing capacity factor of the CPT test ranges from 10 to 20 with an average of 14 (Robertson 2009).

6.6 Tables

Table 6.1: Brief description of 1-g model vertical load tests in laponite

Identifier	Test bed	Type	Description
L-1G-AR1-V-Mono-1	L-1G-TB1	Undrained, monotonic	Compression
L-1G-AR1-V-Mono-2	L-1G-TB1	Undrained, monotonic	Uplift
L-1G-AR2-V-Mono-1	L-1G-TB2	Undrained, monotonic	Compression
L-1G-AR2-V-Mono-2	L-1G-TB2	Undrained, monotonic	Uplift
L-1G-AR1-V-Mono-3	L-1G-TB3	Undrained, monotonic	Compression
L-1G-AR1-V-Mono-4	L-1G-TB3	Undrained, monotonic	Uplift
L-1G-AR2-V-Mono-3	L-1G-TB4	Undrained, monotonic	Compression
L-1G-AR2-V-Mono-4	L-1G-TB4	Undrained, monotonic	Uplift

6.7 Figures

Figure 6.1: The two laponite 1-g model suction caissons with L-1G-AR1 shown on the left and L-1G-AR2 shown on the right

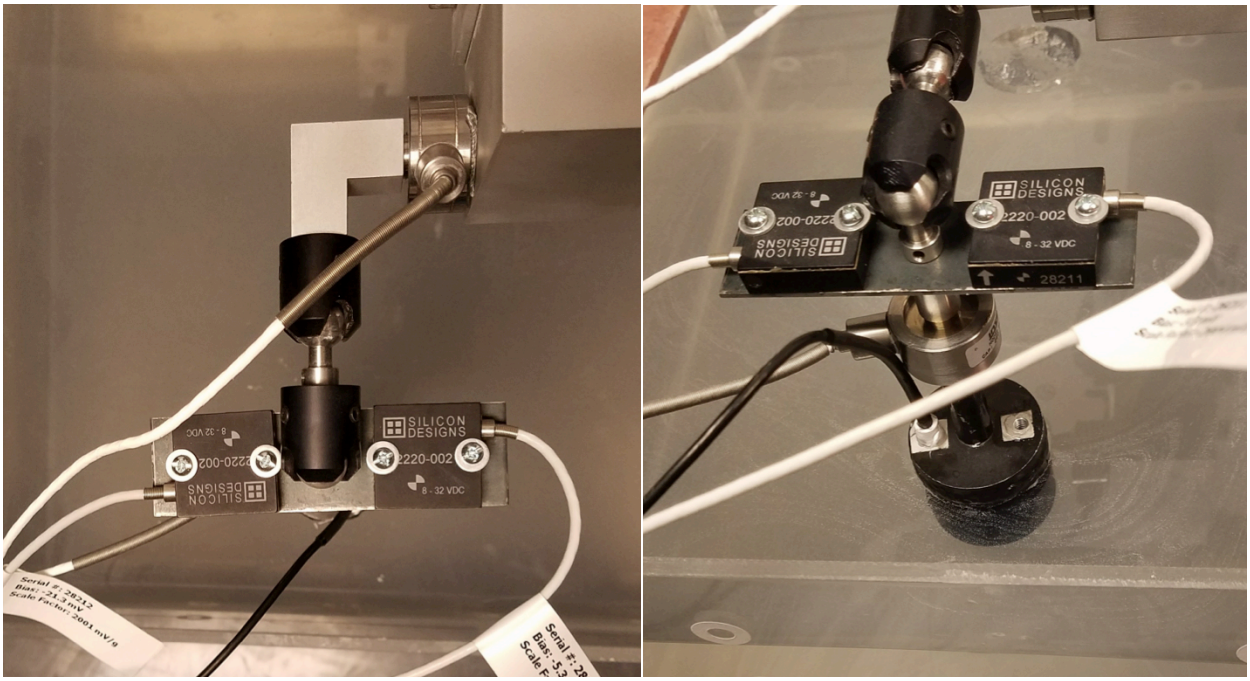

Figure 6.2: Two views of the loading rod and associated built in sensors for the two laponite 1-g model suction caissons

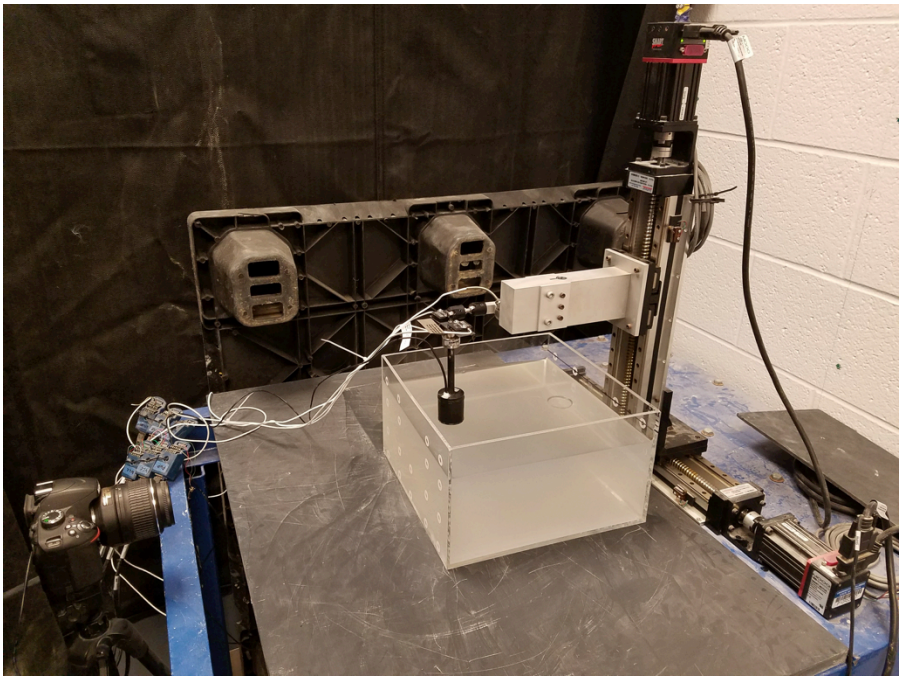

Figure 6.3: The loading apparatus as shown positioned above the test bed container along with the DSLR camera

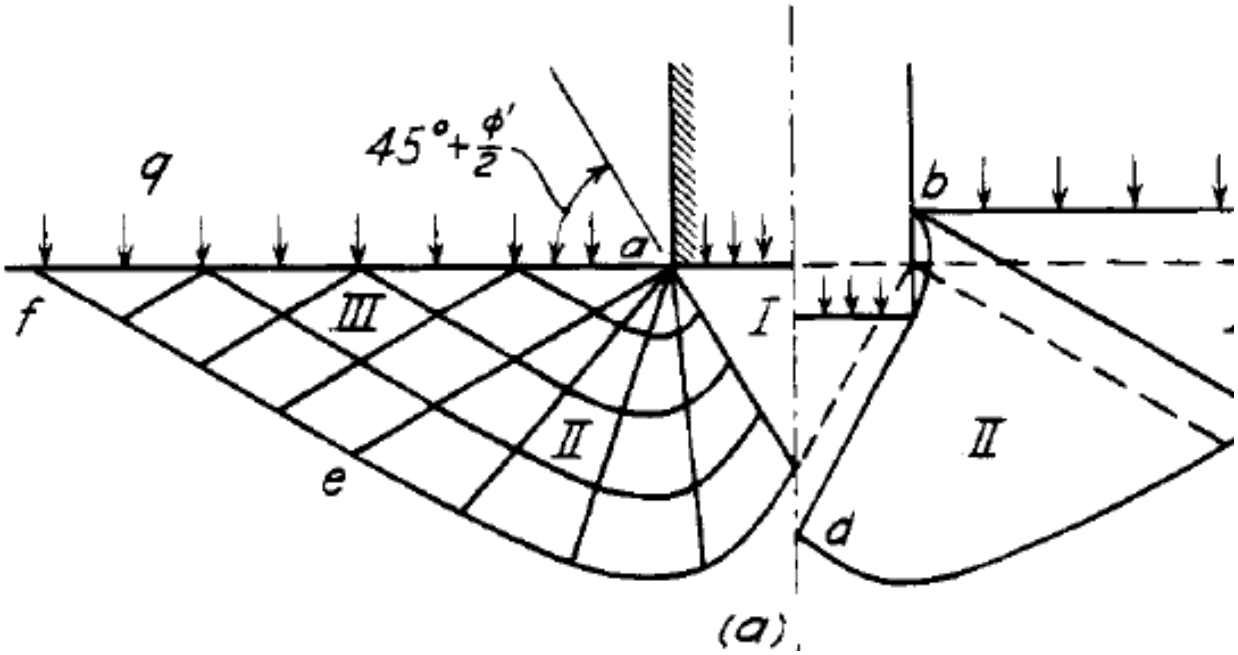

Figure 6.4: Example of a general shear mechanism for shallow foundations (Terzaghi et al. 1996)

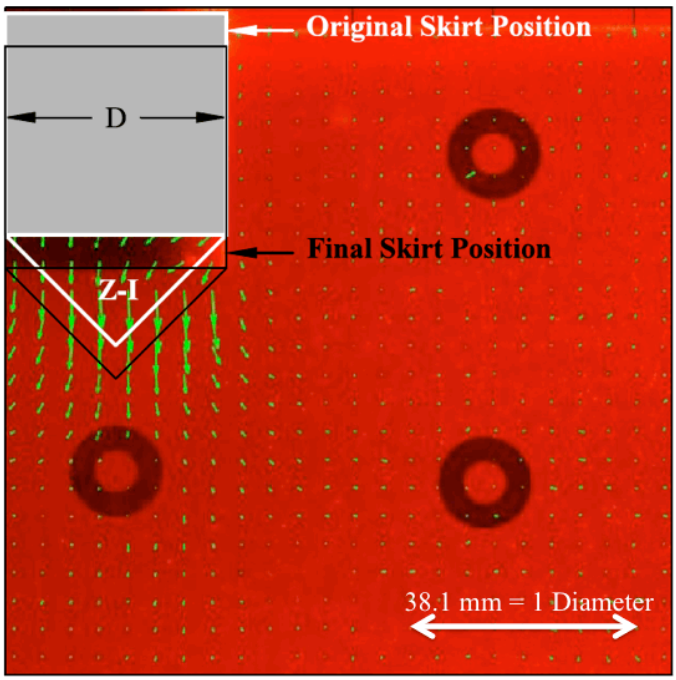

Figure 6.5: Optical flow estimation results for the compression load test L-1G-AR1-V-Mono-1 with an overlay of the Zone I triangular elastic wedge based on the analysis

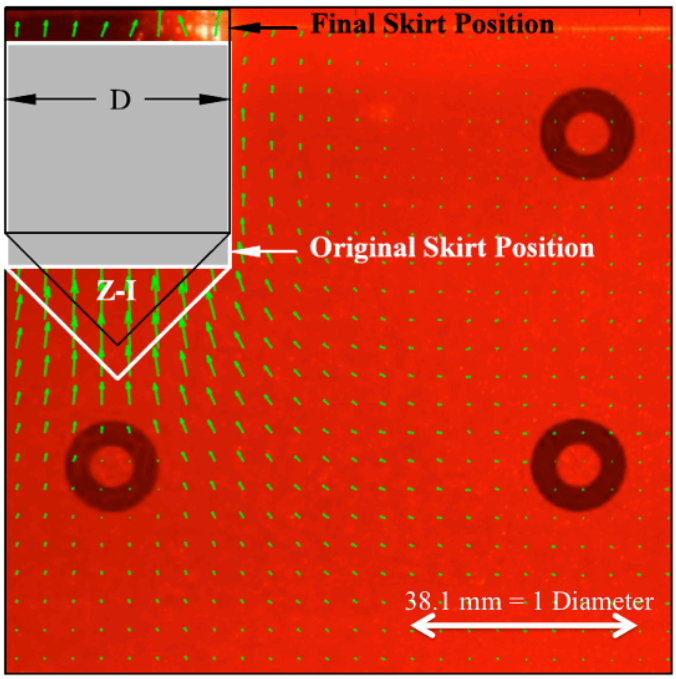

Figure 6.6: Optical flow estimation results for the uplift load test L-1G-AR1-V-Mono-2 with an overlay of the Zone I triangular elastic wedge based on the analysis

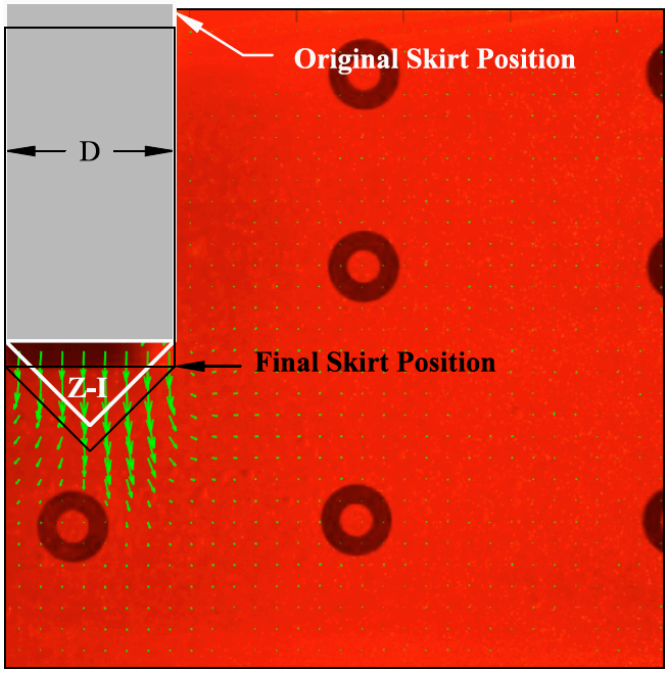

Figure 6.7: Optical flow estimation results for the compression load test L-1G-AR2-V-Mono-1 with an overlay of the Zone I triangular elastic wedge based on the analysis

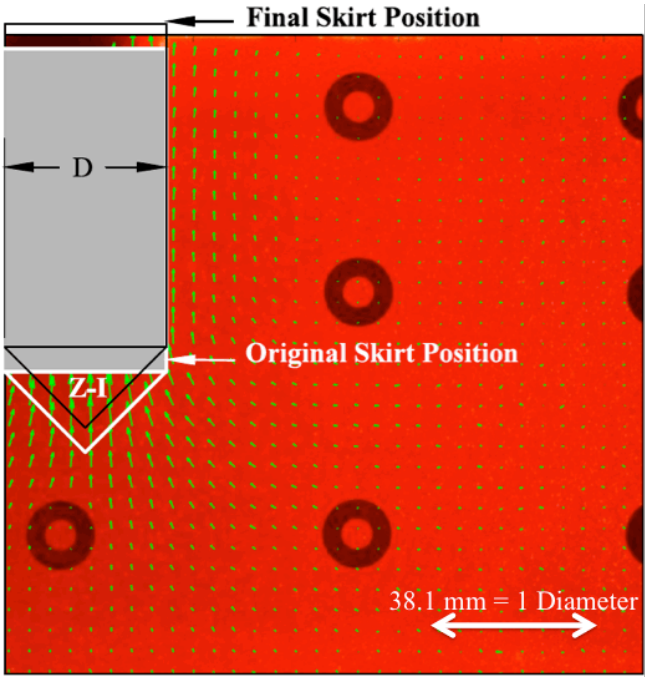

Figure 6.8: Optical flow estimation results for the uplift load test L-1G-AR2-V-Mono-2 with an overlay of the Zone I triangular elastic wedge based on the analysis

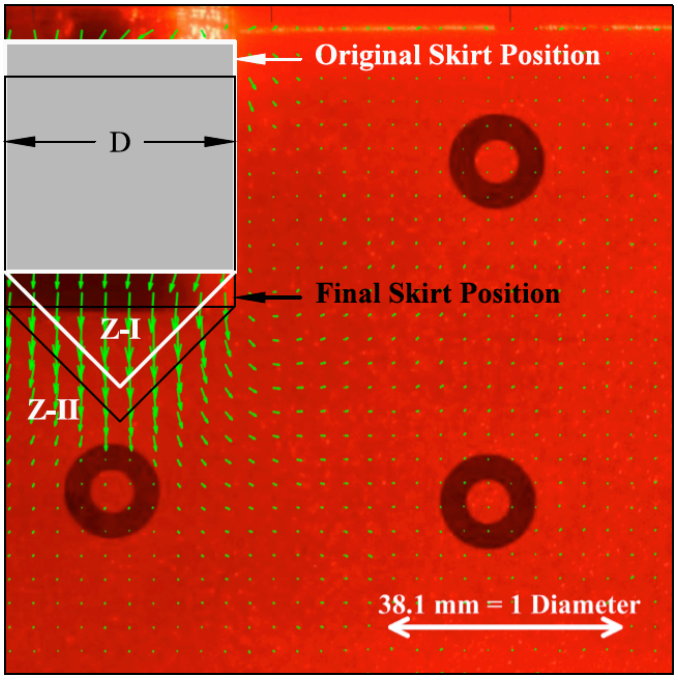

Figure 6.9: Optical flow estimation results for the compression load test L-1G-AR1-V-Mono-3 with an overlay of the Zone I triangular elastic wedge based on the analysis

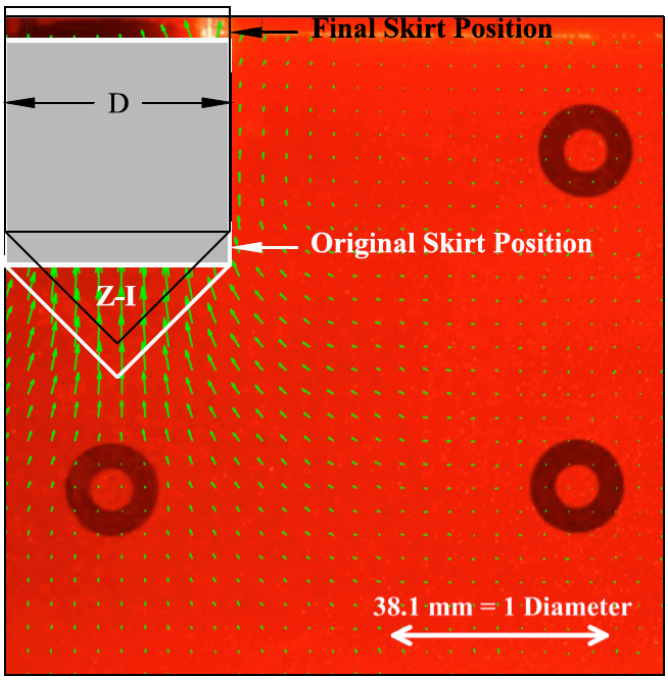

Figure 6.10: Optical flow estimation results for the uplift load test L-1G-AR1-V-Mono-4 with an overlay of the Zone I triangular elastic wedge based on the analysis

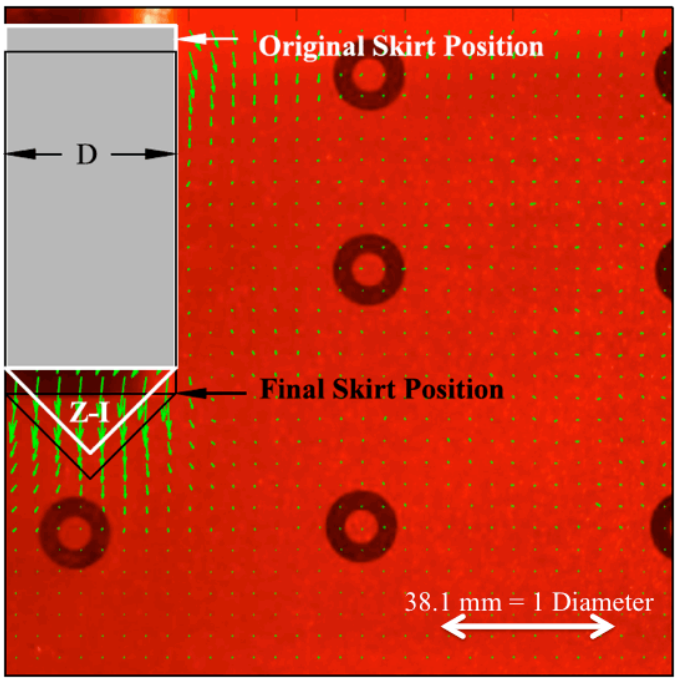

Figure 6.11: Optical flow estimation results for the compression load test L-1G-AR2-V-Mono-3 with an overlay of the Zone I triangular elastic wedge based on the analysis

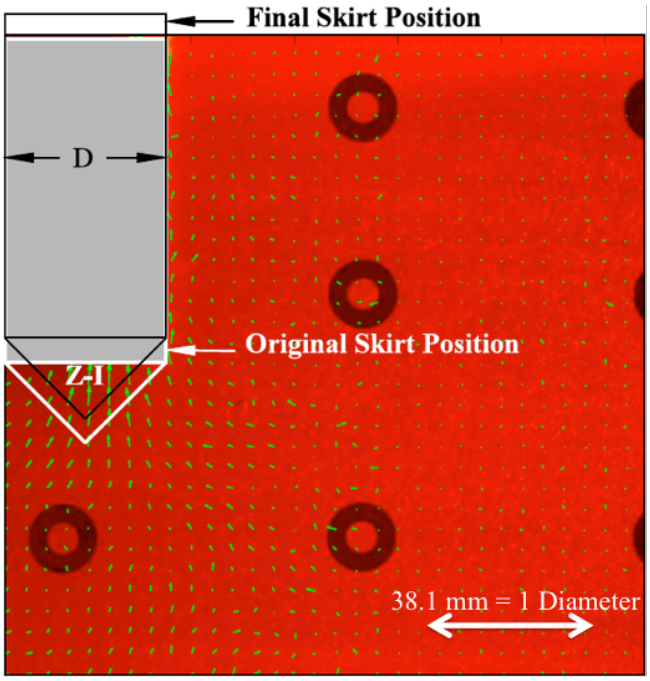

Figure 6.12: Optical flow estimation results for the uplift load test L-1G-AR2-V-Mono-4 with an overlay of the Zone I triangular elastic wedge based on the analysis

6.8 References

API RP 2GEO. (2011). "Geotechnical and Foundation Design Considerations." ANSI/API Recommended Practice 2GEO, First Edition, American Petroleum Institute.

Chini, C.M., Wallace, J.F., Rutherford, C.J. & Peschel, J.M. (2015). "Shearing Failure Visualization Using Digital Image Correlation and Particle Image Velocimetry in Soft Clay Using a Transparent Soil." *Geotech. Test. J.* 38(5):1-17.

Robertson, P.K. (2009). "Interpretation of cone penetration tests – a unified approach." *Can. Geotech. J.* 46:1337-1355.

Skempton, A.W. (1951). "The bearing capacity of clays." *Proceedings, Building Research Congress*. London, UK.

Terzaghi, K., Peck, R.B. & Mesri, G. (1996). *Soil Mechanics in Engineering Practice*. 3rd Edition. John Wiley & Sons, Inc. New York City, New York, USA.

Xu, L., Jia, J., & Matsushita, Y. (2012). "Motion Detail Preserving Optical Flow Estimation." *IEEE Transactions on Pattern Analysis and Machine Intelligence*. 34(9):1744-1757.

Zheng, J. & Hryciw, R. (2014). “Optical Flow Analysis of Internal Erosion and Piping in Soil Images Captured by the VisCPT.” *Tunneling and Underground Construction GSP 242*. 55-64. American Society of Civil Engineers. Aston, Virginia, USA.

CHAPTER 7. SUMMARY, RECOMMENDATIONS, AND CONCLUDING REMARKS

7.1 General

The results of the 1-g load tests in kaolin (CHAPTER 4), 90-g load tests in kaolin (CHAPTER 5), and 90-g load tests in laponite (CHAPTER 6) along with each of their respective test beds (CHAPTER 3) have been discussed in this dissertation. This chapter summarizes and synthesizes the conclusions of the three types of scaled load testing and presents the final design recommendations derived from the results of the load tests. Based on the observed behaviors, future work will also be suggested that fell outside of the scope of this study.

7.2 Summary and synthesis

The three types of load tests described in previous chapters each provided multiple conclusions regarding the behavior of suction caisson foundations under loading conditions applicable to tidal energy converter applications with aspect ratios (or length to diameter ratios) of 1 and 2. The 1-g load tests in kaolin provided insights into the behavior of the foundations in the multipod and monopod configurations under monotonic loading, short period (5 seconds) cyclic loading, and extreme loading. The 1-g kaolin test beds provided soil conditions that were highly overconsolidated. The 90-g load tests in kaolin provided insights into the behavior of the foundations in the multi-pod configuration under monotonic loading, longer period (15 minutes and 10.8 hours) cyclic loading, and extreme loading. The 90-g test beds provided soil conditions that were lightly overconsolidated. The differences between the overconsolidation ratios of the two tests beds allowed for the consideration of the potential wide range of overconsolidation ratios at tidal energy converters due to erosion from the high speed currents. The 1-g load tests in laponite provided insights into the failure mechanism beneath the suction caisson under vertical loading.

7.2.1 Comparison of 1-g and 90-g load tests in kaolin

The Kelly et al. (2006) non-dimensionalization procedures utilized in this study provided an adequate avenue of scaling the model lab tests for field or design use in the future as described in Sections 2.3.5, 4.4.1, and 5.4.1. While the non-dimensionalization procedures were intended for the scaling up of the model load tests in the future, they also allowed for comparison of the 1-g and 90-g load tests. The load tests that had counterparts in the two differing model

scales were the monotonic undrained compression and uplift tests on both the respective AR1 and AR2 foundations. The comparison of these counterpart load tests are shown in Figure 7.1 for the comparison of K-1G-AR1-V-Mono-1 to K-90G-AR1-V-Mono-1, Figure 7.2 for the comparison of K-1G-AR1-V-Mono-2 to K-90G-AR1-V-Mono-3, Figure 7.3 for the comparison of K-1G-AR2-V-Mono-1 to K-90G-AR2-V-Mono-1, and Figure 7.4 for the comparison of K-1G-AR2-V-Mono-2 to K-90G-AR2-V-Mono-3. In general, the non-dimensionalized ultimate capacities of the 1-g load tests displayed adequate agreement with its corresponding 90-g load test with differences ranging between -32% to +7%. However, the load-displacement response displayed significant differences. The load response of the 1-g load tests was strain-softening while the load response of the 90-g load tests was strain hardening. This difference however stems from the difference in stress-state resulting in a significant difference in OCR of the two test beds. Element level tests on clay exhibit the same difference in load response for heavily and lightly overconsolidated specimens. The Kelly et al. (2006) procedures do not account for differences in undrained shear strength and diameter of the foundation, but do not account for the OCR of the clay. Therefore, the use of the reported results must carefully consider the OCR of the clay in question.

7.2.2 Multi-pod versus mono-pod configuration

The 1-g load tests in kaolin investigated the feasibility of the multi-pod configuration and mono-pod configuration for the suction caisson foundations. Due to serviceability constraints of most offshore energy structures and the resulting assumption of small rotations of the overall structure, the foundation configuration results in the transmission of the tidal current's loads on the structure to horizontal/moment loads on mono-pod foundations and vertical loads on multi-pod foundations. In general the lower the aspect ratio, the lower the horizontal/moment loading of the foundation. For the investigated aspect ratios, the horizontal ultimate capacities were 14% to 20% of the vertical ultimate capacities in heavily overconsolidated kaolin. These lower horizontal capacities in additional to the strain-hardening behavior of the horizontal loading response led to the conclusion that the multi-pod configuration would commonly lead to a more efficient foundation design. This was primarily due to the multi-pod transferring the current load on the structure as vertical loads on the foundation.

7.2.3 Vertical loading failure mechanism

While the 1-g load tests in laponite were conducted after the two series of load tests conducted in kaolin, they provided key observations that provided further insight to those observed during the two scales of load tests in kaolin. The failure mechanisms observed beneath both the aspect ratio 1 and 2 suction caissons during undrained vertical load tests were punching failure mechanisms similar to that of a cone penetrometer in both uplift and compression. The uplift failure mechanism was very similar to the compression failure mechanism, but in the opposing direction. The partial formation contradicts the assumption of full development of the theoretical failure surface that serves as the basis of the design recommendations for bearing capacity of suction caissons provided by the American Petroleum Institute. A contradiction of some form, however, was expected since the Skempton (1951) bearing capacity theory that was referenced in API RP 2GEO (2011) assumes that the soil was an ideal stiff or hard material.

Of the assumed theoretical failure mechanism, the triangular wedge of soil immediately below the foundation (Zone I) showed full development during the load tests. The extents of these triangular wedges coincided with 45^{o}-45^{o}-90^{o} right triangles. The deformations outside of the Zone I triangle, were characterized by higher magnitudes of displacement with decreasing distance from Zone I and displacement directions more akin to radial displacements observed during cone penetrometer movement visualized by Chini et al. (2015) rather than those predicted by plastic equilibrium theory of shallow foundations. The Skempton (1951) bearing capacity theory of shallow foundations suggests a bearing capacity of 9 at full embedment while Robertson (2009) suggests values of 10 to 20 with an average of 14 for cone penetrometers in clay.

The higher bearing capacity factors for the cone penetrometer and the similarities between the observed deformations for suctions caissons with that of the cone penetrometer explains the primarily higher back-calculated bearing capacity factors during the 1-g and 90-g vertical undrained load tests in kaolin. The circular scarping that formed around the 1-g and 90-g vertical undrained load tests in kaolin, particularly during the extraction process, coincided with a partial formation of the theoretical bearing capacity mechanism for shallow foundations. The kaolin and laponite load tests therefore all concluded that a partial formation of the theoretical bearing capacity failure mechanism was mobilized for suction caisson vertical loading in soft clay.

7.2.4 Load response differences due to overconsolidation ratio

The monotonic load response of the suction caissons in highly overconsolidated kaolin (1-g load tests in kaolin) displayed a strain-softening response when loaded without any prior cycling. The suction caissons in lightly overconsolidated kaolin (90-g load tests in kaolin) displayed a strain-hardening behavior when loaded without any prior cycling. This type of behavior generally follows the behavior of element undrained strength tests on highly overconsolidated clays and lightly overconsolidated clays (Terzaghi et al. 1996). This behavior, however, was contingent on no significant prior foundation displacements occurring before the monotonic undrained compression or uplift loading. Cycling above the elastic threshold described in Section 7.2.6 or significant displacement due to prior compression loading caused the behavior to transition from strain-softening to strain-hardening.

7.2.5 Critical nature of load induced pore pressure generation

The 90-g load tests in kaolin allowed for the testing of two different loading rates during the monotonic load tests. The rapid loading rate resulted in non-dimensional velocities that were significantly within the range indicating undrained loading. The slow loading rate, however, was very close to the threshold between undrained loading and partially drained loading conditions. Due to the inherent variability of soil and potential for the introduction of variations due to research environments, the possibility of these loading rates falling into the partially drained loading conditions were possible. The comparison of the rapid and slow load tests indicated that the mobilized foundation resistances in uplift were highly dependent on the generation of pore water pressures within the suction caisson during loading. This was especially true during uplift where the mobilization of a reverse bearing capacity failure requires negative excess pore water pressures to be generated in the suction caisson cavity to ensure the plug moves upward with the foundation. Any drainage generated a pull out failure where the resistance of the foundation was mobilized primarily via side resistance on the inside and outside of the skirt walls. In compression, the mobilized resistances of the slow load tests were lower than those of the rapid load tests. These increases in resistance could not be accounted for simply by the increase in undrained shear strength due to loading rate indicating that the compression resistance was influenced by the potential for drainage to occur in the plug. Any drainage would allow for plug compression during loading.

7.2.6 Elastic threshold and cyclic degradation

The undrained cyclic loading of the suction caisson displayed a zone of cyclic displacement amplitudes during which the cyclic load amplitude exhibited none to insignificant degradation with increasing number of cycles. Based on combining the results of 1-g and 90-g load tests in kaolin, this threshold was between 0.05% and 0.075% of the diameter and 0.0525% and 0.074% of the diameter for the AR1 and AR2 suction caissons respectively during vertical loading and was between 0.74% and 1.3% of the diameter and 0.96% to 1.8% of the diameter for the AR1 and AR2 suction caissons during horizontal loading. Undrained cycling that occurred at displacements higher than these values did exhibit cyclic degradation with increasing number of cycles. Similar behavior has been observed at the element level in clay (Mortezie and Vucetic 2016).

Partially drained cyclic loading exhibited capacity degradation with cycling for all tested amplitude as low as 0.0049% of the diameter for both AR1 and AR2 foundations. This indicated that the elastic threshold displacement for the partially drained and undrained case were different. Since the undrained and partially drained case resulted in different mobilized failure mechanism, a given reference foundation displacement does not correlate to the same element level soil strains across the two drainage conditions. For suction caissons, this resulted in larger foundation displacements required to reach the capacity degradation threshold strain in the undrained case than those in the partially drained case.

7.2.7 Extreme loading response

The extreme loading response was examined by monotonic load tests conducted post-cyclic load tests. This modeled a ship collision occurring after operation of the tidal current generator had occurred for a period of time. These post-cyclic monotonic load tests both at 1-g and 90-g in kaolin indicated that the extreme loading response was highly dependent on the displacement the suction caisson had undergone during cycling. In general, the peak capacity post-cycling decreased as the suction caisson underwent increasing cyclic displacement amplitudes. However, the displacement required to significantly decrease the peak capacity of these post-cyclic monotonic load tests in comparison to the ultimate capacity of the baseline load tests did not coincide with the threshold for elastic cycling behavior described in Section 7.2.6 and were typically 1 to 2 orders of magnitude greater. The threshold also did not match for the compression and uplift mechanisms. For the highly overconsolidated cases, the threshold

coincided with the displacement at which the ultimate capacity was mobilized or approximately 2% of the diameter.

The uplift mechanism provided an avenue for a more catastrophic failure during extreme loading events. This was due to the potential for failure at the plug connection to the soil test bed. Typically the plug failed after significant deformations. A response commonly described as ductile in material sciences. In cases where the failure surface was not significantly remolded due to prior undrained cycling (those in the elastic threshold range) or monotonic compression displacements, the plug failed after displacements < 5% of the suction caisson diameter resulting in a rapid decrease in uplift capacity.

7.2.8 Variation from API design recommendations

The 1-g and 90-g undrained baseline monotonic load tests in kaolin resulted in back-calculated values varying from the design recommendations provide by API RP 2SK (2008) and API RP 2GEO (2011) for suction caisson foundation design. The α values back-calculated from the presented load tests were 0.14 to 0.30 for the 1-g load tests in kaolin and 0.16 to 0.31 for the 90-g load tests in kaolin. The values recommended by API RP 2SK (2008) however were 0.63 for the 1-g load tests in kaolin and 0.59 for the 90-g load tests in kaolin. These design recommendations were based on utilizing the inverse of sensitivity implying that the failure mechanism occurred at a soil-soil interface. However, the lack of significant amounts of clay clinging to the outside skirt wall model foundations upon extraction indicated that the failure mechanism was a soil-structure mechanism. This soil-structure mechanism typically results in the reduction of the interface strength and therefore the decrease in the back-calculated values from the design recommended values of α.

The 1-g and 90-g undrained baseline monotonic load tests in kaolin resulted in back-calculated N_c values that were higher than those recommended by API RP 2GEO (2011). The N_c value recommendations were derived from Skempton (1951) resulted in design recommendations of 7.6 and 8.4 for aspect ratios of 1 and 2. The 1-g load tests resulted in N_c values of 11.7 to 14.6 when using the α values back-calculated from installation phases. The 90-g load tests resulted in N_c values of 9.8 to 15.5 when using the α values back-calculated from installation phases. These back-calculated values were higher than those recommended by Skempton (1951), but were within the range of bearing capacity factors for the cone

penetrometer of 10 to 20 (Robertson 2009). The laponite load tests resulted in deformation visualizations indicating a failure mechanism with similarities to that of the CPT in clay. These back-calculated values also coincide with those from previous studies of El-Sherbiny (2005) and Luke et al. (2005) of 6 to 16.

7.3 Final design recommendations

Based on the summary and synthesis of the results of the three types of load tests described above, the following design recommendations were made regarding suction caisson foundations for tidal energy applications:

1. The multi-pod configuration will likely provide the more economical and efficient foundation option as it transmits the current loads on the structure as vertical loads on the foundations.
2. Careful consideration of the current design recommendations for α values and N_c values must be made when considering both values independently. In general, the overestimation of α values (by approximately 50%) and underestimation of N_c values (by approximately 30%) will offset one another in design if both are considered. However, in cases when only side resistance is factored an overestimate in capacity may occur. Additionally, the differing α values for the installation phase and monotonic loading phase as defined by API RP 2SK (2008) and API RP 2GEO (2011) are not recommended as the mechanism of the mobilization of unit side resistance will not differ between the two phases. Ideally, α values back-calculated during an installation phase should be utilized to update the monotonic capacity on site.
3. The potential for plug failure to occur after relatively small uplift displacements during extreme loading conditions must be examined to prevent a rapid decrease of foundation capacity.
4. Cyclic capacity degradation must be accounted for in design as designing the suction caissons to operate in the range of cyclic displacements that exhibit insignificant capacity degradation will likely not be ideal for the following reasons:

a. The resistance mobilized at these low displacements would likely result in an inefficiently oversized footings when considering monotonic capacities.
b. The low cyclic displacements would result in little to remolding of the failure surface resulting in the increase potential for plug failure to occur in a ‘brittle’ manner rather than a ‘ductile’ manner.

7.4 Future work

While this study allowed for significant observations into the response of suction caisson foundations during loading conditions applicable to tidal energy converters, it also provides additional avenues of research to further investigate behaviors that were outside of the scope of the load tests conducted during this research study. The following is a list of a small selection of these potential areas for research:

1. Investigation of the progression of the failure mechanism beneath the suction caisson during cycling and its correlation to the observed threshold of elastic foundation response
2. Determining the correlation of the element level threshold strain to the foundation threshold displacement at which cyclic degradation is observed
3. Whether the shear induced pore pressures during short period cycling will influence the response of the foundation during the long period cycling that occurs simultaneously
4. Improvement of the laponite displacement visualization method to allow for visualization of deformation during significantly smaller strains
5. Scaling effects of element level behavior to field scale foundations

7.5 Figures

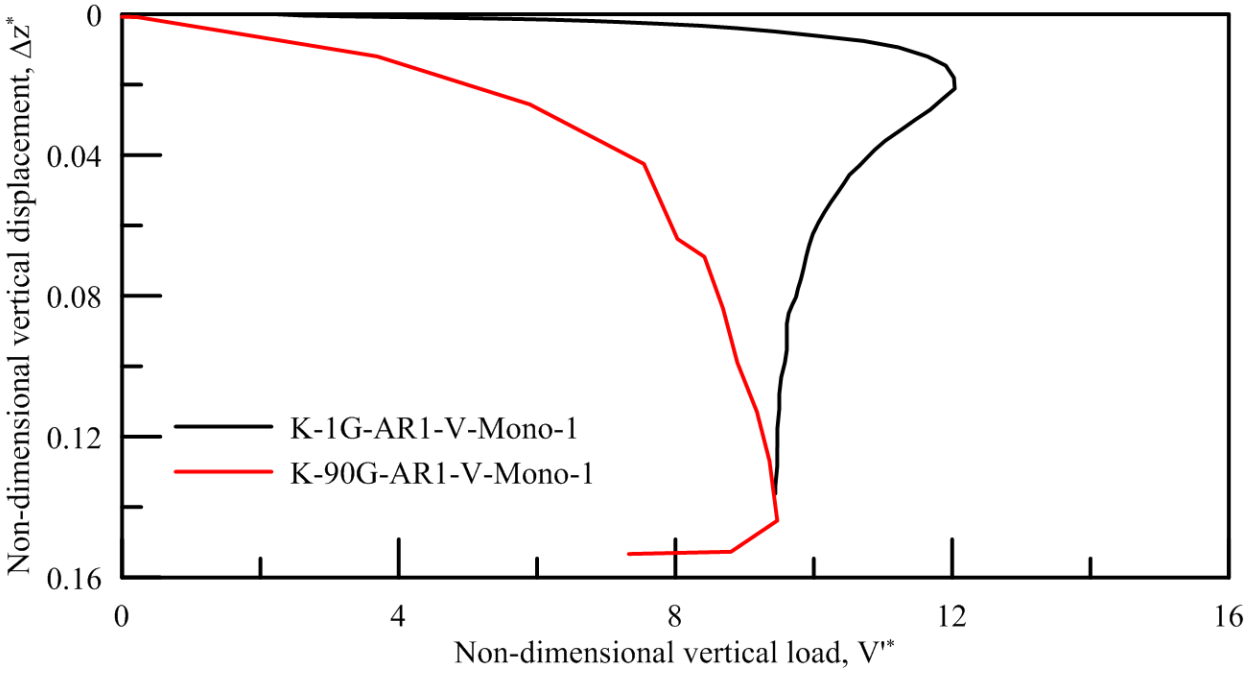

Figure 7.1: Comparison of the undrained monotonic compression load test of K-1G-AR1-V-Mono-1 and K-90G-AR1-V-Mono-1

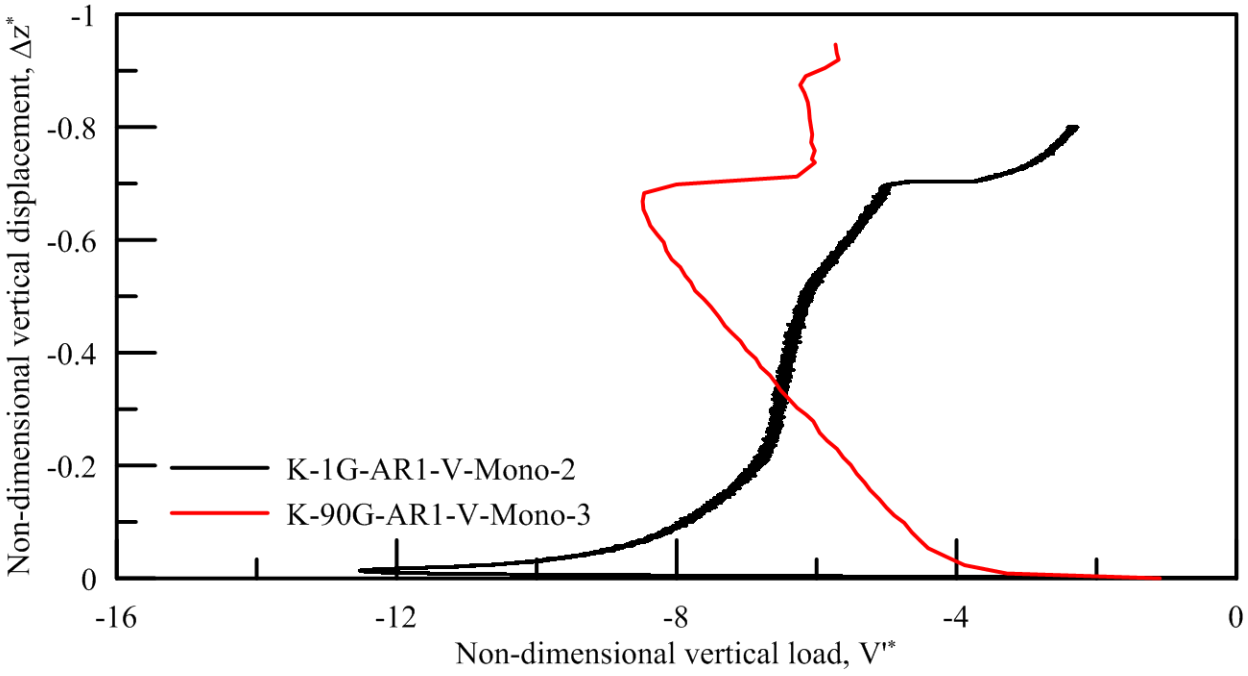

Figure 7.2: Comparison of the undrained monotonic compression load test of K-1G-AR1-V-Mono-2 and K-90G-AR1-V-Mono-3

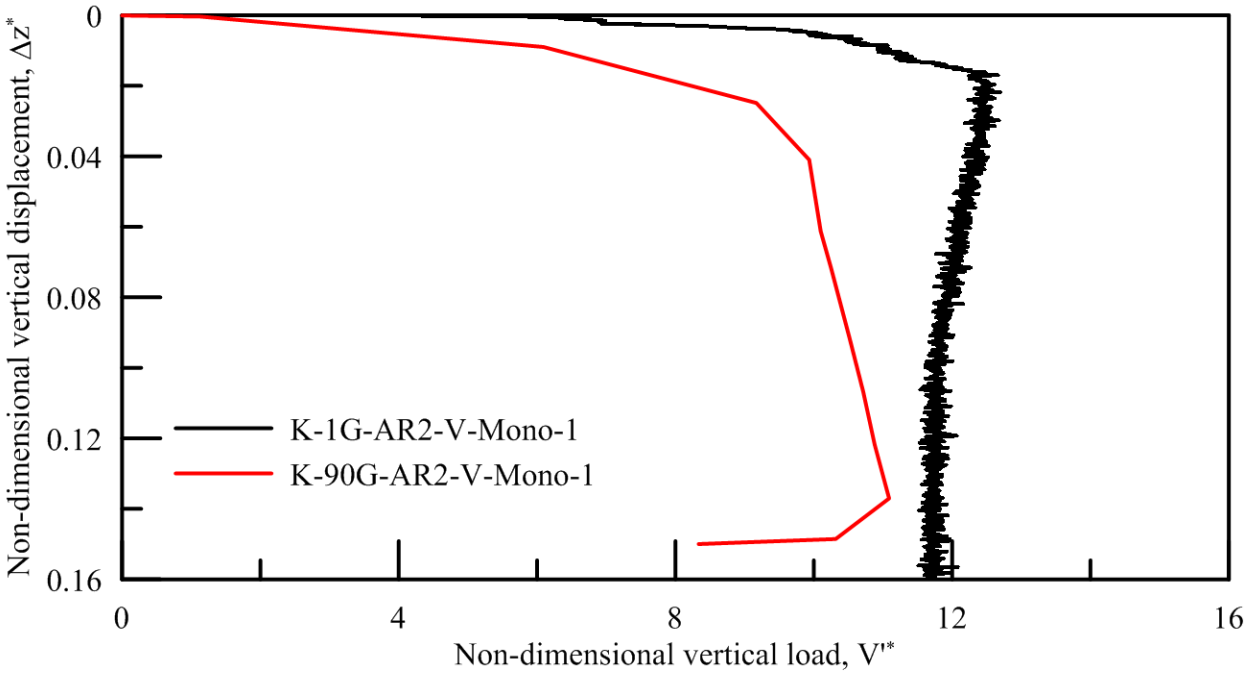

Figure 7.3: Comparison of the undrained monotonic compression load test of K-1G-AR2-V-Mono-1 and K-90G-AR2-V-Mono-1

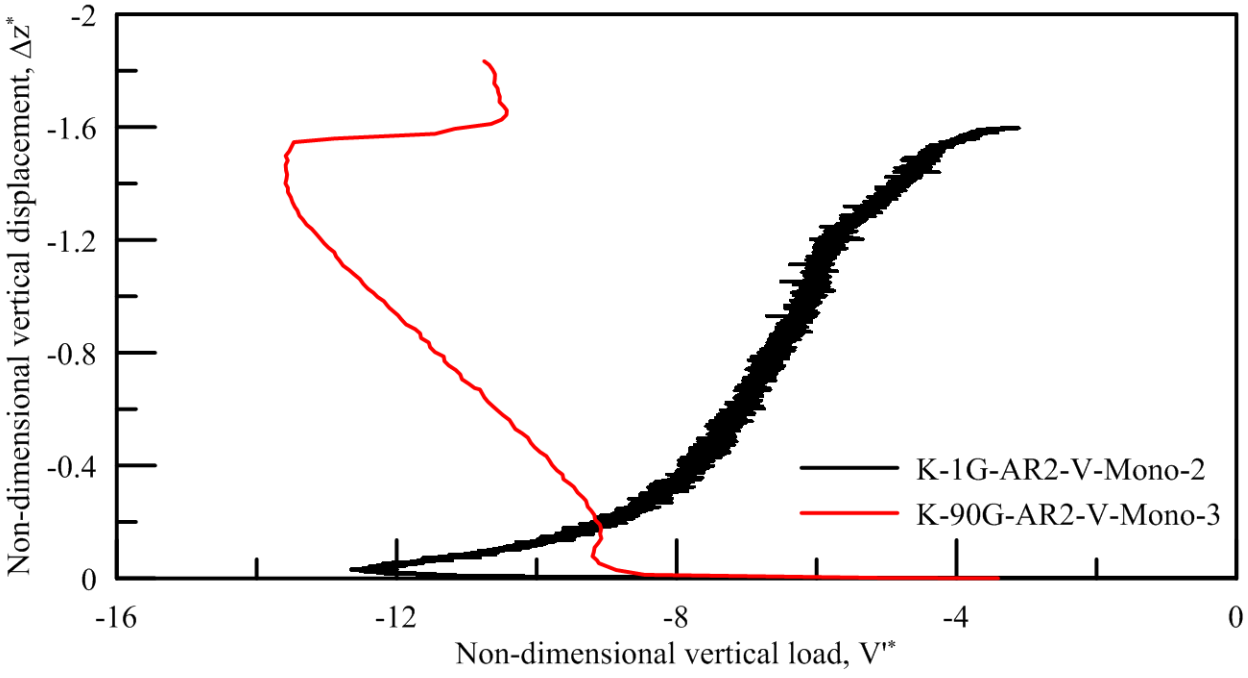

Figure 7.4: Comparison of the undrained monotonic compression load test of K-1G-AR2-V-Mono-3 and K-90G-AR1-V-Mono-4

7.6 References

API RP 2GEO. (2011). "Geotechnical and Foundation Design Considerations." ANSI/API Recommended Practice 2GEO, First Edition, American Petroleum Institute.

API RP 2SK. (2008). "Design and Analysis of Stationkeeping Systems for Floating Structures." API Recommended Practice 2SK, Third Edition, American Petroleum Institute.

Chini, C.M., Wallace, J.F., Rutherford, C.J. & Peschel, J.M. (2015). "Shearing Failure Visualization Using Digital Image Correlation and Particle Image Velocimetry in Soft Clay Using a Transparent Soil." *Geotech. Test. J.* 38(5):1-17.

Einav, I. & Randolph, M.F. (1990). *Manual for estimating soil properties for foundation design*. Electrical Power Research Institute. Polo Alto, California, USA.

El-Sherbiny, R. (2005). Performance of Suction Caisson Anchors in Normally Consolidated Clay. Ph.D. Dissertation, The University of Texas at Austin.

Kelly, R.B., Houslby, G.T. & Byrne, B.W. (2006). "A comparison of field and laboratory tests of caisson foundations in sand and clay." *Geotechnique*. 56(9):617-626.

Luke, A.M., Rauch, A.F. Olson, R.E. & Mecham, E.C. (2005). "Components of suction caisson capacity measured in axial pullout tests." *Ocean Engineering.* 32:878-898.

Mortezaie, A. & Vucetic, M. (2016). "Threshold Shear Strains for Cyclic Degradation and Cyclic Pore Water Pressure Generation in Two Clays." *Journal of Geotechnical and Geoenvironmental Engienering*. 142(5):1-14.

Skempton, A.W. (1951). "The bearing capacity of clays." *Proceedings, Building Research Congress*. London, UK.

Terzaghi, K., Peck, R.B., & Mesri, G. (1996) *Soil Mechanics in Engineering Practice*. 3rd Edition. John Wiley & Sons, Inc. New York City, New York, USA.

Weemees, L., Howie, J., Woeller, D., Sharp, G., Cargill, E. & Greig, J. (2006). "Improved techniques for the in-situ determination of undrained shear strength of soft clays." *Sea to sky géotechnique*. Canadian Geotechnical Society, Richmond, Canada. 89-95.

APPENDIX A. "GEOTECHNICAL PROPERTIES OF LAPONITE RD®" ARTICLE

The journal article "Geotechnical Properties of Laponite RD®" where the author of this dissertation was the first author is attached to this document as a supplemental electronic file. This article provides the results of a series of laboratory tests conducted as verification of laponite as an offshore soft clay surrogate. The laponite material was utilized in this study to visualize the deformations of soft clay beneath suction caisson foundations as described primarily in CHAPTER 6.